Cross-correlation searches for persistent gravitational waves with Advanced LIGO and noise studies for current and future ground-based gravitational-wave detectors.

A DISSERTATION
SUBMITTED TO THE FACULTY OF THE GRADUATE SCHOOL
OF THE UNIVERSITY OF MINNESOTA
BY

Patrick Michael Meyers

IN PARTIAL FULFILLMENT OF THE REQUIREMENTS
FOR THE DEGREE OF
DOCTOR OF PHILOSOPHY

Vuk Mandic

May, 2018

Acknowledgements

First, thanks to Vuk for being supportive, kind, and endlessly enthusiastic about my work over the last six years. I could not think of any other person for (and with) whom I would rather work. You are someone who I try to model myself after every day.

Next, a thank you to Michael Coughlin, who I met my first week working with LIGO, has become a great friend, and who has more patience (and somehow more time) for my BS than almost anyone else.

I want to give a special thanks to Nelson Christensen, Eric Thrane, and Gwynne Crowder, who have had as much of an influence on the scientist and researcher I am today as anyone else (I hope you take that as a compliment!). Your support and encouragement has meant the world to me.

Next comes a shout out the Minnesota LIGO group. Thanks to Tanner Prestegard and Sharan Banigiri for putting up with me as an office mate. Rich Ormiston, your passion for vim and zsh (and life) is perhaps unparalleled. Shivaraj, thank you for knowing everything. Finally, thanks to Andrew Matas for sitting with me at lunch while I complain about everything.

Ive had the privilege of working with quite a few wonderful scientists in the Stochastic group over the last several years, including (but certainly not limited to!) Letizia Sammut, Joe Romano, and Tom Callister. I learn something new every time we talk!

A big thanks to the members of the Detector Characterization group. Especially to Josh Smith, Andy Lundgren, Laura Nuttall, Jess McIver, Duncan Macleod, and Keith Riles. I have learned a tremendous amount from all of you. Your leadership, both in terms of science and in terms of promoting inclusion and mutual respect among members of the LIGO Collaboration have made working with you a delight.

I also want to thank Victor Tsai, Daniel Bowden, Gary Pavlis, Ross Caton, Terry

Stigall, and Tom Regan, as well as the rest of the SURF staff for their tremendous work on the Homestake seismic array project. The project was a pleasure to work on, as much because of the people involved as the science we have done!

A thanks to the friends I have made this journey with in the UMN physics department. I will miss spending time and working with all of you!

The last of the physics-related thanks goes to my first physics teachers: Cicc and Mal at Penncrest and the whole Kenyon College physics department. Your enthusiasm is what pushed me into and kept me moving on this journey that started ten years ago.

My family is nothing if not supportive and always excited to hear about science! I will not name everyone, but the enthusiasm you all show for my research and the support you have given over the last several years has helped me through some very tough times.

Finally, a huge thanks to Zach and the whole Lesko family for treating me like one of their own. I hope someday I will be able to return that kindness.

Dedication

For Dad, Mom, and Travis.

Abstract

Over the last three years, the Advanced Laser Interferometer Gravitational-wave Observatory (LIGO) has detected signals from colliding black holes and a signal from colliding neutron stars. These detections ushered in a new era of gravitational-wave (GW) astrophysics and multimessenger astronomy that allows us to probe new regions of the universe. One of the next frontiers for gravitational-wave astronomy is the detection and characterization of the stochastic GW background (SGWB). A measurement of the SGWB from unresolved compact binary systems could come as Advanced LIGO reaches design sensitivity, and future detectors will be important for digging beyond that astrophysical background towards trying to measure signals from relic gravitational waves produced in the early universe.

In this dissertation, I present cross-correlation-based searches for a SGWB and other persistent sources of GWs. I introduce and use a new method for setting limits on the strain amplitude of a potential source of GWs in the directions of Scorpius X-1, the galactic center, and Supernova 1987a in the frequency band from $20 - 1726$ Hz. I also set limits on persistent, broadband point sources of GWs across the whole sky. Finally, I show how we can implement data analysis techniques to improve the Advanced LIGO detector sensitivity to persistent sources of GWs.

Improving sensitivity of current detectors and planning for future detectors is vital to the effort to measure and understand the SGWB. This will requires a better understanding of the noise sources that limit sensitivity, especially at lower frequencies. To this end, I outline a method for estimating and modeling correlated magnetic noise between spatially separated GW detectors. I also present results from a 3D seismometer array deployed at the Homestake Mine, aimed at characterizing seismic and Newtonian noise for future GW detectors. I estimate the fundamental Rayleigh-wave eigenfunction, and then use it in a seismic radiometer algorithm to separate different components of the seismic field that contribute differently to the Newtonian noise. Finally, I present estimates of the Newtonian noise as a function of depth in the frequency band from $0.5 - 5$ Hz based on results from the seismic radiometer.

Contents

List of Tables

List of Figures

Chapter 1

Gravitational waves and detectors

Einstein's theory of general relativity (GR), published in 1915, marked a paradigm shift in the understanding of gravitational physics [2]. Since that publication, GR has passed every test posed to it. One prediction of GR is the existence of gravitational waves (GWs), which are weak perturbations to the spacetime metric that satisfy the wave equation. GWs were not indirectly observed until the discovery of the Hulse-Taylor binary pulsar system in 1974 [3] and subsequent analysis by Weisberg and Taylor [4]. The first direct measurement did not come until the detection of the merger of two black holes in 2015 by the LIGO Scientific Collaboration [5].

Early GW detectors were resonant bar detectors [6], but today most GW detectors are ground-based interferometric detectors like Advanced LIGO [7], Advanced Virgo [8], KAGRA [9], GEO [10], and the planned LIGO India detector. There are also two proposed ground-based experiments known as Cosmic Explorer [11] and Einstein Telescope [12], and a proposed (now approved) space-based detector, LISA [13]. All of these detectors seek to directly measure the distance change between separated test masses due to passing GWs.

Since the first directly observed signal due to the inspiral and merger of two black holes, several similar signals have also been seen [14, 15, 16, 17]. In August 2017, the merger of two neutron stars was detected, first with GWs [18], two seconds later with a short gamma ray burst, and then in the entire electromagnetic spectrum in the days and weeks that followed [19].

In this chapter, we offer a brief introduction on the mathematical formalism of general relativity and gravitational waves in section 1.1. This includes a discussion of different sources of GWs in section 1.2. We then discuss ground-based interferometric GW detectors, with an emphasis on the Laser Interferometer Gravitational-wave Observatory in section 1.3.

1.1 General relativity and gravitational waves

1.1.1 Notation and definitions

Throughout this chapter we use a Minkowski spacetime metric given by

$$\eta_{\mu\nu} = \mathrm{diag}(-1, 1, 1, 1). \tag{1.1}$$

We also use Einstein summation notation, where we implicitly assume a sum over repeated indices. Greek indices $(\mu, \nu, \ldots)$ will be assumed to run from 0 to 3, while latin indices $(i, j, \ldots)$ will be assumed to run from 1 to 3 and indicate spatial coordinates. Finally, commas denote partial derivatives with respect to a specific coordinate. For example, the partial derivative acting on a vector field ξ^μ is written as

$$\frac{\partial \xi^\mu}{\partial x^\nu} = \xi^\mu{}_{,\nu}. \tag{1.2}$$

We will use $g_{\mu\nu}$ for the general spacetime metric, which defines for us proper distances between spacetime events that are separated by dx^μ

$$ds^2 =_{\mu\nu} dx^\mu dx^\nu. \tag{1.3}$$

From the spacetime metric, we can define the Christoffel symbols

$$\Gamma^\rho_{\mu\nu} = \frac{1}{2} g^{\rho\sigma}(g_{\sigma\mu,\nu} + g_{\sigma\nu,\mu} - g_{\mu\nu,\sigma}), \tag{1.4}$$

and then Riemann curvature tensor, which tells us about the geometry of spacetime

$$R^\mu_{\ \nu\rho\sigma} = \Gamma^\mu_{\nu\sigma,\rho} - \Gamma^\mu_{\nu\rho,\sigma} + \Gamma^\mu_{\alpha\rho}\Gamma^\alpha_{\nu\sigma} - \Gamma^\mu_{\alpha\sigma}\Gamma^\alpha_{\nu\rho}. \tag{1.5}$$

There are two useful quantities related to the Riemann curvature tensor, known as the

Ricci tensor and the Ricci scalar

$$R_{\mu\nu} = g^{\sigma\rho} R_{\sigma\mu\rho\nu} \tag{1.6}$$
$$R = g^{\mu\nu} R_{\mu\nu}.$$

We will use most of these definitions in the course of the coming discussion of general relativity and gravitational waves.

1.1.2 The Einstein field equations

The Einstein field equations relate the curvature of spacetime to mass and energy. They are succinctly written as

$$G_{\mu\nu} = \frac{8\pi G}{c^4} T_{\mu\nu}. \tag{1.7}$$

In this case, $G_{\mu\nu}$ is the Einstein tensor, and it carries with it information about the curvature of spacetime. $T_{\mu\nu}$ is the stress-energy tensor, and it describes the mass and energy that create that curvature. G is Newton's constant and c is the speed of light. The Einstein tensor is defined in terms of the Ricci tensor and Ricci scalar

$$G_{\mu\nu} = R_{\mu\nu} - \frac{1}{2} g_{\mu\nu} R. \tag{1.8}$$

1.1.3 The weak field limit

In the weak field limit, we write our general spacetime metric as the sum of the Minkowski metric of special relativity with some small perturbation

$$g_{\mu\nu} = \eta_{\mu\nu} + h_{\mu\nu}, \text{ where } |h_{\mu\nu}| \ll 1. \tag{1.9}$$

If we substitute this into the expression for the Riemann curvature tensor in equation (1.5) and only keep terms to leading order in h, we find

$$R_{\mu\nu\rho\sigma} = \frac{1}{2} \left(h_{\mu\sigma,\nu\rho} + h_{\nu\rho,\mu\sigma} - h_{\nu\sigma,\mu\rho} - h_{\mu\rho,\nu\sigma} \right). \tag{1.10}$$

From here, it is customary to define a "trace-reversed" metric $\bar{h}_{\mu\nu} = h_{\mu\nu} - \frac{1}{2}\eta_{\mu\nu} h$ where $h = \eta^{\mu\nu} h_{\mu\nu}$. Making this substitution and calculating the Ricci tensor and Ricci scalar allows us to write the Einstein tensor in terms of this trace-reversed perturbation and substitute it into the field equations:

$$\bar{h}_{\mu\nu,\rho}{}^{\rho} + \eta_{\mu\nu}\bar{h}_{\rho\sigma}{}^{,\rho\sigma} - \bar{h}_{\mu\rho,\nu}{}^{\rho} - \bar{h}_{\nu\rho,\mu}{}^{\rho} = -\frac{16\pi G}{c^4}T_{\mu\nu}. \tag{1.11}$$

1.1.4 The transverse trace-less gauge

We still have gauge freedom that we can use to simplify our expressions, which we can see by looking at how $\bar{h}_{\mu\nu}$ transforms under a small coordinate transformation. If we take $x^\mu \to x^\mu + \xi^\mu$, and we assume that $|\xi^\mu{}_{,\nu}|$ are of order $|h_{\mu\nu}|$, then

$$\bar{h}'_{\mu\nu} = \bar{h}_{\mu\nu} - (\xi_{\nu,\mu} + \xi_{\mu,\nu} - \eta_{\mu\nu}\xi^{\rho}{}_{,\rho}) \tag{1.12}$$

and under this transformation the Riemann curvature tensor does not change to leading order in h. This means we have found a symmetry in our linearized theory, and we are free to choose ξ^μ as we like (so long as it satisfies our one constraint that its derivatives are small). Specifically, we will choose it such that

$$\bar{h}_{\mu\nu}{}^{,\nu} = 0 \tag{1.13}$$

which is known as “harmonic gauge.” We are free to make this choice because, under the same coordinate transformation, this expression transforms as

$$\bar{h}'_{\mu\nu}{}^{,\nu} = \bar{h}_{\mu\nu}{}^{,\nu} - \Box\xi_\mu, \tag{1.14}$$

where $\Box\xi_\mu \equiv \xi_{\mu,\rho}{}^{\rho}$ is the d’Alembertian. Since the d’Alembertian is invertible, we can always find ξ_μ such that it satisfies $\Box\xi_\mu = \bar{h}_{\mu\nu}{}^{,\nu}$. In this case equation (1.11) reduces to

$$\bar{h}_{\mu\nu,\rho}{}^{\rho} = -\frac{16\pi G}{c^4}T_{\mu\nu}. \tag{1.15}$$

We will consider only cases away from sources, so that we are in a region of space where $T_{\mu\nu} = 0$. In this case, it is common to make $\bar{h}_{\mu\nu}$ traceless and transverse. That is, we choose $\bar{h} = 0$, and $h^{0i} = 0$. The harmonic gauge condition in equation (1.13) coupled with these assumptions defines what is known as “transverse-traceless gauge.”

1.1.5 Waves and polarizations

When we are in free space and have moved to transverse traceless gauge, it is clear that the field equations reduce to a set of wave equations, and so the simplest solution is

$$h_{\mu\nu}^{\mathrm{TT}} = A_{\mu\nu}^{\mathrm{TT}} e^{ik_\alpha x^\alpha} \tag{1.16}$$

which we call a gravitational wave[1]. In this case, k_α is the wave-vector, which is consistent with a wave that travels at the speed of light (i.e. $k_\alpha k^\alpha = 0$). Our gauge condition also tells us that we have a transverse wave $h_{\mu\nu}^{\mathrm{TT}} k^\nu = 0$.

If we choose a coordinate system where the wave travels along the z axis then we can easily write down the amplitude from our wave equation, $A_{\mu\nu}^{\mathrm{TT}}$

$$A_{\mu\nu}^{\mathrm{TT}} = \begin{pmatrix} 0 & 0 & 0 & 0 \\ 0 & h_+ & h_\times & 0 \\ 0 & h_\times & -h_+ & 0 \\ 0 & 0 & 0 & 0 \end{pmatrix}. \tag{1.17}$$

The full perturbation in transverse-traceless gauge now reads $h_{\mu\nu}^{\mathrm{TT}}(z,t) = A_{\mu\nu}^{\mathrm{TT}} \cos(\omega t - kz/c)$. In this case we use h_+ and $h_\times$ to define our two polarizations. We can decompose this onto a set of polarization tensors that we call $e_{\mu\nu}^{+}$ and $e_{\mu\nu}^{\times}$

$$e_{\mu\nu}^{+} = \begin{pmatrix} 0 & 0 & 0 & 0 \\ 0 & 1 & 0 & 0 \\ 0 & 0 & -1 & 0 \\ 0 & 0 & 0 & 0 \end{pmatrix}, \; e_{\mu\nu}^{\times} = \begin{pmatrix} 0 & 0 & 0 & 0 \\ 0 & 0 & 1 & 0 \\ 0 & 1 & 0 & 0 \\ 0 & 0 & 0 & 0 \end{pmatrix} \tag{1.18}$$

so that $A_{\mu\nu}^{\mathrm{TT}} = h_+ e_{\mu\nu}^{+} + h_\times e_{\mu\nu}^{\times}$.

1.1.6 The effect of GWs on separated test masses

Consider two test masses separated in space, initially with coordinates $(t, x_1, 0, 0)$ and $(t, x_2, 0, 0)$ in the TT gauge. These could be the input and end test mass for one of the

---

[1] The superscript (TT) reminds us that we are working in transverse-traceless gauge.

interferometer arms in figure 1.3, for example. In TT gauge the coordinate distance, (x_2 - x_1) between these two test masses remains constant due to a passing GW[2]. However, the proper distance between these events changes as a gravitational wave (GW) propagates in the z direction, and is given by equation (1.3)

$$s = \sqrt{ds^2} = (x_2 - x_1)(1 + h_+ \cos(\omega t))^{1/2} \approx (x_2 - x_1)\left(1 + \frac{1}{2}h_+ \cos(\omega t)\right) \tag{1.19}$$

For two similar test masses separated only in the y-direction (but with the same x and t-coordinates) we would have

$$s = \sqrt{ds^2} \approx (y_2 - y_1)\left(1 - \frac{1}{2}h_+ \cos(\omega t)\right). \tag{1.20}$$

and so we can see that GWs will cause the proper distance to increase for events separated in the x-direction, while it decreases for events separated in the y-direction. More generally, for two events with the same time coordinate, but separated spatially by vector $\vec{l}$ we can write down the proper distance

$$s^2 = l_i l_i + h_{ij}(t) l_i l_j. \tag{1.21}$$

It is worth noting that the change in the proper distance is proportional to the initial spatial separation between the two events. This is the motivation for the very long arms of the GW interferometers we will discuss in section 1.3. In figure 1.1 we show the effect of a plus-polarized (top) and a cross-polarized (bottom) GW moving into the page on a ring of test masses.

1.1.7 Generation of GWs

A full treatment of the generation of GWs is beyond the current scope, but it involves inversion of equation (1.15) using the Green's function of the d'Alembertian [20]. GWs are generated by a time-varying mass quadrupole moment

$$h_{ij}^{\mathrm{TT}} = \frac{2G}{c^4 r}\ddot{I}_{ij}(t - r/c) \tag{1.22}$$

---

[2] This can be seen by looking at the equation of geodesic deviation between the two test masses. A good discussion can be found in [20]

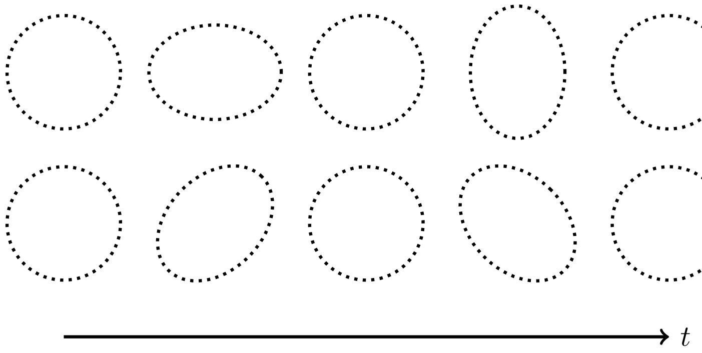

Figure 1.1: The top line shows effect of a plus-polarized GW propagating into to the page on a ring of test masses. The bottom line shows effect of cross-polarized GW propagating into the page on a ring of test masses.

where r is the distance between the observer and the source, G is Newton's constant, c is the speed of light and $\ddot{I}_{ij}$ is the spatial part of the trace-free mass quadrupole moment, which is written in terms of the mass density ρ

$$I_{ij} = \int dx^3 \, \rho(t, \vec{x}) \left(x_i x_j - \frac{1}{3} \delta_{ij} |\vec{x}|^2 \right) . \tag{1.23}$$

The pre-factor of $G/c^4 \sim 10^{-44}$ N^{-1} means that very energetic events are needed to generate GWs that could be detectable by ground-based instruments, which are typically sensitive to strains around 10^{-23} in their most sensitive frequency band. In [21], Saulson gave an estimate of the amplitude of GWs a distance r from two bodies of mass M rotating around one another with frequency f and a separation radius of r_0 for a reasonable set of parameters one could produce in a lab on Earth:

$$\begin{aligned} |h| &= \frac{32\pi^2 G}{rc^4} M r_0^2 f^2 && (1.24) \\ &= 9 \times 10^{-39} \left(\frac{M}{1000 \text{ kg}} \right) \left(\frac{300 \text{ km}}{r} \right) \left(\frac{r_0}{1 \text{ m}} \right)^2 \left(\frac{f}{1 \text{ kHz}} \right)^2 , && (1.25) \end{aligned}$$

which is much lower than the sensitivity of ground-based interferometric detectors.

1.2 Common sources of GWs

The strain sensitivity of the GW detectors we will discuss in section 1.3 is now $\sim 10^{-23}$ Hz$^{-1/2}$ in their most sensitive frequency bands. Equation (1.24) expresses the fact that to detect events at that strain level, we need to observe very energetic events. As we will discuss in chapter 2, sources of GWs that last for very long periods of time are detectable at levels below the typical noise in the instruments, but often require very long observation times. Here we discuss a few sources of GWs that are targeted by the current generation of GW detectors.

Compact binary systems

The merger of two black holes produced the first directly-detected GW signal [5]. Since that first detection several more binary black hole (BBH) signals have been detected [14, 15, 17], along with a binary neutron star (BNS) merger [18]. The latter was observed with an electromagnetic counterpart [19], kicking off the field of multi-messenger astronomy.

Compact binary systems radiate GWs as the two bodies orbit one another. The loss of energy in GWs results in a corresponding increase in the frequency of rotation and decrease in the radius of the orbit [22]

$$f_{GW}^{-8/3}(t) = \frac{(8\pi)^{8/3}}{5}\left(\frac{G\mathcal{M}}{c^4}\right)^{5/3}(t - t_c) \tag{1.26}$$

$$r^3 = GM/\omega^2 \text{ for keplerian orbits.} \tag{1.27}$$

In this expression, r is the semi-major axis of the orbit, ω is the angular velocity of the orbit, f_{GW} is the frequency of GWs being emitted, $\mathcal{M} = (m_1 m_2)^{3/5}(m_1 + m_2)^{-1/5}$ is the chirp mass, and t_c is the coalescence time, where the two compact objects get close enough that they merge together, forming a single remnant. As the binary system loses energy and the objects rotate faster around one another, the frequency of GWs emitted increases as well. This produces a characteristic "chirp"-like signal, so named because the frequencies happen in the audio band and the characteristic rise in frequency resembles the chirping of a bird. An example of the signal seen from the merger of black holes is shown in figure 1.2.

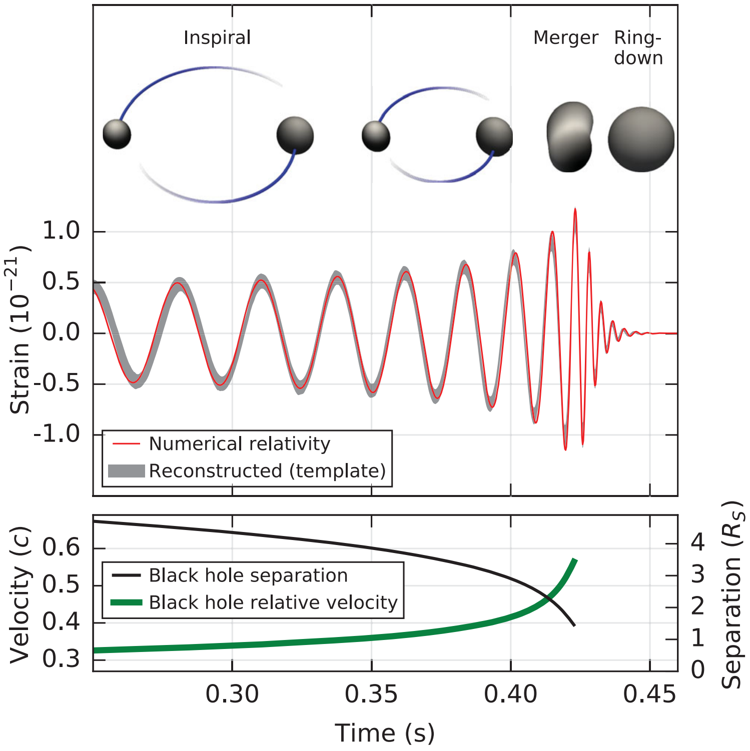

Figure 1.2: An example of a chirp signal from the merger of two black holes. The top illustrates numerical relativity estimates of the black hole horizons during the inspiral, merger, and ringdown phases. The middle shows the best-fitting waveforms with the estimated strain amplitude in the Hanford detector. This image is reproduced from [5].

Rapidly rotating neutron stars

Isolated, rapidly rotating neutron stars can produce GWs if they have some ellipticity. The characteristic amplitude of GWs produced by rapidly rotating neutron stars is given by [20]

$$h = \frac{16\pi^2 G}{c^4}\frac{\epsilon I_{zz} f^2}{r}, \tag{1.28}$$

where f is the rotation frequency of the neutron star, I is the principle moment of inertia, and $\epsilon = (I_{xx} - I_{yy})/I_{zz}$ is the ellipticity of the star.

Sources of this kind produce nearly-sinusoidal signals and last for very-long timescales.

Current searches tend to target known radio pulsars whose proposed GW emission frequency is in the frequency band of GW detectors, as well as directions where one expects a rotating neutron star to exist (a supernova remnant, for example) [23, 24, 25]. Searches that observe for very long periods of time can find signals that are well below the typical noise-level of the detectors.

Supernovae

Full-scale simulations of supernovae is a common area of research, but there is not a shortage of schemes in which a core-collapse supernova can generate GWs. A few include neutrino-driven convection, standing-shock instabilities (SASIs), and r-mode pulsations in the resulting protoneutron star [26]. GWs from core-collapse supernovae are expected to last for, at most $\mathcal{O}(\mathrm{s})$, and their GW signature is not well-modeled. This means that searches for these signals typically focus on finding large bursts of coincident power in multiple GW detectors [26, 27].

Stochastic background

The stochastic gravitational wave background (SGWB) is a superposition of unresolved sources of GWs in the universe. One of the most promising sources right now is the background due to unresolved compact binary coalescences [28]. Other sources could include the combined signal from unresolved, rapidly rotating neutron stars in the Milky Way galaxy [29], and relic GWs from the earliest epochs of the universe [30, 31, 32]. The stochastic background is typically defined in terms of a dimensionless energy density parameter

$$\Omega_{\mathrm{GW}}(f) = \frac{f}{\rho_c}\frac{d\rho_{\mathrm{GW}}}{df} \tag{1.29}$$

where ρ_c is the critical energy density to close the universe, and ρ_{GW} is the energy density in GWs, which is given by [20]

$$\rho_{\mathrm{GW}} = \frac{c^2}{32\pi G}\langle \dot{h}_{ij}^{\mathrm{TT}}\dot{h}_{ij}^{\mathrm{TT}}\rangle. \tag{1.30}$$

We will discuss sources for a SGWB further in chapter 2, as searching for a SGWB is a major focuses of this thesis.

Name	Dates	Operational instruments	# of published detections[3]
O1	September 2015 – January 2016	H1, L1	2
O2	November 2016 – August 2017	H1, L1, V1[4]	4

Table 1.1: Observation run dates and detections made with Advanced LIGO and Advanced Virgo instruments. H1 and L1 refer to the Advanced LIGO instruments in Hanford, WA, and Livingston, LA, respectively. V1 refers to the Advanced Virgo interferometer.

1.3 Advanced LIGO interferometers

The Laser Interferometer Gravitational-wave Observatory (LIGO) is a large, collaborative scientific project whose primary aim is the direct detection of GWs. The current incarnation of LIGO (known as "Advanced LIGO") consists of two identical, 4 km long interferometric detectors, in Hanford, WA, and Livingston, LA. The initial run of the LIGO instruments came from 2002-2007 and from 2009-2010, where strain sensitivities as low as $\sim 10^{-22}$ Hz$^{-1/2}$ were achieved, but no direct detection of GWs was made. From 2010-2015, the LIGO instruments underwent numerous upgrades and became known as Advanced LIGO. The first observing run for Advanced LIGO began in September, 2015, which kicked off the "advanced detector" era with an immediate detection of GWs from coalescing BBHs [5]. A summary of the Advanced LIGO and Advanced Virgo observation runs is given in table 1.1.

In this section we discuss the layout and configuration of the Advanced LIGO detectors, how they differ from their predecessors, and what noise sources limit the sensitivity of the instruments.

1.3.1 Detector description and layout

The Advanced LIGO instruments are Michelson interferometers with Fabry-Pérot cavities in the arms [7]. A depiction of the interferometer during the first observing run

---

[3] As of May 2018.

[4] Virgo was only operational during August 2017.

is given in figure 1.3. The instrument uses an Nd:YAG laser with a wavelength of $\lambda = 1064$ nm, currently operating at 25 W. The input and end mirrors for the cavities double as test masses, which are assumed to be freely falling at frequencies far above the resonant frequency of the pendulum system from which they are suspended (roughly 1 Hz). The instruments are configured such that when there is no GW passing, there is very little light moving towards the bottom photodetector, while when a GW is present, the length of the two arms changes differentially and the phase of the laser that has traveled through one arm is slightly different from that which has traveled through the other, and so there is a change in the power of the light at the bottom photodetector.

The Fabry-Pérot cavities are designed such that resonant light bounces many times within it before exiting. This increases the effective length of the interferometer, and therefore the phase shift imprinted on the light due to a passing GW. During O1, the light bounced within the cavity roughly 270 times [33].

Due to the fact that LIGO operates on a "dark fringe," meaning that very little light is sent to the output mode cleaner, most of the light leaves the system propagating back towards the laser. A power recycling mirror (PRM) is employed to recycle light leaving the system in this fashion back into the cavities, effectively increasing the power in the arms by a factor of 38 [33], and significantly reducing shot noise (discussed in the next section).

In a similar fashion to the PRM, there is also a signal recycling mirror (SRM), which recycles light that is leaving through the antisymmetric port (see figure 1.3) back into the arms. Tuning the length of this cavity can broaden the response of the interferometer's sensitivity. The SRM was a new implementation in the Advanced LIGO configuration that was not used in the initial instruments [33].

Finally, during the last run of the initial LIGO instruments, there was an addition of an output mode cleaner (OMC), which is a "bow tie" shaped cavity at the antisymmetric port that is used to reject unwanted modes in the laser that have been introduced in the arm cavities, and also filter out unwanted radio frequency sidebands on the light that are used for the Pound-Drever-Hall locking and control of different resonant cavities in the instrument [33, 34].

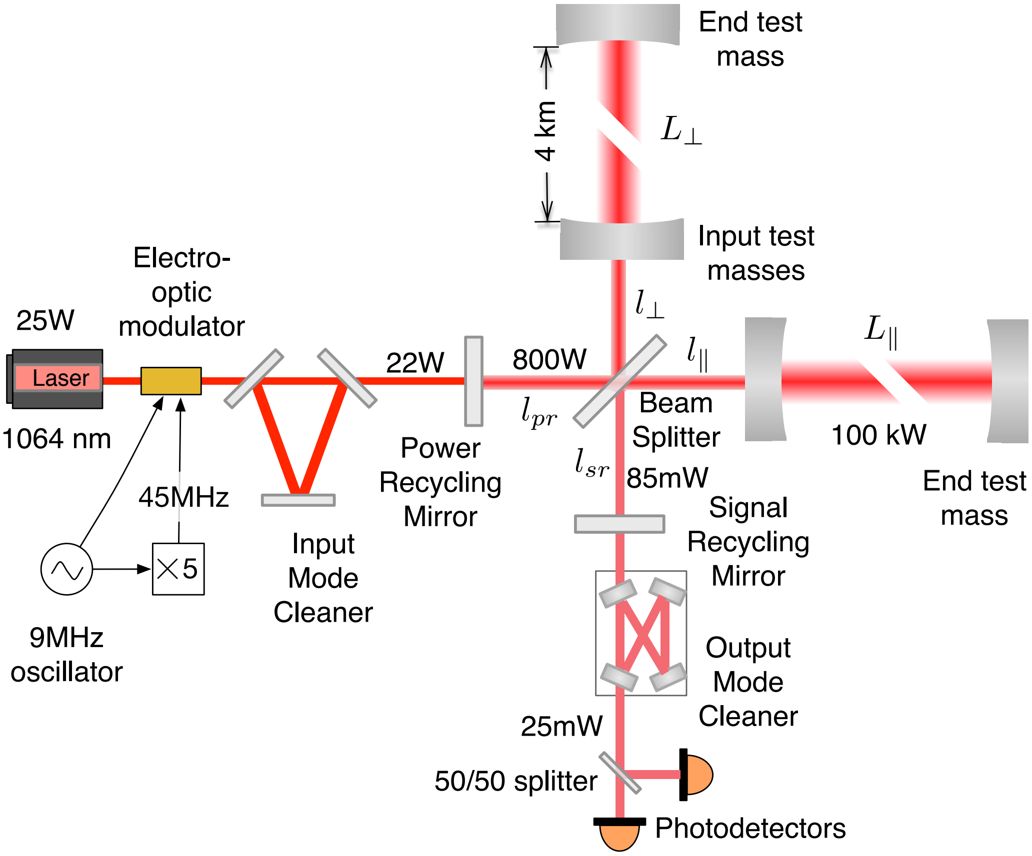

Figure 1.3: The Advanced LIGO interferometer layout, along with design values. We see several systems discussed in the text, including the input mode cleaner (IMC), the power recycling mirror (PRM), the Fabry-Pérot cavity arms, the signal recycling mirror (SRM), and the output mode cleaner (OMC). This plot is reproduced from Fig. 1 in [33].

1.3.2 Interferometer controls and calibration

The test masses typically move as much as 1 μm near the frequencies associated with the oceanic microseism, which is much larger than the wavelength of the laser. To keep the interferometer “locked” such that the change in the laser power leaving the OMC is linear with respect to the differential length of the two arms, the test masses are passively isolated using a quadruple pendulum system and actively controlled using a global feed-forward system and electrostatic actuation [35, 36, 37].

Similar control systems are needed at higher frequencies as well, and it is the error signal in the control loop for the differential arm motion that is proportional to the strain imposed by GWs. In general, there is a signal, s, sent to the end test masses where a reaction mass actuates directly on the end test mass with strength A. In addition, the configuration of the interferometer means that the output signal power is not directly proportional to the error signal, e, of that control loop. In the end the strain signal, h, is related to s and e via

$$h(f) = As + C^{-1}e \tag{1.31}$$

where C, known as the "optical transfer function," is a frequency-dependent quantity that depends upon the gain in power in the arms due to the presence of the PRM and the number of bounces in the Fabry-Pérot cavities. A full expression can be found for the O1 Advanced LIGO configuration in [33].

C is typically tracked with a "photon calibrator," which is a 2 W laser with $\lambda = 1047$ nm that applies a sinusoidally varying signal directly on the test masses themselves via radiation pressure. The known motion, h, induced by the radiation pressure can be used to track the properties of C as a function of time [38, 39].

1.3.3 Noise sources

Anything that can cause the mirrors to move is, in principle, indistinguishable from GWs. As we discuss in the next section, it is usually through a very specific signal seen in multiple detectors simultaneously, or the coincidence of a loud, coherent increase in power in multiple detectors, that we make a direct detections of GWs. However, the less the mirrors move due to anything other than GWs, the easier it is to make these detections. At low frequencies ($10-50$ Hz), the sensitivity is typically limited by seismic noise and noise in the optical angular control systems. At higher frequencies (>200 Hz) the noise is dominated by laser shot noise, and in between ($50-200$ Hz) we are limited by noise due to thermal fluctuations in the coatings used on the test masses. A plot indicating the estimated contribution from many different known sources of noise is shown in figure 1.5, at the end of this section. In the rest of this section, we discuss some of these noise sources in a bit more detail.

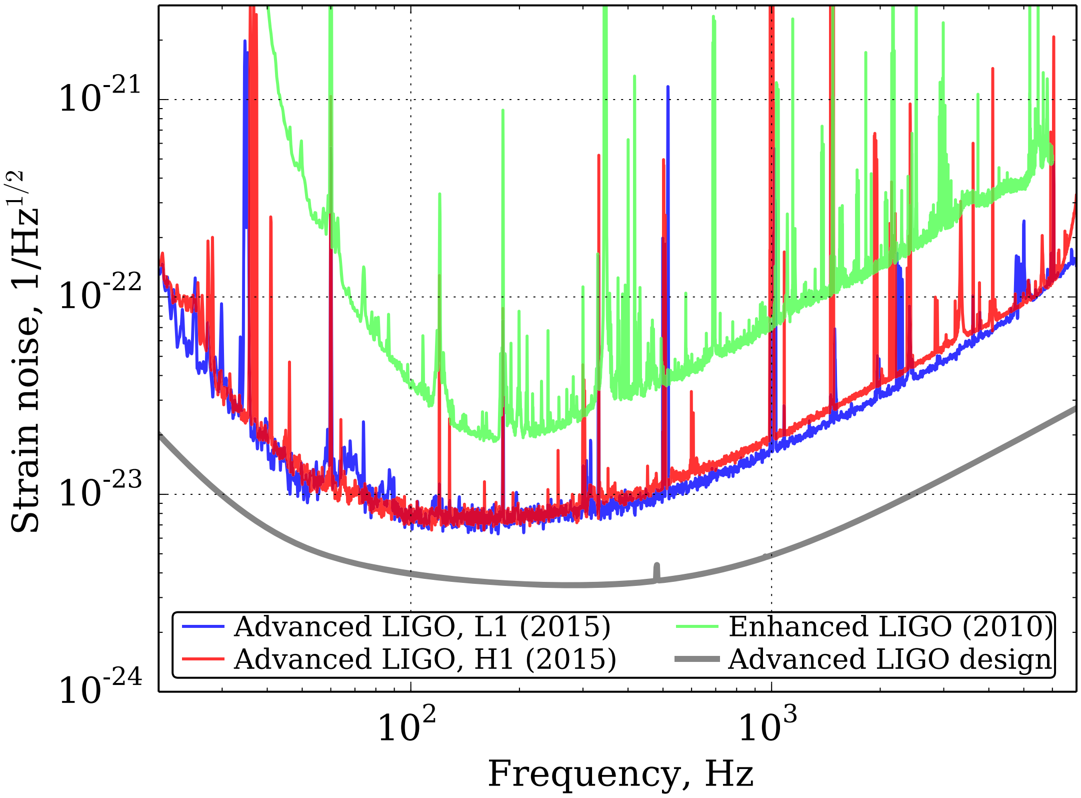

Figure 1.4: Sensitivity of Advanced LIGO detectors at the start of the first observing run. The sensitivity from the last science run of initial LIGO is also shown for comparison. Large spikes are typically caused by mechanical resonances in the suspensions of the test masses, or injected calibration signals. The most prominent resonances can be seen near 500 Hz, which are the "violin modes" of the suspension fibers for the test masses. This plot is reproduced from [33]

Seismic noise

Ground motion due to seismic waves can be as large as 10^{-9} m/$\sqrt{\text{Hz}}$ at 10 Hz, which is much larger than the Advanced LIGO goal sensitivity at that frequency. To isolate the test masses from ground motion, the Advanced LIGO input and end test masses are suspended from quadruple pendula. Each of the four pendula offers $(f/f_0)^{-2}$ suppression, where f_0 is the resonant frequency of the pendulum ($\sim 0.5 - 1$ Hz) [7]. Feed-forward schemes using seismometers on the ground and inertial sensors and actuators on the suspension platforms are also used to actively suppress motion of the platforms and the mirrors [7]. This isolation increases strain sensitivity, and is also vital to the process of bringing the interferometer into the "locked" regime where power at the antisymmetric point is linear with respect to the motion of the arms. The passive and active isolation helps reduce the time to it takes lock the instrument, improving the total observation time of the instrument.

Quantum noise

Quantum noise, in general, is driven by vacuum fluctuations of the optical field at the antisymmetric port that then enter the interferometer and become amplified [40, 41]. Shot noise is the noise that arises from the statistical uncertainty, introduced by those vacuum fluctuations, of the number of photons circulating in the arms and exiting through the OMC [41, 40]. Those statistical fluctuations are interpreted as fluctuations in laser power, and therefore in strain [33, 42, 43]. In the first LIGO observing run, the shot noise estimate was given by [33]

$$L(f) = \frac{\lambda}{4\pi G_{arm}} \left(\frac{2h\nu G_{src}}{G_{prc} P_{in} \eta} \right)^{1/2} \frac{1}{K(f)} \tag{1.32}$$

where $G_{(\cdot)}$ gives the optical gain due to the arm, power recycling cavity, or signal recycling cavity, P_{in} is the input power from the laser, 25 W in O1, η represents optical losses, and $K(f)$ is the optical response function that depends upon the properties of the numerous coupled optical cavities that comprise the instrument. Shot noise is the limiting noise source of most interferometric GW detectors at high frequencies.

Vacuum fluctuations can also create displacement noise by applying a changing radiation pressure upon the test masses [44]. An estimate of the radiation pressure noise is discussed in [33] and is given by

$$L(f) = \frac{2}{cM\pi^2 f} \left(h\nu G_{-} P_{arm} \right)^{1/2} K(f) \tag{1.33}$$

where c is the speed of light, M is the mass of the test masses, P_{arm} is the total power circulating in the Fabry-Pérot cavities, and G_{-} is an extra factor that depends upon the properties of the interferometer.

Thermal noise

Thermal noise refers to mechanical losses throughout the interferometer. Problems especially arise in the connections between the suspension systems and the test masses themselves [45], as well as in the optical coatings on the mirrors [46, 47]. Thermal noise is typically estimated to be the limiting noise source in the instruments from $50-200$ Hz, but in the case of observing run 1 (O1), it is lower than the observed noise by a factor of ~ 3, and a cause for the discrepancy has not yet been identified [33].

Newtonian noise

Newtonian noise represents fluctuations in the gravitational field at the test masses. This can be caused by temperature fluctuations in the atmosphere, vibration of the walls of the surrounding building, and seismic waves in the Earth [48, 49, 42]. Newtonian noise is not currently a limiting noise source for LIGO detectors, but predictions indicate that will be the case at low frequencies in the future [48]. We will discuss Newtonian noise further in chapter 6.

Correlated noise

One of the assumptions of most searches for GWs using LIGO data is that the noise between spatially separated interferometers is uncorrelated. For searches for transient GWs this is typically a good assumption. It is very unlikely that there would be a source of transient noise large enough to cause fluctuations above the typical levels of noise in the instruments that is also correlated between the two LIGO interferometers on a time scale consistent with the light travel time between the detectors (~ 1 ms). Moreover, tests are done to check that signals that might satisfy those criteria (like bursts of magnetic power due to large lightning strikes) would also be observed in environmental monitors like magnetometers [50] and would therefore be rejected as GW event candidates.

On longer time scales, GW searches “dig into” the noise and search for signals that are lower than the typical noise fluctuations in the instrument, and so noise from similar electronics at both detectors [51], as well as long-wavelength magnetic fields, can cause issues [52, 53, 1]. We will discuss estimates of correlated noise in cross-correlation searches in chapter 4, and ways to deal with it in chapter 5.

Other sources of noise

Sources of noise that limit the sensitivity of the interferometer on long timescales and over broad frequency ranges have been the focus of this section to this point. Transient noise in the interferometer, often associated with malfunctioning electronics or large environmental disturbances, are also major problems for transient searches for GWs. A thorough understanding of how to deal with and understand transient noise is a priority for being able to reliably detect GWs, and discussions of it are somewhat common in the literature [50, 54].

There are also sources of noise that cause significant losses in sensitivity in very narrow frequency ranges. We often refer to these as “lines” because of how they appear on the sensitivity curves (these are evident in figure 1.4). These lines are often caused by narrow mechanical resonances with large quality factors, local electronics on site, or aliasing in digital filters. Understanding and mitigating this type of noise is less common in the literature, but that is changing [51]. I will discuss understanding and mitigating lines in the LIGO detectors in chapters 3 and 4.

1.3.4 Data analysis techniques

Matched filtering

Matched filtering is a data analysis technique that correlates a data stream with a known signal to try to detect the presence of that signal in the data stream. It is the optimal linear filter for maximizing the signal-to-noise ratio (SNR) of a known waveform. In GW data analysis, matched filtering is used to search for deterministic signals that can be calculated analytically or numerically, like those from BBHs and BNSs [55, 56, 57], and it played a vital role in the first detection of those signals [5, 14, 15, 16, 17, 18]. Matched filtering is also used in the $\mathcal{F}$-statistic searches and Bayesian searches for signals from rapidly rotating neutron stars [58, 59].

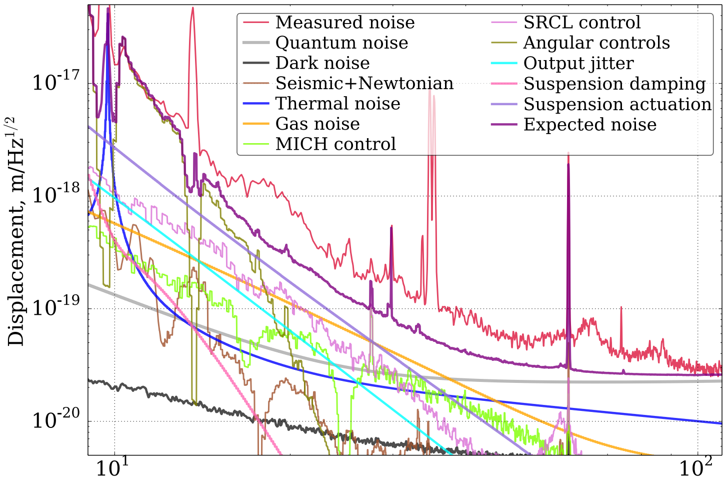

(a) LIGO Livingston Observatory

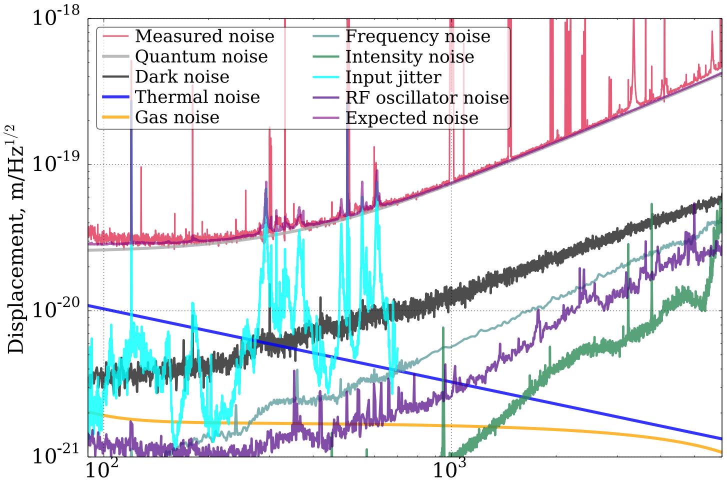

(b) LIGO Hanford Observatory

Figure 1.5: Top: noise sources at low frequencies at the LIGO Livingston interferometer. Bottom: noise at high frequency in the LIGO Hanford interferometer. Both plots show noise at the start of the first Advanced LIGO observation run in September, 2015. At low frequencies noise is dominated by seismic noise, noise from the angular optical control systems and an unknown source of noise believed to be light scattering noise. At high frequencies the noise is dominated by quantum noise in the form of shot noise. This plot is reproduced from [33].

Coincident bursts

When searching the data for transient GW signals that do not have a deterministic waveform, it is common to search for coincident "bursts" of strain power in multiple detectors. These types of searches are used for sources like supernovae and any other signal that does not have a deterministic waveform [27, 60, 26, 61]. Often these searches either cross-correlate data between the detectors and look for larger-than-expected cross-power, or they look for large, simultaneous excursions in the power in the individual detectors. A combination of both can also be used [62].

Long-duration cross-correlation

Searches for long-lived signals that are not well-modeled, like the SGWB, typically rely upon cross-correlating the data in pairs of detectors [63] to search for a signal common to both instruments. This method can also be used to search for rapidly rotating neutron stars [64, 24, 25]. We will discuss cross-correlation based searches for long-duration signals extensively in chapters 2 and 3.

1.4 Concluding remarks

In this chapter we discussed GWs and interferometric detectors. We introduced the mathematical formalism used when discussing GWs, and how GWs interact with interferometric detectors like Advanced LIGO and Advanced Virgo. We also briefly discussed several different sources of GWs, as well as a cursory overview of different data analysis techniques used in searching for them. In the next chapter, we expand on searches for persistent GWs like the SGWB or rapidly rotating neutron stars, and in the subsequent chapter we present results for those searches using data from O1.

Chapter 2

Cross-correlation searches for persistent gravitational waves

The stochastic gravitational-wave background (SGWB) is a promising source of gravitational waves (GWs) that is expected to arise due to the superposition of many individually unresolvable GW sources. It carries information about unresolved stellar sources of GWs and potentially sources of GWs from the earliest epochs in the evolution of the universe, such as inflation. To be consistent with the way different types of energy in the universe are treated in cosmology, the SGWB is usually discussed in terms of a dimensionless energy density parameter

$$\Omega_{\mathrm{GW}}(f) = \frac{1}{\rho_c}\frac{d\rho_{GW}}{d\ln f} \tag{2.1}$$

where $\rho_c = \frac{3H_0^2c^2}{8\pi G}$ is the critical energy density to close the universe, and $d\rho_{GW}/d\ln f$ is the energy density in GWs per logarithmic frequency bin.

The rest of this chapter will discuss sources of an SGWB and methods of searching for it using the Advanced LIGO and Advanced Virgo detectors. In section 2.1, we discuss sources of an SGWB before moving on to current direct and indirect limits on the SGWB in several different frequency bands. In section 2.3, we discuss the cross-correlation strategy used to search for an isotropic SGWB in LIGO detectors. In section 2.4, we discuss how the isotropic assumption about the SGWB can be relaxed so that we can search instead for an anisotropic background of GWs. Finally, in section 2.5 we discuss an unmodeled, directed search for GWs in each frequency bin and present a new method for setting limits on the strain amplitude of a rapidly rotating neutron star using that search.

2.1 Sources

Sources of the SGWB can be stellar in nature, like the inspiral and merger of many unresolved compact binary systems [65, 66, 67, 68, 69, 70, 71], or non-stellar, like those arising from inflationary models [72, 32, 73, 74, 75, 76, 31, 77], early-universe phase transitions [32, 78, 79], or cosmic strings [80, 81, 82, 83, 84]. In this section, I describe a few of these sources in more detail.

2.1.1 Unresolved compact binary coalescences

The superposition of GW signals from unresolvable mergers of compact objects will contribute significantly to the SGWB in the LIGO and Virgo frequency band. Studies based on the recent LIGO detections of binary neutron star [18] and binary black hole [85, 14, 15, 17] systems indicate that a detection of this background is possible when the current generation of detectors reaches design sensitivity [28].

We will follow the the methods outlined in [28, 86] for estimating the amplitude and spectrum of this source. The background due to unresolved CBCs is generally characterized by a set of average parameters, $\vec{\theta}$, and a merger rate that is dependent on these parameters and the redshift, $R_m(z;\vec{\theta})$. The parameters are quantities like chirp mass and spin, and represent the ensemble average over all binary systems that can contribute GWs in the LIGO/Virgo frequency band. We can write the SGWB due to these sources as

$$\Omega_{\rm GW}(f,\vec{\theta}) = \frac{f}{\rho_c H_0}\int_0^{z_{\rm max}} dz\, \frac{R_m(z;\vec{\theta}) dE_{\rm GW}(f_s;\vec{\theta})/df_s}{(1+z)E(\Omega_M,\Omega_\lambda,z)}. \tag{2.2}$$

In this case, $dE_{GW}(f_s;\vec{\theta})/df_s$ is the energy spectrum of the source in the source frame, f_s is the source frequency, and $E(\Omega_M,\Omega_\lambda,z)$ accounts for cosmology. We have also set a cutoff for our integration over redshift at $z_{\rm max}$.

It is customary to treat the background due to BBHs and BNSs separately due to differences in their energy spectra, formation conditions, and mass distributions. For BNS systems, only the inspiral phase is considered because the merger happens at a higher frequency, which means the energy spectrum is $dE/df_s \propto M_c^{5/3} f_s^{-1/3}$ where M_c is the chirp mass of the system. In this case, $\Omega_{\rm GW}(f) \propto f^{2/3}$. For BBHs, it is common to consider full waveforms that include the merger and ringdown phase as well [66, 70, 87, 65, 88].

The merger rate is typically assumed to track the star formation rate with some time delay

$$R_m(z;\vec{\theta}) = \int_{t_{\rm min}}^{t_{\rm max}} R_f(z_f;\vec{\theta}) p(t_d;\vec{\theta})\, dt_d, \tag{2.3}$$

where $R_f(z_f;\vec{\theta})$ is the binary formation rate at the time a binary is formed, z_f is the redshift at the formation time, and $t_{\rm min}$ is the minimum time delay between formation of the binary system and merger. The formation time of the system can be written as $t_f = t(z) - t_d$, where $t(z)$ is the merger time and t_d is the delay time from formation to merger of the binary events. When using equation (2.3), we will use the star formation rate from [89], although the final SGWB estimates are somewhat insensitive to the choice of SFR. In general it is assumed that $p(t_d) \propto t_d^{-1}$. For BBH events, $t_{\rm min}$ is chosen to be 50 Myr and for BNS events $t_{\rm min} = 20\,{\rm Myr}$ [28]. R_m is normalized to the local rate (i.e. $z = 0$), which is estimated from LIGO observational results. For BBH events where either component mass is $> 30\ M_\odot$, the binary merger rate is rescaled based on the fraction of star formation at metallicity $Z < Z_\odot/2$ because high-mass BBHs tend to form in metal-poor environments [90, 28, 86].

For BNS events, the masses are drawn uniformly between 1 and 2 $M_\odot$ and the local merger rate is estimated to be $R_m(0,\vec{\theta}) = 1540^{+3200}_{-1220}$ Gpc^{-3}yr^{-1} [18]. Replacing the uniform distribution of masses with a Gaussian distribution centered on 1.4 $M_\odot$ changes the results by less than the Poisson error in the merger rate [28]. For BBH events we assume component masses where m_1, m_2 are greater than 5 $M_\odot$, $m_1 > m_2$, and $m_1 + m_2 < 100\ M_\odot$. We also assume a power-law distribution in the first component mass, $p(m_1) \propto m_1^{-2.35}$, and uniform for the other mass. Under this assumption, the local merger rate of BBHs is taken to be $R_m(0,\vec{\theta}) = 103^{+110}_{-63}$ [91, 15].

The resulting estimates for the BBH and BNS contributions to the SGWB are summarized in figure 2.1, which is reproduced, with slight modifications, from [28].

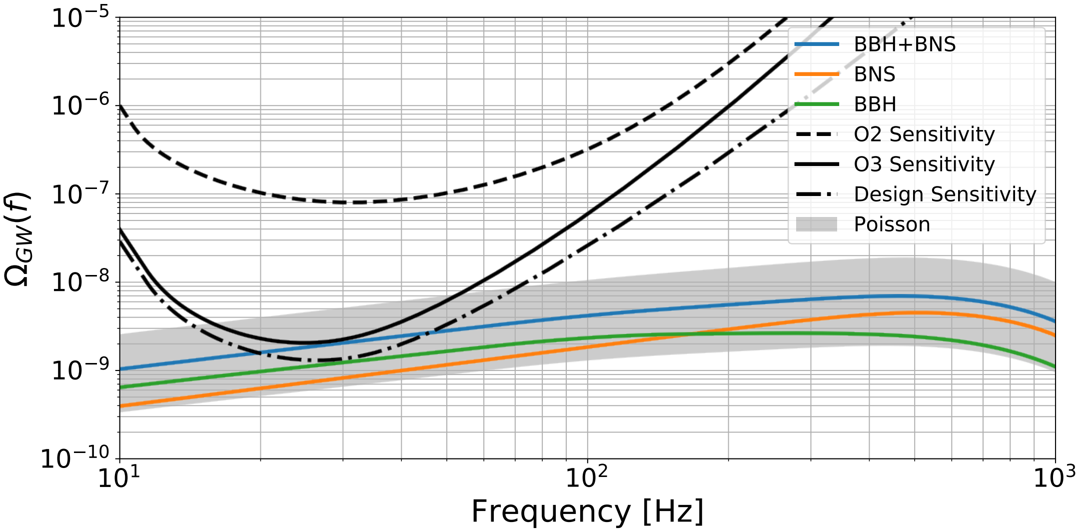

Figure 2.1: We show the expected SGWB due to unresolved binary mergers. The sensitivity curves are shown as 1σ power law integrated curves (PI curves) [92] integrated over 1 year. Any line crossing a PI curve for a large section of frequency space is detectable by that search at the 2σ level. This plot is reproduced (with some minor formatting changes) from [28].

2.1.2 Rotating neutron stars

Another source of persistent GWs are rapidly rotating neutron stars. These are most commonly observed in the form of radio pulsars, named for their periodic pulses of radio waves. The searches for an SGWB that I will discuss later can be used to search for an ensemble of non-axisymmetric rotating neutron stars that are distributed on the sky. However, the last search method I will discuss has also been modified to target specific directions where we expect isolated neutron stars or neutron stars in binary systems. Here, I will briefly discuss all three cases.

Isolated rotating neutron stars

A rapidly rotating neutron star that is not axisymmetric will emit GWs. GW emission, in concert with magnetic braking, will contribute to the slow increase in the period of rotation of the neutron star, often referred to as “spin-down.” The typical strain amplitude for a neutron star that has some ellipticity is

$$h_0 = \frac{16\pi^2 G}{c^4}\frac{\epsilon I_{zz} f^2}{r}. \tag{2.4}$$

In the above expression, f is the rotational frequency of the neutron star, I_{zz} is the moment of inertia about the principle axis, $\epsilon = (I_{xx} - I_{yy})/I_{zz}$ is the ellipticity of the star, and r is the distance from the source. The time evolution of this signal in a GW detector is nearly periodic, and can be written as

$$h(t) = F^{+}(\hat{n},\psi) h_0 \cos\iota \cos(2\phi(t)) + F^{\times}(\hat{n},\psi) h_0 \left[\frac{1+\cos^2\iota}{2}\right] \sin(2\phi(t)). \tag{2.5}$$

We have used ι, the angle between the spin axis and the line of site, and $F^{+,\times}$, the detector responses to plus and cross-polarizations, which will be discussed further in section 2.3.1. It is also worth noting that the frequency of the GW signal is twice the frequency of rotation of the neutron star. That is, $\phi(t)$ is the phase of the rotation of the neutron star.

It is possible to use conservation of energy to put a naïve upper limit on the GW emission of an isolated neutron star that is spinning down. If one assumes that the spinning down of the neutron star is *solely* due to the emission of GWs, then it can be shown that [93, 94]

$$h_{SD} = \left(\frac{5}{2}\frac{G I_{zz} |\dot{f}|}{c^3 r^2 f}\right)^{1/2}. \tag{2.6}$$

Recent results from LIGOs first observing run include limits on 200 isolated radio pulsars. Eight of these limits are lower than the spin-down limit, while another 32 are within an order of magnitude of this limit [23].

Accreting neutron stars

Accreting neutron stars in binary systems with a low-mass donor often exhibit high X-ray emission as particles fall onto the neutron star and rapidly heat up. These systems are most obviously visible when the neutron star is accreting near its Eddington limit, and are typically referred to as low mass X-ray binary (LMXB) systems [95]. In these systems, neutron stars are subject to torque both due to the accreting mass, which will spin the star up, and due to GW emission, which will spin it down.

Most neutron stars observed in these systems have relatively stable spins in a range near $\sim 250 - 650$ Hz [96], which is well below most theoretical limits for the maximum spin frequency. This has led some to postulate that the neutron star is in equilibrium. If one assumes equilibrium and that all X-ray emission is due to accretion onto the neutron star, then there is a direct relationship between the strain amplitude and the X-ray flux [97]

$$h_0 = 5 \times 10^{-27} \left(\frac{300\ \text{Hz}}{f_{\text{rot}}}\right)^{1/2} \left(\frac{F_x}{10^{-8}\ \text{erg cm}^{-2}\ \text{s}^{-1}}\right)^{1/2} . \tag{2.7}$$

It is evident from this expression that the largest source of GWs correspond to the brightest X-ray sources, which suggests that a useful target would be the first-discovered and largest source of extra-solar X-rays: the LMXB Scorpius X-1 [98]. Given that the spin frequency of the neutron star in Scorpius X-1 is unknown, it is possible to use the X-ray flux to set a frequency-dependent estimate of the strain amplitude [99], commonly referred to as the "torque-balance limit"

$$h_0^{\text{scox1}}(f) \approx 3 \times 10^{-26} \left(\frac{540\ \text{Hz}}{f}\right)^{1/2} . \tag{2.8}$$

Detection of ensemble of neutron stars

We can also search for the collective contribution to the SGWB of GWs from rapidly rotating neutron stars in the Milky Way. This involves constructing an estimate of the frequency distribution of neutron stars in the galaxy using either a catalog or a population synthesis model, as discussed in [29]. One can also construct a model for the distribution of those stars on the sky using pulsar catalogs [100]. As we will see in section 2.4, it is possible to create an optimal cross-correlation search for such a distribution. While we will not discuss this further here, work by other members of LIGO on constructing such a search is ongoing.

The discussion in the previous paragraph does not target *known* radio pulsars, instead attempting to look for the background due to unresolved rapidly rotating neutron stars. If assumptions are made about the ensemble properties of some set of known radio pulsars, it is possible to optimally combine their individual detection statistics into one final detection statistic. I will not discuss such a search further, but a discussion of a possible implementation can be found in [101].

2.1.3 Early universe models

There are numerous models for GW production in the early universe. A few common models are those involving amplification of vacuum fluctuations at the end of inflation [72, 32, 73, 74, 75, 76, 31, 77], GW production as a result of phase transitions in the early universe [32, 78, 79], and pre-Big bang models [102, 103, 104].

A direct detection of relic GWs would be a monumental discovery. However, reaching that point requires a thorough understanding of the astrophysical foreground. General rules of thumb for the characteristic amplitude and frequency of relic GWs are somewhat common in the literature [32, 105] and for phase transitions models, for example, tend to indicate a background in the range of $\Omega_{\mathrm{GW}} \sim 10^{-12\pm2}$. A detection at this level would require third generation ground-based detectors with phenomenal low-frequency sensitivity or a detection at a lower frequency band by Pulsar timing arrays [106, 107, 108] or proposed detectors like LISA [109], Big Bang Observatory [110], or DECIGO [111].

The spectral shape of relic GWs is heavily model dependent, and I will not discuss the details of any specific models here. Many cosmological models produce a flat spectrum for Ω_{GW}, and so the flat spectrum limit tends to be the "value of merit" used in many LIGO searches. However, as I will discuss in chapter 5, we are developing methods for searching for and distinguishing between differently-shaped spectra and making statements about how well the data support some models over others.

2.2 Current limits on the SGWB

A good discussion of limits on the SGWB across many decades in frequency can be found in [112]. These limits fall into broad categories of "direct" and "indirect." Observations of both type are vital to an understanding of the GW spectrum across the history of the Universe. Direct limits include those made from attempts to directly observe the effect of GWs on the detector. These include limits made by ground-based interferometers like LIGO and Virgo, which fall into the frequency band from $10 - 10^{3}$ Hz, and those from pulsar timing arrays (PTAs), which fall in the band from $10^{-9} - 10^{-7}$ Hz. The most recent limits from LIGO were the first from advanced detectors [113] and a detection of an astrophysical background could come in the next decade [28]. Limits from the Parkes Pulsar Timing Array (PPTA) [106] are beginning to reach the expected background due to super massive back holes, as are a few other PTA collaborations [108, 107].

Observational limits based on the effect of GWs on the CMB polarization attempt to put constraints on the tensor-to-scalar ratio, r, as well as the spectral index of the GW power spectrum. These tend to fall into the region of $10^{-17} - 10^{-15}$ Hz. Recent limits come from the BICEP2 and Keck arrays [114], Planck [115], and SPTpol [116].

Indirect limits based on Big Bang Nucleosynthesis (BBN) and Baryon Acoustic Oscillations (BAO) are limits on the total, integrated, GW energy density at the epoch at which they are measured. These can be converted into spectra using the formalism of power-law integrated curves [92] under the assumption that the SGWB is well-characterized by a power law and has some maximum frequency cut-off (often chosen to be consistent with frequencies at the scale of inflation) [112].

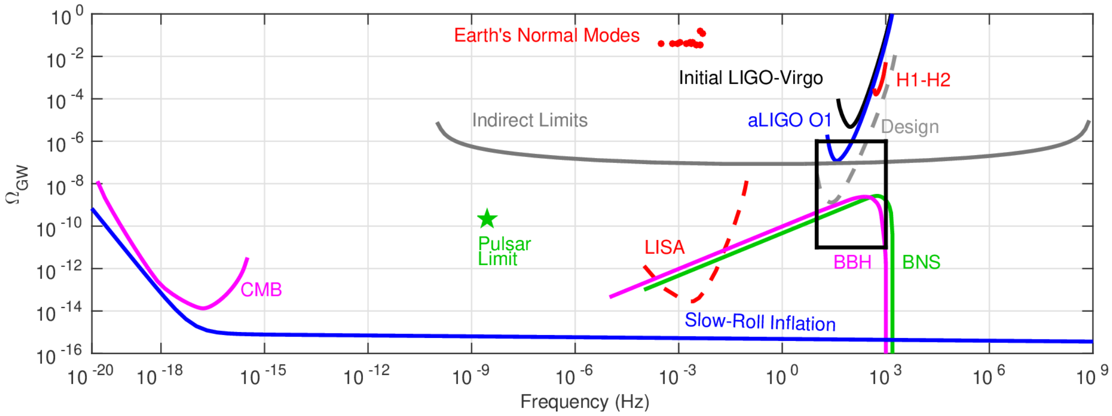

Figure 2.2: We show limits on the SGWB in the form of power law integrated (PI) curves [92]. Limits from LISA are made using the assumptions from [92], while those for indirect limits are the BBN and BAO limits, as displayed in [112], and CMB measurements are from [117]. Pulsar timing limits are from [106]. This plot is reproduced from [113].

LIGO will continue to set limits on, and hopefully detect, an SGWB. As this happens, it will be important to keep in mind the context of these limits in the broader field of GW cosmology.

2.3 A cross-correlation search for an Isotropic SGWB

We want to effectively search for an SGWB, but we have no *a priori* template for how the SGWB will manifest itself in the output of our detectors. Instead, we cross-correlate the output of our detectors and rely on the fact that the SGWB will show up similarly in both detectors. In this section, I will discuss how an isotoropic superposition of GW plane waves interact with an interferometric detector and what that means for the cross-correlation of two detectors that are mis-aligned and spatially separated. I will then discuss an optimal search for an isotropic SGWB based on this cross-correlation method.

2.3.1 Effect of a plane-wave on LIGO detectors

We can down metric perturbations in the transverse-traceless gauge [63],

$$h_{ab}(t, \vec{x}) = \sum_A \int df \int d\hat{n}\, h^A(f, \hat{n}) e^{2\pi i f(t - \hat{n}\cdot\vec{x}/c)} e^A_{ab}(\hat{n}), \tag{2.9}$$

where A is represents polarization and $e^A_{ab}(\hat{n})$ is a polarization tensor. Next we specify our coordinate system in terms of the polar angle, θ, and the azimuthal angle, ϕ, defining $\hat{n}$ as the direction of propagation of the wave

$$\hat{n} = \cos\phi\sin\theta\hat{x} + \sin\phi\sin\theta\hat{y} + \cos\theta\hat{z} \tag{2.10}$$

$$\hat{m} = \cos\phi\cos\theta\hat{x} + \sin\phi\cos\theta\hat{y} - \sin\theta\hat{z} \tag{2.11}$$

$$\hat{l} = -\sin\phi\hat{x} + \cos\phi\hat{y}. \tag{2.12}$$

The choice of $\hat{m}$ and and $\hat{l}$ are somewhat arbitrary, as we can rotate them around $\hat{n}$ by some angle ψ and keep a right-handed coordinate system. Some sources of GWs that have a well-defined axis of symmetry interpret ψ as the *polarization angle of the source* [118].

We define our polarization tensors in terms of these coordinates

$$e^+_{ab}(\hat{n}) = \hat{m}_a\hat{m}_b - \hat{l}_a\hat{l}_b \tag{2.13}$$

$$e^\times_{ab}(\hat{n}) = \hat{m}_a\hat{l}_b + \hat{m}_b\hat{l}_a. \tag{2.14}$$

The interaction between the different polarizations of a plane-wave and an interferometer with arms in the $\hat{X}$ and $\hat{Y}$ directions is then given by

$$F^A(\hat{n}) = e^A_{ab}\frac{1}{2}\left(\hat{X}^a\hat{X}^b - \hat{Y}^a\hat{Y}^b\right), \tag{2.15}$$

which is sometimes referred to as the "antenna pattern" or the "detector response." We use this to write down the GW strain measured by a given detector (we will call it detector "1")

$$h_1(t, \vec{x}_1) = \sum_A \int df \int d\hat{n}\, h_A(f, \hat{n}) F^A_1(\hat{n}) e^{2\pi i f(t - \hat{n}\cdot\vec{x}_1/c)}. \tag{2.16}$$

2.3.2 Cross-correlation of separated and misaligned detectors

We have no deterministic model for how the SGWB will show up in the time-domain in our detectors. Therefore, we cross-correlate the output of our two detectors. A GW signal will show up differently in two detectors that are not colocated and co-aligned, but if we make some reasonable assumptions about the GW background (namely isotropy, stationarity, and that the background is unpolarized) then we can calculate how the GW signal will be different in the two detectors.

We begin by constructing a cross-correlation estimator in the frequency domain

$$Y = \int df \int df' \delta_T(f - f')\tilde{s}^*_1(f)\tilde{s}_2(f')\tilde{Q}(f'). \tag{2.17}$$

where $\tilde{s}_1(f) = \tilde{n}_1(f) + \tilde{h}_1(f)$ is the output of the detector in the Fourier domain, and h_1 represents the gravitational-wave signal in detector 1, while n_1 represents the intrinsic detector noise in detector 1. Tilde indicates Fourier transform and an asterisk indicates complex conjugation. We have added an an arbitrary, $\tilde{Q}(f)$, which we will eventually use to maximize our signal-to-noise ratio. $\delta_T(f - f')$ is the finite time approximation to the Dirac delta function, where $\delta_T(0) = T$ and T is the observation time. If we consider the expectation value of this quantity and assume that the detector noises are uncorrelated with the GW signal and themselves (an assumption we will come back to in chapter 5), we find

$$\langle Y\rangle = \int df \int df'\, \delta_T(f-f')\langle \tilde{h}_1^*(f)\tilde{h}_2(f')\rangle \tilde{Q}(f'). \tag{2.18}$$

The expression inside of the integration can now be re-expressed according to equation (2.16)

$$\langle \tilde{h}_1^*(f)\tilde{h}_2(f')\rangle = \sum_A \sum_{A'} \int d\hat{n}\, d\hat{n}'\, \langle h_A^*(f,\hat{n}) h_{A'}(f',\hat{n}')\rangle F_1^A(\hat{n}) F_2^{A'}(\hat{n}') \tag{2.19}$$

$$\times\, e^{2\pi i f(t-\hat{n}\cdot\vec{x}_1/c)} e^{-2\pi i f'(t-\hat{n}'\cdot\vec{x}_2/c)}. \tag{2.20}$$

The two-point correlation function inside of the integral is where we now impose some assumptions about the SGWB. We assume statistical independence for GWs of different polarizations, frequency, and direction. We also assume that the background is stationary. This is equivalent to saying that

$$\langle h_A^*(f,\hat{n}) h_{A'}(f',\hat{n}')\rangle = \delta(f-f')\delta^2(\hat{n},\hat{n}')\delta_{A,A'} H(f), \tag{2.21}$$

where $H(f)$ is the gravitational wave power spectrum. If we substitute equation (2.21) into equation (2.19) then we find

$$\langle \tilde{h}_1^*(f)\tilde{h}_2(f')\rangle = \frac{8\pi}{5}\delta(f-f') H(f)\gamma(f). \tag{2.22}$$

We have defined the overlap reduction function

$$\gamma(f) = \frac{5}{8\pi}\sum_A \int d\hat{n}\, F_1^A(\hat{n}) F_2^A(\hat{n}) e^{2\pi i f \hat{n}\cdot\Delta\vec{x}/c}, \tag{2.23}$$

which depends upon the separation, $\Delta\vec{x} = \vec{x}_1 - \vec{x}_2$, and orientation (encapsulated in the F functions) of the two detectors. The normalization is chosen such that $\gamma(f) = 1$ for colocated and co-aligned detectors. A plot of $\gamma(f)$ for several different detector pairs can be found in figure 2.3. If we substitute this expression back in to equation (2.18) we find

$$\langle Y\rangle = \frac{8\pi}{5} T \int df\, \gamma(f) H(f) \tilde{Q}(f) \tag{2.24}$$

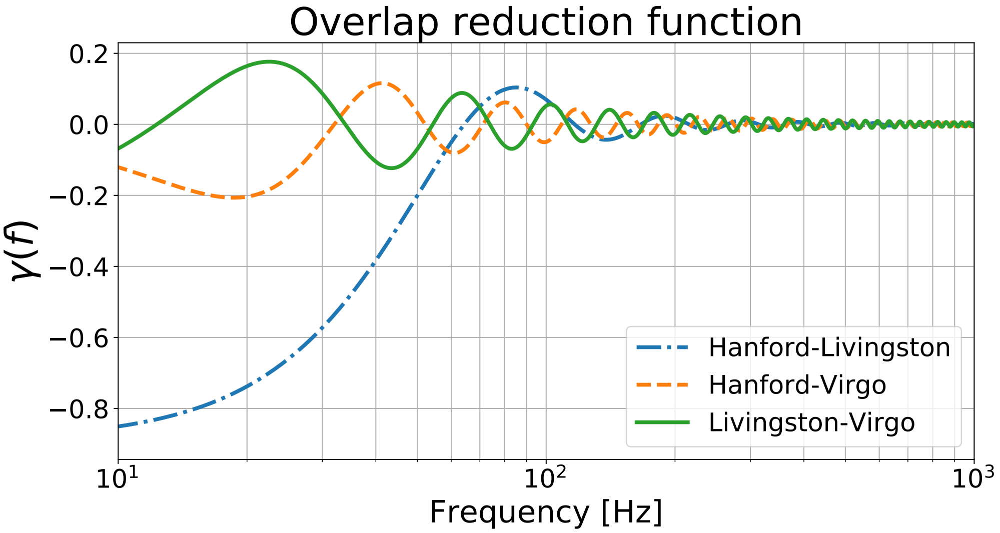

Figure 2.3: The overlap reduction function for several different detector pairs.

We have taken two finite-time Dirac delta functions and made one a "true" Dirac delta function and integrated over it, while evaluating the other at $f = f'$, giving us a factor of T [63]. Now we would like to rewrite this in terms of $\Omega_{\mathrm{GW}}(f)$, which we defined back in equation (2.1). We note that $\rho_{GW} = \frac{c^2}{32\pi G}\langle \dot{h}(t,\vec{x})\dot{h}(t,\vec{x})\rangle$. The expectation can be written down in the frequency domain for the plane-wave expansion. We get a factor of $4\pi^2 f^2$ from the derivatives, a factor of 4π from the integration over direction, and a factor of 2 if we decide to integrate over only positive frequencies. We end up with $\rho_{GW} = \frac{4\pi c^2}{G}\int_0^\infty f^2 H(f)\,df$. Substituting this back in to equation (2.1) and substituting in for ρ_c we can solve for $H(f)$

$$H(f) = \frac{3H_0^2}{32\pi^3} f^{-3}\Omega_{\mathrm{GW}}(f). \tag{2.25}$$

Putting this back in to equation (2.24) we see our cross-correlation is now in terms of $\Omega_{\mathrm{GW}}(f)$

$$\mu = \langle Y\rangle = T\frac{3H_0^2}{20\pi^2}\int df\, f^{-3}\gamma(f)\Omega_{\mathrm{GW}}(f)\tilde{Q}(f). \tag{2.26}$$

Note that our cross-correlation statistic loses sensitivity to Ω_{GW} at higher frequencies. This is one motivation for improving the sensitivity of ground-based detectors at lower frequencies; something that I explore in chapter 6.

Next we need to explore the variance of our statistic $\langle Y \rangle$,

$$\sigma^2 = \langle Y^2 \rangle - \langle Y \rangle^2 \approx \langle Y^2 \rangle. \tag{2.27}$$

We are still using the assumption that the signal and the detector noise are uncorrelated, and so terms that look like $\langle hn \rangle$ and $\langle n_1 n_2 \rangle$ are taken to be zero. If we assume that our signal is much smaller than the intrinsic noise in our detectors, then we can ignore terms that look like h^2. It follows that

$$\sigma^2 = \frac{T}{4} \int df\, P_1(f) P_2(f) |\tilde{Q}(f)|^2, \tag{2.28}$$

where we have defined the power spectral density of the detector

$$\langle \tilde{n}_1^*(f) \tilde{n}_2(f') \rangle = \frac{1}{2} \delta_T(f - f') P_1(|f|). \tag{2.29}$$

Following [119] we define an inner product,

$$(A, B) = \int_{-\infty}^{\infty} df\, A^*(|f|) B(|f|) P_1(|f|) P_2(|f|), \tag{2.30}$$

where the P's are the power spectral densities of our detectors. Our statistic and its variance can now be written in this notation

$$\mu = \frac{3H_0^2}{20\pi^2} T \left(\frac{\gamma(f)\Omega_{\rm GW}(f)}{f^3 P_1(f) P_2(f)}, \tilde{Q}(f) \right) \tag{2.31}$$

$$\sigma^2 = \frac{T}{4} \left(\tilde{Q}(f), \tilde{Q}(f) \right) \tag{2.32}$$

$$\mathrm{SNR}^2 = \frac{\mu^2}{\sigma^2} = \left(\frac{3H_0^2}{10\pi^2} \right)^2 T \frac{\left(\frac{\gamma(f)\Omega_{\rm GW}(f)}{f^3 P_1(f) P_2(f)}, \tilde{Q}(f) \right)^2}{\left(\tilde{Q}(f), \tilde{Q}(f) \right)}. \tag{2.33}$$

It is now evident that the expression for the square of the signal-to-noise ratio, SNR^2, looks like a projection onto the filter function, and so the filter should be given by

$$\tilde{Q}(f) = \mathcal{N} \frac{\gamma(f)\Omega^{\rm M}_{\rm GW}(f)}{f^3 P_1(f) P_2(f)} \tag{2.34}$$

where $\Omega^{\rm M}_{\rm GW}(f)$ is now a *spectral shape* that weights frequency bins according to some expectation of the spectral shape of the SGWB. Common choices include a flat spectrum, and a powerlaw weighting according to $f^{2/3}$ to match the expected background due to CBC signals [120]. In the powerlaw case, $\Omega^{\rm M}_{\rm GW}(f) = (f/f_{ref})^{\alpha}$. In chapter 5 we will discuss an estimator for the background in *each individual frequency bin* and how that can be used to extract information about the spectrum of the SGWB. If we consider the broadband spectrum, though, it makes intuitive sense that our SNR will be maximized when we use an optimal filter that matches the true spectrum of the SGWB. One can, of course, do the search over a range of optimal filters and attempt to maximize the SNR.

The optimal SNR for a given background[1] is then

$$\mathrm{SNR} = \sqrt{T}\frac{3H_0^2}{10\pi^2}\left[\int_{-\infty}^{\infty} df\, \frac{\gamma^2(|f|)\Omega^2_{\rm GW}(|f|)}{f^6 P_1(|f|)P_2(|f|)}\right]^{1/2}. \tag{2.35}$$

The SNR is proportional to $\sqrt{T}$, which means that the longer we observe, the larger the SNR. As noted previously, the SNR is proportional to f^{-3}, which means that we are more sensitive at lower frequencies.

When we substitute equation (2.34) in to equation (2.17), we complete the definition of our cross-correlation statistic, up to an overall normalization factor. It is common practice to choose a normalization factor that causes the expectation value of our statistic to be proportional to the energy density, $\langle Y\rangle \propto T\Omega_\alpha$ where Ω_α is the amplitude of a power law with spectral index α at some reference frequency $f_{\rm ref}$. In that case the normalization for our statistic, with an optimal filter for a power law of spectral index α, comes out to

$$\mathcal{N}_\alpha = \left[\frac{3H_0^2}{20\pi^2}\int df\, \frac{\gamma^2(f)\,(f/f_{\rm ref})^{\alpha}}{f^6 P_1(f)P_2(f)}\right]^{-1}. \tag{2.36}$$

2.3.3 Bin-by-bin estimator

Using a similar calculation to the one in the previous section, we can calculate an estimator for $\Omega_{\rm GW}(f)$ in each frequency bin, as opposed to an integrated statistic that assumes a power law [118, 121]. This will be useful for several studies we present in

---

[1] By this we mean that our spectral model matches the true spectral shape of $\Omega_{\rm GW}(f)$.

future chapters. We use a hat to denote that this is a measured quantity.

$$\hat{\Omega}_{\mathrm{GW}}(f) = \frac{2}{T}\frac{f^3}{\gamma(f)}\frac{10\pi^2}{3H_0^2}\mathrm{Re}\left[\tilde{s}_1^*(f)\tilde{s}_2(f)\right] \tag{2.37}$$
$$\sigma^2(f) = \frac{1}{2T\Delta f}\frac{f^6}{|\gamma(f)|^2}\left(\frac{10\pi^2}{3H_0^2}\right)^2 P_1(f)P_2(f).$$

2.3.4 Noise non-stationarity

One of the implicit assumptions of the derivation we have presented is that the power spectral density of the instrumental noise of each detector is constant over the observation time. In practice, this is not true. Anthropogenic noise can cause a marked increase in the noise floor during the day as compared to night time. A general rule of thumb is that the noise changes by ∼10% on 10 minute time scales.

The non-stationarity of noise in our detectors leads us to break the analysis into smaller segments, and combine those segments together. Generally, we choose 60 s chunks of time, but in some analyses where finer frequency resolution is needed we have used as long as 192 s segments [122, 24, 84]. Combining segments is done assuming each individual segment is drawn from a separate Gaussian distribution

$$\hat{Y} = \frac{\sum_i \hat{Y}_i \sigma_i^{-2}}{\sum_i \sigma_i^{-2}} \tag{2.38}$$
$$\sigma^2 = \left(\sum_i \sigma_i^{-2}\right)^{-\frac{1}{2}}$$

where i labels time segments. This method naturally weights times of higher noise less than times of lower noise, and optimizes the final SNR.

2.3.5 Setting upper limits and extracting information from the search

Traditional upper limits and detection methods

The SNR that we have constructed should, in principle, be normally distributed with a mean given by the measured background and variance of unity. This tends to be true in practice as well. This is because the analysis is done over many short time segments which are combined in post-processing into one final estimator and uncertainty measurement. The central limit theorem then says that the sum over these many time segments should give us a final statistic that is drawn from a normal distribution.

What has been done in the past is to look at the optimal SNR for several values of α that are consistent with some common models for the spectral shape of the background. The typical choices are $\alpha = (0, 2/3, 3)$. A "soft" detection would then correspond to an SNR of 3 and a gold-plated detection would be an SNR of 5.

If SNR$<$ 3 for the values of α we have chosen, we then set upper limits on Ω_α for several values of α. The 90% upper limit Ω_α^{90} is then defined as:

$$0.90 = \int_{-\infty}^{\Omega_\alpha^{90}} p(\hat{\Omega}_\alpha|\Omega_\alpha)p(\Omega_\alpha)\, d\Omega_\alpha \tag{2.39}$$

$$0.90 = \int_{0}^{\Omega_\alpha^{90}} \frac{1}{\sqrt{2\pi\sigma^2}} e^{-\frac{(\hat{\Omega}_\alpha-\Omega_\alpha)^2}{2\sigma_\alpha^2}}\, d\Omega_\alpha. \tag{2.40}$$

We have now defined our measurement using hats, $\hat{\Omega}_\alpha = \langle Y_\alpha \rangle / T$. In this case, $p(A|B)$ means the conditional probability of statement A given statement B, and $p(\Omega_\alpha)$ is the prior probability we set on the background having a specific amplitude. This could be from a previous measurement, or some model we have. Moving from the first line to the second line above assumes a flat prior probability distribution (i.e. no preference). We performed the upper limits using data that is a frequentist optimal estimator, but with a Bayesian framework so that we can impose the fact that physically Ω_α will be greater than or equal to zero, but our estimator $\hat{\Omega}_\alpha$ can be negative. We will use a similar methodology in chapter 5 as well.

If there is uncertainty in the calibration of the detectors, then it is also common to marginalize over that uncertainty in the above expression. Typically, we assume that instead of being proportional to Ω_α our estimator is proportional to $\lambda\Omega_\alpha$ where λ represents some calibration factor that is normally distributed with mean 1 and uncertainty σ_λ, determined by the calibration process [123].

Joint limits on Ω_α vs. α can also be set, and will be discussed in chapter 5.

2.4 A cross-correlation search for an anisotropic SGWB

The assumption that the SGWB is isotropic is likely a good one if the SGWB is dominated by GWs of primordial origin. If the SGWB is dominated by a limited number of astrophysical sources, the assumption may not hold. It is also worthwhile to take an eyes wide open approach to searching for an SGWB, and part of this means relaxing assumptions that we have made when constructing our search. In [124], the authors lay out a method to create an optimal filter based on a *known* distribution of GW power on the sky using harmonics in the GW spectrum caused by the rotation of the earth. More recent discussions, like those in [125, 126] attempt to solve the inverse problem of inferring the GW power on the sky given the data.

Current searches for an anisotropic SGWB with LIGO fall into two categories: a search for point sources ("radiometer") [127, 125] and a search for diffuse sources using a spherical harmonic decomposition [126]. The original presentation of these searches, on the surface, appear to be quite different. However, [118] offers a very natural connection of the two methods that highlights assumptions made in each case, and so the presentation of these searches draws heavily from discussions in that review article. In addition, a very similar formalism is used in chapter 6 to explore the directional dependence of the seismic field.

2.4.1 Directional dependence of the SGWB

A natural extension to the previous analysis is to assume that the GW power has a directional dependence, $P(\hat{n})$. We will assume that the frequency dependence of the anisotropic background is not direction dependent, and so the GW power can be factored into a directional term and a frequency term

$$H(f, \hat{n}) = S(f)P(\hat{n}), \tag{2.41}$$

where $S(f)$ is dimensionless and weights our frequency spectrum according to some model, and $P(\hat{n})$ carries units of strain power per steradian. This means that the power, $P(\hat{n})$, does not pull out of the integral in equation (2.19) and so instead we find

$$\langle \hat{C}(t;f)\rangle = \frac{2}{\tau}\langle \tilde{s}_1(t;f)\tilde{s}_2(t;f)\rangle = \frac{5}{8\pi}S(f)\int d\hat{n}\, P(\hat{n})\gamma(t;\hat{n},f), \tag{2.42}$$

where $\gamma(t;\hat{n},f)$ is the integrand of equation (2.23). We have changed the definition of our statistic a bit from the previous section, normalizing the cross-correlation by the observation time and removing the finite-time Dirac delta; however, the delta function in the definition of $\langle h(f)h(f')\rangle$ still gives us a factor of τ that cancels with the one in the denominator. The variable t is a label that represents the mid-point of the time over which this cross-correlation was done. The rotation of the earth causes $\gamma(t;\hat{n},f)$ to change over the course of a sidereal day. Therefore, we need to break our analysis into many time segments. We then evaluate $\gamma(t;\hat{n},f)$ at the midpoint of each time segment of the analysis. To reduce error due to the rotation of the earth, we choose segments of duration $\tau \ll T_{\text{sidereal day}}$ but much larger than the travel time between the detectors. This does not change the analysis in practice, as we already break the analysis into segments of time with duration between $60 - 200$ s because the assumption that the noise in the detector is stationary does not hold over long time-scales (see section 2.3.4).

We can also project $P(\hat{n})$ onto a set of basis elements $Q_\alpha(\hat{n})$, such that $P(\hat{n}) = \sum_\alpha P_\alpha Q_\alpha(\hat{n})$. If we do this, then we rewrite equation (2.42) as

$$\begin{aligned}\langle C(t;f)\rangle &= \frac{5}{8\pi}S(f)P_\alpha \int d\hat{n}\, Q_\alpha(\hat{n})\gamma(t;\hat{n},f)\\ &= \frac{5}{8\pi}S(f)\gamma_\alpha(t;f)P_\alpha,\end{aligned} \tag{2.43}$$

where $\gamma_\alpha(t;f) \equiv \int d\hat{n}\, Q_\alpha(\hat{n})\gamma(t;f,\hat{n})$. The basis elements, $Q_\alpha(\hat{n})$, could correspond to spherical harmonics, $Y_{lm}(\hat{n})$, or pixels, where $Q_{\hat{n}'}(\hat{n}) = \delta^2(\hat{n},\hat{n}')$.

If we consider a vector of time, frequency pairs, labeled with (f,t), then equation (2.43) can be written abstractly as

$$\hat{C}_{(f,t)} = M_{(f,t),\alpha}P_\alpha \tag{2.44}$$

where matrix multiplication has taken the role of integration over directions on the sky, and $M_{(f,t),\alpha} = \frac{5}{8\pi}S(f)\gamma_\alpha(t;f)$.

We can also write down the covariance matrix for our cross-correlation statistic over many times and many frequencies, assuming small signals, no correlated noise between detectors, and stationary noise

$$\begin{aligned}\mathcal{N}_{tf,t'f'} &= \langle \hat{C}(t;f)\hat{C}(t';f')\rangle - \langle \hat{C}(t;f)\rangle\langle \hat{C}(t';f')\rangle \\ &\approx \delta_{t,t'}\delta_{f,f'}P_1(t;f)P_2(t;f).\end{aligned} \tag{2.45}$$

From here, we generate an abstract Gaussian likelihood using our matrix representation

$$\ln p(\hat{C}|P) = -\frac{1}{2}\left(\hat{C}_{(f,t)} - M_{(f,t),\alpha}P_\alpha\right)^\dagger (N^{-1})_{(f,t),(f',t')}\left(\hat{C}_{(f',t')} - M_{(f',t'),\alpha'}P_{\alpha'}\right).$$

Supressing indices for a moment, the maximum-likelihood estimators for our power distribution P follow immediately, $\hat{P} = F^{-1}X$ where

$$F \equiv M^\dagger \mathcal{N}^{-1} M, \text{ and } X \equiv M^\dagger \mathcal{N}^{-1}\hat{C}. \tag{2.46}$$

The matrix F is the Fisher information matrix, the matrix X is referred to as the "dirty map," and $\hat{P}$ is referred to as the "clean map." It is worth pointing out that F may not be invertible, and so it may require regularization. If we put our indices back in, then we can write down F and X in terms of our previous quantities

$$X_\alpha = \sum_t \sum_f \gamma^*_\alpha(t;f)\frac{S(f)}{P_1(t;f)P_2(t;f)}\hat{C}(t;f) \tag{2.47}$$

$$F_{\alpha,\alpha'} = \sum_t \sum_f \gamma_\alpha(t;f)\frac{S^2(f)}{P_1(t;f)P_2(t;f)}\gamma_{\alpha'}(t;f). \tag{2.48}$$

It also follows simply from our likelihood function that the variance of our estimators $\hat{P}$ is given by the inverse of the Fisher matrix. If the Fisher matrix is not invertible, we will need to regularize it, which introduces a bias in our recovered parameters and in their variance.

GW radiometer

We take point sources from widely-separated directions as a signal model for the GW power on the sky:

$$P(\hat{n}) = \mathcal{P}_{\hat{n}_0}\delta(\hat{n}, \hat{n}_0). \tag{2.49}$$

This would be applicable to a GW background dominated by a limited number of widely-separated point-sources (how widely separated depends on the point-spread function, given by the elements of the Fisher matrix [118]). Signals that are close enough together on the sky will interfere with one another. In this method, the inverse of the Fisher matrix, used in the definition of our estimators, gets replaced by the reciprocal of the diagonal elements of the Fisher matrix:

$$\hat{\mathcal{P}}_{\hat{n}} = (F_{\hat{n},\hat{n}})^{-1} X_{\hat{n}}. \tag{2.50}$$

This method ignores correlations between neighboring pixels. This method should *not* be confused with simply using a pixel basis for our definition of the Fisher matrix and the dirty map. This is a choice of basis, but it is also an explicit assumption that the point-spread function is small and that when we have many time segments covering most of the sidereal day, the correlation between pixels is smaller than the spread of sources we will attempt to recover with this method.[2]

In the end, this method becomes equivalent to explicitly defining an estimator for each location on the sky, in analogy with equation (2.17)

$$Y(t;\hat{n}) = \int_{-\infty}^{\infty} df\, \tilde{s}_1^*(t;f)\tilde{s}_2(t;f')Q(t;f',\hat{n}) \tag{2.51}$$

$$Q(t;f,\hat{n}) \propto \frac{\gamma(t;f,\hat{n})S(f)}{P_1(f)P_2(f)}. \tag{2.52}$$

Within the GW community, this was the traditional starting point for the GW radiometer analysis [125, 127]. In any case, the interpretation of a map created with the GW radiometer method should always be that *each pixel is a measurement of the GW power from a potential point source coming from that direction.* It should *not* be interpreted

---

[2] I make this point so vociferously because we will use a similar method in chapter 6 where we use the pixel basis but we will perform a *full inversion* of the Fisher information matrix.

as an unbiased map of the GW power on the sky.

An estimate of the correlation between pixels is found by looking at the rows of the Fisher matrix, sometimes referred to as a *point spread function.* Plotting a map of a single row of the Fisher matrix corresponds to how a signal at the direction associated with that row gets spread into other pixels. An example of the point-spread function for different choices of $S(f)$ and different declinations is shown in figure 2.4. A full characterization of the Fisher matrix for this method (including full inversion techniques that extend it), along with an analytical estimate of the point-spread function using a stationary-phase approximation can be found in [127].

Spherical harmonic decomposition

If we take diffuse sources to be our signal model, then it makes sense to decompose the sky onto spherical harmonics (we refer to this as the “SHD” method). We can create an overlap reduction function in that basis by decomposing $\gamma(t;f,\hat{n})$ onto spherical harmonics

$$\gamma(t;f,\hat{n}) = \sum_{l=0}^{\infty}\sum_{m=-l}^{l} \gamma_{lm} Y^{*}_{lm}(\hat{n}) \tag{2.53}$$

$$\gamma_{lm} = \int d\hat{n}\,\gamma(t;f,\hat{n}) Y_{lm}(\hat{n}). \tag{2.54}$$

Equations (2.47) and (2.48) still hold, where now $\alpha = (lm)$, and our estimators are now $\hat{P}_{lm} = (F^{-1})_{lm,l'm'} X_{l'm'}$.

In general, our search is not sensitive to arbitrarily small angular scales, and therefore arbitrarily high l’s. A rough estimate of the maximum l to which we are sensitive comes from looking at the diffraction limited spot size

$$\theta = \frac{c}{2df} \tag{2.55}$$

$$l_{\max} \approx \pi/\theta. \tag{2.56}$$

In this case f is roughly the frequency that contributes the most to our sensitivity and d is the distance between our detectors. For $f \approx 50\,\mathrm{Hz}$ we find $l_{\max} \approx 3$ and for $f \approx 250\,\mathrm{Hz}$ we have $l_{\max} \approx 16$ [24].

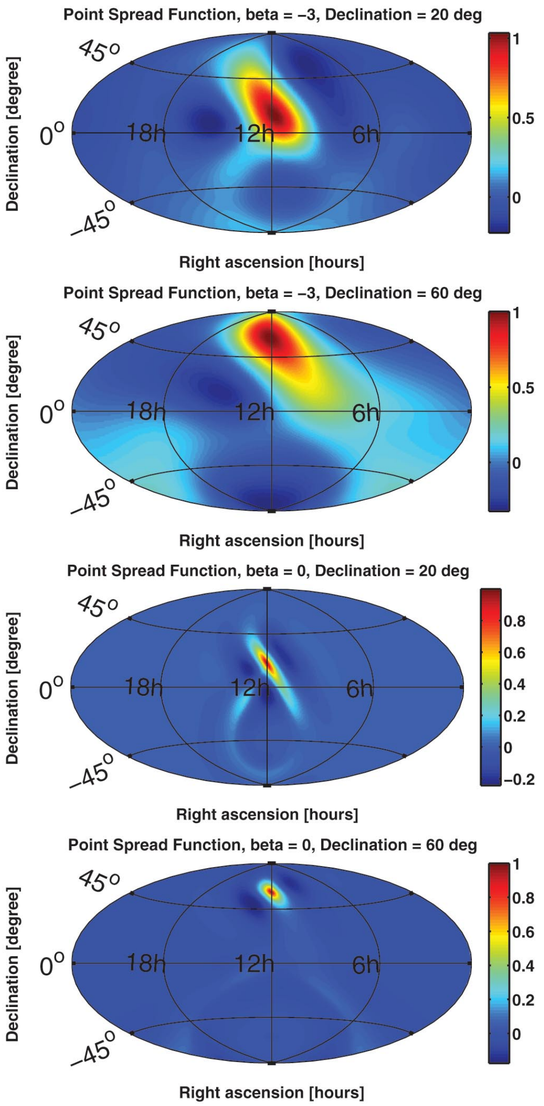
Point Spread Function, beta = −3, Declination = 20 deg

Point Spread Function, beta = −3, Declination = 60 deg

Point Spread Function, beta = 0, Declination = 20 deg

Point Spread Function, beta = 0, Declination = 60 deg

Figure 2.4: A map of the point-spread functions for the GW radiometer method. This plot is reproduced from [122]. The first two are injections at two different declinations for $S(f) = (f/f_{\rm ref})^{-3}$ and the second two are for $S(f) = const$.

The relatively poor resolution of our search might also lead one to think that there are directions to which we are not sensitive. In fact, this is the case, and one symptom of this issue is that the Fisher matrix is singular. The typical procedure in this case is to regularize the matrix. We perform a singular value decomposition of the Fisher matrix and impose a minimum cut-off for the singular values. That is, all singular values below some minimum value are either set to zero or are set to the minimum value. A singular value decomposition is effectively a method of diagonalization where we factor the Fisher matrix into three matrices

$$F = U\Sigma V^\dagger \tag{2.57}$$

If F is an $n \times m$ matrix, then U is $n \times n$, Σ is $n \times m$ and V is $m \times m$.[3] The singular values are then the diagonal elements of Σ, assumed (without loss of generality) to be arranged in decreasing order. We can define the *pseudo-inverse* of the Fisher matrix

$$F^+ = V\Sigma^+ U^\dagger \tag{2.58}$$

where Σ^+ is generated by imposing the cutoff and then taking the reciprocal of the remaining diagonal elements of Σ. We now define a new estimator based on the pseudo-inverse

$$\hat{P}_{lm} = (F^+)_{lm,l'm'} X_{l'm'}. \tag{2.59}$$

There is a bias introduced by this method of matrix inversion. It can be estimated by looking at $F^+F \neq \mathbb{I}$[4]. In addition, the proper variance of our new estimator is written in terms of this bias: $\mathrm{var}\left(\hat{P}_{lm}\right) = F^+FF^+$ [126].

From these estimators, it is also possible to calculate the angular power spectra, C_l [126]. These describe the angular scale structure in the clean map. Like the other parameters, they require an adjustment due to bias introduced by regularization of the Fisher matrix

$$\hat{C}_l \equiv \frac{1}{2l+1} \sum_m \left(|\hat{P}_{lm}|^2 - (F^+)_{lm,lm} \right). \tag{2.60}$$

The estimators, $\hat{P}_{lm}$, can also be converted back into estimates of the GW power in each pixel on the sky

$$\hat{P}(\hat{n}) = \sum_{l=0}^{l_{\max}} \sum_{m=-l}^{m=l} \hat{P}_{lm} Y^*_{lm}(\hat{n}). \tag{2.61}$$

---

[3] In this specific case, F is a square matrix, but that does not necessarily need to be the case to construct a pseudo-inverse using this method.

[4] A longer discussion of this in the present context is given in [118], while a similar issue is discussed in greater detail for the Homestake seismic array in chapter 6.

These can then be used to create a map of the GW power or GW energy density on the sky.

Making a detection and setting limits with the GW radiometer and SHD searches

As with the isotropic search, we assume that the integration over many time segments and many frequency bins means that our estimators are Gaussian random variables. However, using either the GW radiometer method or the SHD method, it is clear that individual pixels will be correlated with one another. Therefore, we simulate maps by generating many realizations of the dirty map, X_α using the measured covariances from the fisher matrix $F_{\alpha,\alpha'}$. We perform ~ 1000 realizations to generate a distribution of pixel SNRs. We then use this distribution to assess the significance of the loudest pixel SNRs in our recovered maps.

In the case where we do not make a detection, we set upper limits on each pixel independently using the same method as in equation (2.39).

Reporting results for the GW radiometer and SHD searches

Past analyses reported results for these two searches in terms of *strain power*, i.e. the units of $H(f)$. However, the most recent set of analyses [24] have chosen to use a more intuitive set of units. The SHD analysis is reported as a map of the energy density parameter, $\Omega_{\rm GW}(f,\hat{n})$. This can be expressed in terms of the strain power[5]

$$\Omega_{\rm GW}(f,\hat{n}) = \frac{8\pi^2}{3H_0^2} f^3 S(f) P(\hat{n}) \tag{2.62}$$

$$\Omega_{\rm GW}(f,\hat{n}) = \frac{8\pi^2}{3H_0^2} f^3 \left(\frac{f}{f_{\rm ref}}\right)^{\alpha-3} P(\hat{n}) \tag{2.63}$$

In terms of our estimators, and after integrating over frequency, the map is

$$\hat{\Omega}_\alpha(\hat{n}) = \frac{8\pi^2}{3H_0^2} f_{\rm ref}^3 \sum_{l=0}^{l_{\max}} \sum_{m=-l}^{l} \hat{P}_{lm} Y_{lm}^*(\hat{n}). \tag{2.64}$$

---

[5] Note that our expressions here differ from those in [24] by a factor of 4. This comes from the definition of $H(f)$ in the two-point correlation function in equation (2.21), where they use a factor of $\frac{1}{4}$ on the right-hand-side.

Note that α and $f_{\rm ref}$ come from the choice of the spectral model, $S(f) = \left(\frac{f}{f_{\rm ref}}\right)^{\alpha-3}$[6], which is applied when constructing the dirty map and the Fisher matrix. This means that our map has units of $\Omega_{\rm GW}$ sr^{-1}.

In the case of the GW radiometer, results are reported in terms of energy flux

$$\mathcal{F}(f, \hat{n}) = \frac{c^3\pi}{G} f^2 S(f) P(\hat{n}). \tag{2.65}$$

In terms of our estimators the map is then

$$\hat{\mathcal{F}}_{\alpha,\hat{n}} = \frac{c^3\pi}{G} f_{\rm ref}^2 \hat{P}_{\hat{n}}. \tag{2.66}$$

where we have integrated over the delta function in the signal model. This means that the units for this map are $\mathrm{ergs\,cm^{-2}\,s^{-1}\,Hz^{-1}}$.

2.5 An unmodeled, directed search for GWs across a wide frequency band

In addition to probing the whole sky for broadband point-sources of GWs, we can use our cross-correlation method to search across the whole available frequency band for GWs coming from a single specific direction. This is often referred to as the "narrowband radiometer" search. It can be used to target sources like non-axisymmetric, rapidly rotation neutron stars. While our search will not be nearly as sensitive as traditional matched-filter searches, it has the benefit of being unmodeled and computationally cheap. This makes it ideal for searching in areas where we expect a source of GWs, but do not know the specific parameters of the source like spin frequency or spin-down. Examples of this would include the low mass X-ray binary Scorpius X-1, which is the brightest extra-solar X-ray source in the sky and almost certainly contains a neutron star spun up by accretion [128, 129]. The spin frequency of the neutron star, however, is unknown. We also commonly search in the directions of the galactic center, where there is potentially an old population of recycled pulsars in globular clusters [130], and

---

[6] The factor of -3 comes from the fact that in this case $S(f)$ is a spectral model for the *strain power* and not the energy density. We would like to continue to use α to denote the spectral index of the energy density parameter, so we need the extra factor of -3.

the core-collapse supernova, Supernova 1987a [131].

The search is done by choosing a direction, $\hat{n}$, and reading off the frequency spectrum. This is equivalent to suppressing the sum over f in the calculation of the Fisher matrix and dirty map in equations (2.47) and (2.48) and looking at a specific $\hat{n}$ (notated as α in equations (2.47) and (2.48)) from the dirty map and the corresponding diagonal element of the Fisher matrix. The spectrum model $S(f)$ is taken to be unity. In this case our estimator and its uncertainty reduces to

$$\hat{Y}(t; f, \hat{n}) = (F_{\hat{n},\hat{n}}(t; f))^{-1} X_{\hat{n}}(t; f) = \lambda \frac{\hat{C}(f, t)}{\gamma(t; \hat{n}, f)} \tag{2.67}$$

$$\sigma_Y^2(t; f, \hat{n}) = (F_{\hat{n},\hat{n}}(t; f))^{-1} = \lambda^2 \frac{P_1(f) P_2(f)}{|\gamma(t; \hat{n}, f)|^2} \tag{2.68}$$

where λ is a normalization constant.

The result is an estimator for the GW power spectral density from a specific direction in a specific frequency bin. The units are strain^2 Hz^{-1}, which we then convert to units of strain^2 by multiplying by the the frequency bin width of the spectrum, Δf (this amounts to effectively integrating over a small frequency range over which our spectrum is assumed to be constant).

2.5.1 Reporting results on strain amplitude

The above search makes a statement about the strain power in the detector associated with a specific direction and at a specific frequency bin. It takes more work to make a statement about the strain amplitude, h_0, of GWs produced by a rapidly rotating neutron star, which is the source we commonly target with this search.

Below, we outline a method that we implemented for setting limits on the strain amplitude h_0 using this search. We also include results that validate the method on realistic simulated signals. Pieces of this method have been discussed in internal LIGO documents for several years [132]. A full implementation that properly takes into account Doppler broadening due to the relative motion of the source and the Earth, and a marginalization over the inclination and polarization angle of the source were not implemented until now.

Source frame frequency

We need to convert the measurements that are in terms of our detector to be in terms of the source. Our search is broken into a set of small frequency bins, $f_i = f_0 + i \times \Delta f$ where f_0 is the central frequency of the lowest frequency bin, i is an index for a specific frequency bin, and Δf is the width of each frequency bin. We will often refer to these bins as "sub-bins"[7], and refer to the detector strain power estimate and uncertainty in each sub-bin in terms of the index i, Y_i and σ_i.

In principle, the emission frequency in the frame of a source will be spread out when viewed in the frame of the detector. Any change in the source frequency due to spin-down can also spread the signal out over multiple frequency bins. We can write down a generic expression for the frequency in our detector at a given time based on the frequency of the source at the start of a run

$$f_{\text{det}} = [1 - A(t) - B(t) - C(t)]\, f_{\text{source}}. \tag{2.69}$$

In this expression we assume that the relative velocity of the source and the detectors is small compared to the speed of light. $A(t)$ is the modulation due to the motion of the Earth with respect to the source, $B(t)$ takes into account the orbital motion for a source in a binary orbit, and $C(t)$ takes into account any other modulation due to intrinsic properties of the source (like spin-down for an isolated neutron star). We use heliocentric equatorial coordinates to describe the motion of the Earth and the direction of the source. The modulation term due to the motion of the earth is

$$A(t) = \frac{\vec{v}_E(t) \cdot \hat{k}}{c} \tag{2.70}$$

where $\vec{v}_E(t)$ is the velocity of the Earth

$$\vec{v}_E(t) = \omega R[\sin\theta(t)\hat{u} - \cos\theta(t)\cos\phi\hat{v} - \cos\theta(t)\sin\phi\hat{w}]. \tag{2.71}$$

In this expression, R is the mean distance between the Earth and the Sun, ω is the angular velocity of the Earth around the sun and $\phi = 23^\circ, 26\text{ min}, 21.406\text{ sec}$ is the obliquity of the ecliptic. The time dependent phase angle, $\theta(t)$, is written as $\theta(t) =$

---

[7] because we will combine them into larger bins later

$2\pi(t - T_{\mathrm{VE}})/T_{\mathrm{year}}$, where T_{year} is the number of seconds in a year and T_{VE} is the time at the Vernal equinox. The unit vector $\hat{k}$ points from the source to the earth and is given by

$$\hat{k} = -\cos\delta\cos\alpha\hat{u} - \cos\delta\sin\alpha\hat{v} - \sin\delta\hat{w} \tag{2.72}$$

where δ is the declination of the source and α is the right ascension.

For a source in a binary system, the modulation due to the binary motion is given by

$$B(t) = \frac{2\pi}{P_{\mathrm{orb}}} a\sin i \times \cos\left(2\pi\frac{t - T_{\mathrm{asc}}}{P_{\mathrm{orb}}}\right) \tag{2.73}$$

where P_{orb} is the orbital period of the binary system, $a\sin i$ is the projection of the semi-major axis onto the line of site (in units of light-seconds), and T_{asc} is the time of the orbital ascending node. In the case of isolated sources this term is set to zero. A plot of $A(t) + B(t)$ for Scorpius X-1 during O1 is shown in figure 2.5.

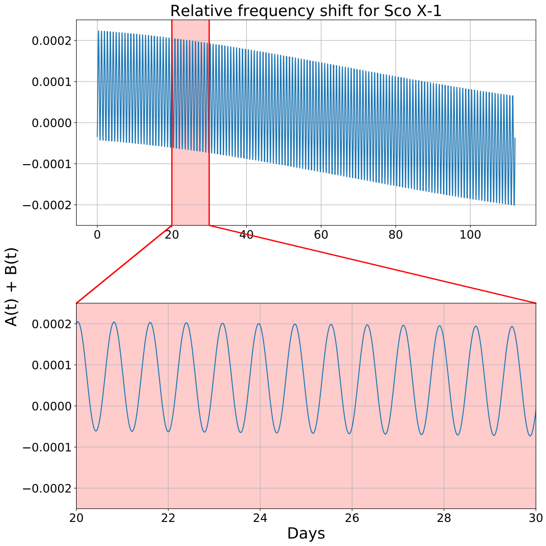

Figure 2.5: The modulation of a signal due to the motion of the earth and the binary motion of Scorpius X-1. The top plot shows the overall change due to the motion of the Earth, the bottom plot zooms in on a few days to show the variation due to the motion of the binary. In this case, I have used $a\sin i = 1.44$ ls.

Combining information from multiple frequency bins

We next consider source frequencies at the center of each frequency bin in our analysis and calculate the minimum and maximum detector frequencies from equation (2.69) over the analysis time using the *edges* of the frequency bins. We then combine detector power from all frequency bins between the minimum and maximum detector frequencies to account for the GW power spread over multiple frequency bins

$$Y_c = \sum_{i=-b}^{a} Y_i \text{ and } \sigma_{Y,c}^2 = \sum_{i=-b}^{a} \sigma_{Y,i}^2 \tag{2.74}$$

where i indexes our original frequency bins and $i = 0$ specifies the bin associated with the source frequency. This means that a and b are the number of frequency bins we want to combine above and below the source frequency bin, respectively. The resulting set of *combined* frequency bins now represent the (observable[8]) GW strain power due to a source whose frequency falls within that frequency bin. The combined frequency bins are also now strongly correlated because they overlap. This helps us avoid issues where the true source falls on the edge of one our original, detector frequency bins, but it also introduces issues related to estimating the significance for our search. Since frequency notching is done on the detector sub-bins, we often find ourselves in a situation where the sum in equation (2.74) includes bins which are notched. If more than half of the bins to be combined are notched, then we remove the combined bin from the analysis. If half or fewer than half of the sub-bins are notched, then we combine the bins that are not notched. The SNR used for a potential detection is calculated using this "uncorrected" combined bin. If no detection is made, then for the purposes of setting upper limits, we rescale Y_c and $\sigma_{Y,c}$ for that combined bin, assuming the notched sub-bins had amplitude consistent with the non-notched sub-bins. Otherwise, we would set a limit that is lower than it should be.

---

[8] Observable here meaning that the source strain power will likely be larger than what we would infer due to our assumption that polarization is optimal. This is discussed later in the section.

Making a detection

In general, we consider the frequency bins in our analysis to be uncorrelated and, because they are the result of averaging over many time segments, drawn from a gaussian distribution. This is generally true of the results in the detector frame. Creating the set of combined bins to estimate source power results in a set of frequency bins that are highly correlated. Therefore, I simulate many realizations of the sub-bins (i.e. detector frame, uncorrelated frequency bins) under the assumption that they are drawn from a gaussian distribution of mean 0 and variance $\sigma^2_{Y,i}$. For each realization, I combine bins as in equation (2.74) and record the maximum SNR across the whole set of combined frequency bins. The goal is to empirically determine the noise distribution of SNRs. I perform ~ 1000 realizations (for each direction I am interested in) to get a distribution of the maximum SNR from the combined bins. This distribution will then yield the significance of our actual data.

Making statements about h_0

By combining frequency bins we have an estimate of the GW power produced by the source that would interact with our detector. For an isolated neutron star the inclination and polarization angles of the star can cause polarizations that violate the initial assumptions of the search (i.e. equal power in plus and cross polarizations). The strain in each polarization can be written in terms of the inclination angle of the neutron star

$$h^{+}(t,f) = A_{+}(f)\cos(\Phi(t,\vec{\theta}) + \phi_0) \tag{2.75}$$

$$h^{\times}(t,f) = A_{\times}(f)\sin(\Phi(t,\vec{\theta}) + \phi_0) \tag{2.76}$$

where $\vec{\theta}$ is a set of parameters that determines the phase angle of the neutron star, and A_+ and $A_\times$ are defined in terms of the strain amplitude h_0,

$$A_{+} = \frac{1}{2}h_0(1+\cos^2\iota) \tag{2.77}$$

$$A_{\times} = h_0\cos\iota. \tag{2.78}$$

In this case ι is the inclination angle of the neutron star spin axis relative to the line of sight.

This means that the assumption of our two-point correlation function in equation (2.21) is incorrect and needs to be re-written

$$\langle h_a^*(f,\hat{n}) h_{a'}(f',\hat{n}') = \delta(f-f')\delta^2(\hat{n},\hat{n}')\delta_{a,a'}A_a^2(f) \tag{2.79}$$

where this a is $+, \times$ (previously we used A, but the notation becomes confusing quickly). It immediately follows that

$$\langle \tilde{h}_1^*(t;f,\hat{n})\tilde{h}_2(t;f,\hat{n})\rangle = (A_+^2 F_1^+(t;\hat{n})F_2^+(t;\hat{n}) + A_\times^2 F_1^\times(t;\hat{n})F_2^\times(t;\hat{n}))e^{2\pi i f(\hat{n}\cdot\Delta\vec{x}/c)}. \tag{2.80}$$

This introduces a bias into our statistic if we want to use it to measure h_0, because an isolated neutron star *certainly* has a well-defined inclination angle. Therefore, we must account for this bias by marginalizing over the inclination angle (since we do not know it) when we attempt to make a statement about the strain amplitude h_0 of the source. We relate the strain amplitude of the source to our statistic Y_c using a parameter $\mu_{\iota,\psi}$

$$h_0^2 \mu_{\iota,\psi} = Y_c. \tag{2.81}$$

The full calculation for $\mu_{\iota,\psi}$ was originally written down in [129] and has been used in other recent analyses [64, 133] where the inclination angle is unknown. In the end the bias factor is

$$\mu_{i,\psi} = \frac{\sum_{j=1}^{M}\left[(\cos\iota)^2 F_{1,j}^+ F_{2,j}^+ + (\frac{1+\cos^2\iota}{2})^2 F_{1,j}^\times F_{2,j}^\times\right](F_{1,j}^+ F_{2,j}^+ + F_{1,j}^\times F_{2,j}^\times)}{\sum_{j=1}^{M}(F_{1,j}^+ F_{2,j}^+ + F_{1,j}^\times F_{2,j}^\times)^2} \tag{2.82}$$

where j is an index for each time segment in the analysis, M is the total number of time segments in the analysis, and we have suppressed any frequency dependence; assuming we are working a single frequency bin.

We write down the posterior distribution for h_0 in terms of $\cos\iota$, the polarization angle, ψ, and a calibration factor, l. We use uniform prior distributions on $\cos\iota$ and ψ, and a Gaussian distribution on l (with uncertainty given by the calibration uncertainty),

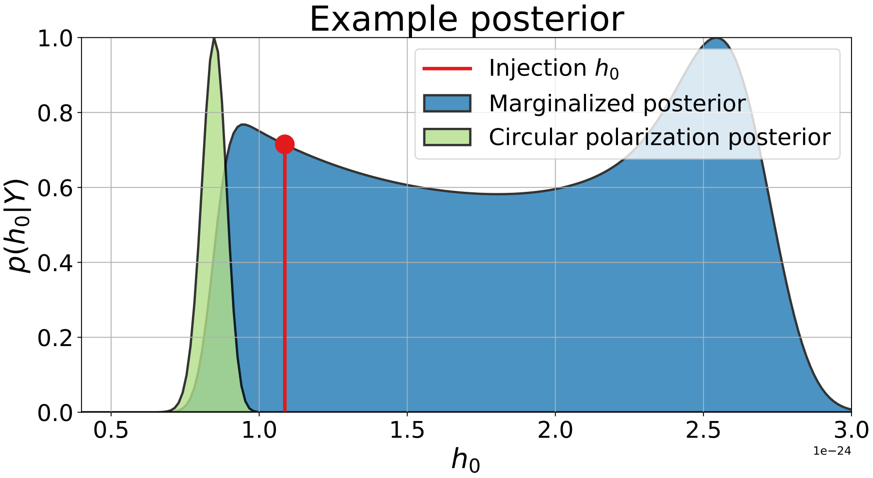

Figure 2.6: An example posterior distribution on the strain amplitude of a pulsar using the narrowband radiometer. We have also plotted the distribution if we ignore the bias factor $\mu_{i,\psi}$ and we see that the "correct" method is much wider.

and then marginalize over all three parameters

$$p(h_0|Y_c) \propto \int_{-1}^{1} d(\cos\iota) \int_{-\pi/4}^{\pi/4} d\psi \int_{-1}^{\infty} dl\, e^{-\frac{1}{2}L(l)} \tag{2.83}$$

$$L(l) = \left(\frac{\mu_{i,\psi} h_0^2 - (l+1)Y_c)}{(l+1)\sigma_c}\right)^2 + \frac{l^2}{\sigma_l^2}. \tag{2.84}$$

The resulting posterior distribution shows a "double-hump" shape, shown in figure 2.6.

Validating new method using simulated injections

I validated this new method using simulated Scorpius-X1-like signals. That is, I injected 139 signals that span the frequency band, and are consistent with a neutron star in a binary system. The parameters of the injections are drawn from distributions consistent with the current estimates of various parameters of Scorpius X-1. These distributions, along with other parameters that define the system, and the orbital parameters of the Earth used for combining frequency bins, are shown in table 2.1. We claim a "detection" for a p-value of 0.01, and in that case we construct 90% confidence intervals on h_0. If we do not recover the signal, then we set 90% upper limits.

Parameter	Description	Distribution or value
	Scorpius X-1 parameters	
$h_0(f)$	Strain amplitude	$\mathcal{U}(0, 3 \times \sigma_{h_0}(f))$
$\cos\iota$	Cosine of inclination angle of neutron star	$\mathcal{U}(0, 1)$
$a\sin i$	Projection of semi-major axis onto line of site	$\mathcal{U}(0.36, 3.44)$
ψ	Polarization angle of source	$\mathcal{U}(-\pi/4, \pi/4)$
t_{asc}	Time (GPS) of the orbital ascending node	897753994
α	Right ascension	$16^{\mathrm{h}}19^{\mathrm{m}}55.0850^\circ$
δ	Declination	$-15^\circ38'24.9''$
P_{orb}	Orbital period	68023.70 s
d	Distance	2.8 kpc
	Earth orbital parameters	
ϕ	Angle between Earth's orbit and its equator	$23^\circ26'21.406''$
T_{VE}	GPS Time of vernal equinox	953141535 s
R	Mean distance between Earth and Sun	1.496×10^{11} m
ω	Orbital angular velocity of Earth	1.99×10^{-7} rad/s

Table 2.1: Values and distributions for key parameters used in creating and recovering software injections. h_0 was drawn between 0 and 3 times the 1-σ uncertainty on h_0 in the bin into which we injected. $\mathcal{U}(a, b)$ indicates a uniform distribution between values a and b.

We detected 47 out of the 139 injected signals. Confidence intervals are constructed by sorting the posterior distribution on h_0 from greatest to least likelihood and integrating over the sorted distribution until we reach 90% of the total area under the curve. This can lead to a disjoint confidence interval. In general, we report the interval spanning from the the minimum of the interval to the maximum, which means that this reported interval likely contains more than 90% of the posterior. In the set of recovered injections, the injected value of h_0 was within the 90% confidence interval for all 47 recovered signals.

In addition to the disjoint nature of the interval, we use a value of $a\sin i = 1.44$ s to perform all recoveries, as opposed to maximizing over it within the range shown in table 2.1. In cases where the true value of $a\sin i < 1.44$, we are adding extra noise into our recovery and thus our interval will be larger and perhaps shifted higher than it should be. In the opposite case, we lose some of the signal because we do not combine over enough frequency bins, meaning we would underestimate h_0. In both cases, however, it would take a very specific combination of injected $a \sin i$ and $\cos \iota$ (i.e. on the edge of the distributions we chose) for our interval to miss the injected value of h_0. It is therefore not a complete surprise that we do not miss any signals in the intervals, when normally we might expect to miss $0.9 \times 47 \approx 5$ of them. A scatter plot of the injected h_0 vs. the median of the 90% confidence interval for all recovered injections is shown in figure 2.7. The colors indicate $|\cos \iota|$ while the sizes indicate $a \sin i$.

In the absence of a detection, we set 90% upper limits on h_0, integrating the posterior distribution

$$0.90 = \int_0^{h_0^{90}} p(h_0|Y_c, \sigma_{Y_c})\, dh_0. \tag{2.85}$$

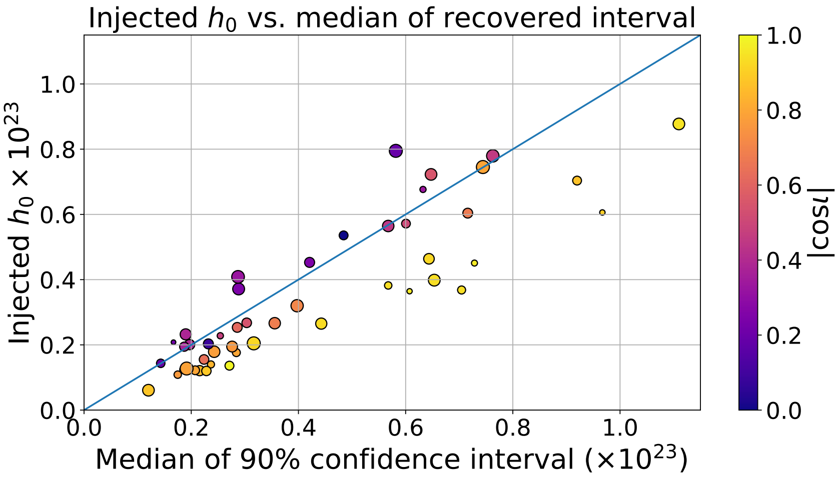

Figure 2.7: A scatter plot of injected vs. recovered values of h_0. The "recovered" value is taken to be the median of the 90% confidence interval. The color indicates $\cos \iota$ and the size indicates $a \sin i$. We see immediately that for large $|\cos \iota|$ we tend to overestimate the injection. The size of the points does not seem to show any obvious pattern.

2.5.2 Software injections to test upper limit coverage

We also tested the method of calculating upper limits using the posterior in equation (2.83) and integral in equation (2.85). We do this by first performing the search with an unphysical time shift between interferometers to remove correlations between signals. We then calculate 90% upper limits as in equation (2.85) for each frequency bin in the analysis. We choose 140 frequency bins at random and run yet another time shifted analysis *with simulated Scorpius X-1-like signals in each frequency bin.* The amplitude of h_0 for each injection is equal to the 90% upper limit set by the first time shifted run. If the limits provide correct coverage then the measurement in the injected bins from the second run should be larger than the measurement from the first run 90% of the time. Indeed, results showed this was true 93% of the time for our case.

2.6 Conclusions

In this section we have discussed searches for persistent gravitational waves using cross-correlation methods. This includes searches for a broadband, Gaussian, unpolarized, and isotropic SGWB as well as an anisotropic, broadband SGWB. Finally, we discussed a narrowband, directed, unmodeled search for persistent GWs and a new method that I implemented to use this search to set limits on the strain amplitude produced by a rapidly rotating neutron star.

Chapter 3

Cross-correlation search results from the first LIGO observing run

In this chapter, we discuss the application of the search methods described in chapter 2 to data from Advanced LIGO's first observing run (O1). We begin with a brief overview of O1 in section 3.1 before discussing data quality studies and data quality cuts used for the analyses in section 3.2. We then present results in section 3.3 for the isotropic and anisotropic searches for an SGWB, along with the unmodeled, directed search for persistent GWs (also referred to as the "narrowband radiometer search").

3.1 The first LIGO observing run

Advanced LIGO was in operation for its first observing run from September 18th, 2015 15:00 UTC to January 12th, 2016 16:00 UTC. The fraction of total time in observation mode for the run was 57% for the Livingston, LA, instrument (L1) and 65% for the Hanford, WA instrument (H1), while the coincident fraction was 43%. In general, H1 was more sensitive than L1, with the H1 interferometer sensitive to signals from binary neutron star inspirals at a range of roughly 75 Mpc compared to 65 Mpc for L1. These last two values represent roughly a factor of 3−5 improvement compared to the range from the final run of initial LIGO [54].

O1 was plagued by several data quality issues, the worst of which was at H1 where there was a bad driver for an electro-optical modulator that is used to imprint 45 MHz sidebands on the light. A good summary of transient data quality issues around the time of the first LIGO detection can be found in [50], and the data quality methods for transient searches for GWs described there apply generally to the rest of the O1 data. The Advanced LIGO detectors also exhibit many narrow spectral features ("lines") that can plague long-duration searches like those for rapidly rotating neutron stars and the SGWB. How these lines are identified and mitigated in the detectors, and how they are dealt with in searches for persistent GWs is discussed in [51], and we will summarize them in section 3.2.4. In the next section, we will discuss these data quality issues and how we dealt with them in the O1 cross-correlation searches.

3.2 Data quality for cross-correlation searches in O1

3.2.1 Signal processing steps

For all of our cross-correlation searches, the data were separated into a list of "jobs" that corresponded to times when the detector was in an observational state. Data quality studies were then performed; typically in the form of "time-shifted" analyses, or coherence studies (which are described below). Data quality cuts were applied and, if necessary, a new list of jobs was made. For each job and each search, the data were downsampled from 16384 Hz to 4096 Hz, and separated into 50% overlapping, 192 s segments. The segments were Hann-windowed and high-pass filtered using a 16th order Butterworth digital filter with a knee frequency at 11 Hz. The data was padded with zeros to double its length, and a discrete Fourier transform (DFT) of the data from both interferometers was taken. The DFTs were then multiplied together and coarse-grained to a frequency resolution of 0.03125 Hz, and the searches were perfromed on the frequency band between $20 - 1726$ Hz. The power spectral density (PSD) of noise in each detector for each 192 s segment was estimated using Welch's method with 32 s time windows on the *adjacent* 192 s segments, giving a total of 22 time-averages in each frequency bin for the PSD estimate. Using off-source data to estimate detector noise reduces bias in the statistic [134].

The segment duration and frequency bin width of our analyses were informed by the data quality studies presented below. It is worth noting that the final values chosen, 192 s and 0.03125 Hz, differ from the traditional choices of 60 s and 0.25 Hz used in previous searches [135, 136]. This choice was made in large part due to a 0.5 Hz "comb" of frequencies seen in the coherence spectrum of the two interferometers. Using longer time segments and smaller frequency bins allowed us to effectively remove the affected frequencies and to keep a larger amount of data than if we had used the traditional choices of 60 s and 0.25 Hz.

3.2.2 Time shift method

It is customary to first run the searches in a way in which we are "blind" to real signals, which helps identify how detector-related issues will show up in our search. We achieve this by applying an unphysical time shift ($>$ 10 ms) between the data streams of the H1 and L1 detectors. It is important to note that this method does not fully blind our analyses to certain types of sources. In the case of isolated pulsars and signals that are very close to periodic, for example, this method might make a signal appear as coming from a different direction or with a different sign, but will not completely blind the search. In the typical search for an isotropic, Gaussian, SGWB, this method is quite effective. This can be seen in Fig. 5 of the supplemental material in [135].

3.2.3 Time-domain data quality

Job list creation

When making our list of jobs, we began by removing a set of times, known as "vetoes," during which the detector was not operating properly, despite the fact that it was in observation mode. These times were decided upon by the LIGO detector characterization group, and collected in what is known as a "veto definer file." We implemented categories 1 and 2 (CATs 1 and 2) from the veto definer file. A veto falls into one of three categories [50]

- **CAT 1**—times when data should not be analyzed because a key detector component is not operating in its nominal configuration or the calibration filters are not behaving properly.

- **CAT 2**—times when a noise source with known physical coupling to the strain channel is active.
- **CAT 3**—data quality triggers that are statistically generated, and data quality flags where the coupling mechanism is not understood[1].

To create the job list we assembled a list of times when both of the interferometers were in observation mode and we found the intersection of times from this list with times that were not vetoed by CAT 1 or CAT 2 vetoes in the veto definer file. The result is a list of times when the interferometers are both in observation mode and functioning properly.

A study of the effect of different vetoes on our search performance was done after most analyses had reached a mature state and so no decisions were made based on that study. We have presented that study at the end of this chapter in section 3.4.

$\Delta\sigma$ cut

While CAT 1 and CAT 2 vetoes were generally effective at removing transient bursts of power due to known detector-related issues, the noise in the detectors was non-Gaussian and non-stationary even after their removal. To deal with this issue we implemented what we call the $\Delta\sigma$ cut. As we mentioned above, the PSD of the instrumental noise of the detectors for a single time segment was estimated using the average of the PSD of the detector noise in the two adjacent time segments [134]. However, if there is a transient artifact in the middle time segment, then using the adjacent segments results in an underestimate of the PSD and an anomolously large SNR. To mitigate this issue, we calculate the theoretical variance of our statistic, shown in equation (2.28), using PSDs from adjacent time segments and compare it to the same calculation using PSDs from the middle time segment. We remove times where these two values differ by $> 20\%$, meaning that for a time segment to be used in the analysis we require

$$0.8 < \frac{\sigma_{\text{adjacent}}}{\sigma_{\text{middle}}} < 1.2. \tag{3.1}$$

---

[1] CAT 3 vetoes were not implemented by the detector characterization group for O1, but we mention them here because they have been used in initial LIGO science runs.

Because σ is calculated by integrating over frequency, this cut can miss transient sources of noise that are localized to a small fraction of the frequency band. This can cause outliers in the narrowband radiometer search because it makes a measurement in each frequency bin individually. To mitigate this issue, we perform the cut where σ is calculated for several different values of the power law spectral index α. The choices of $\alpha = (-5, 0, 3)$ emphasize different parts of the frequency spectrum. The list of times to remove from the analysis are then taken to be the union of the times removed from those three runs.

Figure 3.1 shows an example of the effect of this cut on the distribution of the SNR calculated in each 192 s time segment for the isotropic search. It is not the final cut that was used, but is presented to show how effective it is. We also performed an analysis to verify that 20% was an acceptable threshold for this cut. A receiver operator characteristic (ROC) curve showing many different choices of the threshold is shown in figure 3.2. The ROC curve plots "true positive" vs. "false positive," where true positive means that we have removed a time segment with the $\Delta\sigma$ cut and the signal-to-noise ratio of that time segment is larger than one would expect from Gaussian noise (in this case we chose —SNR— = 4.5 for that threshold). False positive means that we have removed a time segment, but the SNR was consistent with fluctuations due to Gaussian noise given the number of time segments over which have observed. A good cut will produce an ROC statistic that is well above the line $y = x$ on the true positive vs. false positive plot. This is clearly the case for the $\Delta\sigma$ cut for many different choices of the threshold in figure 3.2. In the bottom plot of figure 3.2 we show the distance between our ROC curve and the line $y = x$, where we see that 20% is a reasonable choice because it is conservative while still being effective.

Low frequency noise

Even after applying the $\Delta\sigma$ cut, there were still several individual jobs in the time-shifted results of the narrowband radiometer analysis that showed loud signal-to-nosie ratios at low frequencies. These artifacts were evident in the $20 - 25$ Hz region, and we designed a cut to remove these automatically. A plot of the SNR spectrum for fifty jobs from the narrowband radiometer analysis can be seen in figure 3.3.

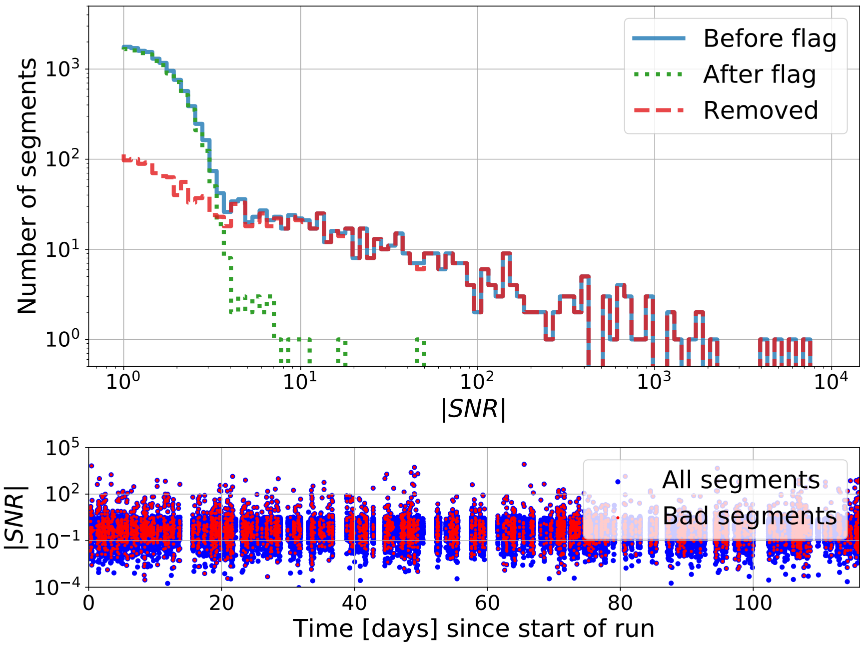

Figure 3.1: An example of the effect of the $\Delta\sigma$ cut on the O1 isotropic search. This cut is made only using information from $\alpha = 0$ and only on SNRs calculated for $\alpha = 0$. The top plot shows the distribution of SNR from all time segments in blue, the distribution of SNRs for segments that fail the delta sigma cut in red. This is done with a job list that implements *no vetoes at all*.

I simulated the point estimate, $Y(f)$, based on the value of $\sigma(f)$ (assuming a Gaussian distribution with mean of 0, standard devation given by $\sigma(f)$ in each bin) and calculated the distribution of the following statistic

$$\mathcal{S} = \frac{\sum_f |Y(f)|\sigma(f)^{-2}}{\sum_f \sigma(f)^{-2}} \times \left(\sum_f \sigma(f)^{-2}\right)^{1/2} . \tag{3.2}$$

We use the absolute value because the noisy frequency bins alternate between positive and negative SNR. The sum over frequency is done over all bins between 20 and 25 Hz because this is where most of the power is concentrated. The distribution of this statistic across all jobs for the simulated case and for the real case is shown in figure 3.4. The vertical line indicates where the cut was made. All jobs to the right of that cut

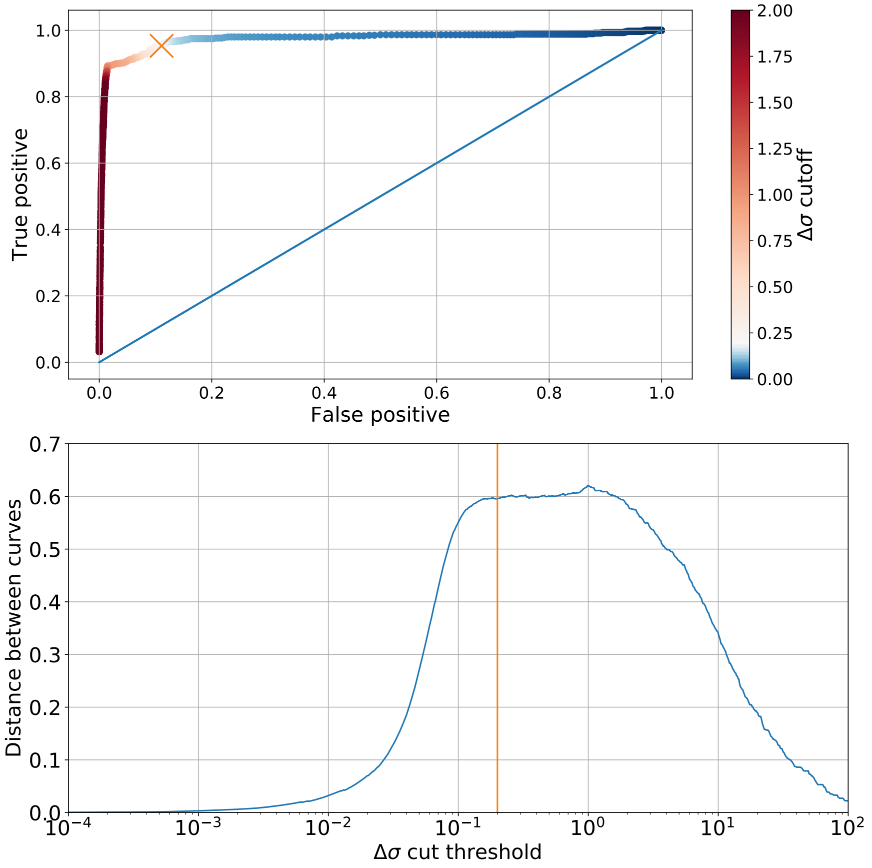

Figure 3.2: Using the same job list as in figure 3.1 we create an ROC curve using different cut values for the $\Delta\sigma$ cut. "True Positive" indicates the segment had $|\mathrm{SNR}| > 4.5$ and was flagged by the $\Delta\sigma$ cut, "False Positive" indicates the segment had $|\mathrm{SNR}| < 4.5$ and was flagged by the $\Delta\sigma$ cut. We see a broad range of cuts that are roughly equivalent under this statistic, and our chosen of value of 0.2 falls on the conservative end of that range. The bottom plot shows the distance between the ROC curve and the line $y = x$. The vertical line indicates the threshold used for the searches.

line are removed from the analysis. This removed a total of roughly 3.5 days of data. The cut was cross-checked by looking at the actual SNR spectrum for each job and this cut produced results that were consistent with what one would produce just using an "eye test"[2]. A final cause of this issue was never identified. One of the more likely

---

[2] There was visible excess cross-power like that shown in figure 3.3) in the 20-25 Hz region for each of the jobs that were removed.

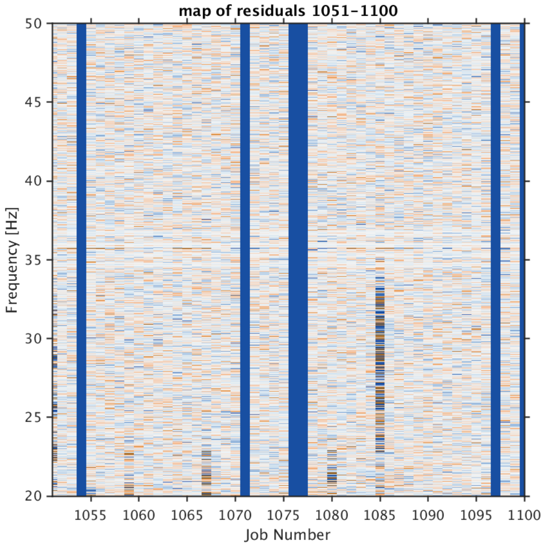

Figure 3.3: SNR spectrogram for fifty jobs in the O1 narrowband radiometer analysis. Each column represents a spectrum that has been generated by summing over each segment in a single job in the O1 job list, which are typically $\mathcal{O}(1000\text{ s})$ long. Darker red and blue pixels in several columns indicate jobs that show significant excess SNR at low frequencies. Blue columns indicate jobs that were not long enough to be analyzed by the analysis.

candidates–elevated ground noise–turned up no obvious correlations in studies that were performed.

Wandering line

From September – December, 2015, the H1 data showed an obvious "wandering line" that could be seen between 600 and 650 Hz and 1200 and 1300 Hz [137, 138]. This line was caused by a beat note between two voltage controlled oscillators (VCOs). The VCOs were used to lock each arm of the interferometer individually, before then locking the full Michelson interferometer. When the interferometer is in observing mode the VCOs are parked at their maximum or minimum voltages. The oscillation frequencies of the two VCOs were nearly equal when parked at their minimum voltages, but their frequencies drift as a function of time and this causes a beat note between the two

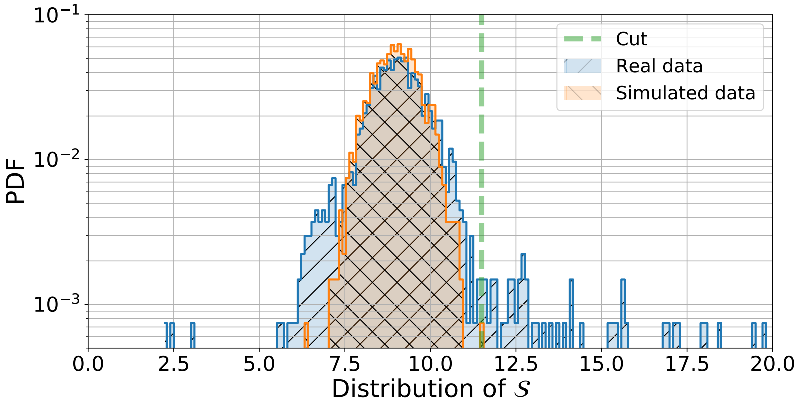

Figure 3.4: The left-hatched curve is the distribution of the $\mathcal{S}$ statistic over all 1300+ jobs in the narrowband radiometer analysis. The right-hatched curve is the distribution over jobs where we have simulated values of $Y(f)$ for each job under the assumption that $Y(f)$ is normally distributed with mean zero and standard deviation $\sigma(f)$.

signals. This beat note then gets picked up by other electronics systems, like control loops used to damp the motion of mirrors, and can then get imprinted on the laser light and show up in our strain data [51]. The line is shown in a spectrogram in figure 3.5. The transition between frequency bins from one time to the next caused poor PSD estimation that happened on such a limited scale in the frequency domain that it was not caught by the $\Delta\sigma$ cut, but still resulted in large SNR for several frequency bins in the narrowband radiometer search.

The narrowband radiometer search was more susceptible to the noise between 1200 and 1300 Hz than the noise between 600 and 650 Hz. Therefore, we removed the whole band between 1200 and 1300 Hz from the analysis. This was a very conservative decision, and a frequency-time-dependent cut based on the value of the two VCOs as a function of time could have been designed. However, it would have required an overhaul to the post processing code that is currently used for our searches, which would have set back the timescale of the analysis by more than a month (at minimum). Therefore, we decided to remove the whole frequency band from the searches.

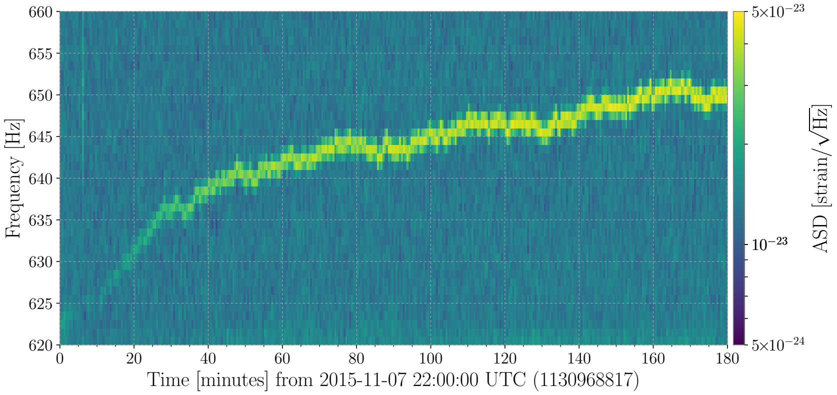

Figure 3.5: Spectrogram illustrating the ∼650 Hz wandering line seen in H1 strain spectrogram for three hours. This line is caused by two voltage controlled oscillators (VCO) creating a beat frequency that is picked up by local electronics systems. The two VCOs are used in the lock acquisition process and during lock itself, their voltages were railed, causing them to have values very close to one another. The solution was to rail one VCO to +10 V and the other to -10 V.

3.2.4 Frequency-domain data quality

In addition to transient artifacts that can cause poor PSD estimation, we also worry about persistent sources of noise that are nearly sinusoidal. We call these features “lines” because of how they look in a spectrum. Lines that are coherent between the two interferometers violate one of the core assumptions of our search statistic (specifically that there is uncorrelated noise between detectors) and lines that are particularly loud but not coherent degrade the sensitivity of our search in that frequency bin.

Below are detailed investigations performed during O1 that attempt to mitigate line artifacts that affected the O1 cross-correlation searches.

General method

We removed well-known lines that are purposely injected into the detectors. These include injected calibration lines, which require a notch of 0.05 Hz on either side of their central frequency, and injected pulsar signals [139], which require a notch that accounts for the simulated Doppler broadening and spin-down of the fake signal. We also notch the $n \times 20$ Hz region on either side of the resonances in the suspension fibers of the test mass ("violin modes"), where n is the harmonic of the mode, the known resonances of several auxiliary mirrors [140]. Both classes of lines are evident in the noise curves shown in figure 1.4. We also notch 0.1 Hz on either side of each harmonic of the 60 Hz power mains.

If we observe a line that is coherent between the H1 and L1 interferometers we launch a follow up investigation to determine if the line is caused by local environmental factors instead of GWs. We define the coherence as a function of frequency between any two channels, s_1 and s_2, by the normalized product of their Fourier transforms

$$C(f) = \frac{|\langle \tilde{s}_1^*(f)\tilde{s}_2(f)\rangle|^2}{\langle|\tilde{s}_1(f)|^2\rangle\langle|\tilde{s}_2(f)|^2\rangle} \tag{3.3}$$

where tilde indicates Fourier transform, star indicates complex conjugation, and $\langle\cdot\rangle$ indicates an average over time. The probability of finding coherence as large as C in a given frequency bin when the coherence is created from many time averages, N_{avg}, is given by an exponential distribution

$$p(C) \sim e^{-N_{\mathrm{avg}}C}. \tag{3.4}$$

The coherence spectrum between H1 and L1 with 1000 s time segments averaged over the whole O1 run, with a frequency resolution of 1 mHz is shown in figure 3.6, along with a histogram (and exponential fit) of that spectrum. A set of coherent lines is identified by choosing frequencies that fall to the right of the exponential fit in the histogram plot.

In following up a line with larger than expected coherence, we cross-correlate the strain channel with as many channels as possible that monitor the local environment and auxiliary degrees of freedom of the interferometer. If we identify significant coherence between the strain channel and one of these monitors at the frequency of interest, we remove that frequency bin from the analysis.[3] The auxiliary channel follow up was performed by students at Carleton College using a tool for searching for very narrow lines [141], by myself using the STAMP-PEM tool, discussed in chapter 4, or by staff

---

[3] The channels we use here are not sensitive to GWs. One method of checking this is by injecting loud signals into the interferometer and checking which auxiliary channels identify a spike in power during that same time. A discussion of this method is given in section 3, paragraph 5 of [54].

members on site at the observatories.

In many cases, a set of lines with a well-defined spacing between them are evident in the individual PSD spectrum of a single interferometer, or in the coherence spectrum between two channels. We refer to this as a "comb."[4]

Inter-site coherence study results

Through the quasi-real-time monitor `stochmon`, we look at the coherence between the H1 and L1 strain channels with frequency resolutions of 0.25 Hz, 0.1 Hz and 0.001 Hz on time scales of days, weeks, and the full observation run. The 0.001 Hz spectrum and its associated histogram are shown in figure 3.6.

The spectrum shows an obvious comb with a separation of 0.5 Hz whose odd harmonics are visible in the H1-L1 coherence spectrum from $20-40$ Hz. This comb was caused by blinking LEDs on timing chips synced to GPS clocks at both sites [51], and attempts have been made to try to mitigate the issue. The comb was initially notched from the SGWB O1 analyses only in the band from $20-40$ Hz [5]. However, when our group ran the search for an isotropic SGWB with an unphysical time shift, the SNR was ~ 3. A follow-up study indicated that while at frequencies >40 Hz, the coherence between H1 and L1 was not significant in any individual frequency bin, the sum over only teeth in the comb showed a value much larger than what is expected from the sum of frequency bins from Gaussian random noise [142, 143, 144]. Therefore, we removed all harmonics above 40 Hz as well.

The comb causes one frequency notch in each 1 Hz interval, and so if we used 0.25 Hz bins we would lose at least 25% of the frequency bins in the analysis. This motivated the decision to use 192 s segments and 1/32 Hz frequency bins for our analyses. While we lost a significant amount of time due to edge effects of breaking our jobs into segments (see section 3.4.1), the amount of time lost moving from 192 s to 60 s represented a smaller loss in sensitivity than notching 25% of our frequency bins. We can use the far left column of table 3.4 to estimate the loss in sensitivity due to the longer time segments. Using 192 s segments results in a drop of roughly $\sim 1-\sqrt{33/37}=6\%$

---

[4] Mathematically, we mean that there are lines of high coherence at a regular spacing, f_s, that might only start at some offset from zero f_o. We can then define all "teeth" in that comb as $f_t = \{n \times f_s + f_o \text{ for } n < N_{\text{teeth}}\}$.

[5] i.e. we removed 20.5 Hz, 21.5 Hz...

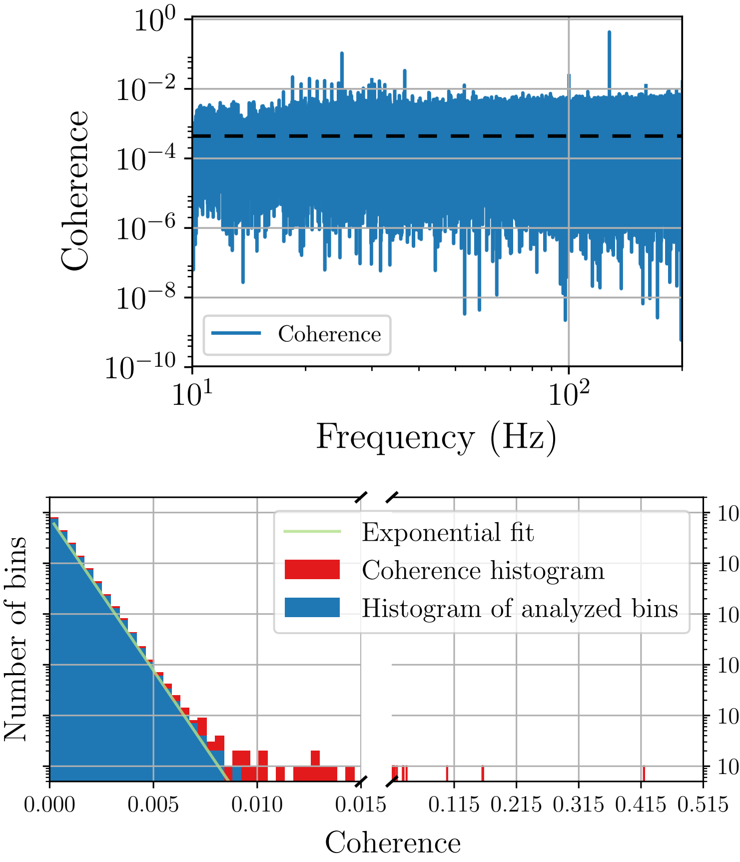

Figure 3.6: Coherent lines in O1. In the left panel, the coherence spectrum is shown between Hanford and Livingston detectors in the frequency band 10-200 Hz with 1 mHz resolution measured over the full O1 data run. The horizontal dashed line shows the expected mean value of the coherence based on uncorrelated Gaussian noise. Individual frequency bins where the coherence rises above the noise floor indicate strongly coherent lines. In the right panel, the distribution of coherences in each frequency bin is shown, compared to the behavior expected for uncorrelated Gaussian noise, in the frequency band 20-200 Hz with 1 mHz resolution. Red bins show the raw coherence. Loud lines are followed up by studying the coherence between the GW and auxiliary channels to determine if the correlation has a terrestrial origin. Blue bins are the resulting distribution of the frequency bins after notching lines known to have known terrestrial origin. These plots also appear in [51].

sensitivity due to lost time, while removing 25% of our frequency bins results in a loss of roughly $\sim 1 - \sqrt{0.75} = 14\%$.

There were also several coherent lines not found in `stochmon` but that did show up with significant SNR in at least one time shifted run of the narrowband radiometer search. In all cases but two we found that these either fell on a known comb that was present in one of the detectors, had significant coherence with an auxiliary channel, or significantly changed its behavior as a function of time in a way not consistent with our source model. In the other two cases, a line at 26.17 Hz and a line at 1352.90 Hz, we notched bins because the lines appeared very strongly in a single detector and with a bandwidth of $< 1/1800$ Hz. It is very unlikely these are GWs based on the orientation of our detectors on Earth, the rotation of the Earth, and the motion of the Earth around the solar system barycenter. Given that these lines appeared in only a single time shift of the radiometer search, and their properties would require a very unlikely set of source parameters (i.e. directly overhead, polarization such that it appears in only one detector), we opted to remove the frequency bins from the final analysis [145].

A table summarizing all of the notches made for the O1 searches can be found in appendix A.

3.3 Results

In this section, We present results for the isotropic and directional cross-correlation searches for persistent gravitational-waves. In section 3.3.1, we show results for the search for an isotropic SGWB. In section 3.3.2, we show results for the search for a broadband anisotropic SGWB from diffuse sources and point sources for three different spectral indices. In section 3.3.3, we show results for the directed, narrowband search for persistent GWs.

3.3.1 Isotropic search for SGWB

There was no evidence of an isotropic SGWB. The data were consistent with statistical fluctuations assuming Gaussian noise. As a result, limits were placed on the energy density assuming a power law form $\Omega_{\mathrm{GW}}(f) = \Omega_\alpha (f/f_{\mathrm{ref}})^\alpha$.

For a spectral index of $\alpha = 0$, the 95% confidence upper limit on energy density is $\Omega_0 < 1.7 \times 10^{-7}$. This represents a 33–fold improvement over the previous best direct limits set in this frequency band [136]. Joint limits on Ω_α vs. α are shown in figure 3.7.

Limits on several other spectral indices, along with their previously-reported values, are shown in table 3.1 with a reference frequency of $f_{\mathrm{ref}} = 25$ Hz.

We also show an estimate of $\Omega_{\mathrm{GW}}(f)$ and $\sigma(f)$ in each frequency bin[6] in figure 3.8. The inset shows the distribution of SNR in each frequency bin, along with a Gaussian fit to that distribution.

α	Frequency band	Amplitude Ω_α	95% CL UL	Previous UL [136]
0	20 – 85.8 Hz	$(4.4 \pm 5.9) \times 10^{-8}$	1.7×10^{-7}	5.6×10^{-6}
2/3	20 – 98.2 Hz	$(3.5 \pm 4.4) \times 10^{-8}$	1.3×10^{-7}	–
3	20 – 305 Hz	$(3.7 \pm 6.5) \times 10^{-9}$	1.7×10^{-8}	7.6×10^{-8}

Table 3.1: For three representative values of the spectral index, α, we show the frequency band containing 99% of the sensitivity for the analysis, the measurement of Ω_α with its associated uncertainty, and 95% confidence upper limits on Ω_α for a reference frequency of 25 Hz. In the last column we show the corresponding previous best limits set from the LIGO/Virgo S6/VSR23 analysis [113, 136]. This information is reproduced from [113].

3.3.2 Broadband search for anisotropic persistent GWs

This search produces three different results: maps of the flux of GWs from broadband point sources (broadband radiometer), maps of the GW energy density from diffuse sources using a spherical harmonic decomposition (SHD), and estimates of the angular power spectrum of GWs. All of these results integrate over the frequency band from 20–500 Hz weighted with a power law model. Depending upon the spectral index of the power law, different searches tend to be more sensitive to different parts of the frequency band.

I show maps of the search for broadband point sources in figure 3.9. The columns represent different choices of the power law spectral index, α, and the top row shows SNR. No directions exhibit SNRs with significant p-values and so limits were set on the energy flux from a broadband point source in each direction, which is defined in equation (2.66). These upper limit maps are shown in the bottom row of figure 3.9, and a summary of the results of the search is in table 3.2.

We show maps of the search for broadband diffuse sources of GWs in figure 3.10.

---

[6] see equation (2.37) or [118] for a definition of the bin-by-bin estimator

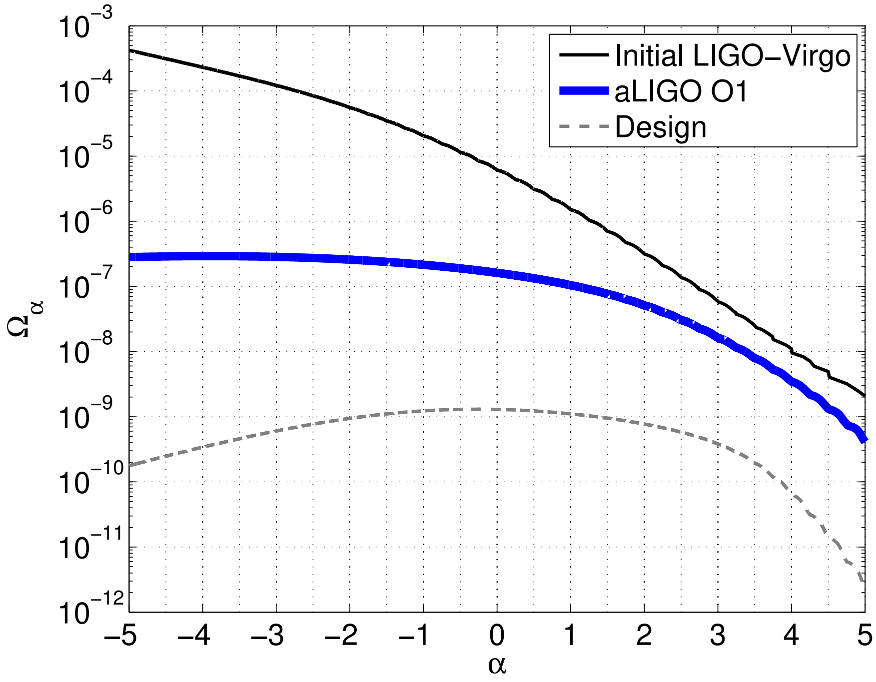

Figure 3.7: Joint 95% confidence contours on Ω_α vs. α for the O1 isotropic search (thick, middle) [113], the joint S6/VSR23 search (top, solid) [136], and an estimate of sensitivity can be set for Advanced LIGO/Advanced Virgo operating at design sensitivity [146] (bottom dashed). This plot is reproduced from [84].

The columns again represent different choices of the spectral index, α, and the top row represents SNR. Like the broadband radiometer search, no SNRs are statistically significant and the map is consistent with statistical fluctuations of Gaussian noise. In the bottom row we set limits on the energy density parameter per steradian in each direction, as defined in equation (2.64). These results are summarized in table 3.2.

Finally, using the estimates for the $\hat{P}_{lm}$'s from this search, we can set limits on the angular power spectra of the GW energy density, as discussed in section 2.4.1. In figure 3.11 we show limits on $C_l^{1/2}$ in units of the energy density parameter per steradian.

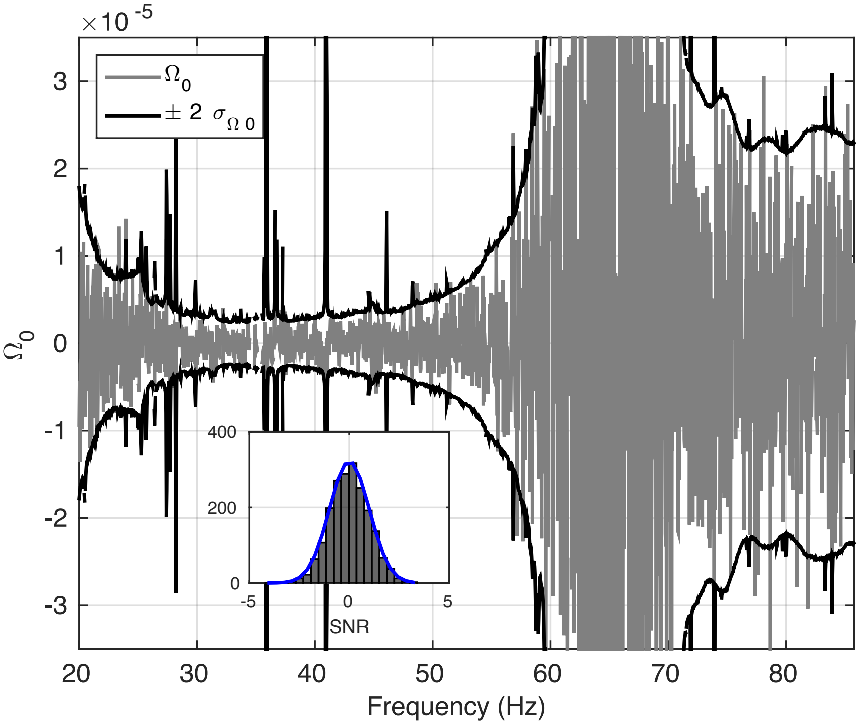

Figure 3.8: We show a frequency bin by frequency bin estimator for the O1 Isotropic, along with its uncertainty. The inset shows the distribution of SNR over frequency bins along with a Gaussian fit. It is clear that the frequency spectrum is consistent with fluctuations due to Gaussian noise, which is one of the assumptions of the search. Parts of this plot are reproduced from [84].

3.3.3 Directed, unmodeled search for persistent GWs

The search for unmodeled, persistent GWs focuses on three directions: Scorpius X-1 (ScoX1), the galactic center (GC), and supernova 1987a (SN1987a). We searched in frequency bins of varying size (described below) between 20 and 1726 Hz. As described in section 2.5, we combine detector-frame frequency bins in order to set limits on the strain amplitude, h_0, for a neutron star rotating at a given frequency in the source's frame of reference. In the case of Scorpius X-1, a low-mass X-ray binary system, we combine frequency bins in order to account for both the binary motion of the potential source, as well as the motion of the Earth over the 116 days of O1. This results in an

			All-sky (broadband) Results			
			Max SNR (% p-value)		Upper limit range	
α	θ (deg)	$l_{\max}$	BBR	SHD	BBR ($\times 10^{-8}$)	SHD ($\times 10^{-8}$)
0	55	3	3.32 (7)	2.69 (18)	10 – 56	2.5 – 7.6
2/3	44	4	3.31 (12)	3.06 (11)	5.1 – 33	2.0 – 5.9
3	11	16	3.43 (47)	3.86 (11)	0.1 – 0.9	0.4 – 2.8

Table 3.2: Values of the power-law index α investigated in this analysis are shown in the first column. The angular resolution θ, and corresponding harmonic order $l_{\max}$ (equation (2.55)) for each α are also shown. The right hand section of the table shows the maximum SNR, associated significance (p-value), and best upper limit values from the broadband radiometer (BBR) and the spherical harmonic decomposition (SHD). The BBR sets upper limits on energy flux [erg cm^{-2} s^{-1} Hz$^{-1}(f/25\text{ Hz})^{\alpha-1}$], while the SHD sets limits on the energy density parameter per steradian [Ω_{GW} sr]. This table is a subset of table 1 in [24].

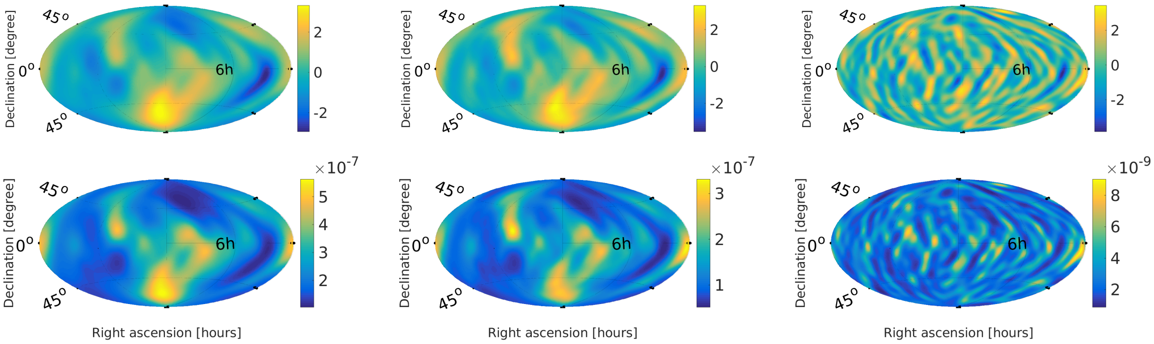

Figure 3.9: All-sky radiometer maps for point-like sources. In the top we show SNR and in the bottom we show upper limits at 90% confidence on energy flux F_{α,Θ_0} [erg cm^{-2}s^{-1} Hz^{-1}]. Each column represents a different power law spectral index from the analysis with $\alpha = 0$, 2/3 and 3, from left to right. The search parameters, maximum SNR, and associated p-values are summarized in table 3.2). These plots are reproduced from [24]

optimal combined-bin size that is frequency-dependent.

In the case of the other two directions, we expect isolated sources of GWs but wish to remain as agnostic about the signal model as possible when making a detection. Therefore, we combine frequency bins to account for the spread of a monochromatic signal in the detectors due to the motion of the Earth according to equation (2.70).

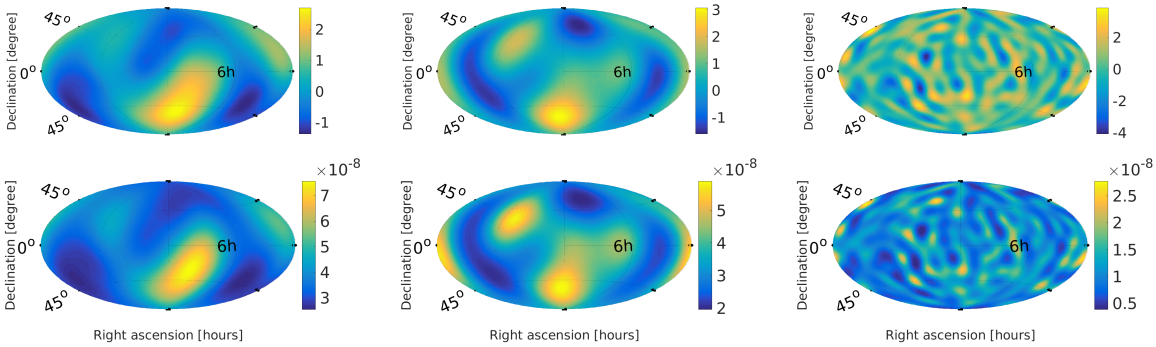

Figure 3.10: All-sky spherical harmonic decomposition maps for extended sources. In the top row we show SNR and in the bottom row we show upper limits at 90 % confidence on the GW energy density parameter in each direction, Ω_α [sr^{-1}]. Each column displays a different choice of the power law spectral index. From left, these correspond to $\alpha = 0$, $2/3$ and 3. The search parameters, maximum SNR, and associated p-values are summarized in table 3.2). These plots are reproduced from [24]

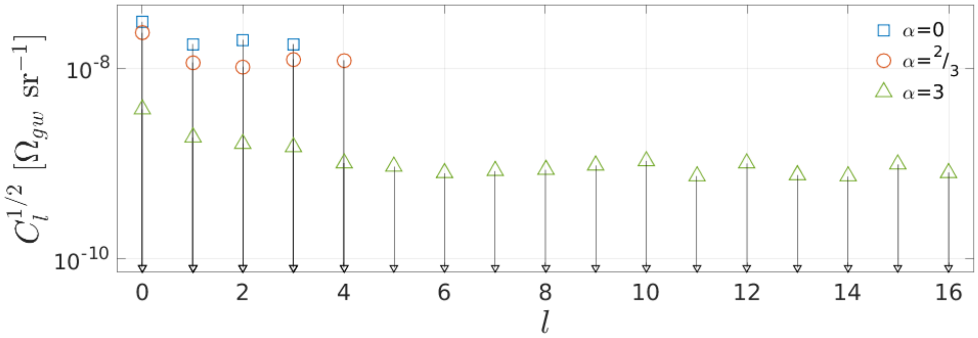

Figure 3.11: Upper limits on $C_l^{1/2}$ at 90% confidence vs l for the SHD analyses for $\alpha = 0$ (top, blue squares), $\alpha = 2/3$ (middle, red circles) and $\alpha = 3$ (bottom, green triangles). This plot and caption are reproduced from [24].

Instead of implementing a frequency-dependent bin size, as we did for ScoX1, we chose the maximum across the frequency band of that spread and all bins were combined to the same width. For SN1987a, we choose a combined bin size of 0.09 Hz. This leaves us sensitive to spin-modulations of a neutron star of up to $|\dot{f}_{\mathrm{spin}}| < 9\times10^{-9}$ Hz s^{-1}. For GC, which is at a lower declination, and therefore likely to experience larger modulation due to the Earth's motion, we choose a bin size of 0.53 Hz across the frequency band. In this

Narrowband Radiometer Results

Direction	Max SNR	p-value (%)	Freq (Hz)	Best UL ($\times 10^{-25}$)	Freq (Hz)
Sco X-1	4.58	10	616 – 617	6.7	134 – 135
SN1987A	4.07	63	195 – 196	5.5	172 – 173
GC	3.92	87	1347 – 1348	7.0	172 – 173

Table 3.3: Results for the narrowband radiometer search for three sky directions. From left we show maximum SNR and the corresponding p-value and 1 Hz frequency band in which the max SNR fell. We also show the 90% gravitational wave strain upper limits, and corresponding frequency band. The best upper limits are taken as the median of the most sensitive 1 Hz band. This table is reproduced from [24]

case, we are sensitive to frequency modulation in the range of $|\dot{f}_{\text{spin}}| < 5.3 \times 10^{-8}\ \text{Hz}\,\text{s}^{-1}$.

In all three cases, we use the method defined in section 2.5 to estimate the background distribution for the SNR of our frequency bins. We find that the resulting measurements are consistent with fluctuations of Gaussian noise. A summary of the maximum SNR and its p-value for each direction is shown in table 3.3. Therefore, we set upper limits on h_0 in each frequency bin using the method described in section 2.5. Plots of the 1σ sensitivity and 90% upper limits on h_0 in each frequency bin are shown in figure 3.12. In table 3.3 we show the best upper limit set in each direction in each frequency bin. Due to the large variation in our measurements from one frequency bin to the next, we take a running median of the upper limits in the 1 Hz region around each frequency bin and report the best of those values.

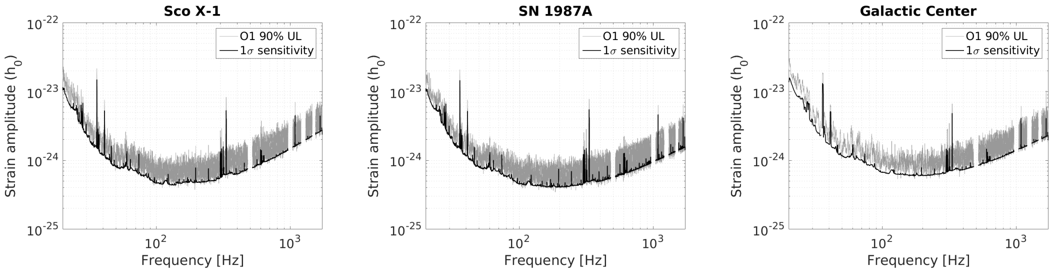

Figure 3.12: Upper limits on h_0 from the narrowband radiometer search in three directions. From left: Scorpius X-1, Supernova 1987a and the Galactic Center. In gray are 90% upper limits in each frequency bin, while in black is the 1–σ sensitivity of the search. The best upper limit in h_0 for each direction is quoted in table 3.3.

At the time of publication, these were the best limits set on h_0 for possible sources from these three directions. Since that time, the limits on a source in the direction of Sco-X1 have been exceeded by two modeled searches that use known parameters of Scorpius X-1 to guide their search [133, 147].

3.4 Post-search studies

In this section, we present several studies we undertook to evaluate the effectiveness of different data quality cuts made during the O1 analyses. Due to the fact that the interferometer was effectively a "new" instrument, we were conservative in our approach to data quality. Below, we re-evaluate the decision about what vetoes to use. we offer some statistics illustrating examples of "effective" vetoes for our search and "ineffective" vetoes for our search, and discuss a general approach to choosing a set of vetoes that effectively removes times when our search will be biased, while keeping times where the vetoes are obviously ineffective. In all cases, we use the isotropic search with an unphysical time shift as the test case. A similar study should eventually be performed for at least the narrowband radiometer search.

3.4.1 Veto analysis

I created a job list using *no vetoes*, and ran the isotropic SGWB search with $\alpha = 0$ and an unphysical time shift on that job list. For each veto, we found which time segments coincided with times when the veto indicated a problem with the detector. We then compared the distribution of |SNR| for that set of time segments with the overall distribution of |SNR| for all time segments. From this, one can calculate an ROC point for each data quality veto to evaluate the effectiveness of the veto, under the assumption that the goal of the veto is to remove time segments with $|\mathrm{SNR}| > 5$[7]. A scatter plot of ROC points for all vetoes can be seen in figure 3.13. We also include the $\Delta\sigma$ cut with a threshold of 20% in this analysis.

It is clear from figure 3.13 that there are many vetoes that should probably not have

---

[7] This is a rough estimate of the threshold where individual time segments are not consistent with fluctuations due to Gaussian noise. A more formal way of doing this would be instead of a binary classification of < 5 or > 5 we use the a multi-trial p-value like $p(|\mathrm{SNR}|) \sim 1 - \mathrm{erf}\left(|\mathrm{SNR}|/\sqrt{2}\right)^{N_{segs}}$

been included in the analysis. One idea was to include all CAT 2 vetoes in the job list for future analyses, especially because most of those “loud” SNR times will be removed by the $\Delta\sigma$ cut anyway. However, it is evident in figures 3.13 and 3.14 that there are several CAT 2 vetoes that are effective.

While many “loud” SNR segments are a subset of the $\Delta\sigma$ cut, it is important to make sure that our PSD estimation gives reasonable results for those segments that *would not be removed* by the $\Delta\sigma$ cut. Otherwise, this could result in a bias of the PSD estimation. An example of a veto where our PSD estimation clearly “makes sense” during times when the veto is active is shown in the bottom right of figure 3.14. In this case, the distribution of the ratio of σ from the middle time segment and σ from adjacent time segments is Gaussian and centered around 1. An example of a veto where the PSD estimation is clearly biased is shown in the left hand side of figure 3.14.

While the choice to remove times from all CAT 2 vetoes when generating our job list was likely too cautious, simply not applying any of them would have been a poor decision as well. That said, CAT 2 vetoes did severely limit the length of our jobs, which in turn increased the time lost due to the fact that jobs do not factor evenly into an integer number of 192 s segments. Table 3.4 shows the live time of different job lists made using different sets of vetoes. We also show live times for both 192 s and 60 s segments. The choice to stay with the original job list (the one that implemented CAT 1 and 2 vetoes) was made because nearly all of the other data quality studies presented were done using this job file. The choice between 60 s and 192 s segments came down to a trade-off between live time losses and losses due to notching narrow lines from our analysis, especially the 0.5 Hz comb (see section 3.2).

The results in table 3.4 do not take into account losses from the $\Delta\sigma$ cut. One might ask whether, after removing all of the times that fail the $\Delta\sigma$ cut when running with a job list that only rejects CAT 1 vetoes, do we end up with a similar amount of live time as the job list where we have rejected CAT2 vetoes as well. Essentially: “do most of the CAT2 vetoes get rejected by the $\Delta\sigma$ cut?” The answer is almost certainly no. While this comparison has not been directly made, the CAT2 vetoes almost all show poor results for the ROC statistics. In addition, for the CAT2 vetoes that remove the most data, all of the plots like the bottom right of figure 3.14, (which shows that the $\Delta\sigma$ statistic is well-behaved during times when the flag is active), indicate that the $\Delta\sigma$

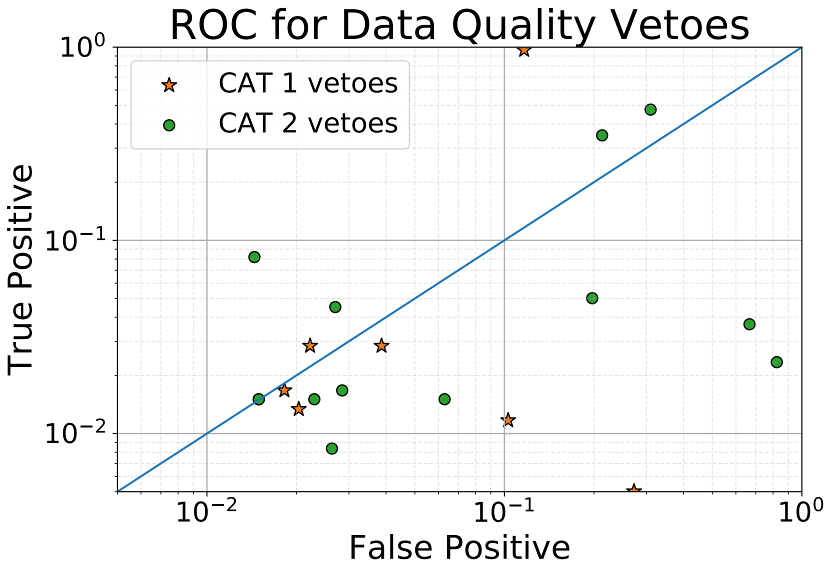

Figure 3.13: Receiver operator characteristic for each data quality veto. True positive and false positive are defined in the same way as figure 3.2. Vetoes that fall in the upper-left of the plot are more effective, while those that fall in the lower right are less effective. Color and shape indicate whether it is CAT 1 or CAT 2. The best veto is the $\Delta\sigma$ cut used in our analysis (threshold of 20%), which is also included on this plot (the top, center star). It is evident that most vetoes are not effective for this search. $|\mathrm{SNR}|$ for $\alpha = 0$ is not the only statistic that matters, however, and so this plot should not be used by itself to decide whether or not to use a specific DQ veto.

cut probably would not remove the majority of these times.

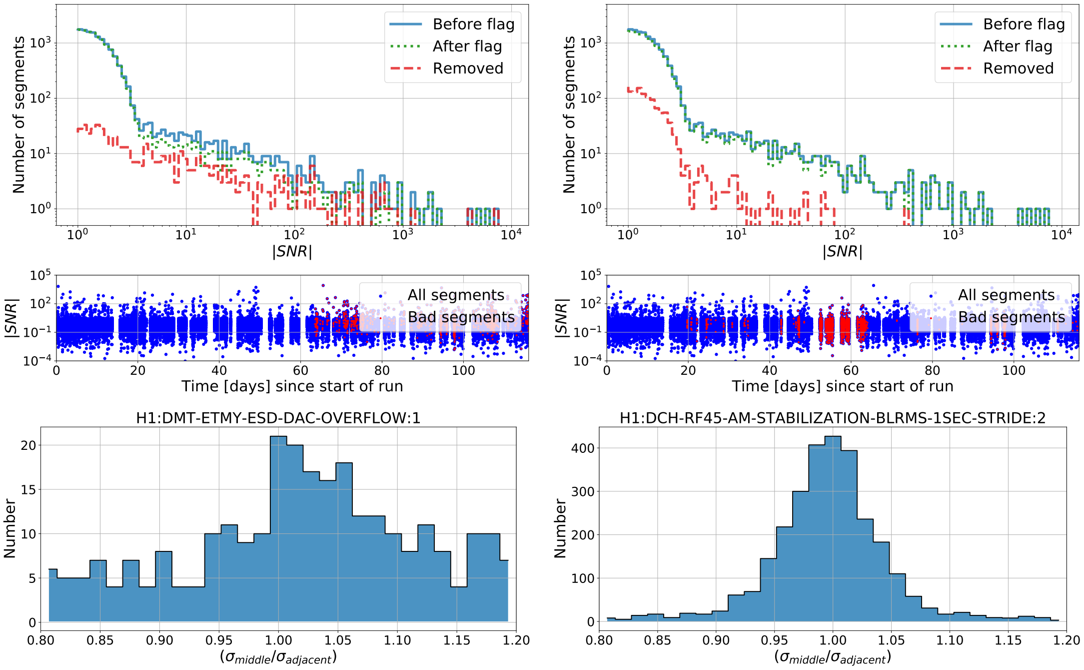

Figure 3.14: Summary of the effect of the CAT 2 vetoes, `H1:DCH-RF45_AM_STABILIZATION_BLRMS_1SEC_STRIDE:2` (right), `H1:DMT-ETMY_ESD_DAC_OVERFLOW:1` (left). Top is the distribution of the absolute value of SNR for all time segments run with a job list with *no vetoes applied*. The two lines indicate the original distribution of SNRs (blue, solid), the distribution of SNRs from times where the veto was active (red, dash-dotted), and the difference between the two (green, dotted). The right top plot shows that during times when this flag is active, we are not seeing larger than expected SNRs. The left top plot shows an example of a "good" veto. The bottom plot looks at the ratio of naive to actual σ values during times where this flag is active and that pass the $\Delta\sigma$ cut. It is clear that the right hand one follows a Gaussian distribution centered on 1, as expected for true noise, while the left hand one does not. While the loud SNR segments associated with `H1:DMT-ETMY_ESD_DAC_OVERFLOW:1` might be removed by the delta sigma cut, the non-loud ones will likely be biased by poor PSD estimation.

Segment Duration [s]	Live time [days]			
	CAT 1 + CAT 2	CAT 1 only	CAT 2 only	No vetoes
60	37.51	46.10	42.21	48.23
192	33.87	44.94	38.65	47.43

Table 3.4: Live time for the O1 SGWB searches when applying different types of vetoes and using different segment durations. These live times do not take into account losses due to the $\Delta\sigma$ cut, which is applied after a job list is already made. The difference between segment durations has to do with dead time associated with splitting a single continuous job into shorter segments. The final choice was 192 s and CAT 1 + CAT 2 vetoes. All original data quality investigations, including $\Delta\sigma$ cuts and low frequency noise investigations discussed in the previous sections, were done with a job file made from CAT 1 + CAT 2 vetoes, and the choice of 192 second segments ultimately came from balancing the loss due to frequency notches (specifically the 0.5 Hz comb discussed below) with the loss due to extra dead time on the ends of jobs. We include the other three columns to exhibit the penalty we incur by using CAT 2 vetoes.

Chapter 4

Characterization of Advanced LIGO detectors

4.1 Introduction

Sources of noise couple into the LIGO instruments in many ways and can degrade the sensitivity of the GW searches. Identification of noise sources is often done on-site by instrumental experts. More involved data analysis techniques are sometimes needed to identify the coupling mechanism of a noise source, or experts in each type of search are needed in order to assess whether a source of noise will be a serious problem for their search. This can help prioritize the effort of hunting down and mitigating the cause of noise sources in the instrument.

The use of data analysis techniques to hunt down noise sources and to assess their affect on the searches is known broadly as "detector characterization." This effort can help identify the coupling mechanism of some sources of noise, aiding on-site commissioners in their own efforts to do the same. The detector characterization effort also results in a summary of known problems that can affect searches. This information is released in the form of a "veto definer file," which identifies periods of time when there are significant malfunctions with the instrument that cause the data to be of poor quality ("glitches" or "transient noise sources"), or in the form of a "line list" which identifies persistent sources of noise that are each localized to a very small region of Fourier-space ("lines" or "persistent noise sources").

A suite of automated tools for performing LIGO detector characterization are used to produce a daily snapshot of the performance of each interferometer each day. The results are summarized in daily web pages that make it easy to identify where and when problems in the interferometer begin, or where some follow up analysis might be needed. Below, we will often refer to these pages as the "daily summary pages," and results from some of the monitoring tools we will discuss below now appear on those pages.

In the rest of this chapter, we describe several examples of detector characterization studies, and the development of tools used to carry them out. In section 4.2, we discuss the development of tools that are used to monitor persistent noise sources in the detector, and how those tools can be used to produce of a list of lines that will affect the cross-correlation searches discussed in chapter 2. I have also helped characterize on-site and inter-site correlated magnetic noise. We will discuss measurements taken of long-wavelength magnetic fields and how we expect them to cause problems for SGWB searches in the future in section 4.3. Finally, a known source of transient noise, referred to as "RF beat notes" or "whistles"[1], is discussed in section 4.4. We discuss how we monitor and characterize their rates, as well as how we think they are generated in the detectors and how they might eventually be removed.

4.2 Identification and characterization of spectral lines

It is common to see large lines in LIGO strain spectra, and often those lines are associated with resonances in the instrument with very high quality factors, like the violin modes of the test mass suspensions which are evident near 500 Hz in figure 1.4. A set of lines that show a well-defined spacing is known as a comb, and we often talk about individual lines in that comb as "teeth." We discussed in chapter 3 how noise lines that are coherent between two interferometers can affect cross-correlation searches for GWs, and gave a brief overview of the follow-up process. In this section, we expand on the methods used to identify, characterize, and mitigate sources of lines and combs. We also discuss and show examples of how those methods can be applied to shorter periods of data to identify new sources of noise that might be introduced after maintenance or

---

[1] These two names come from their likely source–beat notes produced from two different radio frequencies–and the way they sound when converted into audio.

commissioning of the interferometers.

4.2.1 Finding spectral lines in the data

`Stochmon`

`Stochmon` is a tool developed by Thomas Callister that monitors certain diagnostic statistics relevant to the cross-correlation GW searches described in chapter 2. It generally operates with a lag time of $\mathcal{O}(1\text{ hour})$. `Stochmon` produces an estimate of the sensitivity of the isotropic search as a function time, an estimate of the contribution of correlated magnetic noise to GW searches, and the modulus of the coherence spectrum of the two LIGO interferometers, defined in equation (3.3). It is this last feature that is commonly used for detector characterization. We identify lines that are coherent between the interferometers using the method described in section 3.2.4. We construct a histogram of the coherence spectrum and compare that histogram to what one would expect for a coherence spectrum generated from Gaussian noise. This was shown in figure 3.6. Any frequency bins found as outliers from that histogram require follow-up to see if they are caused by a known detector issue or if they could potentially be caused by GWs. This follow-up is often performed using STAMP-PEM or the coherence tool, which are discussed in section 4.2.2.

The comb seen with 1 Hz spacing and 0.5 Hz offset from the integer that was discussed in section 3.2 (colloquially referred to as the “0.5 Hz comb”) was observed first in `stochmon` coherences and `FScans` (discussed below) and eventually the source of this comb was found to be blinking LEDs on timing chips [51].

Time shifts of SGWB searches

As described in section 3.2.2, we often perform our cross-correlation searches with an unphysical time shift in an attempt to identify detector-related issues. For broadband searches for a Gaussian SGWB, this method is good at blinding our searches. When we use the data for individual frequency bins to try to detect signals from sources like rotating pulsars or to try to identify spectral artifacts, we must be careful because an unphysical time-shift will not remove correlations due to GWs. It will change the relative phase between the detectors (making it appear as though the signal is coming from a different direction), but it does not remove the signal from the data. Therefore, we cannot simply notch narrow frequency bins that have excess cross-correlation just because they are outliers in a time-shifted search. We must treat them the same way we do lines we find from `stochmon`: we need compelling evidence that this noise is *not* caused by GWs.

Most of the lines marked “unknown” in appendix A were identified as issues for the O1 SGWB searches due to time shifted runs. We followed up on these lines with a combination of the coherence tool, STAMP-PEM, and `FScans`; all of which are discussed below.

Comb finder

Many stochastic searches integrate over frequency. While we need to remove obvious excess coherence, there are also cases where an integration over sub-threshold combs yield a broadband excess in coherence. By this we mean that there is not an obvious single frequency exceeding the typical levels of noise, but there is a set of frequencies with a specific spacing that, when summed together, gives something larger than expected if the same number of frequency bins were chosen from random noise and summed. To deal with this we developed a “comb-finder” which sums power over many possible tooth-spacings and offsets and checks whether that sum is larger than expected.

For a time-shifted isotropic SGWB search, we calculate the signal-to-noise-ratio (SNR) from the cross-correlation bin-by-bin estimator $\hat{Y}(f_i)$ and the associated uncertainty $\sigma_Y(f_i)$, defined in equation (2.37), for a variety of different potential combs. We then combine these bins using a weighted sum (the same weighted sum as in equation (2.38) except over frequency bins instead of time segments). For a comb with N teeth, the combined statistic becomes

$$\hat{Y}^N_{\text{comb}} = \frac{\sum_i^N \hat{Y}_i \sigma_{Y_i}^{-2}}{\sum_i^N \sigma_{Y_i}^{-2}} \tag{4.1}$$

$$\sigma^N_{Y_{\text{comb}}} = \left[\sum_i^N \sigma_{Y_i}^{-2}\right]^{-1/2} . \tag{4.2}$$

The subscript indicates the discrete frequency bin f_i so that, for example, $\hat{Y}_i = \hat{Y}(f_i)$.

We parameterize a specific comb by the offset of the first bin from the start of the search band and the frequency spacing between the teeth of the comb. The offset number of bins m and spacing n determine which frequency bins contribute to the comb in question. For a search over a given frequency band $\Delta f = f_{\rm max} - f_{\rm min}$, with a frequency resolution of df, the number of teeth in a comb with bin spacing n will be given by $N = 1 + \texttt{floor}\left[\frac{\Delta f}{n}\right]$. We then define the combined SNR statistic using our optimal combination method

$$\mathcal{S}_{m,n} = \frac{\hat{Y}^{(m,n)}_{\rm comb}}{\sigma^{(m,n)}_{Y_{\rm comb}}} = \frac{\sum_i^N \hat{Y}(f_{m+ni})\sigma_Y^{-2}(f_{m+ni})}{\left[\sum_i^N \sigma_Y^{-2}(f_{m+ni})\right]^{1/2}} \,. \tag{4.3}$$

Figure 4.1 shows an example output of the comb-finder tool demonstrating the 0.5 Hz comb found during O1. Excess SNR is visible at regular 1 Hz spacings and offsets of 0.5 Hz.

This tool also identified an 8 Hz comb in the observing run 2 (O2) time shifted SGWB results, which was eventually identified as a detector artifact using the coherence tool.

`FScans` and `FineTooth`

`FScans` and `FineTooth` are tools that are used to identify narrow lines in the strain spectrum of the individual interferometers, as well as auxiliary channels. They are maintained by researches at the University of Michigan. `FScans` generates 1800 s amplitude spectral densities for the strain channel and many auxiliary channels. The long-duration spectra allow for very narrow frequency resolution, which is often necessary when performing very sensitive searches for known rapidly rotating neutron stars. `FineTooth` then sorts and searches through the spectra produced by `FScans` to identify combs that are evident in the spectra and track the amplitude of those combs over time. It can be used to identify new combs, potentially introduced by changes in the interferometers, as well as quantify the effect of efforts made by commissioners to mitigate sources of those combs and lines.

For SGWB searches, we commonly use the results of `FScans` and `FineTooth` as follow up tools to identify whether coherent lines that show up in time shifted results

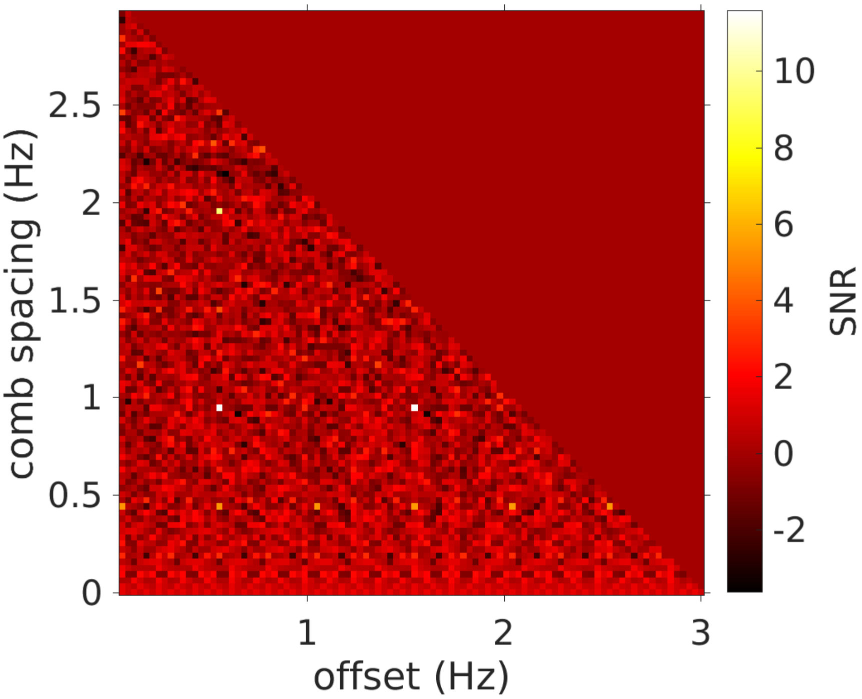

Figure 4.1: Example output of the comb-finder. White pixels indicate strong SNR. The loudest pixels indicate a coherent 1 Hz comb with 0.5 Hz offset identified during O1. This comb is also discussed in section 3.2

or inter-site strain channel coherences appear in just a single interferometer, both interferometers, or are part of an obvious comb in one of the detectors. A source of GWs would be expected to have a measurable amplitude in both detectors and because the Earth rotates and moves relative to any prospective source of narrowband GWs, there is an expected Doppler broadening that should smear any real GW signals over multiple 1/1800 Hz frequency bins. Therefore, large lines that are seen in just a single frequency bin in one detector for spectra that have been averaged over several hundred days are very likely caused by digital noise in the detectors.

This analysis technique was very useful in removing several coherent lines identified by time shifted SGWB studies and recorded in appendix A.

4.2.2 Identifying a cause for narrow spectral lines

In some cases, the best we can do is make the argument discussed in the `FScans` section above to identify that a coherent line is *not* caused by GWs. However, it is helpful to both our searches, and commissioners, to try to find the actual source of the noise lines. For searches for rapidly rotating neutron stars, each frequency bin is a separate search for a potential source. For broadband SGWB searches, a forest of coherent lines and combs require frequency notches. Individually, each notch may not significantly reduce the search sensitivity, but in large numbers they do begin to meaningfully affect the SGWB to which we could be sensitive. They also reduce confidence in a potential detection; especially sub-threshold combs like the 0.5 Hz comb. Therefore, we work hard to try to identify and remove as many of the sources of spectral lines as possible.

STAMP-PEM

STAMP-PEM[2] is a tool used to calculate coherence between the strain channel and many other environmental monitoring channels. It can be run as a way of trying to identify a cause of a spectral line we already know about. During observational and engineering runs, it is automatically run every two hours to monitor coherence between the strain channel and $\mathcal{O}(1000)$ auxiliary channels. STAMP-PEM is maintained as a code package written in python [148] based on GWpy [149]. It is capable of submitting

---

[2] STAMP for “Stochastic transient analysis multidetector pipeline” and “PEM” for “physical environmental monitor”

many coherence calculations to run in parallel on a scientific computing cluster. The coherence results, which typically use a frequency resolution of 0.1 Hz and are averaged over thirty minute time spans, are archived. There are tools in the code package for accessing and visualizing archived data.

Monitoring—STAMP-PEM can be used to monitor coherence between the strain channel[3] and many auxiliary channels throughout the interferometer. It produces a daily web page that is updated every two hours with new information. Data are presented in the form of "coherence matrices." A coherence matrix is a list of channels on the y-axis, frequency on the x-axis and coherence as the color. Channels from the same subsystem of the interferometer are generally grouped together, which helps to make couplings stand out on the plots, since many channels from the same subsystem will often witness the same source of noise.

There is a top-level page that gives information about the times over which the coherence has been averaged, and a (very large) coherence matrix for the full interferometer. An example of this top-level page is shown in a screen shot in figure 4.2. From this large coherence matrix, one can pick out subsystems that exhibit couplings to the strain channel and navigate to the individual subsystem pages, which show coherence matrices with only channels from those subsystems. There are also interactive plots written in D3js [150] that can automatically sort columns (most coherent frequencies for a given channel) and rows (most coherent channels for a given frequency).

Finally, a table colloquially known in the LIGO Collaboration as a "BruCo table"[4] is also produced from the data each day. Each row of the BruCo table is the list of the most coherent channels with the strain channel at a single frequency. This table is also displayed on the daily summary pages because it a terse and easily interpretable visualization of the STAMP-PEM results. An example of how the STAMP-PEM results appear on the daily summary pages, including this BruCo table, is shown in figure 4.3.

Follow up—The follow up part of the tool allows for users to pull coherence data from any time when the interferometer is locked during an observational run. There is a

---

[3] Or any other channel.

[4] Named for the tool that originated this particular visualization of coherence between many channels.

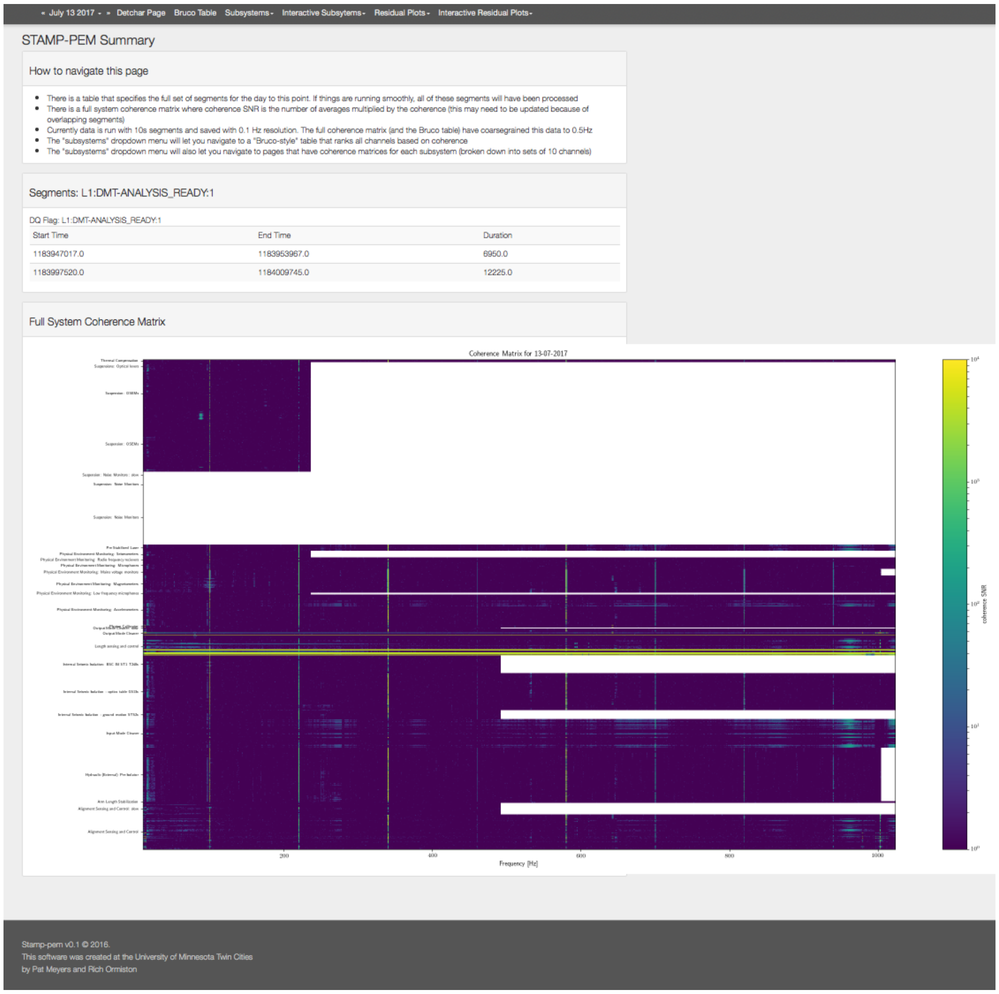

STAMP-PEM Summary

How to navigate this page

- There is a table that specifies the full set of segments for the day to this point. If things are running smoothly, all of these segments will have been processed
- There is a full system coherence matrix where coherence SNR is the number of averages multiplied by the coherence (this may need to be updated because of overlapping segments)
- Currently data is run with 10s segments and saved with 0.1 Hz resolution. The full coherence matrix (and the Bruco table) have coarsegrained this data to 0.5Hz
- The "subsystems" dropdown menu will let you navigate to a "Bruco-style" table that ranks all channels based on coherence
- The "subsystems" dropdown menu will also let you navigate to pages that have coherence matrices for each subsystem (broken down into sets of 10 channels)

Segments: L1:DMT-ANALYSIS_READY:1

DQ Flag: L1:DMT-ANALYSIS_READY:1

Start Time	End Time	Duration
1183947017.0	1183953967.0	6950.0
1183997520.0	1184009745.0	12225.0

Full System Coherence Matrix

Stamp-pem v0.1 © 2016.
This software was created at the University of Minnesota Twin Cities
by Pat Meyers and Rich Ormiston

Figure 4.2: Screen shot of top-level STAMP-PEM monitoring web page from July 2017. At the top there is a navigation bar for changing days, viewing the BruCo table for the current day, and looking at coherence matrices for individual subsystems. Below that is a set of instructions for navigating through the STAMP-PEM web page, followed by a table indicating the data over which STAMP-PEM has been run for that day. Finally, there is a large coherence matrix. The y-axis labels are subsystems and the individual rows are channels in those subsystems. The x-axis is frequency, and the color is coherence SNR. The 60 Hz power mains are evident throughout, as is noise around 300 Hz from the resonance of a periscope on the same table as the pre-stabilized laser. Large white areas indicate channels or subsystems that have failed, or that an individual channel is not sampled fast enough to produce data at those specified frequencies.

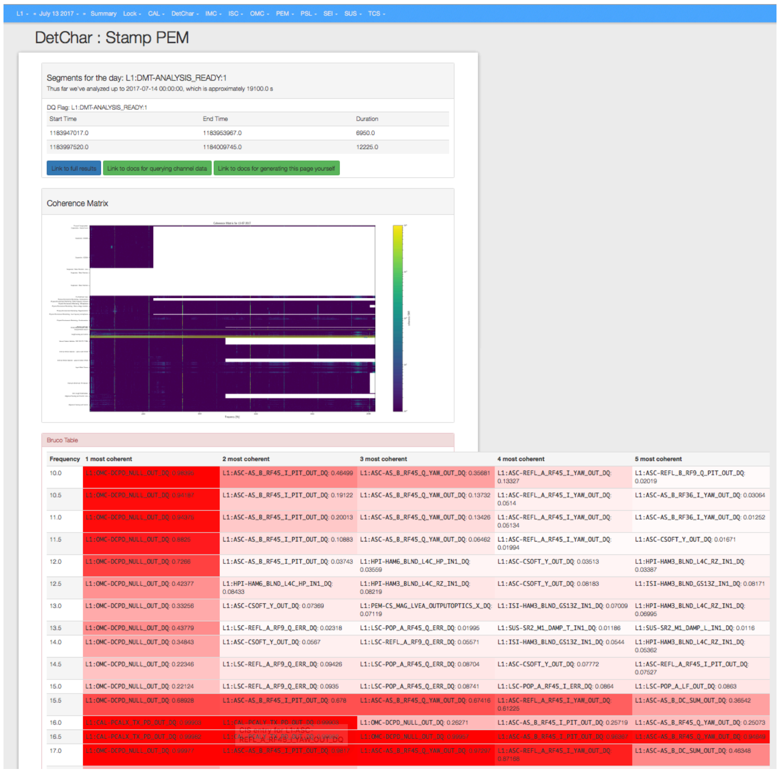

DetChar : Stamp PEM

Segments for the day: L1:DMT-ANALYSIS_READY:1

Thus far we've analyzed up to 2017-07-14 00:00:00, which is approximately 19100.0 s

DQ Flag: L1:DMT-ANALYSIS_READY:1

Start Time	End Time	Duration
1183947017.0	1183953967.0	6950.0
1183997520.0	1184009745.0	12225.0

Frequency	1 most coherent	2 most coherent	3 most coherent	4 most coherent	5 most coherent
10.0	L1:OMC-DCPD_NULL_OUT_DQ: 0.98396	L1:ASC-AS_B_RF45_I_PIT_OUT_DQ: 0.46499	L1:ASC-AS_B_RF45_Q_YAW_OUT_DQ: 0.35681	L1:ASC-REFL_A_RF45_I_YAW_OUT_DQ: 0.13327	L1:ASC-REFL_B_RF9_Q_PIT_OUT_DQ: 0.02019
10.5	L1:OMC-DCPD_NULL_OUT_DQ: 0.94187	L1:ASC-AS_B_RF45_I_PIT_OUT_DQ: 0.19122	L1:ASC-AS_B_RF45_Q_YAW_OUT_DQ: 0.13732	L1:ASC-REFL_A_RF45_I_YAW_OUT_DQ: 0.0514	L1:ASC-AS_B_RF36_I_YAW_OUT_DQ: 0.03064
11.0	L1:OMC-DCPD_NULL_OUT_DQ: 0.94375	L1:ASC-AS_B_RF45_I_PIT_OUT_DQ: 0.20013	L1:ASC-AS_B_RF45_Q_YAW_OUT_DQ: 0.13426	L1:ASC-REFL_A_RF45_I_YAW_OUT_DQ: 0.05134	L1:ASC-AS_B_RF36_I_YAW_OUT_DQ: 0.01252
11.5	L1:OMC-DCPD_NULL_OUT_DQ: 0.8825	L1:ASC-AS_B_RF45_I_PIT_OUT_DQ: 0.10883	L1:ASC-AS_B_RF45_Q_YAW_OUT_DQ: 0.06462	L1:ASC-REFL_A_RF45_I_YAW_OUT_DQ: 0.01994	L1:ASC-CSOFT_Y_OUT_DQ: 0.01671
12.0	L1:OMC-DCPD_NULL_OUT_DQ: 0.7266	L1:ASC-AS_B_RF45_I_PIT_OUT_DQ: 0.03743	L1:HPI-HAM6_BLND_L4C_HP_IN1_DQ: 0.03559	L1:ASC-CSOFT_Y_OUT_DQ: 0.03513	L1:HPI-HAM3_BLND_L4C_RZ_IN1_DQ: 0.03387
12.5	L1:OMC-DCPD_NULL_OUT_DQ: 0.42377	L1:HPI-HAM6_BLND_L4C_HP_IN1_DQ: 0.08433	L1:HPI-HAM3_BLND_L4C_RZ_IN1_DQ: 0.08219	L1:ASC-CSOFT_Y_OUT_DQ: 0.08183	L1:ISI-HAM3_BLND_GS13Z_IN1_DQ: 0.08171
13.0	L1:OMC-DCPD_NULL_OUT_DQ: 0.33256	L1:ASC-CSOFT_Y_OUT_DQ: 0.07369	L1:PEM-CS_MAG_LVEA_OUTPUTOPTICS_X_DQ: 0.07119	L1:ISI-HAM3_BLND_GS13Z_IN1_DQ: 0.07009	L1:HPI-HAM3_BLND_L4C_RZ_IN1_DQ: 0.06995
13.5	L1:OMC-DCPD_NULL_OUT_DQ: 0.43779	L1:LSC-REFL_A_RF9_Q_ERR_DQ: 0.02318	L1:LSC-POP_A_RF45_Q_ERR_DQ: 0.01995	L1:SUS-SR2_M1_DAMP_T_IN1_DQ: 0.01186	L1:SUS-SR2_M1_DAMP_L_IN1_DQ: 0.0116
14.0	L1:OMC-DCPD_NULL_OUT_DQ: 0.34843	L1:ASC-CSOFT_Y_OUT_DQ: 0.0567	L1:LSC-REFL_A_RF9_Q_ERR_DQ: 0.05571	L1:ISI-HAM3_BLND_GS13Z_IN1_DQ: 0.0544	L1:HPI-HAM3_BLND_L4C_RZ_IN1_DQ: 0.05362
14.5	L1:OMC-DCPD_NULL_OUT_DQ: 0.22346	L1:LSC-REFL_A_RF9_Q_ERR_DQ: 0.09426	L1:LSC-POP_A_RF45_Q_ERR_DQ: 0.08704	L1:ASC-CSOFT_Y_OUT_DQ: 0.07772	L1:ASC-REFL_A_RF45_I_PIT_OUT_DQ: 0.07527
15.0	L1:OMC-DCPD_NULL_OUT_DQ: 0.22124	L1:LSC-REFL_A_RF9_Q_ERR_DQ: 0.0935	L1:LSC-POP_A_RF45_Q_ERR_DQ: 0.08741	L1:LSC-POP_A_RF45_I_ERR_DQ: 0.0864	L1:LSC-POP_A_LF_OUT_DQ: 0.0863
15.5	L1:OMC-DCPD_NULL_OUT_DQ: 0.68928	L1:ASC-AS_B_RF45_I_PIT_OUT_DQ: 0.678	L1:ASC-AS_B_RF45_Q_YAW_OUT_DQ: 0.67416	L1:ASC-REFL_A_RF45_I_YAW_OUT_DQ: 0.61225	L1:ASC-AS_B_DC_SUM_OUT_DQ: 0.36542
16.0	L1:CAL-PCALX_TX_PD_OUT_DQ: 0.99903	L1:CAL-PCALY_TX_PD_OUT_DQ: 0.99903	L1:OMC-DCPD_NULL_OUT_DQ: 0.26271	L1:ASC-AS_B_RF45_I_PIT_OUT_DQ: 0.25719	L1:ASC-AS_B_RF45_Q_YAW_OUT_DQ: 0.25073
16.5	L1:CAL-PCALX_TX_PD_OUT_DQ: 0.99982	L1:CAL-PCALY_TX_PD_OUT_DQ: 0.99982	L1:OMC-DCPD_NULL_OUT_DQ: 0.99957	L1:ASC-AS_B_RF45_I_PIT_OUT_DQ: 0.96367	L1:ASC-AS_B_RF45_Q_YAW_OUT_DQ: 0.94649
17.0	L1:OMC-DCPD_NULL_OUT_DQ: 0.99977	L1:ASC-AS_B_RF45_I_PIT_OUT_DQ: 0.9817	L1:ASC-AS_B_RF45_Q_YAW_OUT_DQ: 0.97297	L1:ASC-REFL_A_RF45_I_YAW_OUT_DQ: 0.87168	L1:ASC-AS_B_DC_SUM_OUT_DQ: 0.46348

Figure 4.3: Screenshot of STAMP-PEM on the LIGO detector characterization daily summary pages. This webpage receives more traffic and links to the web page shown in figure 4.2. At the top are instructions and times over which the analysis was performed. Below that is the full-interferometer coherence matrix, followed by the BruCo table that shows the five most coherent channels at each frequency for the data that day. The darker the shade of red in the BruCo table, the higher the coherence. There are also links to documentation about how to query archived STAMP-PEM data.

simple tool that allows one to pull archived data from the monitoring pipeline to easily track coherence of a specific channel over very long time scales. It is also possible to regenerate the coherence matrices from the monitoring pages with averaged coherences over arbitrary time scales.

These follow up tools are useful in two main contexts. First, they can be used to identify when a new source of noise coupling has started. If we identify a channel that is coherent with the strain channel at a frequency where a new noise source has popped up, the spectrogram tool can be used to help identify when the coherence first appeared and therefore when this new noise source likely started. This can help identify if certain maintenance or commissioning on the interferometer was the cause of the noise source.

The follow up tools are also useful for identifying the source of noise that causes narrow spectral lines, which can cause problems for searches for persistent or long-duration transient gravitational waves. If there is a spectral line that is coherent between the sites, STAMP-PEM can be used to check if there are possible couplings within the interferometer that could be the cause of that line.

Examples of the use of STAMP-PEM

Acoustic coupling of fans—In April 2014, STAMP-PEM was used to identify acoustic noise coupling into the length degree of freedom of one arm of the LIGO Hanford Observatory (LHO) interferometer. At the time, the full interferometer had not been locked, but one arm was locked on a regular basis and we monitored coherence between the length degree of freedom of that arm and many environmental monitoring channels. Strong coherence at 55 Hz and 85 Hz was seen in the STAMP-PEM results between the length channel and a mix of accelerometers, magnetometers, and microphones in the building housing the X-end test mass. A commissioner on site posited that this could be caused by a fan that was constantly running to cool electronics. He placed a large piece of plastic on the top of the fan. This reduced the rotation frequency of the fan and the coherence showed a simultaneous downward shift in frequency. Coherence matrices for a group of channels before and during this test are shown in figure 4.4.

Angular control coupling— A search for very-long-duration, $\mathcal{O}(10^4\,\mathrm{s})$, GW transients identified spectral lines at 197 Hz, 203 Hz, 217 Hz and 333 Hz on November 20, 2015, as the dominant source of background triggers. This means that this specific noise source makes the search much less sensitive, and so identifying a specific cause of these spectral lines (which only appear for roughly one day) would allow those running the search pipeline to safely remove these frequencies from the analysis during that day without fear that they were removing a true gravitational-wave signal.

STAMP-PEM was re-run for that day with a narrower frequency resolution than usual and it showed strong coherence with three channels associated with the angular sensing and control of the interferometer: `H1:ASC-AS_B_RF36_I_PIT_OUT_DQ`,

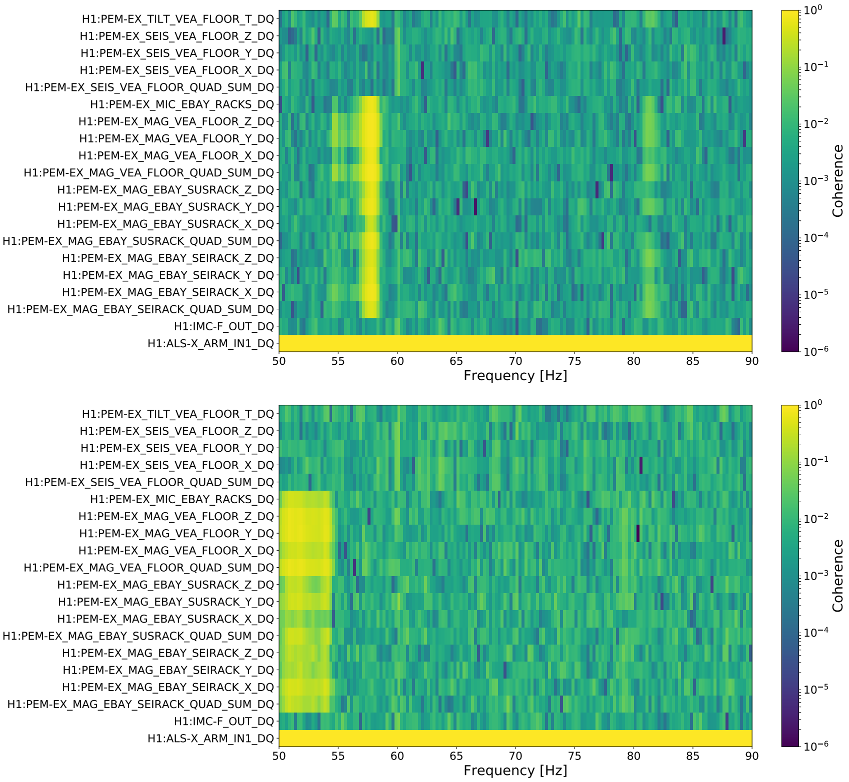

Figure 4.4: Top: coherence matrix showing strong coherence between the single-arm length channel and many environmental monitors. Bottom: the same coherence matrix after plastic was placed on top of the fans that were identified as the likely source of noise. We see on the right that the coherence has dropped significantly in frequency for one of the lines and is essentially gone for the other. These channels include a mix of seismometers, microphones, and magnetometers in the building housing the X-end test mass at LHO.

`H1:ASC-AS_B_RF45_Q_PIT_OUT_DQ` and `H1:ASC-AS_B_RF36_I_PIT_OUT_DQ`. It was found that during that day, sensors were installed to monitor changes that had been made to a malfunctioning driver used to imprint radio frequency sidebands on the light. Those sensors were the cause the noise lines seen by the search. The sensors were removed the following day and the noise lines that caused problems for the search went away.

Monitoring the 0.5 Hz comb in O1— The comb discussed in the comb-finder section above can immediately be seen as coherent between many magnetometer channels and the strain channel at LHO. During O1, I ran a separate instance of STAMP-PEM to monitor these lines. It used a much finer frequency resolution of 1/900 Hz, and only monitored coherence over a small subset of magnetometers that we knew witnessed this noise. An example of coherence between the strain channel and a single magnetometer that witnessed this comb, integrated over 20 hours of archived STAMP-PEM data, is shown in figure 4.5.

Using the full channel list at this frequency resolution would require very large storage, and so STAMP-PEM with very fine frequency bins can only be used for a subset of channels to monitor a known noise or a known set of channels where one might expect very narrow features to crop up. Otherwise, the coherence tool should be used.

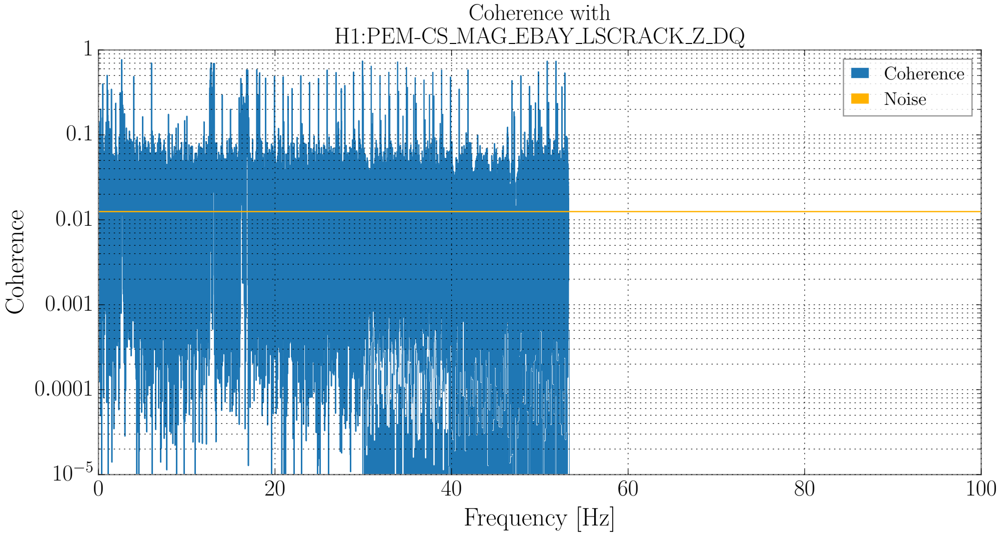

Figure 4.5: A witness channel for the 0.5 Hz comb seen as coherent in the O1 SGWB searches. The orange line shows the expected level of noise given the number of segments we have averaged together. This comb was caused by blinking LED lights on timing chips [51]. This channel is a magnetometer in the room that contains most of the electronics for the corner station (the building housing the LVEA, where the beam splitter, laser, and readout systems are located).

Coherence tool

The "coherence tool" is very similar to STAMP-PEM, in that it calculates coherence between the strain channel at a given interferometer and many auxiliary and environmental monitoring channels [151]. The main differences are that it focuses on longer durations and smaller frequency resolutions. It is run on a weekly basis, and so is less useful for finding a specific day for when a new noise source arises, but it is better at identifying coherence between the strain channel and auxiliary channels for very narrow spectral lines.

During observing run 1 (O2), there is an 8 Hz comb seen as coherent between the LIGO Livingston Observatory (LLO) and LHO strain channels. The teeth of these combs are visible in a single 1 mHz frequency bin, which means that the wider, 0.1 Hz bins used for STAMP-PEM were not able to resolve any obvious correlations. However, the coherence tool, which uses frequency bins on the order of 1 mHz, identified the same comb in the coherence spectrum between the power mains monitors at LLO and the strain channel at LLO. This is shown in figure 4.6.

This tool was also used to find auxiliary channels that were witnesses to coherent spectral lines found with time shifts in the O1 SGWB searches, including lines at 20.22, 47.69, and 453.32 Hz.

4.3 Long-wavelength magnetic fields

A source of correlated noise we expect to eventually cause problems for SGWB searches is long-wavelength, correlated magnetic fields, like Schumann resonances [152]. Correlated noise is insidious for SGWB searches because one of the main assumptions of the search is that correlated noise is negligible. We need to make sure we understand the level of correlated noise due to Schumann resonances so that we can help to distinguish it from GWs. I discuss methods for distinguishing between GWs and correlated noise due to Schumann resonances in chapter 5. In this section, I discuss ways of modeling and estimating the level of correlated noise we expect to eventually see.

Schumann resonances are eigenmodes of the Earth-ionosphere resonant cavity, and are typically excited by lightning strikes [153]. An example of a measurement of the Schumann resonances is apparent in the spectra shown in the left hand side of figure 4.7.

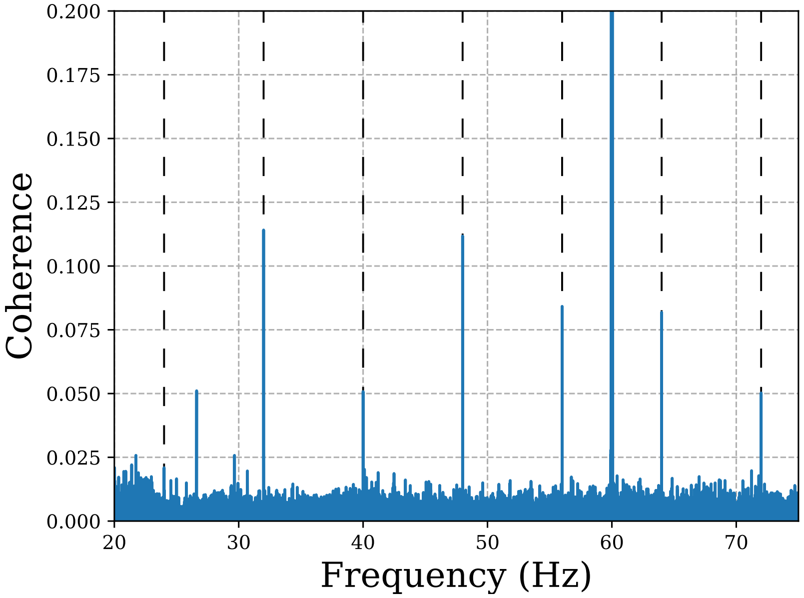

Figure 4.6: Follow-up of a coherent 8 Hz comb seen in O2 using the coherence tool. The harmonics of the comb are marked with a dashed black line. The auxiliary channel used to make this plot is a monitor of the power mains at LLO.

The first four peaks at roughly 8, 14, 20, and 26 Hz are evident in this spectrum. These resonances are coherent across very long distances, as seen in a plot of the coherence of magnetometers at widely separated locations in figure 4.7.

Magnetic noise is not currently a limiting source of noise for the LIGO interferometers. An estimate of how magnetic fields couple into the interferometers can be found by performing "physical environmental monitoring injections" (PEM injections). These coupling estimates can be combined with measurements of the correlation of the magnetic fields on long distance scales to give us an idea of the level of correlated strain noise we expect to see between widely separated interferometers.

In the rest of this section, I discuss a global array of magnetometers we use to monitor Schumann resonances, how magnetic noise can couple into the interferometer, estimates of the strength of current magnetic coupling, and an estimated budget for the level of correlated noise SGWB searches could expect to see in the future. I reserve a

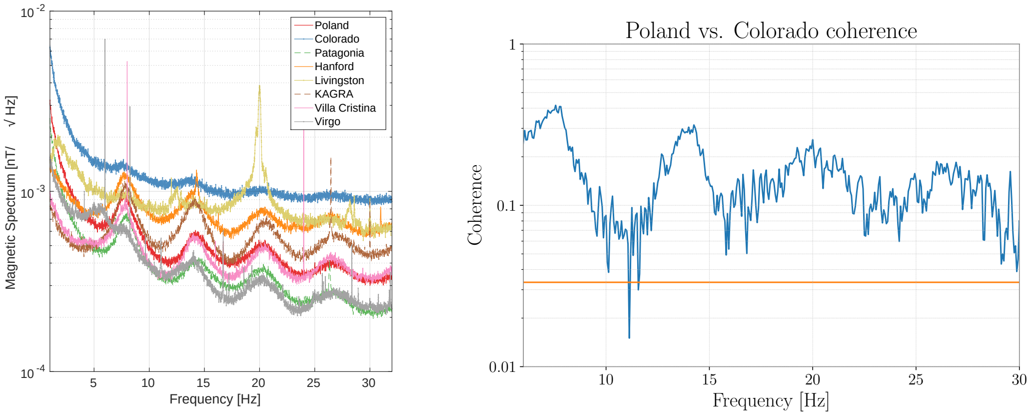

Figure 4.7: Left: spectra from several low-frequency magnetometers around the world that exhibit Schumann resonances. Right: coherence spectrum between magnetometers in Poland and Colorado, which are separated by $\sim 10^4$ km. A map showing the location of these instruments can be found in figure 4.8. The left hand plot is reproduced from [1].

discussion of distinguishing correlated magnetic noise from GWs for chapter 5.

4.3.1 Global array of magnetometers

For the rest of this section, we will use data from a global array of magnetometers [1]. A figure showing where these magnetometers are located can be found in figure 4.8 and information for each sensor used is shown in tables 4.1 and 4.2. Most of these sensors are in magnetically quiet locations, which means they are buried underground in remote areas. The LIGO magnetometers are not placed in the LVEA near the instrument, but instead outside along the arms of the beam tubes as far away as possible from the buildings on site. These sites are not as magnetically quiet as those in Colorado (Hugo station) and Poland (Hylaty station), for example, and so we use the COL and POL magnetometers to do some of our characterization studies below.

4.3.2 Magnetic coupling mechanisms and measurements

Magnetic coupling measurements are made by LIGO commissioners on site by generating large magnetic fields in various locations around the interferometers [157]. These

	acronym	Location	Orientation
Hanford	H1	46°27’42.2”N 119°25’03.6”W	X, Y arms
Livingston	L1	30°32’12.9”N 90°45’57.5”W	X, Y arms
Virgo	V1	43°37’54.7”N 10°30’20.1”E	NS, EW
Villa Cristina	VC	43°32’22.2”N, 10°24’36”E	NS, EW
KAGRA 1	K1	36°24’33.5”N 137°18’39.4”E	NS, EW, Vertical
KAGRA 2		36°24’42”N, 137°18’18”E	NS, EW
Hylaty	POL	49.2°N, 22.5°E	NS, EW
Hugo	COL	38.9°N, 103.4°W	NS, EW
Patagonia	PAT	51.5°S, 69.3°W	NS, EW

Table 4.1: Properties of all the magnetic antennas occurring in the text. There are two LEMI magnetometers each at Hanford and Livingston, aligned along the arms of the interferometers. This table and caption are is reproduced from [1]. COL is short for “Colorado, U.S.A” and POL is short for “Poland.”

	acronym	Type	Notes
Hanford	H1	LEMI-120 [154]	permanent
Livingston	L1	LEMI-120 [154]	permanent
Virgo	V1	MFS-06 [155]	permanent (8-26 Aug 2017)
Villa Cristina	VC	MFS-06 [155]	temporary (20-22 July and 22-24 Nov 2016)
KAGRA 1	K1	MFS-06 [155]	temporary (20-22 July 2016)
KAGRA 2		MFS-06 [155]	temporary
Hylaty	POL	AAS1130 [156]	permanent
Hugo	COL	AAS1130 [156]	permanent
Patagonia	PAT	AAS1130 [156]	permanent

Table 4.2: Properties of all the magnetic antennas occurring in the text. This table and caption are is reproduced from [1]

magnetic fields can couple into the strain channel. There are two likely coupling mechanisms:

1. Coupling to the magnets on the second-to-last stage of the quadruple pendulum suspensions for the test masses.
2. Coupling through electronics.

The first mechanism is likely to produce coupling that falls off in frequency as f^{-5}. This

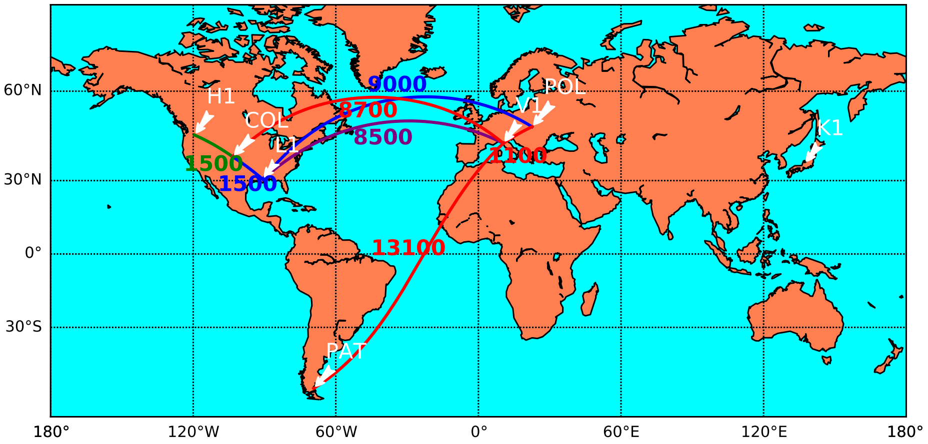

Figure 4.8: Map of the location of global array of magnetometers. Numbers indicate distance between stations. This figure is reproduced from [1].

comes from a factor of f^{-2} from converting from acceleration noise to displacement noise (i.e. a force is applied to the mirror, but we measure strain), f^{-1} from eddy current damping due to the steel skin of the vacuum chambers [158], and f^{-2} from the fact that the coupling happens in the second-to-last stage of the suspensions, and so there is the extra suppression in moving from the second-to-last to the bottom stage of the quadruple pendulum. The second mechanism will likely produce a different coupling that does not fall off as quickly with frequency.

Measurements of these coupling functions are made by generating large magnetic fields at a specific set of frequencies in various locations around the LIGO interferometers. These fields will then couple into the strain channel and be seen as lines in the strain spectrum. Coupling is calculated by taking the ratio of the peak seen in the strain channel with the peak seen in a magnetometer in the building where the injection is made[5]. The peak will be seen in several magnetometers, and so the magnetometer that

---

[5] These are different from the low-noise, low-frequency LEMI magnetometers discussed in the previous

Amplitudes [m/T]	
T_{LHO}	1.5×10^{-8}
$T_{\text{LLO},1}$	1.1×10^{-8}
$T_{\text{LLO},2}$	7.1×10^{-11}
Spectral indices	
α_{LHO}	-3.55
$\alpha_{\text{LLO},1}$	-4.61
$\alpha_{\text{LLO},2}$	-0.95

Table 4.3: Estimates of the parameters in the power law model that was fit to the coupling functions at LLO and LHO. The expressions that use these parameters are summarized in equation (4.4).

sees the largest peak is used for the coupling measurement for that injection. Since the magnetometers are not colocated with the coupling location, and the distances to the injection source are small[6] there is a good chance that this is an *overestimate* of the coupling.

In figure 4.9 we show the maximum coupling measurements at each frequency across each site. The color of the dot indicates which injection location produced the largest coupling measurement. The location of the injections that were made can be found in [157].

We fit the coupling measurements with power laws in one case and the sum of power laws in the other case. The model is:

$$T_{\text{LHO}}(f) = T_{\text{LHO}} \left(\frac{f}{10 \text{ Hz}}\right)^{\alpha_{\text{LHO}}} \tag{4.4}$$

$$T_{\text{LLO}}(f) = T_{\text{LLO},1} \left(\frac{f}{10 \text{ Hz}}\right)^{\alpha_{\text{LLO},1}} + T_{\text{LLO},2} \left(\frac{f}{10 \text{ Hz}}\right)^{\alpha_{\text{LLO},2}} \tag{4.5}$$

I performed a least squares fit of the models to the data to estimate the model parameters. The results are summarized in table 4.3.

These measurements indicate that electronic coupling through cabling is probably

---

section.

[6] This means that small differences in distance to the source still matter in terms of source amplitude.

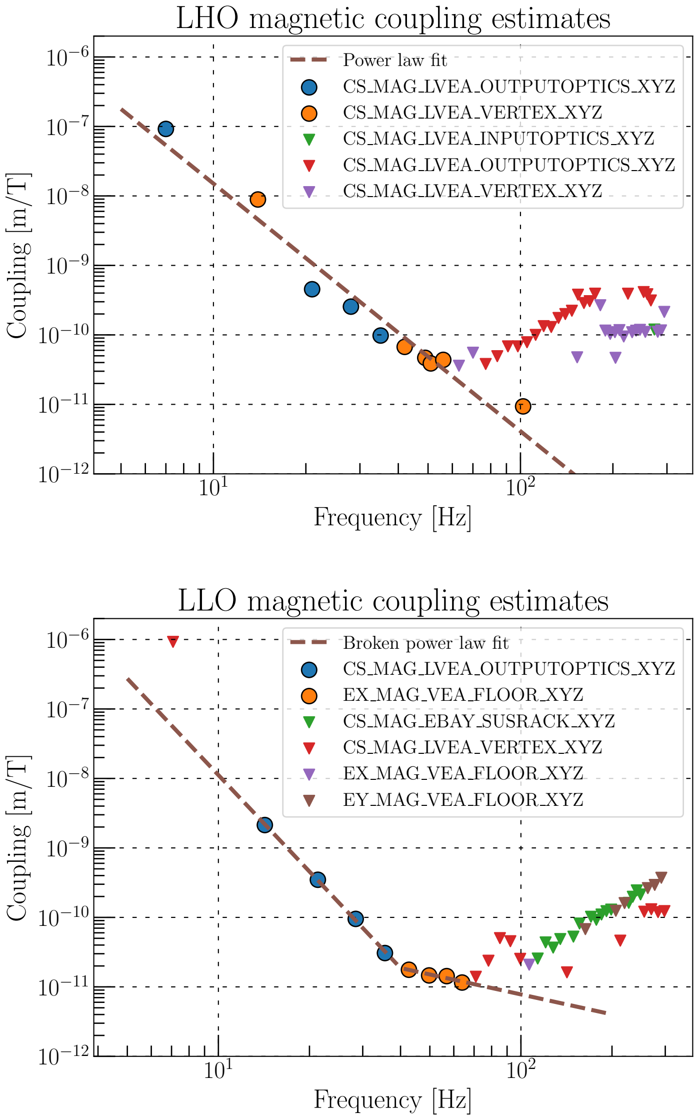

Figure 4.9: Left: results of coupling measurements at LHO. Dots indicate measurements, triangles indicate the injection was not seen in the strain channel and so an upper limit on the coupling was set. Right: the same measurements at LLO. These plots are reproduced from [157]. The fits to these coupling functions are also included, and their parameters are summarized in table 4.3.

the dominant coupling mechanism and so there is the potential that general maintenance and commissioning of the interferometers could drastically change these coupling functions on short time scales. There have been proposals to continuously inject a magnetic “calibration” line or lines that could be used to monitor the strength of this coupling in the future.

4.3.3 Properties of Schumann resonances

Schumann resonances are coherent on very large distance scales, and their amplitudes exhibit variations that happen on time scales of 12 hours, 24 hours, and 24 days. The first two variations are due to the fact that the resonances are generally excited by lightning strikes from storms that start at roughly the same time and roughly the same place each day. The last variation is due to the rotation of the sun, which can cause changes in the ionosphere that will affect the quality factor, amplitude, and central frequency of the resonance peaks in the spectrum.

I have developed a simple method to track the properties of the Schumann resonances, and this allows us to estimate at what times their amplitudes are larger and what the typical diurnal fluctuation in amplitude is near the LIGO sites. This method could be used to re-weight the optimal combination of time segments, expressed in equation (2.38), to give larger weight to times when the amplitude of the Schumann peaks are lower and less weight to times when the peaks are higher.

We track the amplitude of the Schumann peaks by fitting a Lorentzian profile to the first four peaks in the spectrum using a least squares fitter provided by `astropy` [159]. This fit gives three parameters for each of the four peaks: amplitude, quality factor, and central frequency. An example of Lorentzian fits to the Poland magnetometer spectrum for each two hours of a single day is shown in figure 4.10. I performed this fitting on spectra from each two hours of data for 10 days using the Poland NS-oriented magnetometer. A plot of the amplitude of each peak as a function of time is shown in figure 4.11. We see obvious diurnal variations where the peak of the first harmonic of the Schumann resonances changes by as much as 40 % over a single day.

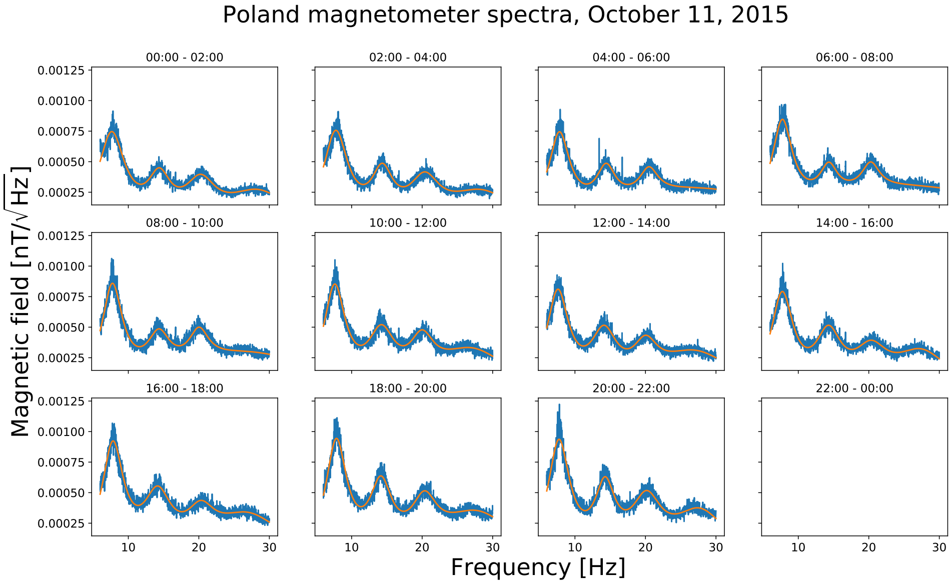

Figure 4.10: Lorentzian fit to the Poland NS-direction magnetometer for the spectra produced from each two hours of the day on October 15th, 2015. The blue is the magnetometer spectrum and the orange is the fit to that spectrum. Note that the peaks change amplitude from one chunk of two hours to the next. The amplitude of each peak as a function of time over ten days is plotted in figure 4.11. The last plot is missing above due to missing data during that time.

4.3.4 Correlated noise budget for SGWB searches

We can use the correlation between the LEMI magnetometers located at the two LIGO sites (summarized in tables 4.1 and 4.2) and the coupling measurements to create a correlated noise budget for the isotropic SGWB search. We use an expression similar to that shown in [52, 53]. We note that the cross-power between our two detectors now has a correlated magnetic noise piece

$$s_1^*(f)s_2(f) = \underbrace{\lambda f^{-3}\gamma(f)\Omega_{GW}}_{\text{GWs}} + \overbrace{T_1^*(f)T_2(f)\mathcal{M}(f)}^{\text{Magnetic Noise}}. \tag{4.6}$$

where λ is a normalization constant, $T_1(f)$ is the coupling function for detector 1, $T_2(f)$ is the coupling function for detector 2 and $\mathcal{M}(f)$ is the power spectrum of correlated

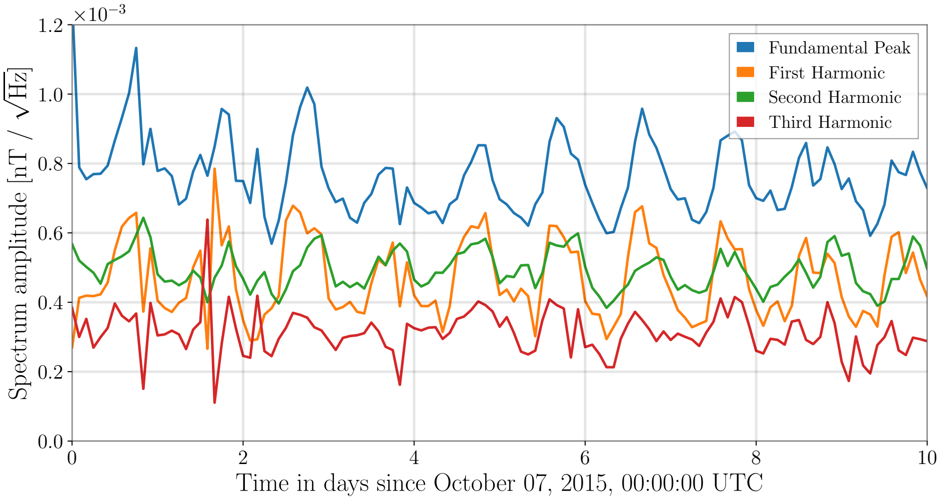

Figure 4.11: Amplitude of the peak for each of the first four harmonics of the Schumann spectrum plotted over ten days. An obvious diurnal variation is present whose amplitude is roughly 0.2 pT/$\sqrt{\text{Hz}}$, corresponding to a daily variation in amplitude of roughly 40 %.

magnetic noise between the two detectors in units of T^2/Hz. Isolating the second piece, if we substitute this in for $s_1^*(f)s_2(f)$ to our bin-by-bin estimator in equation (2.37) then we find that the contribution to our estimate of $\Omega_{\text{GW}}(f)$ in each frequency bin due to correlated noise is given by:

$$\Omega_{\text{GW}}^{\text{MAG}}(f) = \frac{10\pi^2}{3H_0^2}\frac{f^3}{\gamma(f)}\text{Re}\left[T_1^*(f)T_2(f)\mathcal{M}(f)\right]. \tag{4.7}$$

We estimate $\mathcal{M}(f)$ by taking the cross-power between magnetometers located onsite at the two detectors, and we use the fits to the estimates of the coupling functions from section 4.3.2 to create the budget. This budget is presented, along with sensitivity estimates for an isotropic SGWB, in figure 4.12. We present many lines for the budget on the same plot to give an idea of the range we expect. The dark line indicates the arithmetic mean of those lines.

These measurements indicate that, given an optimal choice of the spectral index, α, we could measure this contamination by the time we reach design sensitivity. There are several proposed methods for reducing this noise. One method, involving Wiener

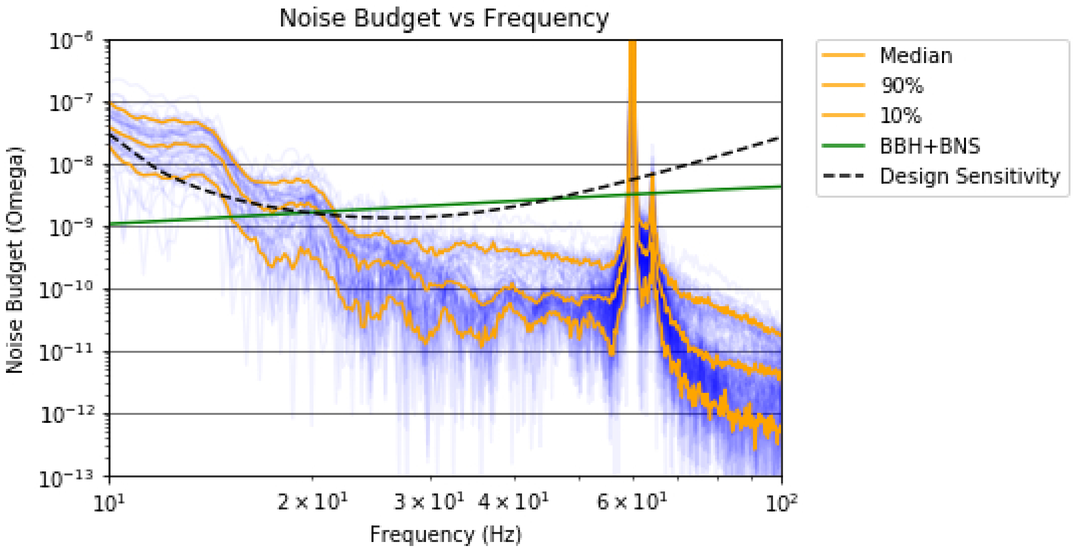

Figure 4.12: An estimate of the correlated magnetic noise budget is shown in light blue lines. Each line represents a different realization, measured with 1 hour of data over the course of four days starting on August 15th, 2017. The blue lines show the varying amplitude of the Schumann resonances. The orange lines represent the median, 10th, and 90th percentile of the blue lines in each frequency bin. The other curves indicate projected 2-σ sensitivity over 1 year of integration time of the isotropic SGWB search at design sensitivty, and the estimated SGWB due to unresolved CBCs [28]. Image credit: Rixing Xu.

filtering using magnetometers as witness sensors [160, 1] is promising, but relies upon using separate witness magnetometers to clean different detectors. However, one worry about this approach is that poor filter construction could result in *injection* of correlated noise using this method. Another method, which leverages the different spectral shapes of this correlated noise and SGWB background due to compact binary coalescences is presented in chapter 5.

4.4 Identifying and mitigating whistle glitches

Searches for transient sources of GWs generally either use matched-filtering techniques to search for compact binary coalescences (CBCs) or they use excess-power statistics to search for unmodeled sources like supernovae [27, 161, 162, 26]. Typically, these searches assess significance of a candidate by performing “time-slide studies,” where they apply an unphysical time-shift to the two detectors, run the search, and look at how often their detection statistic takes on certain values by random chance. The (usually reasonable) assumption is that there is not a source of correlated, transient noise between the two detectors, and so this method will give an independent estimate of how often, by chance, glitches in the detectors might overlap in time with one another and cause a multi-detector detection statistic to take on a certain value. This is used to generate the background distribution against which detection candidates are compared.

It seems obvious, then, that reducing the overall occurrence of glitches in the detector will improve the background distribution used to set a significance threshold for detection. At minimum, if we know the source of the glitches, but cannot change the detector configuration or hardware to make them stop happening, then we can remove times when those glitches happen from the analysis completely. This means that we lose time that could be used for detecting GWs, but we also remove glitches we know are not GWs from our background.

Below, we discuss one type of transient glitch that I have spent time working to understand and characterize.

4.4.1 Whistle glitches introduction

A common class of glitches in the LIGO detectors are known as “whistle glitches” because of the sound they make when converted to audio. In frequency-time space they quickly sweep through the full 8 kHz band to which LIGO is sensitive in less than a second. Right now, these glitches are most prevalent at LLO, and so unless otherwise noted, the following discussion relates to that detector.

The current hypothesis is that whistles are the product of a beat note between two radio frequency (RF) sources. One of those sources is a voltage controlled oscillator (VCO) used to modulate the laser wavelength as part of the common mode servo[7]. The other source varies. In some cases, it is a different VCO and in other cases it is an ambient RF signal. Henceforth, we refer to this “other” RF signal as a “stationary

---

[7] The “common mode servo” is used to control the common motion of the two arms of the interferometer.

line.”

We test this hypothesis by plotting the time series of the VCO in question, the input mode cleaner VCO (PSL-VCO) (which is discussed in more detail in section 4.4.3), below a strain spectrogram containing a whistle glitch. An example is shown in figure 4.13. We see that twice during this time, the whistle hits zero frequency when the PSL-VCO crosses a specific value. We also fit the whistle by calculating a beat note between the PSL-VCO and the stationary frequency, and we overlay that fit on the spectrogram in red and green. We discuss in section 4.4.2 how to generate the fast read back of the PSL-VCO to create the time series in the bottom plot, as well as different methods of automatically finding the frequency of stationary lines which cause beat notes that appear as glitches.

Whistles are also seen in many auxiliary channels in the LIGO detectors, and some efforts to reduce RF pickup and increase shielding of cables have resulted in a reduction of whistles in those channels.

4.4.2 Characterizing and monitoring whistle glitches

Fast readback of PSL-VCO

The radio frequency of the PSL-VCO is sampled at just 1 Hz, but stored in data frames as if it is sampled at 16 Hz; meaning the data stream consists of 16 repeated samples followed by a change and 16 more repeated samples. It is unclear what the proper time stamp is for the repeated sample. On short time-scales, this channel is linearly related to the `IMC-F_OUT_DQ` channel, which is the explicit control signal sent to the VCO, which is in turn sent to an acousto-optic modulator (AOM) that is used to modulate the laser wavelength.[8]

We fit the `IMC-F_OUT_DQ` channel with the PSL-VCO frequency repeatedly using a linear model, changing the time stamps at which the 1 Hz samples of the PSL-VCO are taken for each fit. The times consistent with the best linear fit correspond to the “true” sampling times of the PSL-VCO channel. We show a plot of the residual of many linear fits in figure 4.14. From here, we create a “new” PSL-VCO channel sampled at

---

[8] We could use this `IMC-F_OUT_DQ` channel to identify whistles, but we see secular changes in the linear relationship between it and the VCO, and so backtracking to identify the frequency of any stationary lines we found using that channel would take extra work.

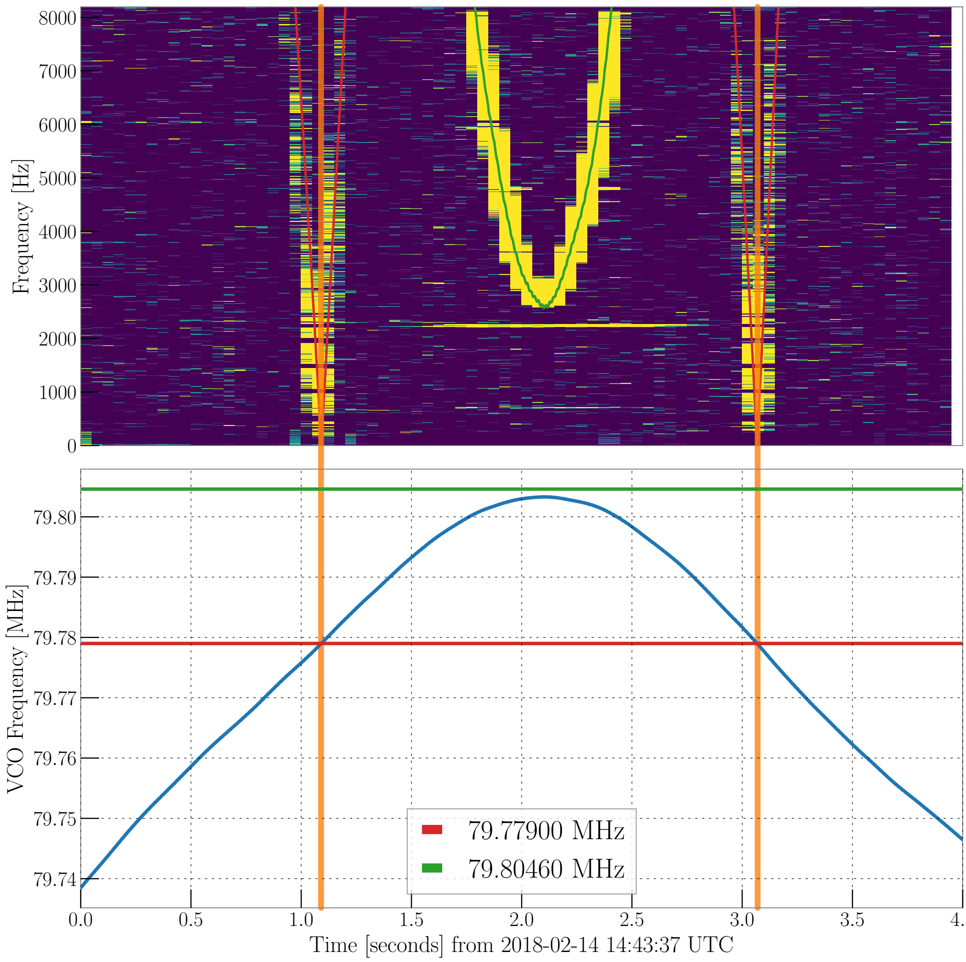

Figure 4.13: Top: example of three whistle glitches caused by two stationary lines at LLO during tests in February 2018. We also show our ability to fit it by calculating a beat note between the PSL-VCO and the stationary lines marked on the lower plot. We calculate a beat note between the blue curve on the bottom plot and the red (green) curve, and multiply that beat note by a factor of 2. That produces the red (green) curve in the upper plot that is overlaid on top of the whistle glitches, which are visible in yellow. The source of the extra factor of 2 is unknown.

just 1 Hz with correct time stamps. We can then up-sample that channel to try to get better resolution by either using a univariate spline interpolation between samples or by measuring the fit between the `IMC-F_OUT_DQ` channel (which is sampled at 16 kHz) and

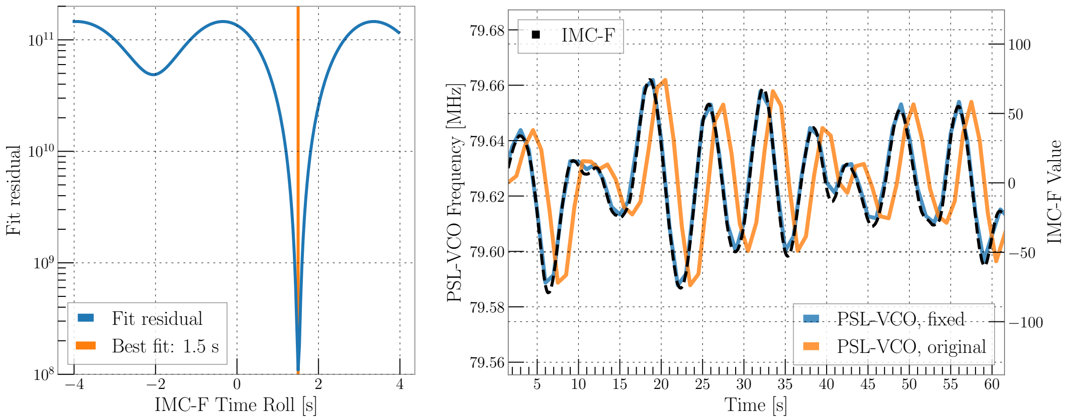

Figure 4.14: Left: fit residuals between the PSL-VCO and IMC-F for various time-delays between the two channels. We fix the time stamps of the PSL-VCO by the negative of the best fit value, meaning in this case we must subtract 1.5 s from the time stamps of the PSL-VCO channel (assuming we originally labeled the time stamp as the time immediately after the samples change values). An example of the time-stamps before and after the shift can be seen on the right.

the PSL-VCO channel and using the fit to generate a "fast" PSL-VCO channel. Both methods produce similar results for our purposes.

Sometimes the whistle glitch does not appear simply as the difference of the two frequencies, but instead as some higher harmonic of that beat note (values between 2 and 6 have been identified), indicating that the coupling mechanism of the beat note into the strain channel could be different for different stationary lines. While RF pickup into essential electronics is likely the culprit, the exact coupling path is still unknown.

It can be a tedious task to fit each glitch and compile a set of stationary lines manually. We have developed methods to either automatically identify these glitches, or at least infer information about their population like the stationary line and the rate at which the glitches are occurring. Once we have a catalog of stationary frequencies, we can try to manipulate the PSL-VCO such that it always remains in a "clean" range in frequency space. This was done at LLO during O1 and was effective at significantly reducing the rate of whistle glitches. This is discussed more in section 4.4.3.

Below, we outline three methods that have been used to try to automatically identify the stationary frequencies that cause problems.

Characterization methods

`Stochtrack` fitting

`Stochtrack` is a “seedless clustering” algorithm that can be used to identify tracks of large amplitude in a frequency-time map (ft-map) [163]. It does so by drawing many tracks in an ft-map. For each track, it sums the value of the pixels the track passes through and normalizes by the square root of the number of pixels the track passes through to generate a “track statistic”. It then records which track has the largest track statistic.

I helped design and implement a custom track-drawing method for `stochtrack` that was optimized for whistles. It produces an ft-map of the PSD of a given channel, and then normalizes each row of that ft-map by the median across all pixels in that row. This helps reduce the effect of loud spectral lines (like calibration lines) and accentuates transient artifacts (an example is the top plot of figure 4.13). The track-drawing method guesses a value of the stationary frequency (and harmonic of the beat note), calculates a beat note between the PSL-VCO and the stationary frequency, and uses this beat note as the track that is drawn on the map. The stationary frequency and harmonic associated with the track with the loudest track statistic is then recorded. In cases where there is not a whistle, this statistic is low and the stationary frequency and harmonics for those tracks are meaningless. In cases where there are whistles, the method does a good job of recovering the correct parameters one would get performing the fit manually, and the track statistic is large.

An example of running `stochtrack` on each 4 s time segment over 4.5 hours of data is shown in figure 4.15. Map pixels in the ft-maps had 1/16 s × 16 Hz resolution. The results show an obvious stationary frequency that dominates most of the tracks. In addition, taking the median track statistic across all tracks in that outlying bin results in a significantly larger value than when the same thing is done for the other bins.

While this method can clearly be effective, it takes a very long time to run and it is not feasible to run in real-time. It could be used to analyze a pre-selected population of whistles, but it is not effective at monitoring data as it is collected. In addition, because only the largest track statistic is recorded for each 4 s stretch of data, if there are multiple whistles from different sources, like what is displayed in figure 4.13, then this method would miss one of the stationary lines causing whistles in that map. Below, I outline two methods that can operate on shorter time scales and with much less computational cost.

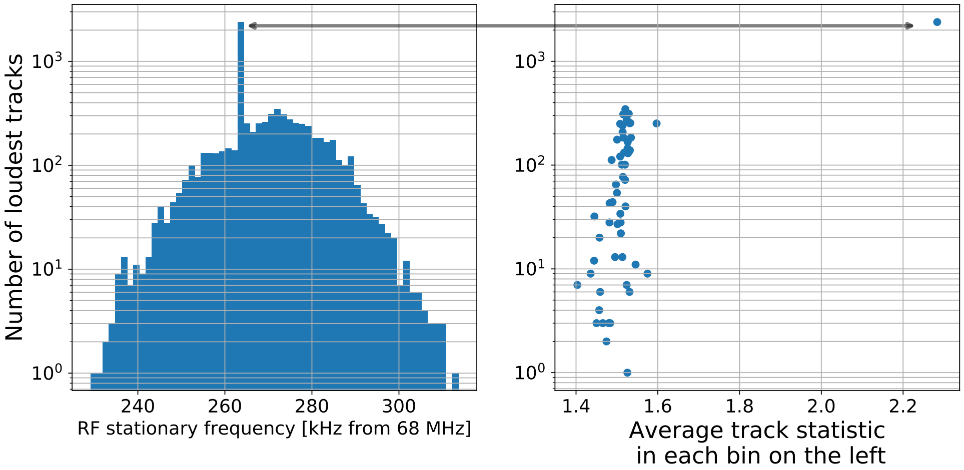

Figure 4.15: Left: histogram of the estimated stationary line frequency for the largest recovered track in each 4 s ft-map that was analyzed. Right: average track statistic for recovered track for each bin in the left hand plot. This indicates that only one bin in the left hand plot was likely consistent with whistles, and it was the outlier near 68.264 MHz. This data was from June 4th 2015 06:00 UTC – 10:30 UTC. The PSL-VCO was operating near 68 MHz, as opposed to where it is now, near 79 MHz. It is important to note that this histogram conveys very different information than those presented in the next section, despite visually looking similar.

Histogram method

We can also look at the rate at which glitches happen when the PSL-VCO sits near certain values. We use the external trigger generator, `Omicron` [164] to construct a list of glitches that occur in the detectors. We measure the frequency of the PSL-VCO value around the time of each glitch and we construct a histogram of those frequencies. VCO frequencies associated with a stationary line should appear as higher bins in that histogram. These histograms are much faster to make, and give similar-quality results to the `stochtrack` fitting method.

I wrote a piece of code to compare the histogram of the VCO frequency at each trigger to the histogram of the time-series values of the VCO. If there are no whistles, then we should be able to rescale the latter to be very similar to the former. The assumption here is that in the absence of whistles, one expects glitches to happen at a specific PSL-VCO frequency in proportion to the rate at which the PSL-VCO crosses that frequency. I used the Markov chain monte carlo (MCMC) sampler[9] `emcee` [165] to simultaneously rescale the histogram of the VCO time series to fit on top of the trigger histogram and estimate excess bin heights above that background. An example plot illustrating the use of this method to estimate the rate of whistles associated with the 4 identified stationary frequencies is shown in figure 4.16.

I used a Gaussian log-likelihood, where I label the trigger histogram bins using T_i, the estimated whistle rate in each bin as w_i, the histogram of the VCO time series as B_i, and estimated rescaling value of the VCO timeseries as r. I have chosen capital letters for measured quantities and lower-case letters for parameters over which we sample. The dimension of the parameter space is $N_{bins} + 1$.

$$\log p(T_i|B_i, w_i, r) = -\frac{1}{2}\left(\sum_i \frac{\left[T_i - (r\,B_i + w_i)\right]^2}{T_i}\right). \tag{4.8}$$

I used a log-uniform prior on the w_i's, which should keep the initial estimates for the whistle rates close to zero. This helps to properly fit the background in the earlier stages of sampling, before the MCMC walkers slowly pick out larger bins. If one is not careful about this selection of initial guesses, then the background can be severely-underfit and the difference is then made-up by the w_i estimates. This issue arises in part because we are using 50 data points to estimate 51 parameters. We use our prior information to inform initial guesses for the start locations of the MCMC walkers to try to make up for this deficiency. Therefore, we start the estimates for the w_i's very low, while we start the estimate for r very near to the overall glitch rate (that includes whistles). These guesses generally serve us well in producing sensible results. An example of this method in action that shows the individual steps for four hundred MCMC chains is shown in figure 4.17. We see that the rate is fit properly first, followed by the individual bins.

From the results of the MCMC sampler, stationary radio frequencies are identified

---

[9] MCMC samplers and Bayesian inference will be discussed in more detail in chapter 5

by taking the the relative maxima of the w_i's (see right hand plot of figure 4.16). We sum over frequency bins adjacent to each of the relative maxima to achieve an estimate of the whistle rate associated with each stationary frequency. The results for the sample data from February 2018, are summarized in table 4.4.

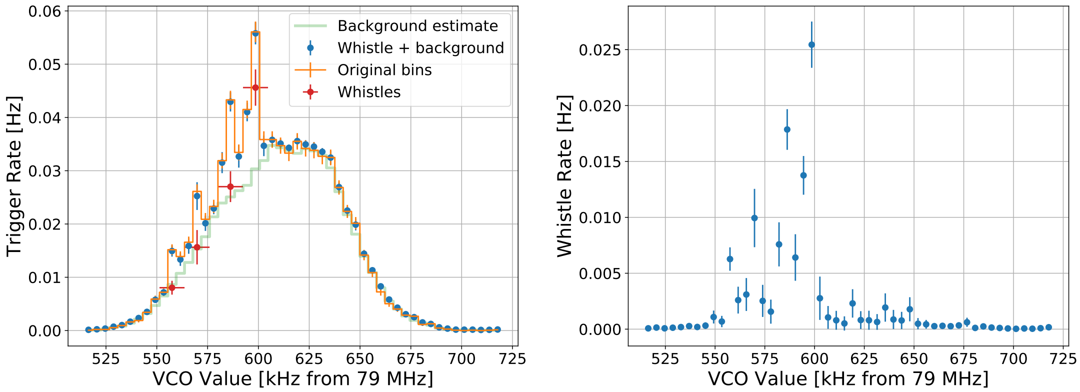

Figure 4.16: Left: reconstruction of trigger histogram using an MCMC sampler. The parameter space is $N_{bins} + 1$ in size; one parameter for the overall rescaling of the VCO time-series and then N_{bins} parameters for the rate of of whistles in each bin. We see four obvious stationary frequencies. Individual bin errors are given by the square root of the number of counts in each bin. Right: estimate of the rate of whistle glitches in each bin.

Stationary Frequency [MHz]	**Rate [Hz]**
79.5575 ± 0.006	0.0076 ± 0.0014
79.5698 ± 0.006	0.016 ± 0.0025
79.5863 ± 0.006	0.027 ± 0.003
79.5986 ± 0.006	0.046 ± 0.0036
Total Whistles	0.119 ± 0.007
Background	0.655 ± 0.012

Table 4.4: Summary of whistle triggers for a 4 hour lock stretch on February 19th, 2018 at LLO.

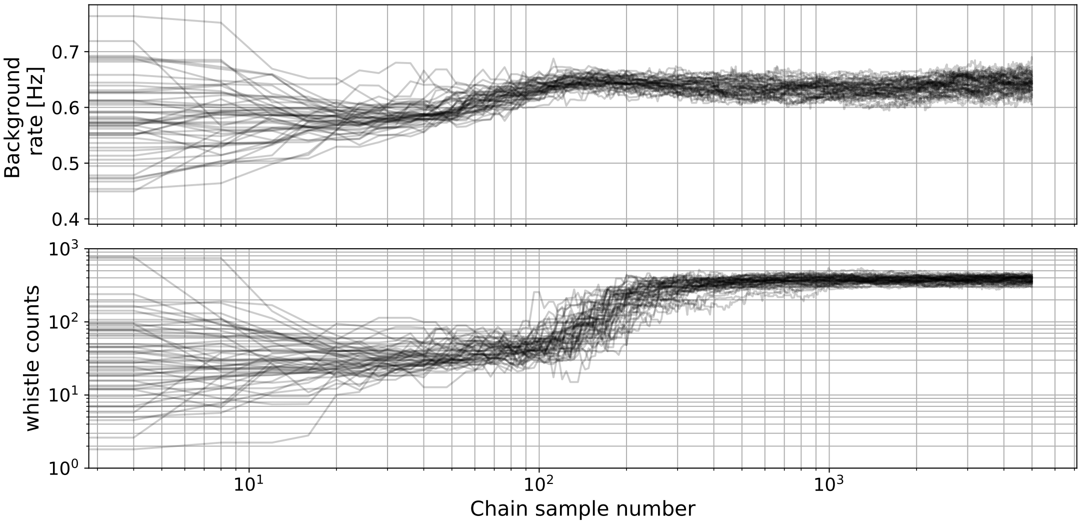

Figure 4.17: The “burn in” MCMC chains for two parameters: the background rate of triggers and the number of whistle counts in the bin with the most whistles. Each trace is a separate MCMC “walker,” and we see the log-uniform spacing of those walkers in the bottom plot allows the convergence of the background rate to a reasonable value first, followed by the migration of the whistle trigger counts increasing to their correct value near roughly 400.

GravitySpy

`GravitySpy` is a citizen-science project that attempts to classify glitches in the detector as belonging to certain families using a machine learning (ML) classifier [166, 167]. It trains the classifier using citizen scientists and then applies that classifier to all of the glitches registered at both detectors. Whistles are one classification of glitches available. `GravitySpy` results are available on time scales of ∼ hours after glitches are registered, and so `GraviySpy` could also be used to characterize whistles. One would likely look at the VCO frequency at each of the glitches classified as whistles.

In the future, the hope is to combine information from the histogram method described above with `GravitySpy` to perform better classification of whistles.

Monitoring

During O1 and O2, I implemented and maintained an online monitor that created histogram diagnostic plots like those discussed above. The MCMC portion of the code was not complete until more recently, but evaluating histograms by eye allowed us to find a region of space in the radio frequency band at LLO[10] where there were relative few stationary lines that caused whistle glitches. The PSL-VCO operated in this region for most of O1 and O2, however, in pre-observing run 3 (O3) cabling has changed and it appears that this region of RF space now contains stationary frequencies that cause whistles. This calls for identification of a new list of stationary frequencies, and hopefully, finding a new area of RF space where the PSL-VCO can operate and not cause whistles.

The monitor waits until two hours after the end of a UTC day, when it then queries a database for segments of time when the interferometer is in an observational state. It then creates trigger and time series histograms for each of the locked segments and displays those histograms on a web page as part of the LIGO Detector Characterization Summary Pages [168]. It does this for triggers for several different channels, including the strain channel. This is done because often there are other channels that witness whistles at the same time as the strain channel, which could be helpful for identifying a coupling mechanism in the future or creating a veto for whistles that could help increase the sensitivity of certain GW searches.

The latest version of the monitor that is in development is based on the latest version of the histogram method described above. It includes explicit estimates for stationary RF lines, as well as the rate of whistles associated with each line, the overall rate of whistles, and the non-whistle glitch rate as identified using the MCMC histogram method described above. It also makes all of the raw data for the plots available for download.

4.4.3 Whistle glitches and the LIGO detectors

How the beat notes couple into the detectors is a difficult question to answer. RF pickup can happen any place there are wires. Simply plugging a coaxial cable into a spectrum

---

[10] where whistles were a much larger problem, compared to at LHO

analyzer in the LVEA shows a forest of lines in the $60 - 200$ MHz frequency band. RF sidebands are imprinted directly on the light to aid in Pound-Drever-Hall locking, and those signals are carried throughout the interferometer to be used for demodulation and recording purposes. Poorly designed cables can lead to leakage that can result in very large RF signals that can then be picked up by other electronics.

The PSL-VCO

The PSL-VCO is used in the common mode servo [169]. In broad terms, the common mode servo adjusts the wavelength of the laser based on the common free-swinging motion of the test masses. However, generally, this must be balanced with the fact that before the light enters the interferometer it goes through a triangular mode cleaner that extracts the Gaussian TEM_{00} mode of the laser [170], and so we must adjust the laser frequency in such a way as to keep both the mode cleaner and the full interferometer locked. In principle, the control signal sent to the laser (known as "MC-F"[11]) consists of the error signal from the mode cleaner and the high-frequency-filtered error signal from the common mode of the free swinging test masses. The former is used because the low-frequency error signal from the common mode of the test masses is used to actuate directly on one of the mirrors in the mode cleaner. The PSL-VCO is used as input to the AOM that controls the laser wavelength. The control signal the PSL-VCO follows is MC-F.

RF survey at LLO and LHO

I performed a survey of the RF fields near most electronics racks in the electronics bay and the laser and output mode cleaner racks in the LVEA at LLO in August, 2015. A similar survey was also conducted the following week at LHO. We used wire coiled around a ferrite core as our magnetic probe, and a simple short 1/2 dipole antenna as an electric field probe. A rough calibration of the probes suggest that pickup values of -70 dBm with the magnetic probe need attention, as they correspond to surface current density values of greater than 1/3 mA/m at a skin depth of 10^{-5} m associated with 100 MHz [171]. At a frequency of 100 MHz, lines with pickup values of -60 dBm or larger

---

[11] This control signal is read out and saved as the `IMC-F_OUT_DQ` channel mentioned above.

with the electric probe need attention. These correspond to electric fields of $\sim$3 mV/m and larger. The maximum values are based on crude estimates of the detectability of RF on forward biased semiconductor junctions and could well be smaller [171].

During the survey, the amplitude of peaks in the frequency band around 80 MHz and 160 MHz were recorded if they exceeded -70 dBm. The two interferometers showed similar amplitudes at each site using the same probes, and most peaks exceeding our threshold were associated with the fundamental and first harmonics of three VCOs. These included the PSL-VCO, discussed above, along with the ALS-COMM and ALS-DIFF VCOs discussed in the wandering line section of section 3.2. These peaks were largest in the electronics racks where these VCOs were plugged in, which are ISC-R1 and ISC-C1. Details on these racks can be found in two LIGO internal documents [172, 173]. Generally, these VCOs are connected to racks using BALUN transformers.

The survey found that RF connections using BALUN transformers showed larger levels of leakage than those that did not. Later tests confirm that these BALUNs greatly increased RF pickup and leakage [174] by a factor of $\sim$1000 unless capacitors were added to provide an RF ground to the metal body of the BALUN. Without the ground, the wires in the BALUN are free to radiate. These capacitors were not used initially, and should be added with caution, as they could change the phase of the signals being run through these wires.

Some mitigation efforts that included removing the BALUNs reduced these peaks, and even mitigated whistle glitches in some auxiliary channels. A more updated survey should probably be performed in the future, with more precise probes.

There are several causes of radiation that have been determined. These are laid out by Richard Abbott in [175, 174].

1. Use of a poor RF connection in the VCO circuit layout of the local oscillator input to phase frequency discriminators.

2. Radiation out of several BALUN transformers.

3. RF emission from cables exiting an amplifier for the PSL-VCO, likely associated with RF imbalance between currents in the shield of the coaxial cable and the center conductor.

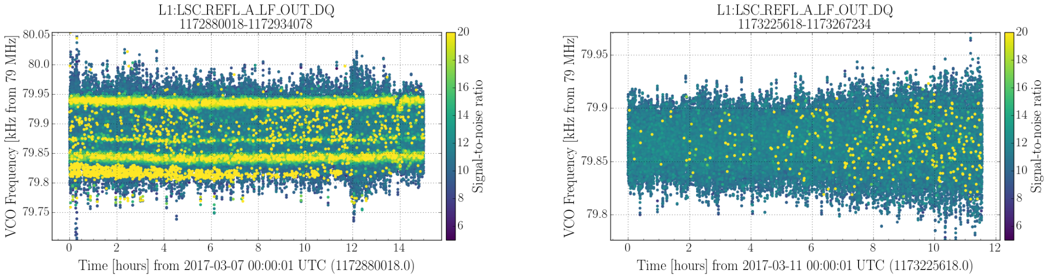

Figure 4.18: Left: Omicron triggers for LSC-REFL at LLO for March 7th, 2017. The y-axis indicates the value of the PSL-VCO and the x-axis is time. Color represents SNR from Omicron. It is clear that there are several stationary lines that cause louder SNRs. Right: Omicron triggers from March 9th, 2017, after RF mitigation efforts [176]. We see no such lines, despite the fact that the PSL-VCO sweeps through a similar range of frequencies.

Mitigation efforts and proposals

Stay away from stationary lines—On days when the common swinging of the test masses is higher[12], the PSL-VCO will take on a broader range in RF space. In general, we have some choice over the range of RF space that the PSL-VCO traverses, as it is relative changes in the VCO value that are useful for the AOM. We can use this choice to try to steer the PSL-VCO into regions where there are no stationary lines that we know cause whistles in the strain channel. During O1 and O2, this method was effective at reducing the rate whistles seen in the strain channel. Several channels, including the power recycling cavity length (PRCL), and the low frequencies of the reflected light from the power recycling cavity (LSC-REFL), still showed whistles throughout most of the runs.

Remove BALUNs—As discussed above, removing the BALUNs can reduce RF pickup and potentially help reduce whistles. During O2, we continued to keep the PSL-VCO in a region away from stationary lines, and so assessing this effect on the strain channel is difficult. We did see a decrease in whistles in LSC-REFL when BALUNs used for RF connections for the three VCOs were removed on March 7th, 2017 [176]. In figure 4.18 we see plots for this channel before and after the removal of the BALUNs.

---

[12] this might happen if the oceanic microseism is elevated, as is often the case during the winter at LLO when there are many storms in the Gulf of Mexico

General methods for reducing RF pickup— Below are several proposals for reducing RF pickup, all suggested by Richard Abbott based on independent testing he performed after the RF surveys were finished. These are summarized in [174]

1. Fix the poor RF connections on frequency discriminator chassis in rack ISC-C1 [177, 173].
2. Remove BALUNs from cables carrying the PSL-VCO, ALS-DIFF, and ALS-COMM VCOs away from the laser racks in the LVEA. These are in racks ISC-C1 and ISC-R1 [172, 173]
3. Remove BALUN serving the intensity stabilization servo AOM in rack PSL-R2.
4. Attach clip-on RF ferrite common-mode chokes around coaxial cable serving the PSL-VCO at the output of the amplifier mentioned in the “causes” list above.

4.5 Conclusions

In this chapter we have presented detector characterization work to help find and mitigate sources of lines in the LIGO interferometers. We have introduced a variety of tools used by members of the LIGO community to find and track lines and combs, as well as a new one used for tracking many channels at once, STAMP-PEM, in detail.

We also discussed one particular source of transient “glitch” that is prevalent in the LIGO Livingston detector. We discussed ways of estimating the rate of these glitches, possible sources, and several routes one could take to try to mitigate the problem.

Chapter 5

Parameter estimation and model selection applications to LIGO SGWB searches

As Advanced LIGO and Advanced Virgo inch closer to their design sensitivities, a detection of an astrophysical SGWB is on the horizon [28]. In the event of such a detection, it is worthwhile to consider making a statement about how strongly the data support the astrophysical models that have been constructed versus any one of the many other models put forth in the literature. If, for example, there is strong support for an astrophysical SGWB, (i.e. a 2/3 power law scaling in frequency), another interest would be in simultaneously accounting for the detection we have made while also trying to set limits on, or detect other models that could contribute at a lower level. In addition, correlated noise will likely affect searches for an SGWB at some point, and this method could also be used to estimate and account for this correlated noise.

In this chapter we seek to provide a general framework for quickly and efficiently making such statements using the data products of the typical LIGO SGWB searches discussed in chapter 2. We do this using a "hybrid" Bayesian approach that is very similar to the method outlined in [178]. The approach we present will produce qualitatively similar upper limits and detection levels for the cases described in chapter 2, under the assumption that the background is a power law, but it also easily generalizes to the other cases of interest. Past methods of applying a similar hybrid Bayesian approach have focused on specific applications, like parameter estimation for simple, low-dimensional models [179], or testing whether the LIGO SGWB searches show consistency with the tensor polarization modes predicted by general relativity [178]. Here, we provide a general framework for performing Bayesian parameter estimation and model selection for a generic set of models using the data products from the LIGO SGWB searches. We then illustrate how this framework can be applied in a few simple, representative examples. Finally, we'll apply this method to full-scale simulations where we use real magnetometer data to simulate correlated magnetic noise in LIGO detectors.

Throughout this chapter we will use the bin-by-bin estimator defined in equation (2.37), but without the normalization by the overlap reduction function, $\gamma(f)$. This makes the estimator, $\hat{Y}$, proportional to $\gamma(f)\Omega_{\mathrm{GW}}(f)$, which mimics the convention in [178]. This allows us to easily generalize the code and the method to searching for alternative polarizations of GWs, as discussd in that manuscript. Therefore, the estimator we use is given by

$$\begin{aligned}\hat{Y}(f) &= \frac{2}{T}\frac{10\pi^2}{3H_0^2}f^3\mathrm{Re}\left[\tilde{s}_1^*(f)\tilde{s}_2(f)\right] \propto \gamma(f)\Omega_{GW}(f) \qquad (5.1)\\ \sigma^2(f) &= \frac{1}{2T\Delta f}\left(\frac{10\pi^2}{3H_0^2}\right)^2 f^6 P_1(f)P_2(f)\end{aligned}$$

where T is the length of the time segments over which we run the analysis, Δf is the width of the frequency bins we use, H_0 is the Hubble constant today, $\tilde{s}_I(f)$ is the Fourier transform of the data in detector I, $P_I(f)$ is the power spectrum in detector I, and $\gamma(f)$ is the traditional isotropic overlap reduction function defined in equation (2.23).

The outline of the rest of this chapter is as follows: in sections 5.1.1 and 5.1.2 we discuss Bayesian parameter estimation and model selection from a bird's-eye view. In section 5.2 we discuss MCMC methods for exploring posterior distributions and for estimating the Bayesian evidence. In section 5.3 we discuss the `SMBS` code package that has been developed to perform parameter estimation and model selection on both real and simulated LIGO data using arbitrary models for the SGWB. We then discuss in greater detail a few specific examples of applying these techniques to making a detection for an SGWB, distinguishing between different models, and even creating a budget for what sources contribute to the SGWB at what levels.

Finally, in section 5.4 we apply these methods to the case where we have correlated noise in the LIGO detectors. We construct a framework for detecting an SGWB in the presence of correlated magnetic noise, and test that framework using simulations with realistic magnetic noise at low frequencies.

5.1 Bayesian inference

5.1.1 Parameter Estimation

We often use Bayes' Theorem to write the probability for a set of parameters, $\vec{\theta}$, given some model $\mathcal{M}(f;\vec{\theta})$, and the measured data $\hat{Y}$

$$p(\vec{\theta}|\hat{Y},\mathcal{M}) = \frac{p(\hat{Y}|\vec{\theta},\mathcal{M})p(\vec{\theta}|\mathcal{M})}{p(\hat{Y}|\mathcal{M})}. \tag{5.2}$$

In this expression $\hat{Y}$ is given by equation (5.1), $\mathcal{M}$ is some pre-determined model for the SGWB, and $\vec{\theta}$ is the set of parameters upon which the model depends[1]. In words, we say the *posterior* distribution is given by the product of the *likelihood* and the *prior* and is normalized by the *marginal likelihood* (or *evidence*).

The prior contains any previously-known information we have on the parameters in the model, and the likelihood function assigns a probability for the data given some model for the SGWB. One common likelihood function, which we use throughout the rest of this chapter, is a Gaussian likelihood

$$\log p(\hat{Y}|\vec{\theta},\mathcal{M}) = -\frac{1}{2}\sum_f \frac{\left(\hat{Y}(f) - \gamma(f)\mathcal{M}(f;\vec{\theta})\right)^2}{\sigma_Y(f)^2}. \tag{5.3}$$

The Gaussian likelihood states that after subtracting the model from the data, the residual distribution should be consistent with Gaussian noise. As we discussed in chapter 2, $\hat{Y}(f)$ is averaged over many short time segments and so, in practice, it should be Gaussian distributed by virtue of the central limit theorem.

---

[1] For a power law model, for example, the parameters would be the amplitude and spectral index of the power law $\vec{\theta} = (\Omega_\alpha, \alpha)$

After choosing a likelihood and prior probability distribution for each parameter, we calculate the joint posterior distribution on $\vec{\theta}$, which makes a statement about which regions of parameter space are preferred by the data. For the purposes of parameter estimation, the marginal likelihood is a normalization factor that has no bearing on the final results. We will come back to it in the next section.

It is worth stressing again that $\hat{Y}(f)$ is the frequentist optimal estimator for the SGWB in each frequency bin, and we are performing a Bayesian analysis on that optimal estimator. This allows us to very quickly test many models without doing a fully Bayesian analysis from the start. This method should be equivalent to a fully Bayesian method, like those employed in the Pulsar timing community [180], under the assumption that the power spectral densities in the detectors are known quantities and not parameters of the model. Indeed, simulations done in [181] compare a fully Bayesian search that marginalizes over the uncertainty in the power spectral density of the detector with the traditional cross-correlation method presented in chapter 2. The two searches show comparable results when power law models are considered. An analytic comparison of the two methods can be found in [182].

5.1.2 Model Selection

Previous studies have made statements about whether one model for the data is more realistic than another using the LIGO bin-by-bin optimal estimator defined in equation (5.1). Some of those studies use the ratio of the maximum likelihood estimates between two different models [183]. In [178] they present a method for identifying alternative polarizations of GWs in LIGO measurements of the SGWB based on Bayesian model selection. It is the latter that we use as the basis for this analysis.

Presented with two different models, $\mathcal{M}_1$ and $\mathcal{M}_2$, we can make a statement about which one is preferred by the data using a ratio of the Bayesian evidences. The evidence, often called the *marginal likelihood*, is given by

$$Z_{\mathcal{M}_1} = p(\hat{Y}|\mathcal{M}_1) = \int d\vec{\theta}\, p(\hat{Y}|\mathcal{M}_1, \vec{\theta})p(\vec{\theta}|\mathcal{M}_1). \tag{5.4}$$

We also define a *Bayes factor* comparing the evidences for the two models

$$\mathcal{B}^{\mathcal{M}_1}_{\mathcal{M}_2} = \frac{Z_{\mathcal{M}_1}}{Z_{\mathcal{M}_2}}. \tag{5.5}$$

A large positive Bayes factor means that model $\mathcal{M}_1$ is preferred to model $\mathcal{M}_2$. We can also construct an odds ratio where we take into account the prior odds of one model relative to the other.

$$\mathcal{O}^{\mathcal{M}_1}_{\mathcal{M}_2} = \frac{Z_{\mathcal{M}_1}}{Z_{\mathcal{M}_2}} \frac{\pi(\mathcal{M}_1)}{\pi(\mathcal{M}_2)}. \tag{5.6}$$

If we are predisposed to believe one model over a second model, i.e. that $\pi(\mathcal{M}_1) > \pi(\mathcal{M}_2)$ then it would take more evidence in favor of the second model to convince us that it is preferred to the first.

In some cases, one model might include a signal (perhaps a power-law background for the SGWB) and the other model might be that there is no signal. Distinguishing between these two models would correspond to making a detection of a power law SGWB. We will discuss this example, and others, in section 5.3. Table 5.1 summarizes the interpretation of bayes factors comparing two models.

$\mathcal{B}^{\alpha}_{\beta}$	$\ln \mathcal{B}^{\alpha}_{\beta}$	Evidence for model $\mathcal{M}_\alpha$ relative to $\mathcal{M}_\beta$
< 1	< 0	Negative (supports model $\mathcal{M}_\beta$)
$1 - 3$	$0 - 1$	No preference
$3 - 20$	$1 - 3$	Some preference
$20 - 150$	$3 - 5$	Strong preference
> 150	> 5	Very strong preference

Table 5.1: Guidelines for the interpretation of Bayes factors that relate some model, $\mathcal{M}_\alpha$ to a different model, $\mathcal{M}_\beta$. This is modified from [118], which in turn is modified from [184].

5.2 Nested sampling for evidence estimation

Some of the examples we discuss below are low-dimensional, and in those cases a brute-force approach can be employed. In the brute-force approach, the posterior is calculated for some pre-determined set of values in the parameter space. If we choose N values to evaluate for each of the d parameters in the model, then the computational cost of this method scales as N^d. This can become prohibitively large very quickly. Therefore, it is worthwhile to also discuss MCMC methods of exploring the posterior distribution. One particularly interesting method that also estimates the evidence is known as "nested sampling."

Developed by John Skilling [185, 186], nested sampling relies upon calculation of the likelihood at n "live points." The live point with the lowest likelihood, L_{min} is replaced by drawing a new point from the prior. Associated with each new point is a width (or volume) in prior space, and the evidence is tabulated as a sum over the likelihood multiplied by that volume in prior space.

The method by which a replacement is chosen depends upon the implementation of nested sampling. Some methods, like `cpnest` [187], choose the new point by performing a Metropolis-hastings walk [188] to try to choose a point that is uncorrelated from the point it is replacing. Other methods, like `MultiNest` [189, 190, 191], draw elliptical iso-likelihood contours in the the d-dimensional likelihood space, which can allow for faster identification of a suitable new point. `MultiNest` is also capable of sampling multi-modal distributions, which it does by clustering live points together and drawing iso-likelihood contours on the separate clusters of live points.

There are many MCMC methods that do not calculate the Bayesian evidence and which are solely concerned with constructing an accurate shape of the posterior distribution of each parameter. It can be overkill to use nested samplers when only the shape of the posterior distribution is desired [192], and so in some cases (where I will explicitly mention it), I use the sampler `emcee` [165] to sample the posterior.

5.3 The `SBMS` package for SGWB inference

I have developed a code package, known as `SBMS`[2], that is built around `PyMultiNest` [193], which itself is a python interface to the `MultiNest` nested sampler [189, 190, 191]. The goal of this package is to allow users to easily estimate parameters and perform evidence calculations for a large number of different models (and combinations of models) for the

---

[2] "stochastic background model selection"

SGWB [3]. The use of a nested sampler like `MultiNest` has the distinct advantage over traditional MCMC samplers of giving a robust estimate of the model evidence, which allows model selection for models with large parameter spaces.

The package features a python application programming interface (API) that allows users to perform parameter estimation and model selection on SGWB models using real or fake LIGO SGWB data. Any model that can be used in the likelihood expression, equation (5.3), can also be used to perform software injections (in the frequency domain). There is also a command-line interface for running similar injections and recoveries based on parameter files. The package includes a set of built-in models for the SGWB, but the included set of models is not nearly a complete survey of the current literature. Therefore, it is possible to define a new model for the SGWB on-the-fly, and perform injections and recoveries with that model.

In the following section are several instructive examples where Bayesian model selection and parameter estimation are useful for understanding the SGWB and potential sources of noise. All of these examples utilize the `SBMS` code package, and code for reproducing those examples are included in the `SBMS` documentation, which is included with the code package.

In all examples below, we generate fake data in the frequency domain. We generate $\sigma_Y^2(f)$ from equation (5.1), where the noise power spectral densities, $P_1(f)$, $P_2(f)$, come from the projected Advanced LIGO design sensitivity curve [28], $T = 1$ year and $\Delta f = 0.25$ Hz in a frequency range from $10 - 100$ Hz. We then generate a realization for $Y(f)$ from this noise curve, $\sigma_Y^2(f)$, by drawing a random gaussian number of mean zero and variance $\sigma_Y(f)$ for each frequency bin. We call this $Y_{\mathcal{N}}(f)$. Finally, we generate a curve for $Y(f)$ in the frequency domain corresponding to the model we plan to inject, $Y_I(f)$, and add it to the noise realization. We then use $\hat{Y}(f) = Y_{\mathcal{N}}(f) + Y_I(f)$ as the data in our likelihood shown in equation (5.3).

Power law detection and parameter estimation

The model selection scheme can be used to discriminate between signal and noise models. A simple noise model, which we will call $\mathcal{N}$, would be that there is no SGWB, i.e.

---

[3] `git.ligo.org/patrick-meyers/sgwb_model_selection`

$\Omega_{\mathrm{GW}}(f) = 0$. Meanwhile, our power law model, $\mathcal{P}$, is given by

$$\Omega_{\mathrm{GW}}(f) = \Omega_\alpha \left(\frac{f}{f_{ref}}\right)^\alpha . \tag{5.7}$$

In this case, our detection statistic is just equation 5.5:

$$\mathcal{B}^{\mathcal{P}}_{\mathcal{N}} = \frac{Z_{\mathcal{P}}}{Z_{\mathcal{N}}} = \frac{\int d\Omega_\alpha \int d\alpha\, p(\hat{Y}|\Omega_\alpha, \alpha, \mathcal{P}) p(\Omega_\alpha, \alpha|\mathcal{P})}{p(\hat{Y}|\mathcal{N})}. \tag{5.8}$$

Using an Advanced LIGO design sensitivity curve, we can compare this detection statistic to the traditional statistic set out in equation (2.35). We do this for different values of $\Omega_{2/3}$ (i.e. the amplitude for a background with a power law index of 2/3). This plot is shown in figure 5.1 where the left axis is our Bayesian statistic and the color represents our traditional frequentist optimal signal-to-noise ratio. We see that a Bayes factor of 8 roughly corresponds to an optimal SNR of 3.

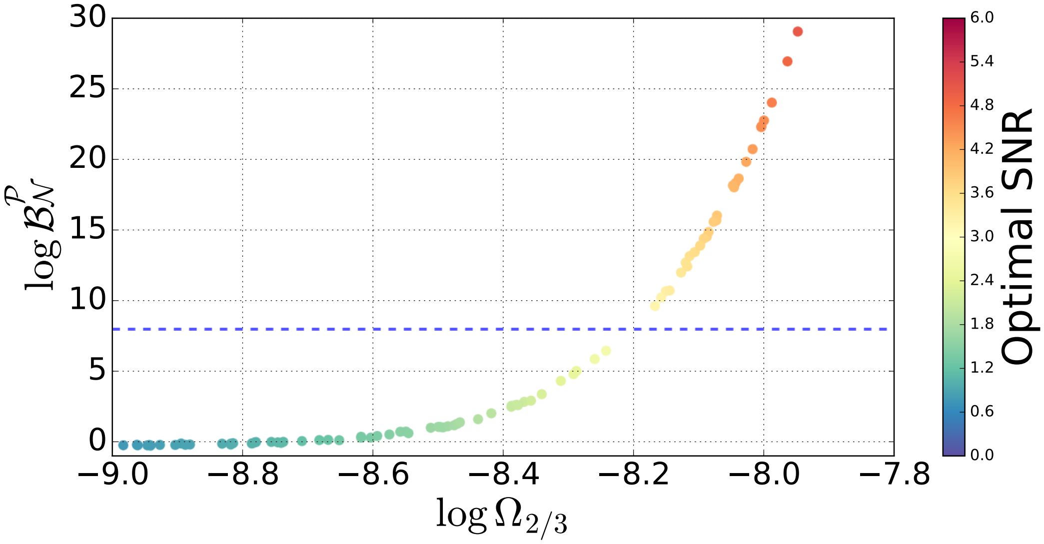

Figure 5.1: We show the correspondence between the odds ratio we have constructed and the traditional optimal SNR. We can use this odds ratio to make a statement about the presence of a stochastic GW background in the same way we can use the optimal SNR. We see that a Bayes factor of 8 corresponds roughly to an optimal SNR of 3.

We have assumed a flat prior on α, a log uniform prior on Ω_α, and that they are independent variables, so that

$$p(\Omega_\alpha, \alpha|\mathcal{P}) = \frac{1}{\Omega_\alpha} \log\left(\frac{\Omega_{max}}{\Omega_{min}}\right) \frac{1}{\alpha_{max} - \alpha_{min}} \tag{5.9}$$

on the intervals where $\alpha_{min} \leq \alpha \leq \alpha_{max}$ and $\Omega_{min} \leq \Omega_\alpha \leq \Omega_{max}$ and zero otherwise.

We can estimate the parameters in the model. In figure 5.2, we show the two-dimensional posterior distribution on Ω_α and α. We see that the two-dimensional posterior peaks at the correct values for the injected values (marked by the blue cross). We also see that the marginalized posterior for each individual parameter allows us to put error bars on our measurement of each variable.

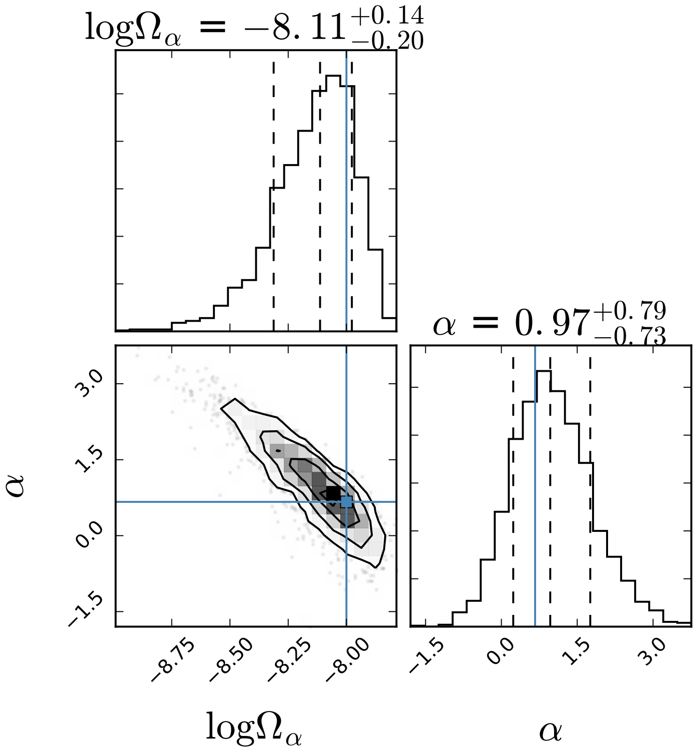

Figure 5.2: Recovery of amplitude and spectral index for power law model. Injection amplitude and spectral index are indicated with blue cross, $(\Omega_\alpha, \alpha) = (10^{-8}, 2/3)$. In this case the optimal SNR is ∼4. The vertical dashed lines indicate 16th and 84th percentiles of the posterior samples from the MCMC chains. This plot is made with the help of the `corner.py` package [194].

In this case we used only a two-dimensional model for the SGWB, and so a brute-force approach for both parameter estimation and model selection would have been feasible. However, this served as a nice example of how the code is used and how we interpret the results.

Discriminating between signal models

This method of model selection can also be used for distinguishing between two different signal models. If, for example, one wanted to determine if the data supports evidence for a "broken" power law, which changes spectral index at a specific frequency, as opposed to a single power law, then this method would be a means to do so. We again consider the case of a power law like equation (5.7), but fix the spectral index to $\alpha = 2/3$ in the recovery to imply we look specifically for an astrophysical background due to binary mergers. We will call this $\mathcal{P}_{2/3}$. We also consider a broken power law model, $\mathcal{K}$, which we write as a piecewise function:

$$\Omega_{\mathrm{GW}}(f) = \begin{cases} \Omega_\star \left(\frac{f}{f^\star}\right)^{\alpha_1} & f \le f^\star \\ \Omega_\star \left(\frac{f}{f^\star}\right)^{\alpha_2} & f > f^\star \end{cases} \tag{5.10}$$

where there are four parameters: $\Omega_\star$, $f^\star$, α_1, α_2. In this case, we fix $\alpha_1 = 2$ and $\alpha_2 = -1$, in both the injection signal and the recovery, which corresponds to a model similar to what is presented in [195].

In figure 5.3, we show different odds ratios for many injected broken power law backgrounds of increasing $\Omega_\star$ at a fixed value of $f^\star = 30$. We show that at the level where one would make a detection of an SGWB relative to noise, the $\mathcal{P}_{2/3}$ model and $\mathcal{K}$ model are essentially indistinguishable. At a value of $\Omega_\star$ about 4 times higher than what would be detectable, one can begin to distinguish between the two different signal models. Obviously, this factor depends strongly on how much the signal models look like one another and what prior information we have on the parameters beforehand. For example, more and more detections of compact mergers can restrict the prior on $\Omega_{2/3}$, which will allow us to better distinguish it from other backgrounds.

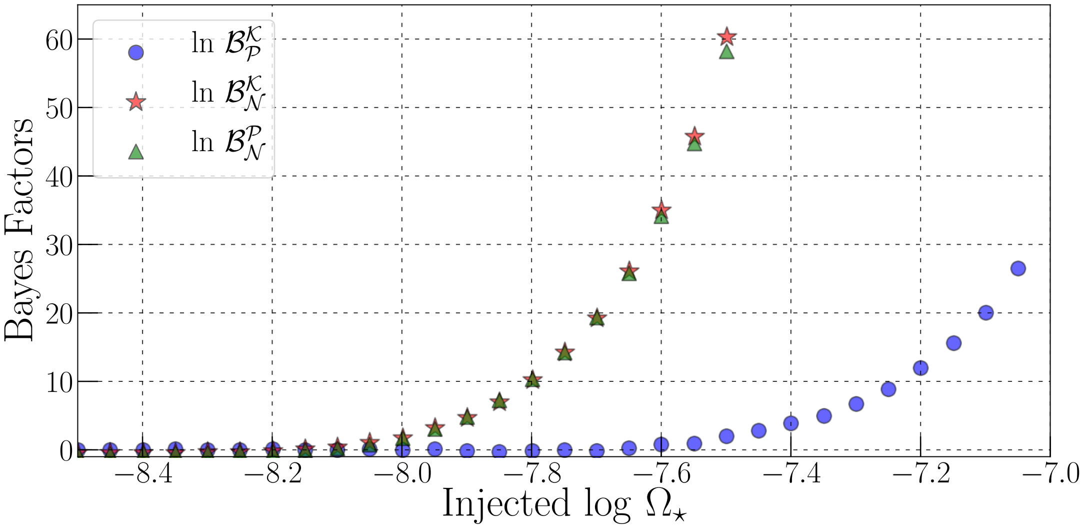

Figure 5.3: Odds ratios comparing different models as we increase the amplitude of a broken power law injection with $\alpha_1 = 2$, $\alpha_2 = -1$, $f^\star = 30$. In each case we use equal prior odds for all models. We see that using our traditional power law search we would make a GW detection at a similar time as using the correct broken power law model. At an amplitude roughly a factor four higher, we are able to make a statement about the ability to distinguish between the two models (blue points).

Budgeting

Based on current estimates of the rate of mergers of compact binary systems, we expect there to be an SGWB due to unresolved CBCs with $\Omega_{2/3} \approx 5 \times 10^{-10} - 5 \times 10^{-9}$ (where $f_{\text{ref}} = 25$ Hz). As shown in [183], the astrophysical SGWB due to CBCs is likely to be indistinguishable from a simple 2/3 power law model, and so we use the simple power law model with $\alpha = 2/3$ as a proxy for the astrophysical SGWB due to CBCs. With suitable priors based on rates and population estimates, we can attempt to simultaneously measure (or set limits on) the astrophysical CBC SGWB and a second power law background.

We injected the sum of two power laws, one at $\alpha = 3$ and the other at $\alpha = 2/3$ with many different amplitudes. We then attempted to distinguish between three different models. One model assumes just a single 2/3 power law background ($\mathcal{P}_{2/3}$), another model assumes just noise ($\mathcal{N}$), and a third includes a 2/3 power law background and a second, generic power law background $\mathcal{P}_{2/3} + \mathcal{P}_\alpha$. The results are indicated in figure 5.4, where we see results for three different odds ratios. Each plot includes contours for where the log odds ratio exceeds a factor of 8. We see especially that at low values of injected Ω_3, the simple $\mathcal{P}_{2/3}$ model is slightly preferred to the combined model. We also see that it takes an extra factor of roughly 2 in amplitude for Ω_3 before we can truly distinguish between the single-power law and the sum of two power law models.

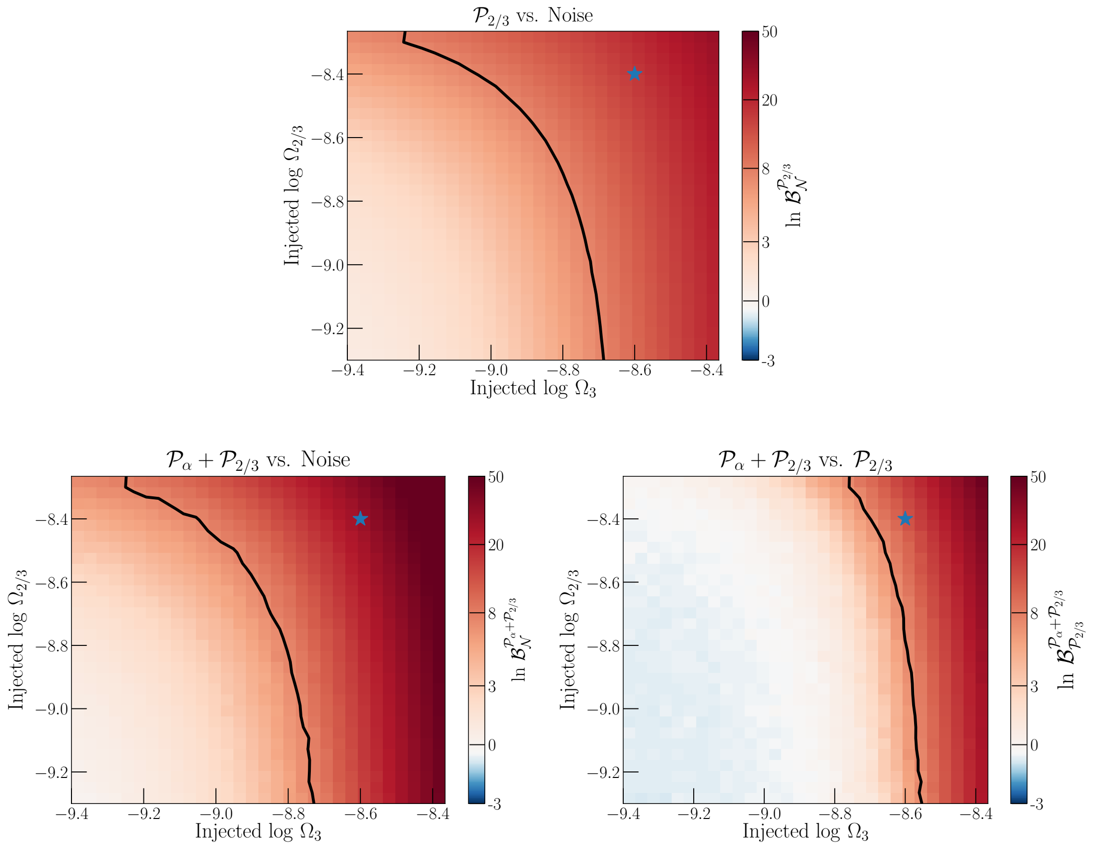
$\mathcal{P}_{2/3}$ vs. Noise

$\mathcal{P}_\alpha + \mathcal{P}_{2/3}$ vs. Noise

$\mathcal{P}_\alpha + \mathcal{P}_{2/3}$ vs. $\mathcal{P}_{2/3}$

Figure 5.4: Axes on all plots indicate injection strength for 2/3 power law (y-axis) and $\alpha = 3$ power law (x-axis). Left: odds ratios between model for a single $\alpha = 2/3$ power law and noise. Center: odd ratios between model consisting of two power law spectra, $\mathcal{P}_{2/3} + \mathcal{P}_\alpha$, and a model consistent with noise. Right: odds ratio between two-spectrum model and one-spectrum model. Injection amplitudes for the $\alpha = 2/3$ models are drawn from the uncertainty band shown in [28] and we have used a LIGO design sensitivity curve and 1 year of integration time. The black contours indicate lines where log $\mathcal{B}$ are 8. We see that, in general at $\Omega_3 = 2.5 \times 10^{-9}$, we should be able to separate this background from the estimated background due to unresolved BNS and BBH events.

We would like to understand how well we can estimate the individual amplitudes of these two models once we have established that both are present. The blue star on the plots in figure 5.4 indicate the injection strengths for the two models whose parameters we attempt to recover in figure 5.5. In figure 5.5 we show the parameter estimation results for 1 (black dashed), 5 (purple solid), and 10 (dash-dotted red) year integration times. We see that the variable power law is generally well-recovered, but it takes a much longer period of time to resolve the amplitude of the 2/3 power law background reliably.

5.4 SGWB detection and parameter estimation with correlated magnetic noise

5.4.1 Correlated magnetic noise model

One issue that could hinder the detection of an SGWB is low frequency, correlated magnetic noise. This was discussed in section 4.3.4 and has also been discussed in the literature [52, 53]. Methods discussed in the literature for dealing with correlated noise often focus on Wiener filtering or creating a magnetic noise budget at low frequencies [52, 53, 1]. Here, we consider a model that depends upon the coupling of magnetic fields into the detectors, $T_i(f)$, and the correlated magnetic spectrum $M(f)$ (in units of $\mathrm{pT^2Hz^{-1}}$ now because of the definition of $T(f)$ below) the same as used in the budget discussed in section 4.3.4. In principle, $M(f)$ can be measured by magnetometers near the detectors, and $T_i(f)$ can be measured using magnetic injections around the sites [53]. Any estimates of the transfer functions made using injections will likely be very uncertain, and so we can also allow for some parameters characterizing its functional form to vary. The model is defined in terms of these quantities

$$\mathcal{M}(f;\vec{\theta}) = \frac{10\pi^2}{3H_0^2} f^3 \mathrm{Re}\left[T_1^*(f;\vec{\theta})T_2(f;\vec{\theta})M(f)\right]. \tag{5.11}$$

When we run the stochastic isotropic search on real data we break our analysis into 60 s time segments and then we optimally combine those time segments using equation (2.38). Therefore, we calculate $M(f)$ in a similar fashion. We calculate $M_i(f)$ for each time segment i of the analysis and we combine those segments using the same

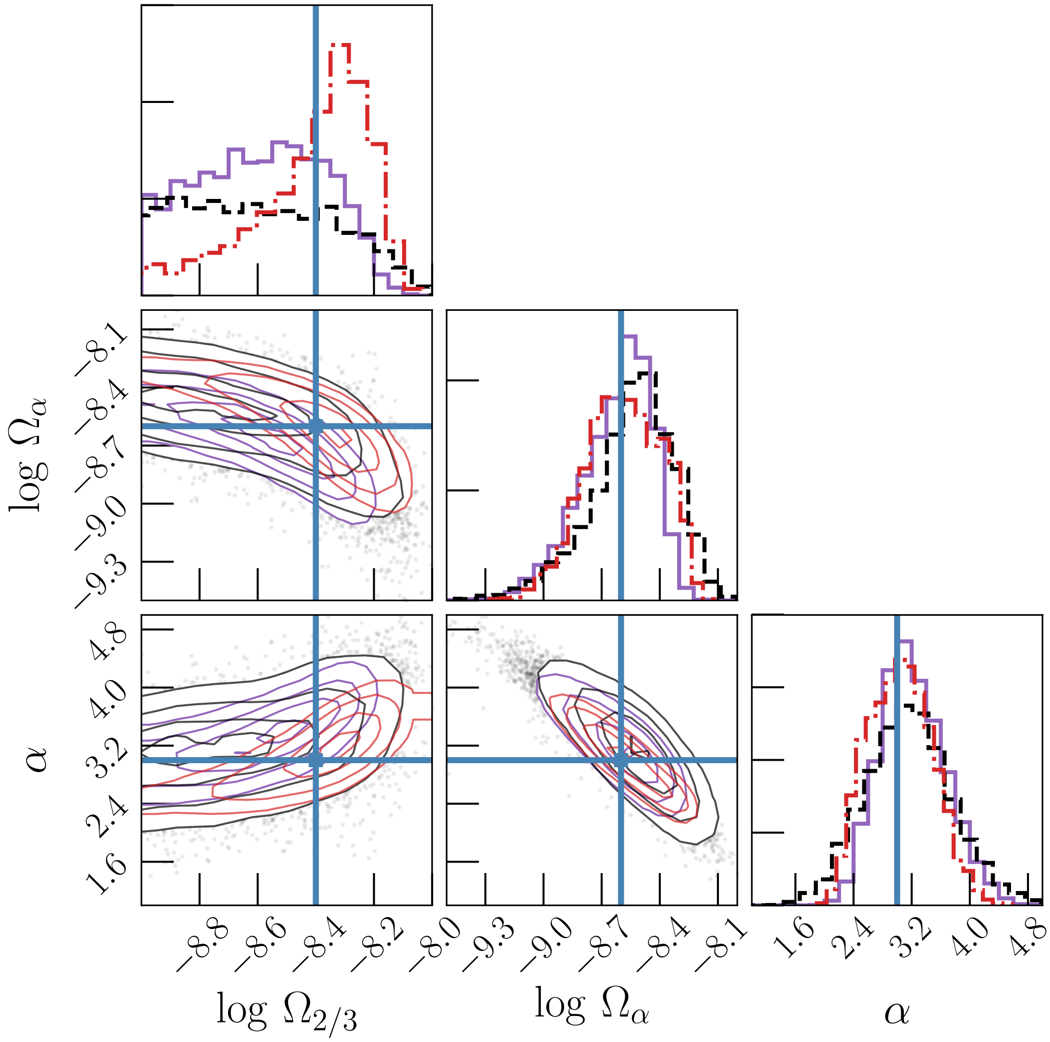

Figure 5.5: Parameter estimation results for the sum of two power laws. We show the parameter estimation results for 1 (black dashed), 5 (purple solid), and 10 (dash-dotted red) year integration times for Advanced LIGO at design sensitivity. We see that the variable power law is generally well-recovered, but it takes a much longer period of time to resolve the amplitude of the 2/3 power law background reliably.

weights used for the stochastic isotropic optimal combination. That is, in the end, we use:

$$M(f) = \frac{\sum_i M_i(f)\sigma_{Y,i}^{-2}(f)}{\sum_i \sigma_{Y,i}^{-2}(f)} \tag{5.12}$$

where $\sigma_{Y,i}$ is the uncertainty on the optimal estimator $\hat{Y}$ for time segment i.

5.4.2 Correlated magnetic noise simulation scheme

We simulate correlated magnetic noise between the Hanford and Livingston detectors using real magnetometer data from the LEMI magnetometers located at each site[4]. The simulation is performed separately for the two data streams. For each data stream we simulate, we take a fast Fourier transform of the data from the local LEMI magnetometer, apply a transfer function in the frequency domain, and take an inverse Fourier transform. We then add this to Gaussian interferometer data simulated using a LIGO design sensitivity curve [146] using the `lalsimulation` package [5]. For simplicity, the functional form of the transfer function is taken to be a power law in all simulations discussed below, and the parameters for that power law are assumed to be the same at both interferometers. While we showed in section 4.3.2 that this is not the exact case we have in our instruments, it is a simple starting point. We consider two parameters, κ and β, which characterize that power law

$$T(f;\vec{\theta}) = \kappa \times 10^{-23}\left(\frac{f}{10\text{ Hz}}\right)^{-\beta}\frac{\text{strain}}{\text{pT}}. \tag{5.13}$$

This expression is consistent with the convention used in [53]. We create injection sets that are three days long, with transfer functions that are larger than is realisitic ($\kappa \approx 0.1$ was the estimate at Livingston presented in chapter 4, for example). This is done to reduce the time it takes to perform the simulations. The results should generalize to longer time scales and smaller coupling functions, but this is something we plan to test explicitly in the future.

Once we have created the timeseries data with correlated noise, we run the full stochastic isotropic search pipeline on a subset of the data to generate $\hat{Y}(f)$ and $\sigma_Y^2(f)$.

---

[4] details on these magnetometers are discussed in chapter 4

[5] `https://wiki.ligo.org/DASWG/LALSuite`

We do this with 60 s time segments and 0.25 Hz frequency bins in a frequency band from $10-128$ Hz[6]. We then determine at what level one could detect a power law background with $\alpha = 2/3$ for different models in the presence of magnetic noise. We do this by injecting, in the frequency domain, sucessively stronger power law backgrounds and running the full parameter estimation and model selection pipeline for several different models. The models considered are summarized in table 5.2. We then construct odds ratios corresponding to several different detection schemes using the results of those individual models and find at what injection level those odds ratios are greater than eight. The detection schemes considered include the odds ratios discussed in the next subsection. We then repeat this process for successively longer subsets of the data. This allows us to look at how the sensitivity to $\Omega_{2/3}$ scales as a function of time in the context of realistic magnetic noise for our different detection methods.

We also save the median, fifth, and ninety-fifth percentile estimates for each model parameter in each model considered in table 5.2. This is done for each power law injection and for each subset of data over which we run, which allows us to look at how the estimate of those parameters scales with time.

Name	Model	parameters
$\mathcal{M}$	only correlated magnetic noise	κ, β
$\mathcal{M}+\mathcal{P}_{2/3}$	correlated magnetic noise and GWs with a 2/3 power law	κ, β, $\Omega_{2/3}$
$\mathcal{N}$	Uncorrelated Gaussian noise	none
$\mathcal{P}$	GWs with a 2/3 background	Ω_α, α

Table 5.2: Models used in parameter estimation and model selection on magnetic noise simulations.

Below, we present odds ratios we will use for interpreting our results, followed by results for several different simulations with different levels of correlated magnetic noise that show the power of this method. In each case, we assume that transfer functions at the two sites that are constant in time and have the same power law parameters at both sites. While it will be imperative to relax these assumptions in the future, for now

---

[6] There are frequency notches around the power mains (2 Hz on either side) and at 20 Hz, where there is a large site-wide magnetic field at the Livingston detector.

it is easier to consider simple situations.

Odds ratios

We define three odds ratios that will help us understand the effect of correlated magnetic noise on our search. The first is between a typical power law model and a model for generic Gaussian noise, $\mathcal{B}^{\mathcal{P}}_{\mathcal{N}}$ (this is comparable to maximizing the optimal SNR, defined in equation (2.35), over power-law spectral index). The second odds ratio is used to discriminate between magnetic noise plus a 2/3 power law and just magnetic noise, $\mathcal{B}^{\mathcal{M}+\mathcal{P}_{2/3}}_{\mathcal{M}}$. In the case where there is no magnetic noise, this should reduce to the case where we compare a 2/3 power-law to generic Gaussian noise [7], and we will consider this our proxy for detecting GWs consistent with a 2/3 power law SGWB in the context of magnetic noise. The third odds ratio is defined to compare our model for magnetic noise plus a 2/3 power law to a generic power law, $\mathcal{B}^{\mathcal{M}+\mathcal{P}_{2/3}}_{\mathcal{P}}$. As we show in the simulation section below, this is included to help justify using the full magnetic model defined in equation (5.11) as opposed to a simple, generic power law model with a steep spectral index to account for magnetic noise. It can also help prove to us that there is correlated magnetic noise contributing to the measured spectrum. In summary, the three odds ratios are

$$\mathcal{B}^{\mathcal{P}}_{\mathcal{N}} = \frac{Z_{\mathcal{P}}}{Z_{\mathcal{N}}} \tag{5.14}$$

$$\mathcal{B}^{\mathcal{M}+\mathcal{P}_{2/3}}_{\mathcal{M}} = \frac{Z_{\mathcal{M}+\mathcal{P}_{2/3}}}{Z_{\mathcal{M}}} \tag{5.15}$$

$$\mathcal{B}^{\mathcal{M}+\mathcal{P}_{2/3}}_{\mathcal{P}} = \frac{Z_{\mathcal{M}+\mathcal{P}_{2/3}}}{Z_{\mathcal{P}}} \tag{5.16}$$

where Z indicates the model evidence for the model specified in the subscript. While this is certainly not the only choice for such odds ratios, they are well-motivated choices that should, when considered together, give a clear picture of what signal models are supported by the data.

---

[7] This statement assumes that κ=0 is included in the prior on κ. If it is not then the model will include a magnetic contribution where there should not be one, and this limiting case will not hold.

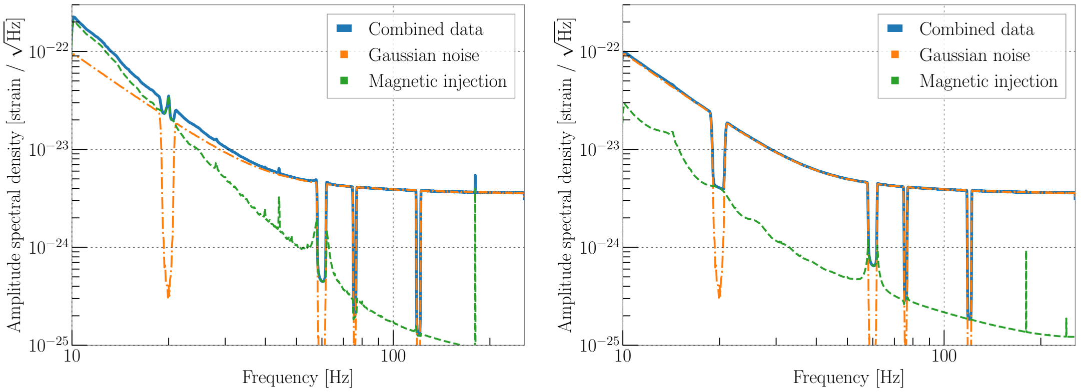

Figure 5.6: Amplitude spectral density of Gaussian detector noise (orange, dashed), simulated magnetic noise (green, dashed-dotted), and the final combination of the two (blue, solid) for Livingston (left) and Hanford (right). We see that at low frequencies at Livingston the spectrum is dominated by magnetic noise. The difference between the two is due to the differing levels of ambient magnetic noise picked up by the magnetometers used for the two separate injections. The large dips are due to a high-pass filter, a notch around 20 Hz (due to a large site-wide magnetic field at Livingston), and a notch around 60 Hz power mains.

Constant transfer function, $\kappa = 6$, $\beta = 3$

We use parameters of $\kappa = 6$ and $\beta = 3$ for the transfer function for both detectors. The choice of κ to be large compared to the measurements discussed in chapter 4 means that we can generate a shorter data set and still observe the tangible effects of real magnetic noise on our simulations. In this case, the magnetic noise is so large that it is comparable to the simulated Gaussian detector noise. The ratio between these contributions is shown in figure 5.6.

A plot of how the detection statistic, $\mathcal{B}_{\mathcal{M}}^{\mathcal{M}+\mathcal{P}_{2/3}}$, scales with time for the magnetic injection with transfer function parameters of $\kappa = 6$ and $\beta = 3$ and an injected 2/3 power law SGWB injection of amplitude $\Omega_{2/3} = 2 \times 10^{-8}$ is shown in the left hand side of figure 5.7. The right hand side of figure 5.7 shows how a simple power law search, using the $\mathcal{B}_{\mathcal{N}}^{\mathcal{P}}$ could be tricked by magnetic noise even when there are no GWs present, along with proof that our model for the magnetic noise is preferred to the simple power law model. This tells us that 1. When magnetic noise is present, our searches could be tricked into thinking there are GWs when there are not and 2. using the cross-power of the magnetometer spectra seems to work better for fitting the magnetic noise than a simple power law would.

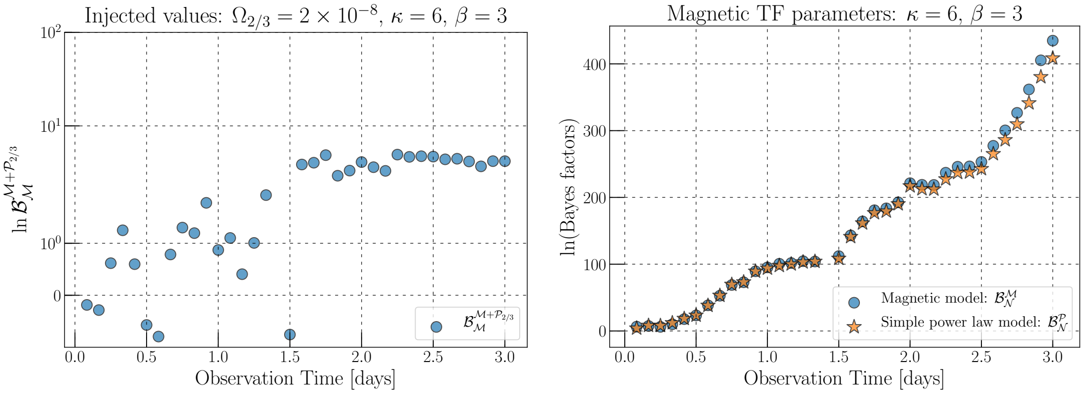

Figure 5.7: Left: A plot of the proxy detection statistic as a function of time for an isotropic 2/3 power law SGWB injection at a level of $\Omega_{2/3} = 2 \times 10^{-8}$. Right: a comparison of our model for magnetic noise to a simple variable power law model when there is no injected SGWB present. We see that using the magnetometer spectrum, $M(f)$, to model the correlated magnetic noise does a better job than if we were to use a simple, strongly negative, power law to fit the magnetic noise.

In figures 5.8 and 5.9 we show how the parameter estimation results for the same medium-strength SGWB injection shown in figure 5.7 change as a function of integration time for the $\mathcal{M} + \mathcal{P}_{2/3}$ model and for the $\mathcal{P}$ models respectively. We see that there is clear bias in the upper limits and recoveries for the $\mathcal{P}$ model, and the spectral index is very low. For the $\mathcal{M} + \mathcal{P}_{2/3}$ model, the $\Omega_{2/3}$ recovery is fairly robust. There does appear be some bias in the parameter estimation recovery for $\Omega_{2/3}$. This is something we are still investigating.

We can also look at how our sensitivity to a SGWB with a 2/3 power law scales with time for the $\mathcal{B}_{\mathcal{M}}^{\mathcal{M}+\mathcal{P}_{2/3}}$ odds ratio considered in section 5.4.2. In this case, we use the method discussed in the previous section for estimating our sensitivity as a function of time. For each subset of the data, we make eighty logarithmically spaced injections of a 2/3 power law SGWB in the range $10^{-9} - 10^{-5}$. We find at which injection the odds ratio of interest exceeds a value of eight or higher. A plot of that sensitivity as a

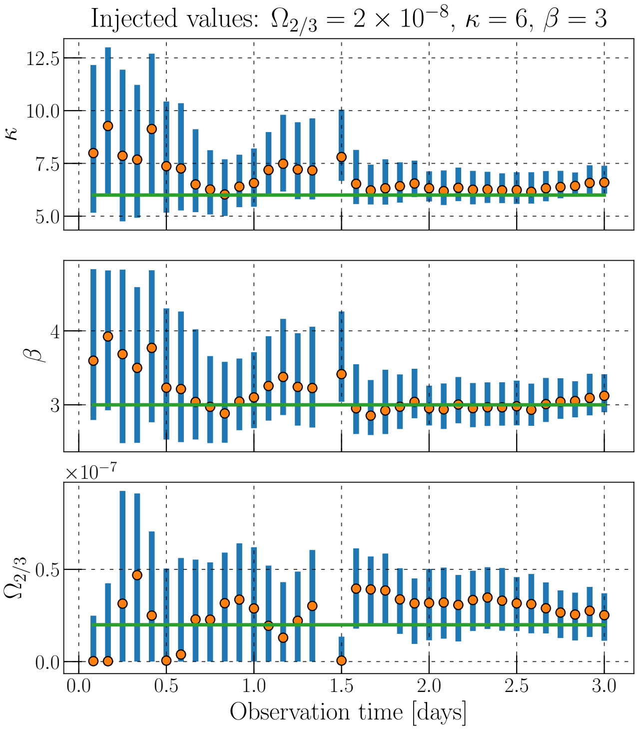

Figure 5.8: Parameter estimation results for $\mathcal{M} + \mathcal{P}_{2/3}$ model for medium strength magnetic injection plus a 2/3 power law injection of amplitude $\Omega_{2/3} = 2 \times 10^{-8}$, which is the same as in figure 5.7. The orange dots indicate the median of the equal weighted posterior samples from the nested sampling. The blue vertical bars indicate the 5th and 95th percentiles of those same samples. The green horizontal line indicates the true injected value. We see that around the time the background becomes detectable the parameter estimation on $\Omega_{2/3}$ also becomes very well constrained. There does appear to be a bias in the recovery of the κ and β parameters. The parameter estimation converges to $\kappa \approx 5.3$ and $\beta \approx 2.6$, as opposed to the true values of 6 and 3 respectively. Likewise, there is a systematic bias in the recovery of $\Omega_{2/3}$ that is a factor of ≈ 2 too large.

function of time for $\mathcal{B}_{\mathcal{M}}^{\mathcal{M}+\mathcal{P}_{2/3}}$ is shown in figure 5.10.

Bias in the results

There is a bias of 10^{-8} in the parameter estimation results for $\Omega_{2/3}$. This bias appears whether or not we perform an SGWB injection. In figure 5.11 we show that this bias

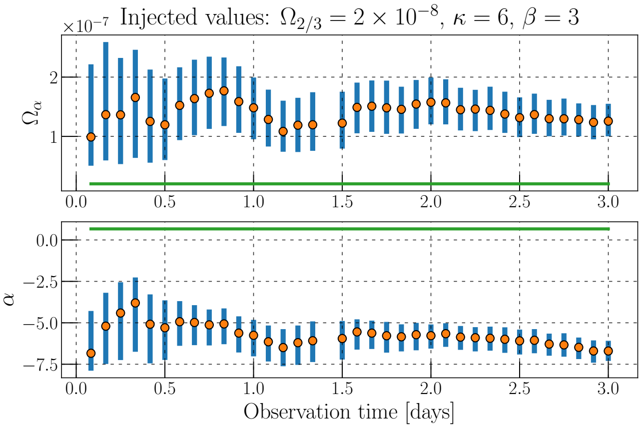

Figure 5.9: Parameter estimation results for $\mathcal{P}$ model for a medium strength magnetic injection plus a 2/3 power law injection of amplitude $\Omega_{2/3} = 2 \times 10^{-8}$, which is the same as in figure 5.7. The orange dots indicate the median of the equal weighted posterior samples from the nested sampling. The blue vertical bars indicate the 5th and 95th percentiles of those same samples. The green horizontal line indicates the true injected value. We see a clear bias in the recovery. The parameter estimation picks up only the magnetic noise in this case, preferring a strong negative power law spectral index.

appears in the parameter estimation recovery of $\Omega_{2/3}$ as we integrate over time for an injection of strength $\Omega_{2/3} = 10^{-7}$. The green line shows the nominal injection strength, while the red-dotted line shows the injection plus the extra bias factor. In figure 5.12 we show that this bias appears when we do not perform an SGWB injection. In this case the injection is at $\Omega_{2/3} = 2 \times 10^{-12}$, but we see a recovery peaked near 10^{-8}.

The source of the bias is unknown at this point. It does not occur when we inject no correlated magnetic noise, but it does occur for the louder injection of $\kappa = 6$ as well as a quieter injection at $\kappa = 2$. One potential cause could be poor magnetometer data quality. Figure 5.7 indicates that around 1.5 days into the simulation there is a sharp change in the way we recover our transfer function parameters, which could indicate a change in the data quality in the magnetometers that significantly affects $M(f)$, but has less impact on $\hat{Y}$ and σ_Y because of the presence of the injected Gaussian noise.

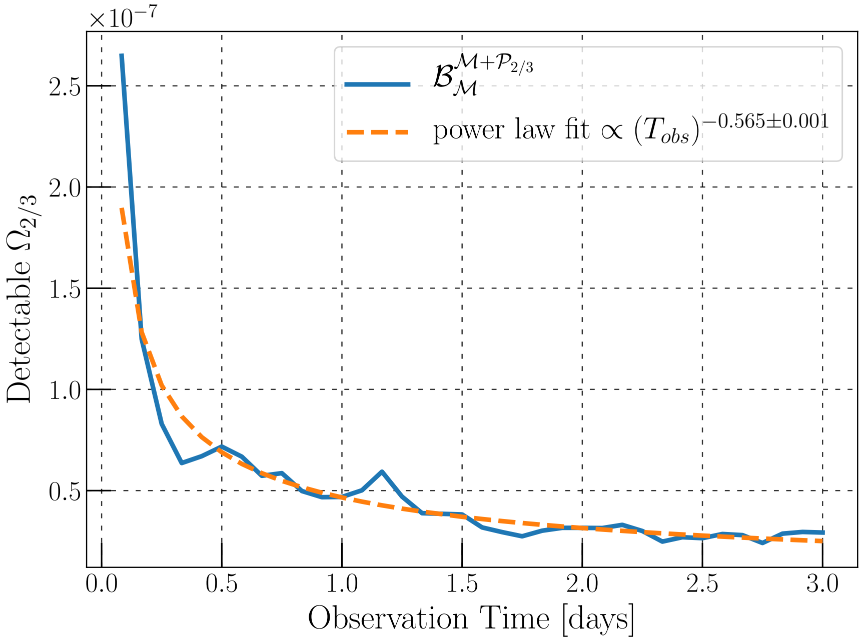

Figure 5.10: The detectable $\Omega_{2/3}$ background as a function of time using our odds ratio $\mathcal{B}_{\mathcal{M}}^{\mathcal{M}+\mathcal{P}_{2/3}}$. We have also included a power law fit to the blue curve. One would expect this curve to scale roughly as $T_{obs}^{-1/2}$ if we had only Gaussian noise.

Comparison of results

When we compare how the detectable level of $\Omega_{2/3}$ scales with time for several different correlated magnetic noise injections, we find that the $\kappa = 6$ and $\kappa = 2$ injections appear to be better than $\kappa = 0$. However, once we account for the bias discussed in the previous section we find that the three injections are comparable. This is shown in figure 5.13. On the left is the uncorrected sensitivity and on the right is the corrected sensitivity.

The cases we have considered are representative of the true situation, but are certainly simplistic. In the future we will need to look at how the model can be extended if there is a time-varying transfer function, how to account for a different transfer function at the two sites, how to account for a transfer function that is described by something different from a simple power law. In many cases, we will have coupling measurements to guide us. In addition, the current methodology does not include uncertainty in the

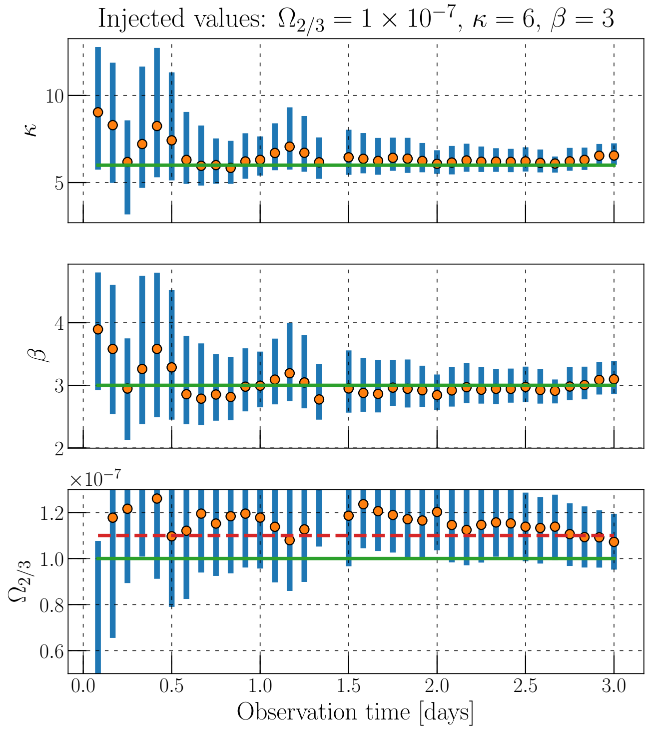

Figure 5.11: Recovery of a $\kappa = 6$ correlated magnetic noise injection with an $\Omega_{2/3} = 10^{-7}$ isotropic SGWB injection showing an obvious bias in the recovery. The red line indicates $\Omega_{2/3} = 1.1 \times 10^{-8}$, while the green line shows in the originally injected value of 10^{-7}. This bias is more evident in figure 5.12, where there is no SGWB injection made at all.

measurement of the correlated magnetic spectrum, $M(f)$. This will need to be included, and one way to do so could be by measuring the mean and variance of the correlated spectrum, $\bar{M}(f)$ and $\sigma_M(f)$, and then treating it with a Gaussian prior, such that

$$\ln p(M(f)|\bar{M}(f), \sigma_M(f)) = -\frac{1}{2}\left(\frac{M(f) - \bar{M}(f)}{\sigma_M(f)}\right)^2 . \tag{5.17}$$

Marginalizing over the parameter $M(f)$ in our likelihood shown in equation (5.3) would then yield a new likelihood that accounts for the variance of the correlated magnetic noise spectrum. In contrast, our current prior is effectively a delta function, where $p(M(f)) \propto \delta(M(f) - \bar{M}(f))$ where $\bar{M}(f)$ is the time-averaged correlated spectrum we have measured with our magnetometers.

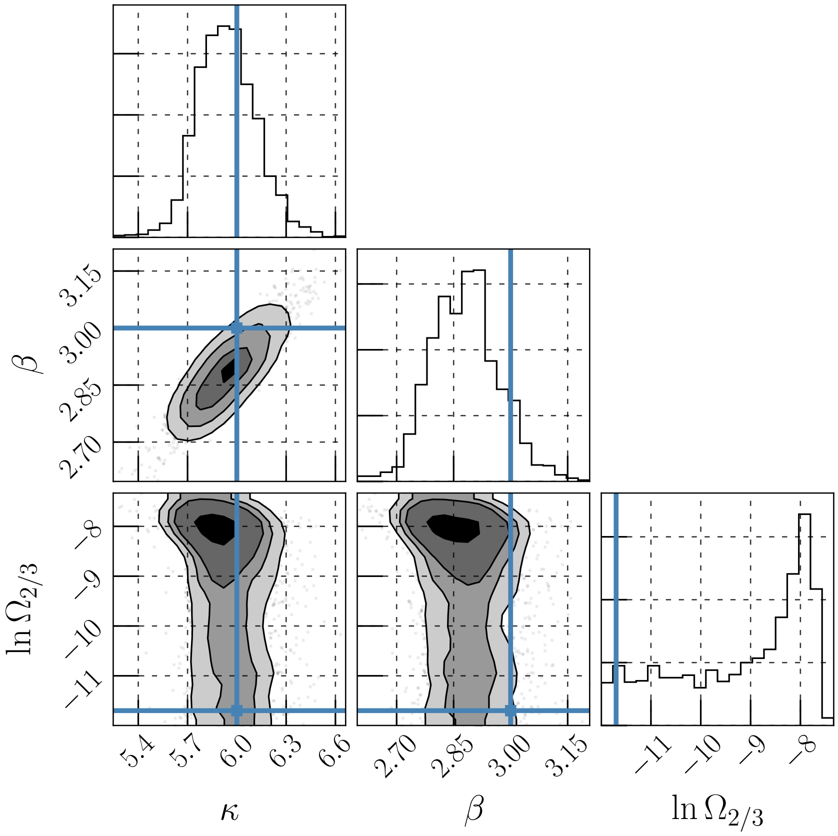

Figure 5.12: Parameter estimation results for a correlated magnetic noise injection of $\kappa = 6$ and $\beta = 3$ with 3 days of integration time. The SGWB injection is at an undetectable level, but the posterior distribution on $\Omega_{2/3}$ still peaks near 10^{-8}. The source of this bias is still unknown.

5.5 Conclusions and future work

In this chapter we have discussed a framework for performing parameter estimation and model selection on the stochastic gravitational-wave background. We introduced a new code package that can be used to compare and combine different SGWB models and run a nested sampling algorithm to compare those models and estimate their parameters.

In the latter half of the chapter we applied this framework to the case where we attempt to measure an SGWB when there is correlated magnetic noise present. We

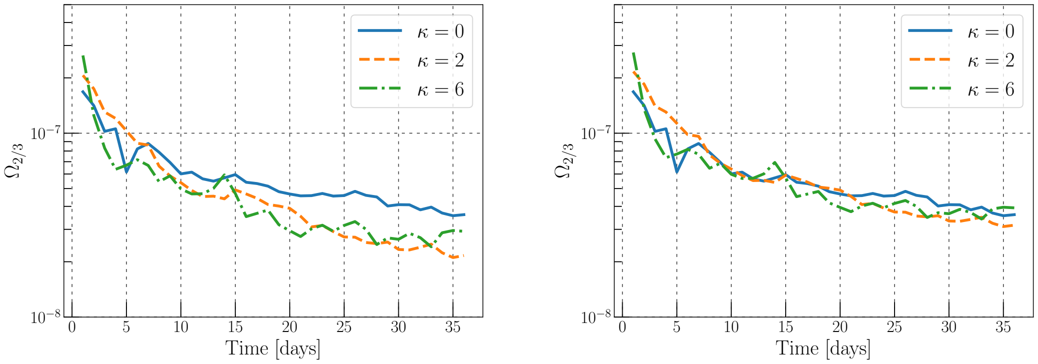

Figure 5.13: Sensitivity as a function of time for three different magnetic noise injections. The left-hand plot does not account for the bias shown in figure 5.12, while the right-hand plot corrects this bias by adding 10^{-8} to sensitivity of both the $\kappa = 2$ and $\kappa = 6$ ($\beta = 3$ in both cases) correlated magnetic noise injections, which were the two injection sets that observed the bias.

have done this by using magnetometers that witness the correlated noise to generate a model that we then apply to our data. The method was tested by injecting real magnetic noise into Gaussian interferometer data at varying levels, and then attempting to simultaneously extract information about the magnetic noise and a potential SGWB signal. While the results are promising, there is still a bias whose source we do not understand. However, when accounting for the bias, it appears that the detectable amplitude of $\Omega_{2/3}$ is independent of the level of magnetic noise that has been injected. We eventually hope to compare this to other methods, like Wiener filtering.

Chapter 6

Seismic and Newtonian noise in the Homestake mine

6.1 Seismic and Newtonian noise in GW Interferometers

The LIGO test masses are susceptible to residual ground motion below 10 Hz. At these frequencies, ground motion can be as high as $\sim 10^{-9}$ m/$\sqrt{\text{Hz}}$, which is ten orders of magnitude larger than Advanced LIGO's goal in that frequency range [33]. The test masses benefit from passive isolation from the quadruple pendulum suspension, which gives $1/f^8$ suppression above the resonant frequency of the pendulums, which is as low as 0.4 Hz [7]. Feed-forward schemes using seismometers on the ground and inertial sensors and actuators on the suspension platforms are also employed to reduce seismic noise [37]. This isolation is useful not just for increasing strain sensitivity but also for bringing the interferometer into the linear regime and keeping it there. This means it takes less time to lock the instrument and the overall duty cycle is greatly improved.

Seismic waves cause the ground motion discussed above, but they are also responsible for Newtonian noise, which is the fluctuation in the gravitational field due to density changes in the earth (i.e. seismic waves) and the atmosphere. As better passive and active isolation systems become available, and noise is reduced in the LIGO optical angular control systems, Newtonian noise will become a limiting noise source for GW interferometers [48]. The dominant source of Newtonian noise is likely to be from surface seismic waves and from atmospheric density fluctuations [48]. In the rest of this section, I'll briefly discuss the basic mathematical formalism of seismic waves, how they create Newtonian noise, and how that noise couples into GW interferometers.

6.1.1 Seismic waves

Introduction and body waves

An intuitive understanding of seismic waves can be quickly understood from basic physics. We'll follow the introductory seismology discussion presented in [196]. In analogy with $F = ma$ we can write down the equation of motion for a continuum

$$f_i + \partial_j \tau_{ij} = \rho \frac{\partial^2 u_i}{\partial t^2} \tag{6.1}$$

where the first term of the left hand side is a "body force" term (which we will ignore for the rest of this introduction), and the next term is the stress tensor, which is a 3×3 matrix that gives the force per unit area in the j direction on the face of an infinitesimal cube with a normal vector pointing in the i direction. The right hand side is the mass density, ρ, multiplied by the second time derivative of the displacement field, which is the displacement of a point particle from its equilibrium position. We can couple this with a linear stress-strain relationship, which expresses how applying a stress to one face of an infinitesimal cube causes a change in the size and shape of the cube

$$\begin{aligned} \tau_{ij} &= \lambda \delta_{ij} e_{kk} + 2\mu e_{ij} \\ \tau_{ij} &= \lambda \delta_{ij} \partial_k u_k + \mu(\partial_i u_j + \partial_j u_i). \end{aligned} \tag{6.2}$$

In the second line we have substituted in for the strain tensor $e_{ij} = \frac{1}{2}(\partial_i u_j + \partial_j u_i)$ in terms of the displacement field. λ and μ are known as the Lamé parameters and are related to the more commonly discussed shear and bulk moduli. It is common practice to define the displacement field in terms of a scalar and a vector potential, ϕ and $\vec{\psi}$ (where $\nabla \cdot \vec{\psi} = 0$), such that $\vec{u} = \nabla\phi + \nabla \times \vec{\psi}$. Combining this with equations (6.1) and (6.2) yields two wave equations

$$\nabla^2\phi = \frac{1}{\alpha^2}\frac{\partial^2\phi}{\partial_t^2} \tag{6.3}$$

$$\nabla^2\vec{\psi} = \frac{1}{\beta^2}\frac{\partial^2\vec{\psi}}{\partial t^2}. \tag{6.4}$$

This tells us that we expect to have two types of waves in a continuous medium, the first, associated with ϕ, we call P-waves (for *primary* because they move faster) and the second we call S-waves. P and S-waves are often referred to as *body waves* because they travel within the body of the medium. The velocity of P and S-waves are given by

$$\alpha = \sqrt{\frac{\lambda + 2\mu}{\rho}}$$

$$\beta = \sqrt{\frac{\mu}{\rho}}. \tag{6.5}$$

Consider a plane-wave propagating through our homogeneous continuum, $\vec{u}(\vec{x}, t) = \vec{A}(\omega)e^{-i(\omega t - \vec{k}\cdot\vec{x})}$. If we take P-waves propagating in the x direction we can use equation (6.3) to say that $\alpha^2\partial_x^2\phi = \partial_t^2\phi$. The general solution to this expression is $\phi = \phi_0(t \pm x/\alpha)$. Therefore, it follows from the definition of the potential that only u_x survives

$$u_x = \partial_x\phi. \tag{6.6}$$

A similar exercise for S-waves tells us that $\vec{u} = \partial_x\psi_z\hat{y} - \partial_x\psi_y\hat{z}$, which is a transverse wave. There are two distinct polarizations. The first is motion parallel to the surface and perpendicular to the direction of motion, which we call S$_h$ waves. The second is motion perpendicular to both the direction of motion and S$_h$ waves. We call these S$_v$ waves.

Surface waves

Surface waves are solutions to the continuum equation of motion when there is a free surface. There are two types of surface waves: *Rayleigh* waves (R-waves) and *Love* waves (L-waves). R-waves are radially and vertically polarized and exist at any free surface, whereas L-waves require some depth-dependence of the velocity. Because surface waves travel along the surface, as the waves travel away from the source, their amplitude falls off slower than body waves. Therefore, when looking at the waveform for an earthquake the amplitude of surface waves is often much larger than that of the earlier-arriving P and S-waves.

Love waves come from constructive interference of S_h waves that reflect off of the surface boundary. If the velocity increases with depth then the waves refract, turn back to the surface, reflect off of the surface again and can repeat the process many times. The travel time between successive reflections off of the surface is different from the travel time along the ray path, and so constructive interference between multiply reflected S_h waves can only occur at certain frequencies [196]. Because Love waves are made up of the constructive interference of S_h waves, they induce displacement only in the direction perpendicular to their horizontal motion and parallel to the ground-surface interface. A visualization of the particle displacement due to Love waves can be found in figure 6.1.

Rayleigh waves are the result of interference between S_v-waves and P-waves at a surface-ground interface. A mathematical treatment [197, 196] involves setting the normal and shear stresses to zero at the surface, which results in a set of coupled linear equations, one solution of which is an evanescent wave that travels along the surface and whose amplitude decays with depth. The displacement field of R-waves is confined to the vertical-radial plane and a $\pi/2$ phase difference between the vertical and radial displacements results in the characteristic retrograde (on the surface) particle motion. That means we can write down the displacement field due to a single R-wave traveling in the $\hat{k}$ direction

$$\vec{u}(\vec{r},t) = r_H(k,z)\cos(2\pi f t - \vec{k}\cdot\vec{x})\hat{k} + r_V(k,z)\sin(2\pi f t - \vec{k}\cdot\vec{x})\hat{z}. \tag{6.7}$$

In this case the two functions r_H and r_V are the fundamental Rayleigh wave eigenfunctions, and they determine how the amplitude in the radial and vertical directions change with depth. In the case of a homogeneous half-space these functions have analytic solutions, which are shown in figure 6.2 for different values of Poisson's ratio[1]. At depth the phase difference between the vertical and radial directions can flip sign and the particle motion can change to prograde motion (something evident in the measurements shown

---

[1] Poisson's ratio is the ratio of the lateral contraction of a cylinder to its longitudinal extension [196]. It can be defined in terms of the Lamé parameters: $\nu = \frac{\lambda}{2(\lambda+\mu)}$

in section 6.3), which corresponds to r_H changing sign. In a homogeneous medium, R-waves do not exhibit dispersion, but in the presence of a vertical velocity gradient it can occur. In fact, vertical S-wave velocity gradients can be used to estimate R-wave eigenfunctions and dispersion curves [198], and we will compare explicit measurements of the R-wave eigenfunctions to those estimates in section 6.3.

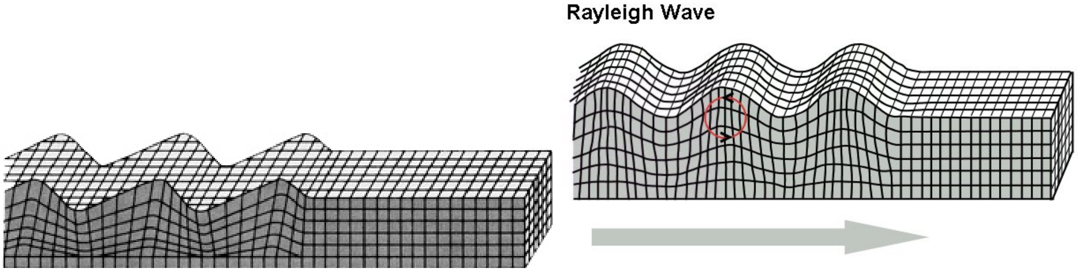

Figure 6.1: Left: a visualization for the particle displacement due to a passing Love wave. Right: the same for a Rayleigh wave. These plots are from [199] and [200].

6.1.2 Newtonian noise due to seismic waves

For this discussion, we'll follow [48]. While seismic waves cause noise in GW interferometers by disturbing the ground and thus the test masses, they also cause density perturbations that result in changes to the local gravitational field. Here, I will talk briefly about how those density changes can cause noise in a GW interferometer. Later, I will extend this to the specific case of Rayleigh waves.

We start our calculation by writing down a continuity equation in terms of local density perturbations

$$\delta\rho(\vec{r},t) = -\nabla \cdot (\rho(\vec{r})\vec{u}(\vec{r},t)). \tag{6.8}$$

We can then write down the gravitational field due to these density perturbations and

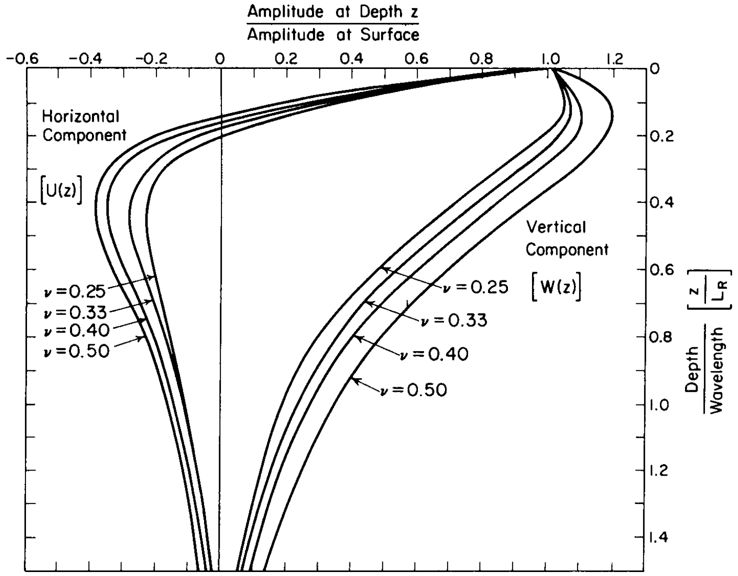

Figure 6.2: Theoretical depth dependence of Rayleigh waves for several different values of Poisson's ratio. Note that the relative sign between the vertical and horizontal curves flips. Figure is from [201].

make a substitution

$$\begin{aligned} \delta\phi(\vec{r}_0,t) &= -G\int dV\,\frac{\delta\rho(\vec{r},t)}{|\vec{r}-\vec{r}_0|} \\ &= G\int dV\,\frac{\nabla\cdot(\rho(\vec{r})\vec{u}(\vec{r},t))}{|\vec{r}-\vec{r}_0|}. \end{aligned} \tag{6.9}$$

Integration by parts and taking all surfaces to be at infinity moves the divergence to a gradient of $1/|\vec{r}-\vec{r}_0|$ term. Then we convert our gravitational field to an acceleration, which is done by taking the gradient of the field with respect to the reference point, $\vec{r}_0$

$$\delta\vec{a}(\vec{r}_0,t) = -G\int dV\rho(\vec{r})(\vec{u}(\vec{r},t)\cdot\nabla_0)\frac{\vec{r}-\vec{r}_0}{|\vec{r}-\vec{r}_0|^3}. \tag{6.10}$$

The noise in the GW channel of an interferometer is the differential length change between the two arms induced by something other than GWs

$$h = \frac{\delta x - \delta y}{L} = \frac{\delta a_x - \delta a_y}{(2\pi f)^2 L} \tag{6.11}$$

where L is the length of the arms of the interferometer. If we consider the motion of four tests masses adding incoherently, then the noise in the GW channel due to the acceleration induced by Newtonian noise can be found by multiplying x and y accelerations by $\sqrt{2}$ and considering only the RMS acceleration

$$h_{\mathrm{NN}} = \frac{\sqrt{2\left(\delta a_{x,\mathrm{rms}}^2 + \delta a_{y,\mathrm{rms}}^2\right)}}{(2\pi f)^2 L}. \tag{6.12}$$

Given that the integral in equation (6.10) is different for different types of seismic waves and in the case where we have a boundary between rock and air, we need to consider contributions from different components of the seismic field separately. The contribution of NN from different components of the seismic field under different circumstances are discussed in [48]. This is part of the motivation for efforts like the seismic radiometer, which is discussed in section 6.4.

6.2 Homestake seismometer array

The Homestake Mine in Lead, SD, is a retired gold mine that is now home to the Sanford Underground Research Facility (SURF). Even before the founding of SURF in 2007, Homestake had a long history of hosting scientific experiments. From the 1960's through the 1990's it was host to Ray Davis's solar neutrino experiment [202]. Today, it is home to several high profile experiments that span from Neutrino physics to Dark Matter searches to the search for the neutrino-less double beta decay.

The Deep Underground Gravity Lab (DUGL) experiment was established in 2008 and involved a three-dimensional seismometer array at Homestake to investigate how seismic noise and Newtonian noise can change with depth and to test techniques for subtraction of noise using a network of sensors. The initial plan for DUGL included nine stations at depths of 300, 800, 2000, 4100 ft [203]. However, during the initial run from December 2009 to January 2010 three stations were inoperative due to poor conditions, and in the end only three stations were used for most analyses [203, 204]. One of the main goals of the initial array was to explore coherent subtraction methods, like Wiener filtering, to clean one seismometer's data stream using the data from another seismometer. While this was shown to work in principle, the initial analysis was limited by the small number of detectors, large timing uncertainty, and cross-talk from electronics in the data acquisition system [204].

Since the decommissioning of the original array, DUGL has expanded to become a larger collaboration, now including seismologists at California Institute of Technology (CIT) and Indiana University. The second generation of the array consisted of 24 stations, including 9 on the surface and 15 underground. It was operational from November 2014 through December 2016. Low-noise broadband seismic instruments and commercial data acquisition systems were rented from the Portable Array Seismic Studies of the Continental Lithosphere (PASSCAL), which is a part of the Incorporated Research Institutions for Seismology (IRIS). The added expertise of our seismology colleagues, along with strong hardware and software support from PASSCAL led to a successful two-year experiment that included up-time near 100 % for most instruments (with the exception of one, which will be discussed later) and several active excitation experiments throughout the mine and the town of Lead.

6.2.1 Array description

The second generation of the Homestake seismometer array took data between November 2014 and December 2016. There were 15 stations below ground and nine stations on the surface. Five surface stations were on SURF property, one was located at the local high school, and three were located on private property at different locations around Lead and Deadwood, SD. Installation took place between September 2014 and May 2015 and decommissioning took place between September 2016 and December 2016.

Figure 6.3 shows the array layout along with contours indicating elevation on the surface and colored lines indicating drifts within the mine. In table 6.1 each station is listed by its ID with a short description of the location. In table 6.2 locations are given for each station. The surface station locations are from GPS data, while underground station locations are maps of mine drifts created by mine surveyors. The uncertainty is $\approx$2 m on these locations.

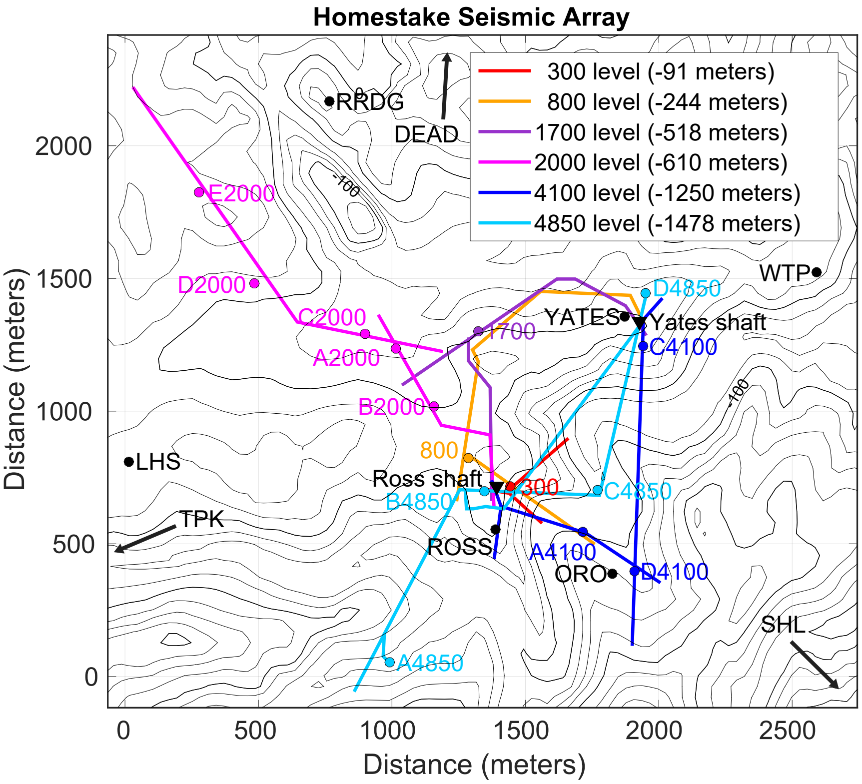

Figure 6.3: Map of the Homestake seismometer array. Contours indicate surface elevation levels. The three stations on private land do not appear here, but the general direction of their locations are indicated by arrows on the edges of the map. The colored lines indicate the drifts in the mine where the stations are located.

6.2.2 Individual station set-up

Each seismic station consisted of at least a seismometer, a data acquisition system, and electronics related to power and timing. Most equipment was rented from PASSCAL.

Twenty stations used Streckeisen STS-2 broadband seismometers [206] and four stations required more rugged, Guralp CMG-3T broadband seismometers [207]. These four stations stations, DEAD, ROSS, YATES, and 300, tended to have concerns about moisture levels.

A Quanterra Q330 datalogger [208], shown in figure 6.4, was used for digitizing the analog seismometer data and powering the seismometer itself. The Q330 can provide

Station ID	Station Type	Station Description
DEAD	Surface	Private landowner's yard in Deadwood
LHS	Surface	At Lead-Deadwood High School
ORO	Surface	Near Oro Hondo shaft
ROSS	Surface	Near Ross warehouse
RRDG	Surface	Rhyolite Ridge
SHL	Surface	Private landowner's yard on Strawberry Hill
TPK	Surface	Private landowner's yard near Terry Peak
WTP	Surface	Near Yates water treatment plant
YATES	Surface	Near Yates administration building
300	Underground	300 level, near side entrance
800	Underground	800 level, near Ross shaft
1700	Underground	1700 level, near Ellison shaft
A2000	Underground	2000 level, near ramp at Y intersection
B2000	Underground	2000 level, near Ross lunch room
C2000	Underground	2000 level, 7 ledge, A limb
D2000	Underground	2000 level, top of ramp
E2000	Underground	2000 level, north 9 ledge
A4100	Underground	4100 level, powder magazine west of Oro Hondo
C4100	Underground	4100 level, Bill Roggenthen's room
D4100	Underground	4100 level, Yates station old locomotive barn
A4850	Underground	4850 level, 17 ledge
B4850	Underground	4850 level, roll-up door
C4850	Underground	4850 level, 4 Winze Wye
D4850	Underground	4850 level, Davis incline

Table 6.1: Station IDs with a brief description of the location for each of the 24 seismic stations in the Homestake seismometer array. This table is reproduced verbatim from [205].

real-time data either through an ethernet connection or through a radio antenna. Data packets were sent to a computer on-site at Homestake and this computer processed and stored the data and then broadcast it to remote computers in Minnesota. All of the channels present in the data packets are shown in table 6.3. The Q330 also saved data to a local hard drive using a serial connection. We used Quanterra PB14 Packet Balers, shown in figure 6.5, for this purpose because they are rugged, water resistant, and made specifically to be used with Q330 digitizers.

The Balers were capable of storing 20 GB of data at a time, which was exceeded

Station ID	**Easting [m]**	**Northing [m]**	**Elevation [m]**	**Install Date**
DEAD	-187	3386	-127.0	05/18/2015
LHS	-1849	-572	59.0	05/19/2015
ORO	-49	-967	-82.0	03/30/2015
ROSS	-474	-796	3.0	11/19/2014
RRDG	-1120	794	52.0	05/20/2015
SHL	3385	-3869	147.0	05/17/2015
TPK	-3687	-1322	115.0	05/19/2015
WTP	730	200	-70.0	01/22/2015
YATES	0	0	0.0	11/19/2014
300	-421	-651	-119.9	01/13/2015
800	-582	-542	-275.0	01/15/2015
1700	-549	-64	-551.2	03/25/2015
A2000	-859	-135	-641.7	03/24/2015
B2000	-712	-344	-641.7	03/25/2015
C2000	-971	-81	-641.9	03/25/2015
D2000	-1389	101	-642.0	03/25/2015
E2000	-1609	442	-641.9	03/25/2015
A4100	-147	-813	-1282.5	01/21/2015
C4100	65	-110	-1282.7	01/21/2015
D4100	46	-955	-1282.6	01/21/2015
A4850	-857	-1313	-1509.8	04/02/2015
B4850	-516	-663	-1510.1	11/19/2014
C4850	-94	-657	-1510.4	11/19/2014
D4850	78	90	-1509.8	11/19/2014

Table 6.2: Coordinates of each seismic station in the Homestake seismometer array. Coordinates are quoted in the UTM coordinate system in zone 13T and all locations are relative to the YATES surface station. The YATES station has absolute coordinates of (Easting, Northing, Elevation) = (599504, 4911750, 1625.0) m. Surface station locations are obtained from GPS data, while underground coordinates are based on maps of the mine drifts. Uncertainties are on the order of ≈2 m.

by the amount of data collected by a station during the full run. Therefore, we made a dedicated trip in April 2016 to "clean" the data from many of the Balers. This provided a second copy of the data in most cases and was the only copy in cases where we did not have telemetry (i.e. the three stations on private property) or telemetry dropped out and data was not continuously available off-site.

Each station received a GPS timing signal so that the timing was synchronized to

Figure 6.4: Quanterra Q330 Digitizer. The seismometer is connected through one of the SENSOR ports on the left. A GPS antenna may be connected to the GPS ANT port. The Quanterra B14 Packet Balers were connected through the SERIAL port. The Q330 is powered either by the POWER port or the QNET port. The Q330 can be connected to a local network, or a local radio antenna, via the QNET port.

sub-μs precision. Surface stations used a local GPS antenna, connected to the Q330s through the GPS ANT port. Underground stations received a GPS signal from an antenna on the roof of the SURF administration building, which was then distributed throughout the mine through optical cables sent down the shafts, and connected to splitters on each level that then sent an optical signal to each station on that level. The optical signals were then converted using custom built GPS transceivers. Details on the optical signals and the real-time data acquisition system can be found in [205].

Surface stations

Stations on the surface required isolation from, among other things, weather, rodents, and humans. Seismometers were placed on a concrete pad in a small enclosure underground (ideally ~3 ft). Putting it below ground kept the seismometer (or the concrete pad) as close to bed rock as possible, while helping to keep the temperature of the instrument as stable as possible. The enclosure consisted of a small log “house” with a foam hut place inside of it and then covered with a sheet of plywood. An example of the log house and concrete pad can be seen in figure 6.6. The seismometer was oriented to North using a magnetic compass, which accounted for magnetic declination.

Electronics, including the Q330, the Baler, and the battery for powering each station

Channel code	**Description**
HHE	East seismic channel (100 Hz)
HHN	North seismic channel (100 Hz)
HHZ	Vertical seismic channel (100 Hz)
LHE	East seismic channel (1 Hz)
LHN	North seismic channel (1 Hz)
LHZ	Vertical seismic channel (1 Hz)
LCQ	Q330 clock quality (percent)
LCE	Q330 clock phase error (μs)
LCC	GPS clock quality (percent)
LPL	Q330 clock phase lock loop status
LCL	Time since GPS lock was lost (seconds)
QBD	Total number of Q330 reboots in last 24 hours
QBP	Logical port buffer percent full from real-time status
QDG	Data gaps (s)
QDL	Current data latency (s)
QDR	Current total input and output data rate (bits/s)
QEF	Overall communications efficiency (percent)
QG1	Total number of data gaps in last hour
QGD	Total number of data gaps in last 24 hours
QID	Total number of Q330 IP address changes in last 24 hours
QLD	Total number of comm link cycles in last 24 hours
QPD	Total number of POCs received in last 24 hours
QRD	Total number of bytes read in last 24 hours
QRT	Current run time (s)
QTH	Current throttle setting (bits/s)
QTP	Ratio of seconds read to real-time clock
QWD	Total number of bytes written in last 24 hours
VCO	Voltage controlled oscillator value
VEA	Antenna current (A)
VEC	Main system current (A)
VEP	Main system voltage (V)
VKI	Main system temperature (°C)
VM1	Mass position for channel 1
VM2	Mass position for channel 2
VM3	Mass position for channel 3
VPB	Packet buffer
VTW	Main system opto inputs

Table 6.3: Q330 and Antelope seismic and state-of-health channels. Channel sample rates are indicated by the first letter of the channel code. H indicates 100 Hz, L indicates 1 Hz, V indicates 0.1 Hz, and Q indicates 0.05 Hz. This table is reproduced verbatim from [205]

Figure 6.5: Quanterra P14 Packet Baler. The QNET serial port is used to connect to the Q330. The ATTN button will turn on the baler and request that Q330 buffer dump its data to the baler.

were locked in a large Pelican case or were placed in a dog house that was sealed with a small custom built door and plumber's putty (these were stations on SURF property where we did not fear equipment would be stolen).

Two solar panels, tilted at an angle and facing south, were used to power the stations. The solar panels were connected to a power box which connected to the Q330 and a 55 A-h battery to help power the stations at night and on cloudy days. The solar panels were mounted on a wooden post, on top of which was a GPS antenna. The GPS antenna was connected to the Q330 via the GPS ANT port. Overall timing error for these stations was typically within ± 5 μs.

The YATES, ROSS, ORO, WTP, RRDG, and LHS stations used Wilan radios [209], connected to the Q330 via the QNET port. The radios were used to transmit data to the Yates Administration building, where another radio was configured as a receiver. The receiver was connected to a master Q330, which transferred data to a local computer.

Figure 6.6: An example of a the small enclosure that housed the surface station seismometers.

The WTP station suffered from a poor line of site to the antenna on the administration building and so dropouts of real time data were frequent.

Three surface stations, DEAD, SHL, and TPK were set up on private land around Lead, SD, and were stand-alone stations. They were installed in May 2015 and then serviced in September 2015, March 2016, and April 2016. The DEAD station showed severe dropouts during January and February 2016 because the sun fell below a line of trees and so the solar panel did not receive direct sunlight. In addition, the RRDG station suffered from large data dropouts during the summer of 2016, in part due to do damage to cables caused by rodents.

Underground stations

There were 15 underground stations at various depths of the mine. Each seismometer was placed on a granite tile, laid using thinset mortar, on top of a concrete pad. The concrete pad was either newly laid or reused from the initial iteration of the array. The

Figure 6.7: An example of a surface station (RRDG) after it is completed. Note the dog house where electronics are stored, the solar panels, the radio on the pole, and the GPS antenna above the radio (the small hemispherical object on top of the pole). A single cable, reinforced to protect against rodents, was run from the electronics house to the seismometer enclosure.

seismometers were then enclosed in two "huts" made of 1" thick Styrofoam to isolate them from their environments. An example of an underground seismometer enclosure can be seen in figure 6.8.

Electronics were placed on a table several feet from the seismometer and covered with plastic tubs to isolate them from dust and moisture.

All underground stations had AC power, which was connected through a 12 A-h battery that was then connected to the Q330. The batteries were kept charged in case of AC power dropouts due to mine construction. They provided enough power to be able to take data for one extra day in the result of an interruption of AC power. A complete underground station, including electronics and seismometer enclosure, can be seen in figure 6.9.

Figure 6.8: An example of the enclosure used for seismometers underground. This was taken at the B4850 station.

Underground stations received a GPS timing signal through a set-up of optical cables, splitters and transceivers that were connected to a GPS antenna on the roof of the Yates administration building. The signal was sent to each level of the mine through optical cables, where it was split and sent to each station, converted from optical to electrical using a GPS transceiver and fed into the Q330 through the GPS EXT port. More details of the GPS signal distribution can be found in [205].

6.2.3 Amplitude spectra

The seismic environment at the Homestake mine is very quiet, often below the Peterson global low noise models [210]. In figure 6.10 we show the median amplitude spectral density for all surface stations and for a station at each depth of the mine. All amplitude spectral densities are taken with 900 s Fourier transforms and all available data are used to generate these medians. In figure 6.11 we show "spectral variance" plots for the A4850 station and the RRDG station. Each column is a separate histogram for that frequency

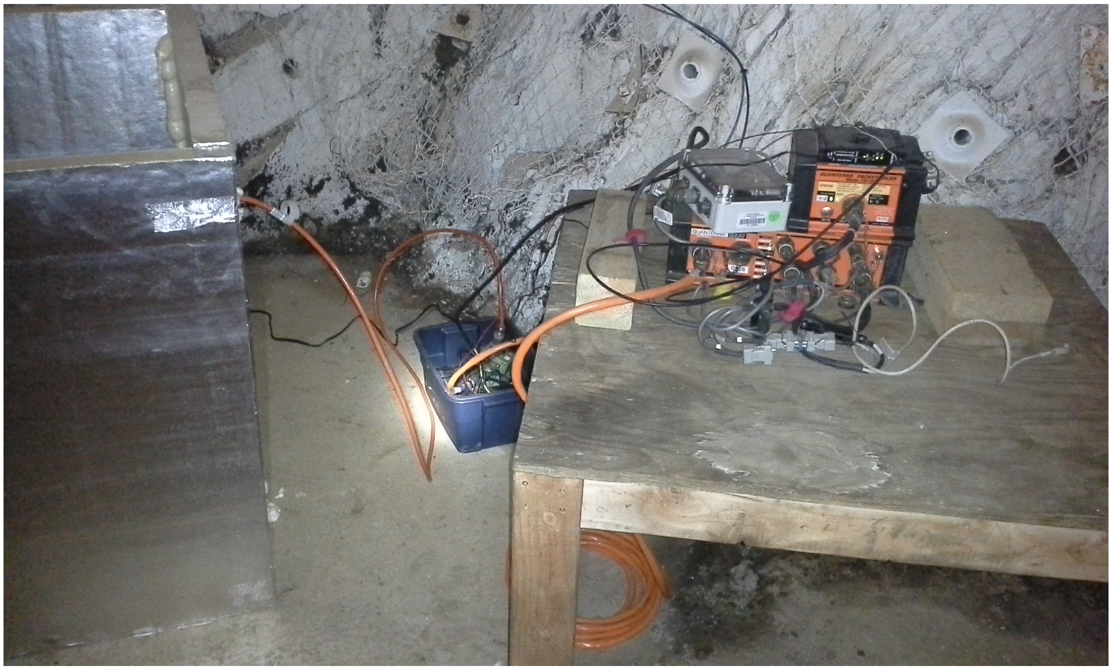

Figure 6.9: A full underground station set-up, with plastic tubs removed to show the electronics. This was taken at the B4850 station.

bin across all of the 900 s amplitude spectral densities we have taken.

For all of these spectra, we use all data, including noise transients and seismic events like earthquakes and mine blasts. All spectra show evidence for the microseismic peak between 0.1 and 0.2 Hz, followed by a sharp drop-off in displacement from $0.2 - 1$ Hz.

We can see in the median ASD plot in the top right of figure 6.10 that above 1 Hz, the spectrum appears to depend more strongly on the location, but with generally less noise with increasing depth. The plot in the top left, showing the median ASD for all surface stations, indicates that there is large variation between stations at higher frequencies. The ROSS and YATES stations, which are located near mine shafts, show significantly more noise than the ORO station, which is located in a remote area. The RRDG station is the loudest at high frequencies, likely because it is exposed to very high winds. At frequencies below the microseismic peak, we see that surface stations tend to show larger amplitudes, likely due to temperature fluctuations. It is also worth noting that at low frequencies the vertical amplitude is almost an order of magnitude lower than the amplitude for the North channels. This is likely due to tilt noise that increases with decreasing frequency for the horizontal components [211].

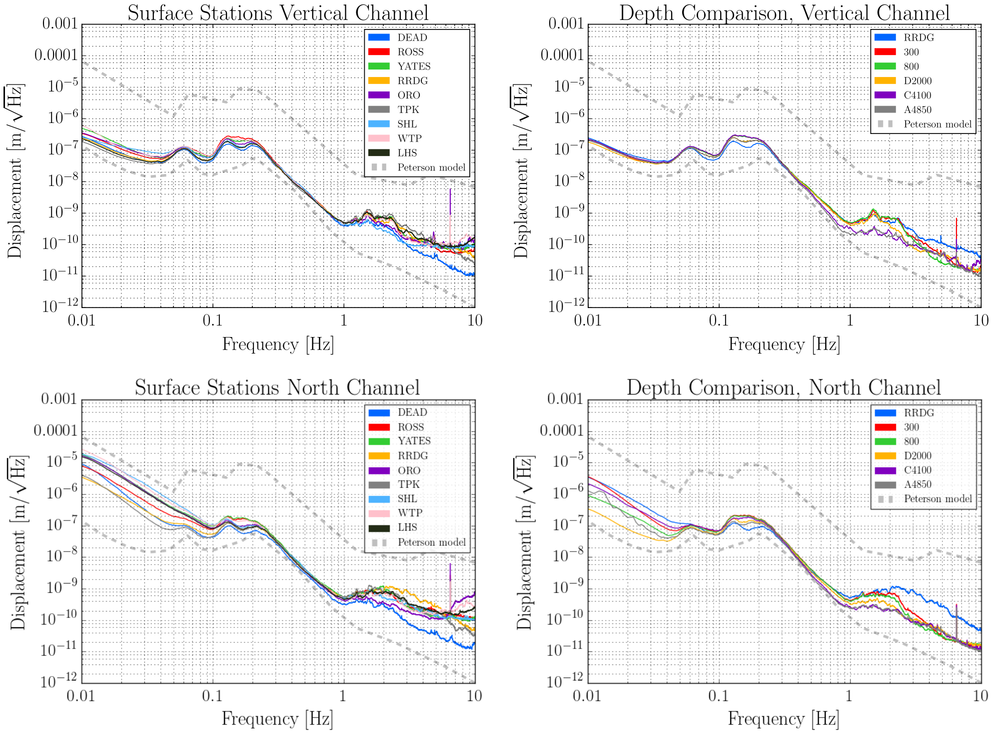

Figure 6.10: Left column: median amplitude spectral density for surface stations across one year of data for the vertical (top) and North (bottom) channels. Right column: the same plot but for one station at each depth of mine. We see that these spectra are regularly close to the Peterson low noise models.

6.3 Rayleigh-wave eigenfunction measurements

We have established that the array shows phenomenal sensitivity across a wide frequency band, so we would like to use it to make substantive measurements that will help us to better understand the seismological environment. One example is a measurement of the Rayleigh wave eigenfunction.

The properties of the Rayleigh wave eigenfunctions determine how R-waves propagate and how the horizontal and vertical amplitudes change with depth. While many

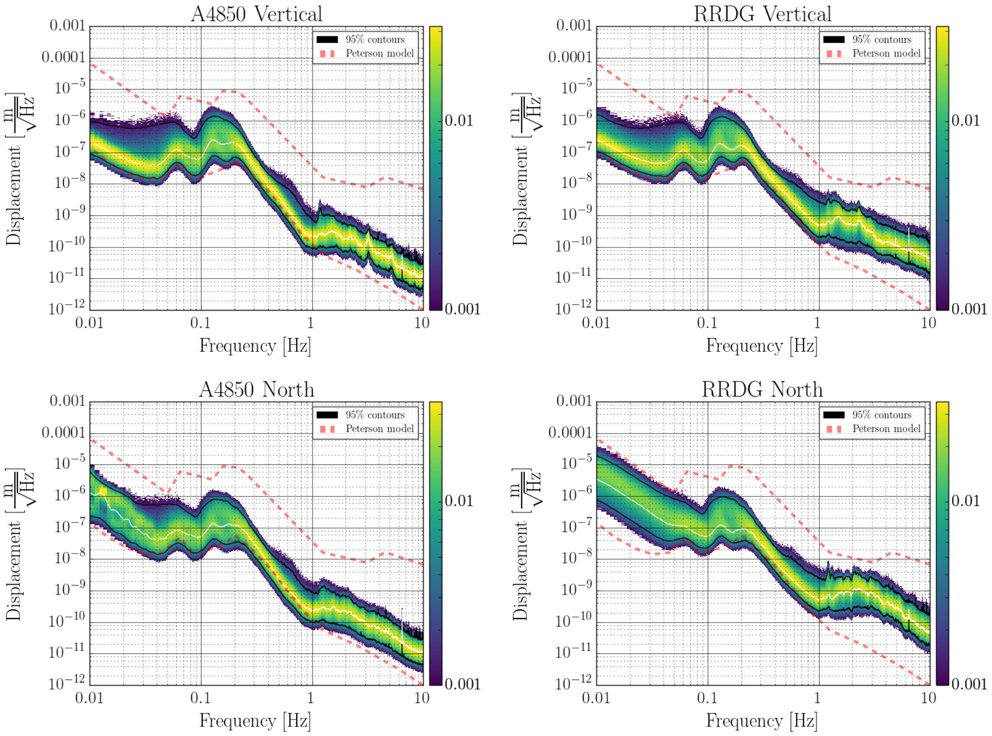

Figure 6.11: Left column: Spectral variance plots for the vertical (top) and North (bottom) channels for the A4850 station. Right column: Spectral variance plots for the vertical (top) and North (bottom) channels for the RRDG (surface) station. These plots are (normalized) histograms of all 900 s amplitude spectral densities taken for all data we have available for the Homestake seismometer array. We see that, especially for the A4850 station, the seismic environment at Homestake is very quiet; seismic activity is often below the Peterson low noise model. The white line indicates the median of all amplitude spectral densities included in the histogram. The black lines indicate the 5th and 95th percentiles.

properties are location-dependent, the eigenfunction typically exhibits a retrograde particle motion at the surface and at some depth the particle motion switches from retrograde to prograde motion. The radial component generally falls off in amplitude at close to an exponential rate at the surface, while the vertical component might increase with depth initially before eventually showing an exponential tail with increasing depth. An example of the theoretical eigenfunctions for a homogeneous half-space are shown in figure 6.2.

An accurate measurement of the eigenfunctions is important for extracting how much power is in different modes of the seismic field, which we will explore in section 6.4. It could also be important for site selection for future GW detectors. If, for example, building a detector 300 m below ground means that whenever there is earthquake the R-wave amplitude from the earthquake is 25% higher at the underground detector than it is on the surface, then perhaps it is better to stay on the surface.

In this section, we discuss a method to estimate the depth dependence of R-waves from a set of mine blasts. In section 6.3.1, we discuss the data processing steps employed for choosing which mine blasts to use and how we extract amplitude and phase information from the data. In section 6.3.2, we present estimates of parameters for a biexponential model for the R-wave eigenfunctions and compare those results to models from the literature.

6.3.1 Analysis of transient events

During the course of its run, the Homestake seismometer array regularly recorded mine blasts that can be used to measure the R-wave eigenfunctions. These events were initially identified and characterized by colleagues at Indiana University (IU), and for each event we have an estimate of the time when the blast occurred, and an estimate of the latitude and longitude of the blast location. Figure 6.12 shows that most of the blasts in this catalogue happen in the Powder River Basin in Wyoming.

We need to identify and isolate which blast events have waveforms with distinct times that are dominated by Rayleigh waves. For each blast, I create plots for several surface stations showing the traces of the radial[2] and vertical timeseries and a spectrogram of the vertical-to-radial phase. We calculate this phase using the complex cross-spectrum of the radial and vertical channels

$$\begin{aligned} \rho &= \tilde{R}^*(f) \times \tilde{Z}(f) \\ \phi_{rz} &= \arctan\left(\frac{\text{Imag}(\rho)}{\text{Real}(\rho)}\right). \end{aligned} \tag{6.13}$$

where $\tilde{Z}(f)$ and $\tilde{R}(f)$ are the fast Fourier transforms of the vertical and radial channels

---

[2] For each event, we use the direction information from IU to apply a rotation from East and North data records to “radial” and “transverse” with respect to the source direction.

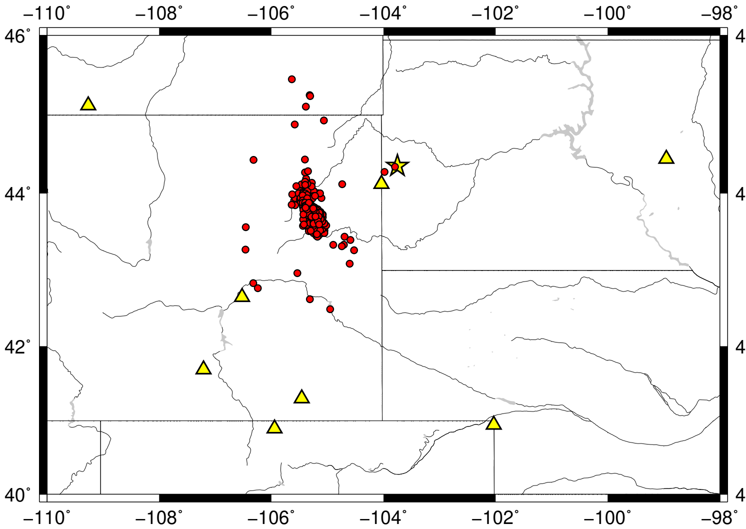

Figure 6.12: The estimated location of many of the mine blasts used in this analysis. The star indicates the Homestake seismometer array.

respectively.

Event waveforms that show consistent vertical-to-radial phase and relatively stable amplitude are ideal for this analysis. We call the piece of the waveform exhibiting these qualities the "Rayleigh region." If a waveform does not clearly have a Rayleigh region at most surface stations then it gets thrown out. This was the case for 22 of the 50 events that were tested, and was likely caused by local noise effects for the station I used to make this determination. An example of a "good" event is plotted in figure 6.13 using a segment duration of 5 s and frequency bin width of 0.2 Hz. For the list of "good" events, I chose a reasonable start and end time to the Rayleigh region by eye (see the green box in figure 6.13). A table showing the start and end times and locations for each event are shown in table 6.4.

We will analyze blast events at frequencies in the range from $f = [0.2, 1.1]$ Hz in increments of 0.1 Hz because these are the frequencies where it is most evident that there are R-waves in the mine blast waveforms. For each event and for each frequency we perform the following set of data analysis steps.

1. Using the estimated blast location, we apply a rotation to the East and North

Time [UTC]	**Start [s]**	**End [s]**	**Latitude**	**Longitude**
07-01-2015 18:06:14	70.0	140.0	43.6738	-105.1743
07-01-2015 23:34:48	50.0	130.0	43.8012	-105.2607
07-02-2015 18:26:23	70.0	130.0	43.8643	-105.3683
07-03-2015 16:18:38	60.0	135.0	43.7044	-105.211
07-03-2015 19:58:32	70.0	125.0	43.765	-105.229
07-03-2015 20:08:52	80.0	130.0	43.4864	-105.133
07-04-2015 18:01:33	70.0	130.0	43.7763	-105.2415
07-05-2015 00:42:03	80.0	120.0	43.825	-105.3284
07-05-2015 18:39:42	60.0	115.0	44.1201	-105.4577
07-05-2015 18:39:47	55.0	110.0	43.5167	-104.755
07-06-2015 23:55:31	70.0	125.0	43.9907	-105.4678
07-07-2015 14:34:39	90.0	135.0	43.7146	-105.2251
07-07-2015 19:19:15	60.0	130.0	43.5741	-105.0976
07-08-2015 19:17:53	55.0	115.0	43.6686	-105.1436
07-08-2015 20:06:45	60.0	120.0	43.4386	-104.7081
07-08-2015 23:32:28	70.0	140.0	43.8375	-105.3513
07-10-2015 16:01:25	50.0	100.0	44.1077	-105.2465
07-10-2015 19:38:10	65.0	125.0	43.6801	-105.2104
07-10-2015 21:05:02	70.0	135.0	43.7104	-105.2142
07-14-2015 18:28:01	70.0	120.0	43.7859	-105.2327
07-14-2015 19:17:30	60.0	130.0	43.5559	-105.0599
07-19-2015 15:34:31	70.0	115.0	43.6938	-105.1198
07-19-2015 18:01:50	70.0	115.0	43.7123	-105.2381
07-20-2015 18:03:39	70.0	110.0	43.7791	-105.2019
07-21-2015 16:06:42	70.0	130.0	43.704	-105.1685
07-23-2015 17:49:23	50.0	90.0	44.0382	-105.2385
07-23-2015 20:17:00	75.0	120.0	43.7242	-105.1273
07-23-2015 22:49:37	70.0	110.0	43.8121	-105.2407

Table 6.4: List of events used for measuring the R-wave eigenfunctions. The start and end columns indicate how long after the time of the event the Rayleigh region we use to make measurements begins. The latitude, longitude, and event times are estimates from IU of the blast location and time. The latitude and longitude are used to generate radial and transverse coordinates by applying a simple rotation to the East/West/North/South orientation.

channels of the data to create radial and transverse channels.

2. We take the amplitude spectral density at the chosen frequency for both the radial

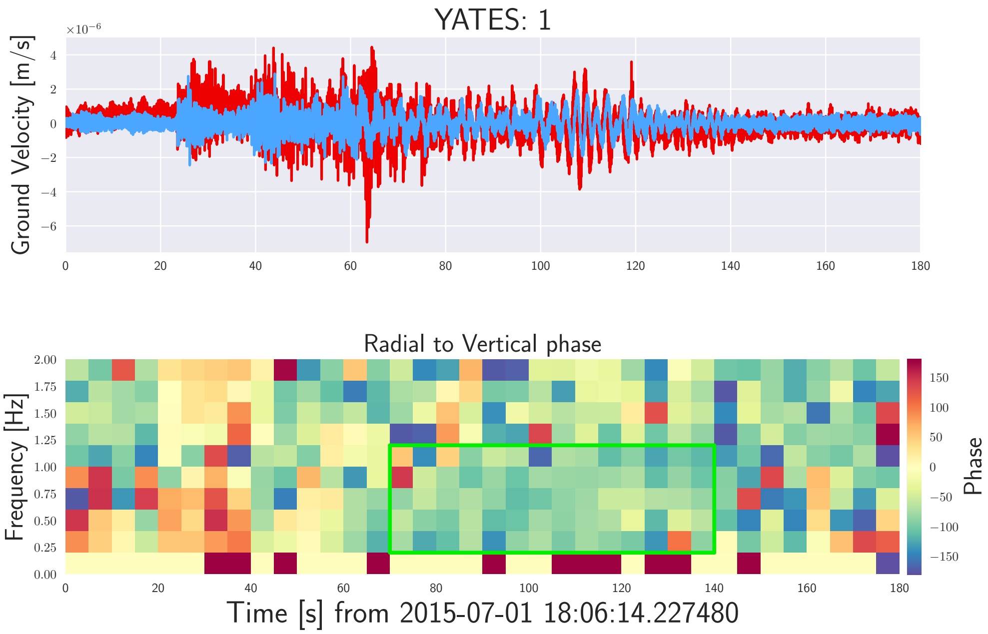

Figure 6.13: Data for an event that is in the analysis. These plots are for the `YATES` station. The top plot shows the timeseries for vertical (blue) and radial (red) channels and the next plot shows the vertical-radial phases. In the bottom plot there is a distinct region of time-frequency space from 0.25-1 Hz and 70-140 s where the vertical-radial phase is roughly - 90°, which is consistent with the expected retrograde motion.

and vertical channels for each 10 s segment in the Rayleigh region. Each segment and each 0.1 Hz frequency bin within our range will be a data point. We now have measurements that can be specified in terms of their depth, frequency and the time at which they were taken: $|\tilde{R}_i(f, z_i; t)|$ for radial and $|\tilde{Z}_i(f, z_i; t)|$ for vertical. The subscript i indicates at which seismometer, at depth z, the data point was taken.

3. We normalize all radial and vertical data points by the mean of the radial amplitude across all surface stations with corresponding time and frequency.

$$\hat{h}_i(f, z_i; t) = \frac{|\tilde{R}_i(f, z_i; t)|}{\text{mean}(\{|\tilde{R}_j(f, z_j; t)| \text{ for } j \text{ where } z_j{=}0\})} \tag{6.14}$$

$$\hat{v}_i(f, z_i; t) = \frac{|\tilde{Z}_i(f, z_i; t)|}{\text{mean}(\{|\tilde{R}_j(f, z_j; t)| \text{ for } j \text{ where } z_j{=}0\})} \tag{6.15}$$

4. To reduce the impact of very large amplitude individual measurements on the mean and standard deviation we will take in item 8, we cut all data points with normalized amplitude greater than 1.5. This removes outliers, likely caused by site-specific effects, that could have a large impact on our measurements, and typically removes surface station data points. This cut removes 14.5% of the data.

5. We take the vertical-to-radial phase associated with each data point as specified in equation (6.13).

6. We assign a negative sign to all vertical amplitudes to be consistent with [198].

7. We take the part of the radial amplitude that is consistent with retrograde motion with respect to the vertical channel. That is,

$$\hat{h}_i(f, z_i; t) \to -|\hat{h}_i(f, z_i; t)| \times \text{Imag}\left(e^{i\phi_{i,rz}(f, z_i; t)}\right) \tag{6.16}$$

   where $\phi_{i,rz}(f, z_i; t)$ is the vertical-to-radial phase for the corresponding data point taken at frequency f, time t, and station i. The minus sign is there to keep the convention that $\hat{h}_i(f, z_i; t)$ is positive if the vertical-to-radial phase is consistent with retrograde motion and negative if it is consistent with prograde motion. We choose to apply this factor to the radial channel because it is expected from the theory of Rayleigh waves that that the radial amplitude falls off faster with depth than the vertical amplitude due to the fact that the P-wave velocity is larger than the S-wave velocity. This is discussed in much greater detail in [212] chapter 4. The tacit assumption here is that the piece of the radial channel measurement that is not consistent with retrograde or prograde motion is due to noise.

8. At each depth and each frequency, we take the mean and standard error of the normalized vertical and radial measurements across all data points.

$$\hat{\hat{h}}(f,z) = \frac{1}{N} \sum_{i \text{ for } z_i = z} \sum_{t} \hat{h}_i(f, z_i; t) \tag{6.17}$$

$$\sigma_h^2(f,z) = \frac{1}{N} \sum_{i \text{ for } z_i = z} \sum_{t} (\hat{h}_i(f, z_i; t) - \hat{\hat{h}}(f,z))^2. \tag{6.18}$$

   where N is the number of times across at all stations at depth, z (that have not been cut). Similar expressions hold for the vertical data as well.

9. We then renormalize all data points again such that the radial amplitude at the surface is 1.

$$\hat{\hat{h}}(f,z) = \hat{\hat{h}}(f,z)/\hat{\hat{h}}(f,0) \tag{6.19}$$

$$\hat{\hat{v}}(f,z) = \hat{\hat{v}}(f,z)/\hat{\hat{h}}(f,0). \tag{6.20}$$

The final data products are radial and vertical amplitudes, $\hat{\hat{h}}(f,z)$ and $\hat{\hat{v}}(f,z)$, as a function of depth for each frequency. In figure 6.14, we show violin plots indicating the distribution of vertical and radial measurements at each depth, $\hat{h}(f, z_i; t)$ and $\hat{v}(f, z_i; t)$. The orange dots indicate the mean over all points at that depth, $\hat{\hat{h}}(f,z)$ and $\hat{\hat{v}}(f,z)$, before the final normalization in equation (6.19). The red points indicate the median over measurements in the violin plots. The black bars indicate the 16th and 84th percentiles for the data.

6.3.2 Biexponential model and parameter estimation

The plot in figure 6.14 shows a distinctive shape that can be fit by a biexponential model. In [198] they construct a model for the fundamental R-wave eigenfunction based on a power-law velocity depth profile for S-waves. They fit a biexponential model to the R-wave eigenfunction for many different theoretical power-law velocity depth profiles and Poisson ratios and calculate the mean and standard deviation of the parameters in those fits.

We use our measurements to constrain the parameters in the biexponential fits to

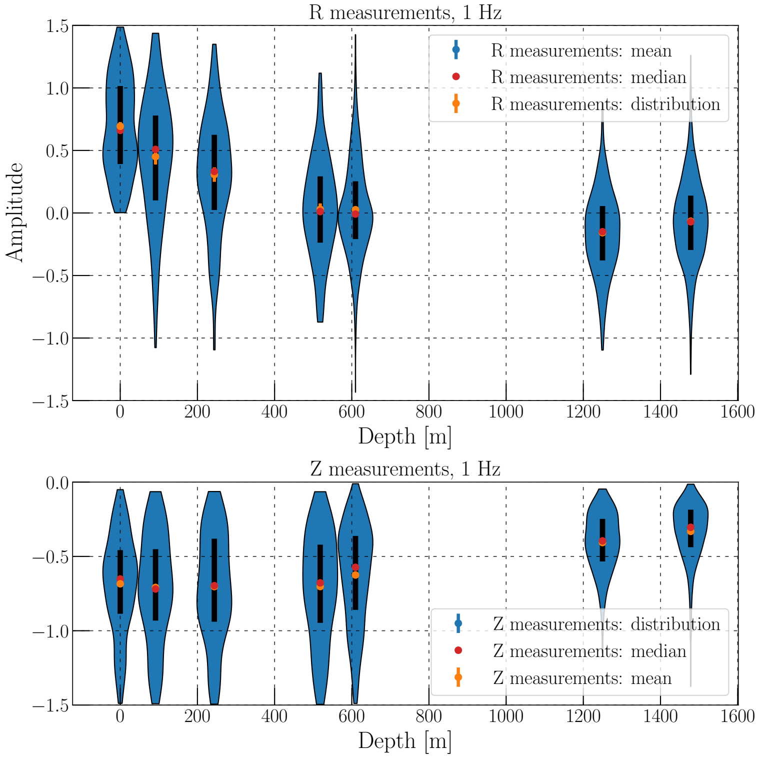

Figure 6.14: Violin plots showing the distributions of measurements of vertical and radial amplitudes at 1 Hz, $\hat{\hat{h}}(1\text{ Hz}, z)$ (top) and $\hat{\hat{v}}(1\text{ Hz}, z)$ (bottom), normalized by mean radial amplitude at 1 Hz at the surface. Data points not consistent with the amplitude criteria have been removed. Each point in the distributions represents a separate 10 s measurement of the Rayleigh region of a specific mine blast at a specific station. The orange points indicate the mean of each distribution before the final normalization, while the black lines indicate the 16th and 84th percentiles of the data points that make up the violin plots. We see that the radial measurements at the 1700 ft and 2000 ft (roughly 500 and 600 m) stations tend to zero, while for the deepest levels we see there is a slight preference for prograde motion. The orange points will be normalized again by the radial measurement on the surface using equation equation (6.19), and then used as data for our likelihood in equation (6.21).

the radial and vertical data points. We use the functions r_H and r_V to refer to the two biexponential functions, and we use a Gaussian likelihood when we do the parameter estimation

$$\ln p(\{\hat{\hat{h}}, \hat{\hat{v}}\}|\vec{\theta}) = -\frac{1}{2}\sum_{f}\sum_{z}\left(\frac{\left[\hat{\hat{h}}(f,z) - r_H(f,z;\vec{\theta})\right]^2}{\sigma_h^2(f,z)} + \frac{\left[\hat{\hat{v}}(f,z) - r_V(f,z;\vec{\theta})\right]^2}{\sigma_V^2(f,z)}\right) \tag{6.21}$$

where $\hat{\hat{h}}(f,z)$ and $\hat{\hat{v}}(f,z)$ are the radial and vertical measurements, z labels depth, f labels frequency, H is for horizontal (radial), and V is for vertical. In this case, for the measurements we use the mean across all time-segments at each depth and for each frequency. For 1 Hz, for example, this corresponds to the orange points in figure 6.14. The two biexponential functions, r_H and r_V, depend on a set of parameters $\vec{\theta}$, depth, z, and frequency f

$$r_H(f,z;\vec{\theta}) = \left(e^{-2\pi f z \frac{a_1}{v_R(f)}} + c_2 e^{-2\pi f z \frac{a_2}{v_R(f)}}\right) \times \frac{1}{1+c_2} \tag{6.22}$$

$$r_V(f,z;\vec{\theta}) = \left(e^{-2\pi f z \frac{a_3}{v_R(f)}} + c_4 e^{-2\pi f z \frac{a_4}{v_R(f)}}\right) \times \frac{N_{vh}}{1+c_4}. \tag{6.23}$$

We try to estimate the parameters in the biexponential model

$$\vec{\theta} = (N_{vh}, c_2, c_4, a_1, a_2, a_3, a_4, \{v_R(f)\})$$

using the data, $\hat{\hat{v}}(f,z)$ and $\hat{\hat{h}}(f,z)$. The assumption that the c's and the a's do not change with frequency is intrinsic to the theoretical model outlined in [198] and could also be relaxed in the future.

Note that we calculate the Rayleigh wave phase velocity at each frequency $\{v_R(f)\}$ assuming a power law dispersion relation whose parameters we allow to vary. The parameters over which we sample are $v_{1\mathrm{Hz}}$ and α where

$$v_{\mathrm{R}}(f) = v_{1\mathrm{Hz}} f^{\alpha}. \tag{6.24}$$

That is, in this case $\vec{\theta}$ now includes α and $v_{1\mathrm{Hz}}$ and for each biexponential function, v_R is calculated at each frequency using this dispersion relation.

We use the `MultiNest` package [190] to perform a MCMC analysis to estimate the parameters, $\vec{\theta}$. `MultiNest` is commonly used in the GW community, is designed to efficiently sample multimodal distributions and large parameter spaces, and offers robust Bayesian evidence estimates. We discuss nested sampling and `MultiNest` in detail in chapter 5.

Due to the large parameter space, it is important to include any prior information we have. We use velocity estimates from [213] to set prior probabilities on the velocity parameters. We also use [198] to inform the Gaussian prior probability distributions we use on the c's and the a's. The definition of our parameters differ slightly from those in [198], but we can generate prior information on each parameter using some combination of information from that manuscript. We also widen the error bars on those parameters enough to allow for sufficient exploration of the parameter space, given that our situation is likely different from the theoretical one considered in [198].

The biexponential model is flexible, and allowing our parameters to vary widely results in multi-modal posterior distributions. Therefore, while we widen the error bars from [198], we do not allow for *very large* excursions into parts of the parameter space that will result in multi-modality of the distribution. Using 28 mine blast events, each with a Rayleigh region that is roughly 50–80 s long, we find reasonable fits to the data using our prior information. The results of the parameter estimation, along with the prior information on each parameter is summarized in figures 6.15 and 6.16 and table 6.5. Figure 6.16 shows that there is very little difference between the prior and posterior distributions, which implies that the measurements generally agree with the theoretical predictions. These measurements represent the first explicit estimate of the depth dependence of the R-wave eigenfunctions using a three-dimensional seismometer array.

6.4 Seismic radiometer

The complexity of the seismic field and the difference in the contribution of surface and body waves to the overall Newtonian noise budget leads us to construct a method for estimating the power in different components of the seismic field coming from each direction. We employ a method that is similar to the GW radiometer [125], and so we call this method the "seismic radiometer" method. The method has been developed by members of the University of Minnesota LIGO group over the last several years, and I have extended this method while also characterizing its limits of use based on

Parameter	Mean	Error	Prior Mean	Prior Error
c_2	-0.76	0.06	-0.8	0.1
a_1	0.86	0.06	0.85	0.1
a_2	0.63	0.06	0.7	0.1
c_4	-0.69	0.07	-0.74	0.1
a_3	0.49	0.06	0.7	0.4
a_4	0.81	0.1	0.8	0.2
N_{vh}	-0.68	0.02	-0.6	0.2
$\ln v_{1\text{Hz}}$	8.11	0.07	8.0	0.5
α	-0.25	0.02	-0.17	0.1

Table 6.5: Results for R-wave eigenfunction parameter estimation. We show estimates and uncertainty for the parameters from the 1-dimensional marginalized posterior distribution on each parameter. We also show the mean and standard deviation of the Gaussian prior probability distribution used for each parameter.

theoretical and numerical arguments.

In this section, I present an extension of the previously-developed method described in [205]. I begin by discussing the seismic radiometer formalism for body waves and Rayleigh waves in sections 6.4.1 and 6.4.2. I then provide a detailed discussion of solving large-dimensional linear equations using matrix methods. Finally, I present a simple extension of the original method that allows for simultaneously extracting multiple components of the seismic field in section 6.4.3. In section 6.4.6, I apply this method to real data for a stationary source of surface waves that appears to turn on and off at various times of the day and the microseismic peak at 0.2 Hz on two different days that show different seismic behavior.

6.4.1 Body wave formalism

We begin by writing down the seismic displacement field due to a specific type of body wave (i.e. P-waves) as a plane-wave expansion over different polarizations, frequencies, and directions. For now we will write this down as a general expression that is independent of the mode of the seismic field:

$$\vec{s}_m(\vec{x},t) = \sum_A \int df\, d\hat{\Omega}\, \tilde{s}_{m,A}(f,\hat{\Omega})\, \vec{e}_A(\hat{\Omega})\, e^{2\pi i f(t-\hat{\Omega}\cdot\vec{x}/v_m)}. \tag{6.25}$$

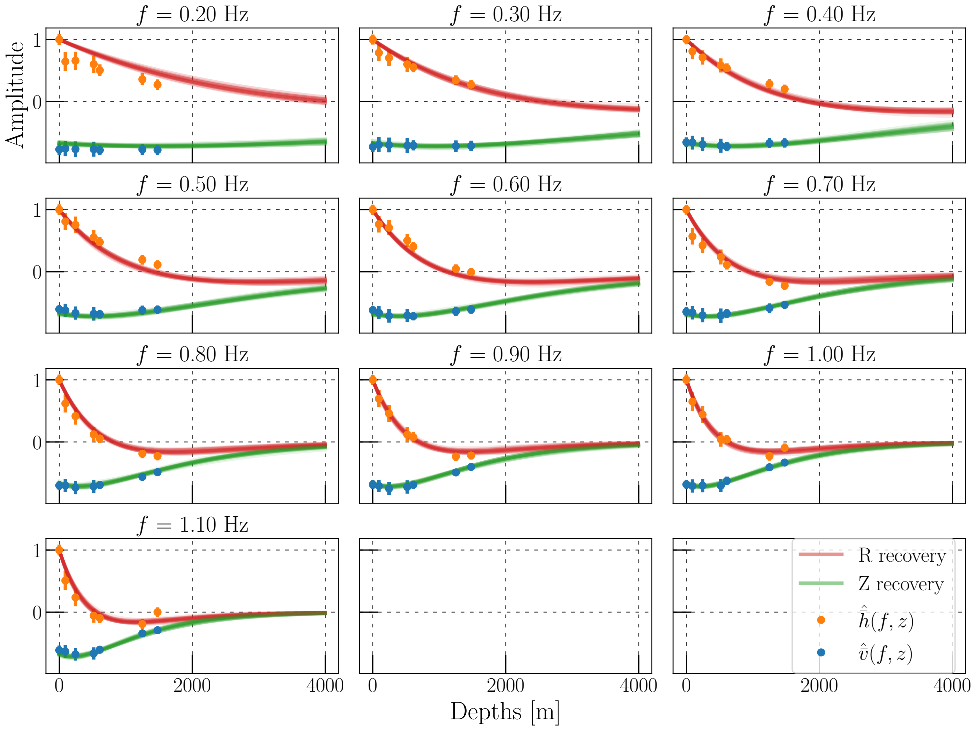

Figure 6.15: Rayleigh-wave parameter estimation fits for all of the data used. The red and green curves are examples of the biexponential models evaluated at parameters whose values are generated with random draws from the posteriors presented in figure 6.16. The width of those lines is proportional to the range of values at each depth one might expect the R-wave eigenfunction to take given the parameter estimation we have performed and the model we have used. The orange points are the data supplied to the sampler. That is, the orange points correspond to $\hat{\hat{h}}(f,z)$ and the blue points correspond to $\hat{\hat{v}}(f,z)$.

In this case, m specifies the component of the seismic field (i.e. P-waves), A denotes the polarization of the wave, $\hat{\Omega}$ denotes propagation direction, and $\vec{e}_{m,A}(\hat{\Omega})$ is a polarization vector for a wave of polarization A traveling in the direction $\hat{\Omega}$[3]. The phase velocity of mode m is given by v_m. $\tilde{s}_{m,A}(f,\hat{\Omega})$ represents the Fourier amplitude in mode m at frequency f coming from direction $\hat{\Omega}$.

This expansion assumes that stationary plane-waves are a good approximation to

---

[3] For a P-wave, $e_{m,A}(\hat{\Omega}) = \hat{\Omega}$), and there is only one polarization. For S-waves, this vector would point perpendicular to $\hat{\Omega}$.

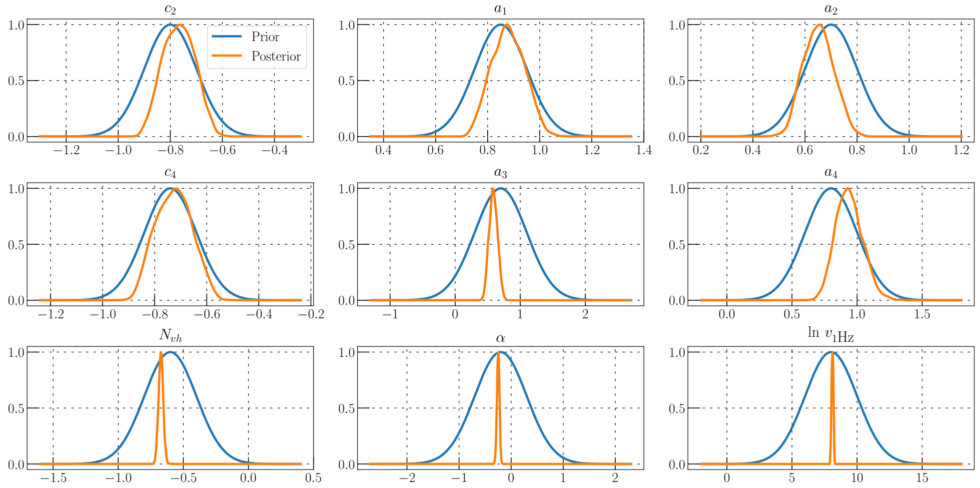

Figure 6.16: Rayleigh-wave parameter estimation posteriors sampling over velocity dispersion.

our data, which which means that the sources for the seismic field are far away and constant in power.

We define a two-point correlation function in which we assume that waves of different modes, directions, polarizations, and frequencies are uncorrelated[4]

$$\langle \tilde{s}^*_{m,A}(f,\hat{\Omega})\tilde{s}_{m',A'}(f',\hat{\Omega}')\rangle = \delta_{A,A'}\delta_{m,m'}\delta^2(\hat{\Omega},\hat{\Omega}')\delta(f-f')H_{m,A}(f,\hat{\Omega}). \tag{6.26}$$

In this case, $H_{m,A}(f,\hat{\Omega})$ is the displacement power spectrum at this frequency coming from direction $\hat{\Omega}$. It therefore has units of $\mathrm{m}^2\,\mathrm{Hz}^{-1}\,\mathrm{sr}^{-1}$. We now consider the cross-correlation of two seismometer channels, assuming that the data in those channels is made up of contributions from different modes of the seismic field. We use Latin indices to denote different seismometers, and Greek indices to denote which channel of the seismometer we are considering (i.e. East, North, vertical). Greek letters with a hat over them indicate a vector pointing in the direction of that channel. We define our cross-correlation statistic

---

[4] For transient events like earthquakes and mine blasts this may not be a good assumption.

$$\langle Y_{i\alpha,j\beta}\rangle = \int_{-T/2}^{T/2} dt\, d_{i\alpha}(\vec{x}_i,t) d_{j\beta}(\vec{x}_j,t) \tag{6.27}$$

$$= \int_{-T/2}^{T/2} dt \int df\, d\hat{\Omega} \sum_m \sum_A H_{m,A}(f,\hat{\Omega}) \left(\vec{e}_{m,A}(\hat{\Omega})\cdot\hat{\alpha}\right) \left(\vec{e}_{m,A}(\hat{\Omega})\cdot\hat{\beta}\right) e^{2\pi i f \hat{\Omega}\cdot\Delta\vec{x}/v_m} \tag{6.28}$$

where $\Delta\vec{x} = \vec{x}_i - \vec{x}_j$ is the vector pointing between the two seismometers. In the second line we have substituted in for the displacement in the two channels with equations (6.25) and (6.26) and integrated (or summed) over the delta functions. If we consider only a small frequency range centered at f with width Δf, over which the amplitude is flat, we can perform the time and frequency integrations trivially (including a factor of 2 to account for positive and negative frequencies)

$$\langle Y_{i\alpha,j\beta}(f)\rangle = 2T\Delta f \int d\hat{\Omega} \sum_m \sum_A H_{m,A}(f,\hat{\Omega}) \left(\vec{e}_{m,A}(\hat{\Omega})\cdot\hat{\alpha}\right) \left(\vec{e}_{m,A}(\hat{\Omega})\cdot\hat{\beta}\right) e^{2\pi i f \hat{\Omega}\cdot\Delta\vec{x}/v_m}. \tag{6.29}$$

We now decompose our amplitudes onto a set of basis vectors $\{Q_a(\hat{\Omega})\}$. One common choice is spherical harmonics, $Y_{lm}(\hat{\Omega})$. A different choice, which we will use in the next few sections is "pixels," $Q_{\hat{\Omega}_0}(\hat{\Omega}) = \delta^2(\hat{\Omega},\hat{\Omega}_0)$. The field is now fully-described by the power associated with each basis vector

$$H_{m,A}(f,\hat{\Omega}) = \sum_a S_{m,A,a}(f) Q_a(\hat{\Omega}). \tag{6.30}$$

It is worth pointing out that in the case where the basis functions are delta functions, the map, S, has units of $\mathrm{m}^2\,\mathrm{Hz}^{-1}$ because the basis functions carry units of sr^{-1}. We can substitute this expression into equation (6.29) and factor $S_{m,A,a}$ out of the $\hat{\Omega}$ integral to get the following result

$$\langle Y_{i\alpha,j\beta}(f)\rangle = 2T\Delta f \sum_m \sum_A \sum_a S_{m,A,a}\gamma^{i\alpha,j\beta}_{m,A,a}. \tag{6.31}$$

where we have defined the "overlap reduction functions[5]" between different channels,

---

[5] we use this name because of the similarity to the function of the same name used in the GW

(i,α) and (j,β) for different basis vectors a of a given mode of the seismic field m and polarization, A, as

$$\gamma_{m,a,A}^{i\alpha,j\beta} = \int d\hat{\Omega}\, Q_a(\hat{\Omega}) \left(\vec{e}_{m,A}(\hat{\Omega}) \cdot \hat{\alpha}\right) \left(\vec{e}_{m,A}(\hat{\Omega}) \cdot \hat{\beta}\right) e^{2\pi i f \hat{\Omega}\cdot\Delta\vec{x}/v_m}. \tag{6.32}$$

The value of γ is different for each seismic wave direction, each set of channels, and each frequency. It is a property of the geometry of our array.

6.4.2 Rayleigh wave formalism

In the case of Rayleigh waves we can write down the plane-wave expansion in a similar fashion to the body waves. However, surface waves are attenuated with depth and the relative amplitude and phase between vertical and horizontal components of Rayleigh waves can also depend on depth. We write the plane-wave expansion for Rayleigh waves in terms of two functions, $r_V(z)$ and $r_H(z)$, which define the fundamental Rayleigh wave eigenfunction. These are real quantities that we measure and discuss in section 6.3.1. The plane-wave expansion in terms of these new functions is then

$$\vec{r}(\vec{x},t) = \int df \int d\hat{\Omega}\, \tilde{r}(f,\hat{\Omega}) \left(r_H(z)\hat{\Omega} - e^{-i\pi/2} r_V(z)\, \hat{z}\right) e^{2\pi i f (t - \hat{\Omega}\cdot\vec{x}/v_R)}. \tag{6.33}$$

Note that the factor of $e^{-i\pi/2}$ imposes the retrograde motion that is characteristic of Rayleigh waves, and the sign between the two functions comes about because of the sign convention used when we defined $r_H(z)$ and $r_V(z)$ in equation (6.22). In this case, $\hat{\Omega}$ is assumed to be confined to the East/West/North/South plane. We can carry out a calculation similar to the one done in the previous section and find the overlap reduction functions for Rayleigh waves

$$\begin{aligned}\gamma_{R,a}^{i\alpha,j\beta} = \int d\hat{\Omega}\, \Big[Q_a(\hat{\Omega}) \left(r_H(z)\hat{\Omega}\cdot\hat{\alpha} - e^{i\pi/2} r_V(z)\, \hat{z}\cdot\hat{\alpha}\right) \times \\ \left(r_H(z)\hat{\Omega}\cdot\hat{\beta} - e^{-i\pi/2} r_V(z)\, \hat{z}\cdot\hat{\beta}\right) e^{2\pi i f \hat{\Omega}\cdot\Delta\vec{x}/v_R} \Big].\end{aligned} \tag{6.34}$$

Because the functions $r_H(z)$ and $r_V(z)$ are normalized such that $r_H(0) = 1$, the interpretation of the R-wave maps should be that they represent the radial amplitude

---

community [214]

induced by the R-wave at the surface. Other directions and other depths can then be inferred using the R-wave eigenfunctions themselves.

6.4.3 Map making

Formalism

We need to create maps of the power contained in each polarization of each mode of the seismic field. To do this, we construct a likelihood function based on the cross-correlation statistic defined in equation (6.31). We begin with a single mode for simplicity. For a single mode of the seismic field, m, and cross-correlation measurements for each pair of detectors, $\mathbf{Y}$ we write a log-likelihood as

$$\log p(\mathbf{Y}|M_a) \propto -\frac{1}{2}\left(\mathbf{Y}-\gamma_m\mathbf{M}\right)^{\dagger}\mathcal{N}^{-1}\left(\mathbf{Y}-\gamma_m\mathbf{M}\right) \tag{6.35}$$

In this case $\mathbf{Y}$ is a matrix of shape $N_{\text{pairs}} \times 1$ which contains our cross-correlation statistic for each pair of channels. γ_m is a matrix of shape $N_{\text{pairs}} \times N_{\text{b.e.}}$ where "b.e." is short for "basis elements." This is a matrix of overlap reduction function values. $\mathbf{M}$ is a matrix of shape $N_{\text{b.e.}} \times 1$ where each element represents the power associated with a specific basis element for a seismic field mode m that we aim to estimate. In the case we are talking about a map for P-waves, we will notate the map with $\mathbf{P}$, for example[6]. This is a matrix representation of equation (6.30). $\mathcal{N}$ is an instrument-noise covariance matrix of shape $N_{\text{pairs}} \times N_{\text{pairs}}$. If we assume that the instrumental noise in each of our detectors is roughly of the same order and is uncorrelated between different instruments and channels, then $\mathcal{N} \propto \mathbb{I}$. What we consider "noise" might depend on what we are trying to measure. In general, however, it will be the instrumental noise and so this approximation will be valid. For now, though, we opt to leave things general. The maximum likelihood estimate for $\mathbf{M}$ can be found by setting the derivative with respect to $\mathbf{M}$ equal to zero. The result is

$$\hat{\mathbf{M}}_{\text{ML}} = (\gamma^{\dagger}\mathcal{N}^{\mathbf{-1}}\gamma)^{\mathbf{-1}}\gamma^{\dagger}\mathcal{N}^{\mathbf{-1}}\mathbf{Y}. \tag{6.36}$$

In the case where $\mathcal{F} \equiv \gamma^{\dagger}\mathcal{N}^{-1}\gamma$ is invertible, this expression is exact. However, it

---

[6] For maps with multiple modes, like R and P-waves, we will use $\mathbf{J}$ for "joint".

is very likely that $\mathcal{F}$, also known as the Fisher information matrix, is singular. This indicates that γ does not have full column rank, and so there are either fewer data points (pairs of detectors) than basis elements we are trying to measure or there are directions to which we are not sensitive.

It is customary to "whiten" the data points using a Cholesky decomposition on the noise matrix $\mathcal{N}$[7]. This means we write $\mathcal{N}^{-1} = \mathbf{L}\mathbf{L}^{\dagger}$ where $\mathbf{L}$ is a lower-triangular matrix. We can then define $\bar{\mathbf{Y}} = \mathbf{L}^{\dagger}\mathbf{Y}$ and $\bar{\gamma} = \mathbf{L}^{\dagger}\gamma$ and rewrite our maximum likelihood expression

$$\hat{\mathbf{M}}_{\mathrm{ML}} = (\bar{\gamma}^{\dagger}\bar{\gamma})^{-1}\bar{\gamma}^{\dagger}\bar{\mathbf{Y}} \tag{6.37}$$

$$\hat{\mathbf{M}}_{\mathrm{ML}} = \bar{\gamma}^{+}\bar{\mathbf{Y}} \tag{6.38}$$

In the second line we have defined the pseudo-inverse of $\bar{\gamma}$, which we denote as $\bar{\gamma}^{+}$. There are several ways of finding approximate solutions to this expression. There are many linear solvers that can be used; common ones include damped LSQR [216] and conjugate gradient methods [217]. Iterative, damped least-squares solvers often end up being very similar mathematically to creating a regularized pseudo-inverse matrix, and I have found in practice that the results are often very similar as well. We opt for the latter because it draws a nice parallel with the spherical harmonics decomposition method discussed in section 2.4. As discussed in section 2.4, we can always construct a pseudo-inverse for a matrix using a singular value decomposition (SVD).

The SVD involves writing a matrix in terms of two unitary matrices $\bar{\mathbf{U}}$ and $\bar{\mathbf{V}}$ of size $N_{\mathrm{pairs}} \times N_{\mathrm{pairs}}$ and $N_{\mathrm{b.e.}} \times N_{\mathrm{b.e.}}$ and one rectangular matrix, $\bar{\Sigma}$, of size $N_{\mathrm{pairs}} \times N_{\mathrm{b.e.}}$. $\bar{\Sigma}$ contains the singular values $\{\bar{s}_k\}$ of the matrix on the diagonal and zeros everywhere else

$$\bar{\gamma} = \bar{\mathbf{U}}\bar{\Sigma}\bar{\mathbf{V}}^{\dagger}. \tag{6.39}$$

The pseudo-inverse is then constructed from these matrices

$$\bar{\gamma}^{+} = \bar{\mathbf{V}}\bar{\Sigma}^{+}\bar{\mathbf{U}}^{\dagger} \tag{6.40}$$

---

[7] A Cholesky decomposition can be performed on any Hermitian, positive definite matrix. Our inverse noise matrix, assumed to be diagonal with entries given by the reciprocal of the product of the power spectral densities will satisfy these requirements [215].

where $\bar{\Sigma}^{+}$ is found by taking the reciprocal of each (nonzero) singular value and then taking the transpose. In this process, we can also regularize this matrix, which means manually setting to zero any singular values that are smaller than some minimum s_{min}. When talking about s_{min} we will typically assume we have normalized the singular values such that the maximum is 1. A plot of the singular values of the P-wave overlap reduction function using all instruments and channels in the Homestake array is shown in figure 6.17.

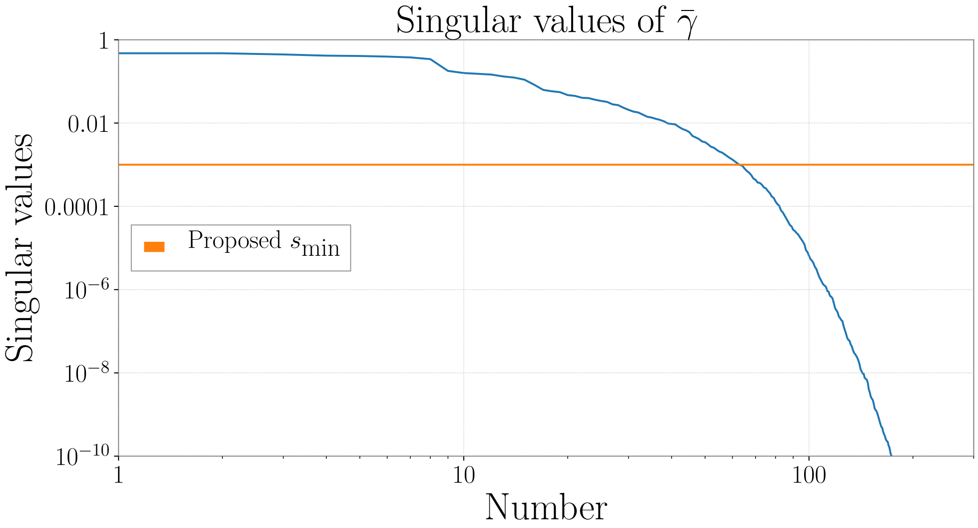

Figure 6.17: Singular values of P-wave overlap reduction function using all instruments and channels in the Homestake seismometer array. In this case we have normalized the singular values such that the maximum is 1. In orange is a proposed cutoff, s_{min}.

The choice of s_{min} is important. Small values of s_{min} will increase the variance of the estimator because we allow for smaller values of $\bar{\Sigma}$ which will cause more large values in $\bar{\gamma}^{+}$. Small s_{min} values, though, will also leave fewer null or close-to-null directions, increasing resolution. On the other hand, large values of s_{min} reduces covariance but increase the number of null-directions and the spread of a point-source on the two-sphere.

$$\text{var}(\hat{\mathbf{M}}_{\text{ML}}) = \langle \hat{\mathbf{M}}_{\text{ML}} \hat{\mathbf{M}}_{\text{ML}}^{\dagger} \rangle - \langle \hat{\mathbf{M}}_{\text{ML}} \rangle \langle \hat{\mathbf{M}}_{\text{ML}}^{\dagger} \rangle \approx \bar{\gamma}^{+} \left(\bar{\gamma}^{+}\right)^{\dagger} . \tag{6.41}$$

Unfortunately, for our purposes this weak signal limit does not hold, and so our covariance matrix is more difficult to calculate. It will typically involve the amplitude of the signal itself. See section 5 of [63], for example. We will not discuss this full calculation further.

Before discussing how to choose $s_{\min}$ we define the “model resolution matrix,” $\mathcal{M}$, and the “map coherence,” $\mathcal{C}$

$$\mathcal{M} = \bar{\gamma}^{+}\bar{\gamma} \tag{6.42}$$

$$\mathcal{C} = \frac{\frac{1}{2}(\mathbf{M}_1^{\dagger}\mathbf{M}_2 + \mathbf{M}_2^{\dagger}\mathbf{M}_1)}{\sqrt{(\mathbf{M}_1^{\dagger}\mathbf{M}_1)(\mathbf{M}_2^{\dagger}\mathbf{M}_2)}}. \tag{6.43}$$

$\mathcal{M}$ helps us look at the bias in our recovery given some regularized pseudo-inverse and $\mathcal{C}$ helps us compare two maps, $\mathbf{M}_1$ and $\mathbf{M}_2$.

$\mathcal{M}$ is a symmetric matrix that is the identity matrix when $\mathcal{F}$ is invertible. The columns of $\mathcal{M}$ show the spread on the sky that one would see assuming a unity-amplitude injection at the pixel associated with that column. We can see this by observing that for some “true” map $\mathbf{M}_{\text{true}}$, our cross-spectra $\mathbf{Y}$, *in the absence of noise*, should be given by $Y = \gamma\mathbf{M}_{\text{true}}$. In this case, our estimator has the form

$$\hat{\mathbf{M}}_{\text{ML}}^{\text{no noise}} = \bar{\gamma}^{+}\mathbf{Y} \tag{6.44}$$

$$= \bar{\gamma}^{+}(\gamma\mathbf{M}_{\text{true}}) \tag{6.45}$$

$$= \mathcal{M}\mathbf{M}_{\text{true}}. \tag{6.46}$$

If $\mathbf{M}_{\text{true}}$ has a single non-zero value, then it corresponds to picking out a column of $\mathcal{M}$. If we plot a column of $\mathcal{M}$ as a map we should see a bright spot whose size depends upon $s_{\min}$, which is done in figure 6.18 for $s_{\min} = 10^{-3}$.

This plot, and all other maps, use the `HEALPix`[8] [218] formalism for pixelating the two-sphere for P and S-waves. This helps reduce over-sampling near the poles and reduces the total number of basis elements we analyze. Plots are made using the `healpy`[9]

---

[8] `http://healpix.sf.net`

[9] `https://github.com/healpy/healpy`

python package. All matrix algebra is performed using the `scipy.linalg`[10]. All simulations are done, and overlap reduction functions calculated, with all available channels in the Homestake seismometer array unless otherwise specified.

In figure 6.19 we show $\mathcal{M}$ and the corresponding P-wave maximum likelihood recovery map, $\hat{\mathbf{P}}_{\rm ML}$, for a simulated signal in the same place (the injection scheme will be discussed further in the next section). We see that for very small values of $s_{\rm min}$, the noise in the map, $\hat{\mathbf{P}}_{\rm ML}$, is very loud and we cannot even see the injection. This comes from very small values of $\bar{\Sigma}$, which correspond to null or near-null directions, amplifying noise in the cross-spectra, $\mathbf{Y}$. This same noise doesn't exist when multiplying $\mathcal{M}$ by $\mathbf{P}_{\rm true}$ because outside of a single pixel, all other values of $\mathbf{P}_{\rm true}$ are zero. As we increase $s_{\rm min}$ the injection emerges, but with very little SNR compared to the surrounding pixels. Finally, we see the spot size grow, but its significance with respect to the other pixels in the map grows as well. This exemplifies the trade-off between covariance and resolution we discussed previously.

In figure 6.20 we attempt to quantify the trade-off discussed in the previous paragraph. We look at the map coherence between $\mathcal{M}\mathbf{P}_{\rm true}$ and $\hat{\mathbf{P}}_{\rm ML}$ for a P-wave propagating in the East direction. We do this for different choices of $s_{\rm min}$. This can be thought of as calculating $\mathcal{C}$ between the left and right columns of figure 6.19. Figure 6.20 shows how the coherence between the ideal recovery and the actual recovered maps change as a function of $s_{\rm min}$. We would like to have very good map coherence between these two cases, but also maintain a reasonable level of resolution. We see that the coherence begins to level off near $s_{\rm min} \approx 10^{-3}$ and so this is a reasonable choice for the SVD cutoff. This choice will likely be source-type specific.

If we want to extend to recovering multiple modes of the seismic field simultaneously we can stack our γ matrices for different modes. So if we want to recover maps for P and R-waves simultaneously, then our new gamma matrix in equation (6.35) becomes

$$\gamma_{\rm tot} = \overbrace{\begin{pmatrix} \underbrace{\gamma_P}_{N_{\rm pairs}\times N_{\rm b.e.}} & \underbrace{\gamma_R}_{N_{\rm pairs}\times N_{\rm b.e.}} \end{pmatrix}}^{N_{\rm pairs}\times(N_{\rm modes}N_{\rm b.e.})} \tag{6.47}$$

and $\mathbf{M}_{\rm ML}$ becomes a column matrix with maps for each mode stacked on top of one

---

[10] `https://docs.scipy.org/doc/scipy/reference/linalg.html`

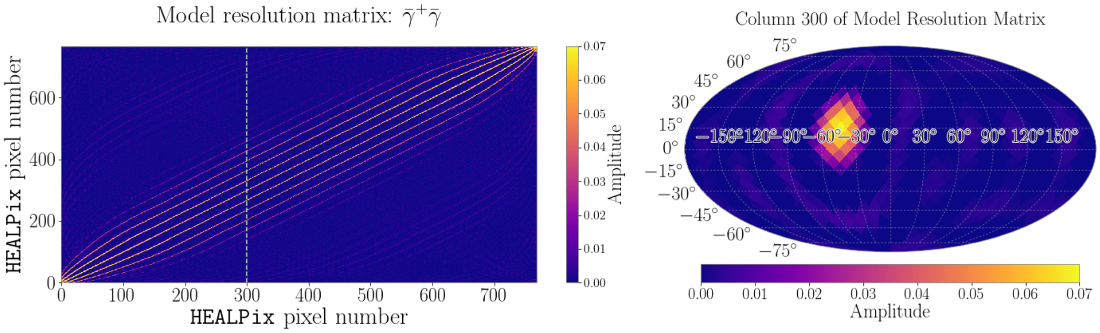

Figure 6.18: The left is a the full model resolution matrix of the P-wave overlap reduction function. On the right is column 300 of the model resolution matrix plotted as a map. The bright lines on the left plot show up as bright pixels on the right plot. In this case, the bright lines on the left plot are separated because of the order in which the `HEALPix` program reads pixels.

another. It now has shape $(N_{\text{modes}}N_{\text{b.e.}}) \times 1$. In figure 6.21 we show a column from each separate block of the model resolution matrix. If we consider now simultaneous recovery of P- and R-waves using an overlap reduction function like equation (6.47), then in figure 6.21 we plot

$$\hat{\mathbf{J}}_{\text{ML}}^{\text{no noise}} = \mathcal{M}\mathbf{J}_{\text{true}} \tag{6.48}$$

under a few different conditions. In this case, we have used "J" to indicate that this is a "joint" recovery of multiple modes of the seismic field at the same time. The top row corresponds to the R- and P-wave portions of $\hat{\mathbf{J}}_{\text{ML}}^{\text{no noise}}$ where $\mathbf{J}_{\text{true}}$ corresponds to a unity-amplitude P-wave injection. The bottom row corresponds to the same thing for a unity-amplitude R-wave injection. This shows us how, in theory, P-wave injections should show up in R-wave maps, and vice-versa.

6.4.4 Angular resolution of seismic radiometer

There are a few ways to study the angular scale we are capable of resolving with the seismic radiometer. The simplest is to use a back-of-the-envelope calculation of the resolution one can achieve using our array based on the extent of the array and the wavelength of the source. This has been used in the GW community to estimate the

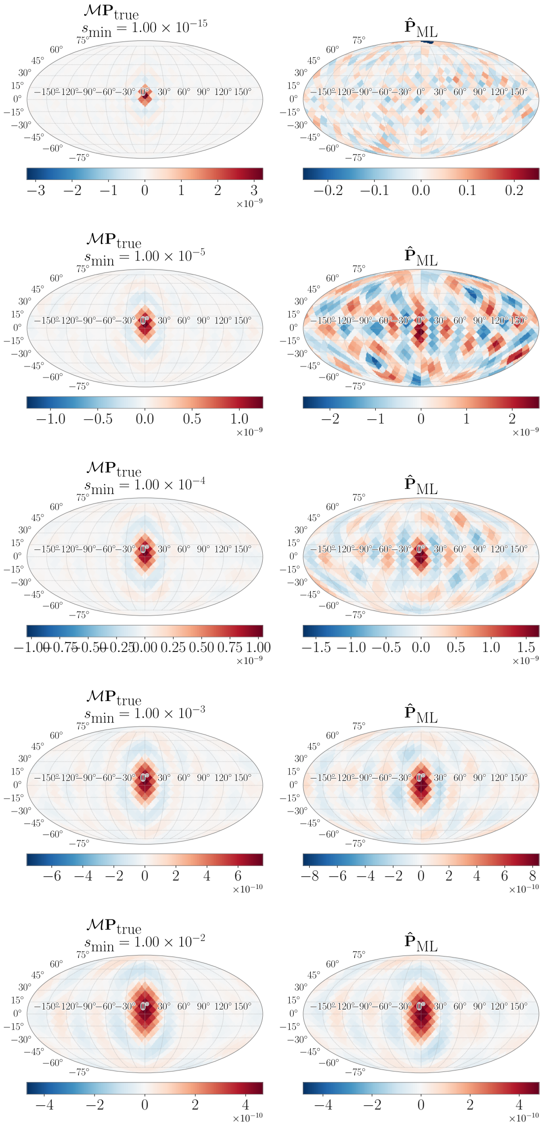

Figure 6.19: The left is a column of the model resolution matrix of the P-wave overlap reduction function, plotted as a map. On the right is the maximum likelihood recovery for a simulated P-wave injection. We discuss how these injections are performed further in section 6.4.5. Each row represents a different choice of s_{min}. We see that as as the spot size in the model resolution plots increases, the covariance in each pixel decreases. This is the trade-off we must make because our system is underdetermined (i.e. $N_{\mathrm{pairs}} < N_{\mathrm{b.e.}}$).

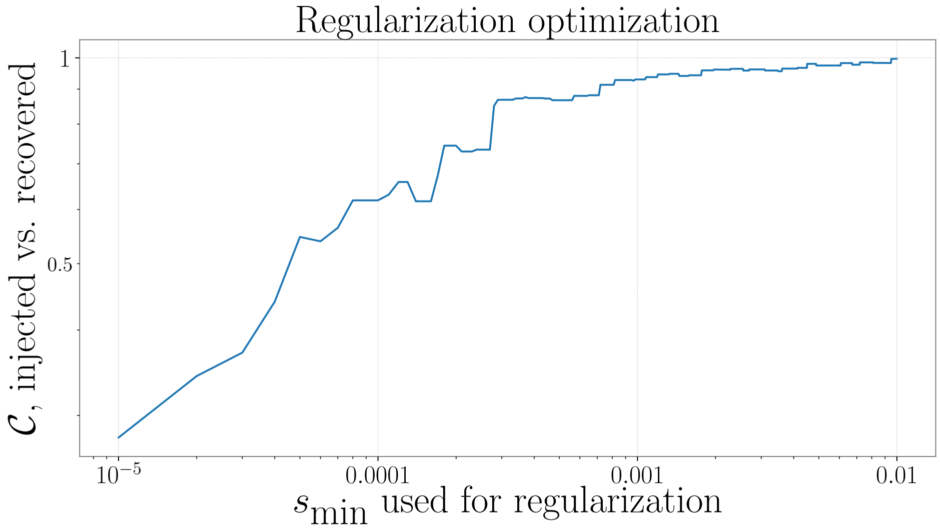

Figure 6.20: Map coherence, $\mathcal{C}$, between a map with a P-wave injected into one pixel, $\mathcal{M}\mathbf{P}_{\text{true}}$, and a map where we inject and recover a simulated P-wave, $\hat{\mathbf{P}}_{\text{ML}}$, for various values of s_{min}. We see that the coherence begins to level off at $s_{\text{min}} \approx 1 \times 10^{-3}$. Smaller values will make the resolution of the recovery worse, while offering minimal increases in coherence between maps.

resolution for the GW radiometer [122], and is common in the astronomical interferometer community as well. The rough estimate of the resolution is given by

$$\Delta\theta \approx \frac{\lambda}{2d} \tag{6.49}$$

where d is the projected distance between stations and λ is the wavelength. In our case this will likely be polar angle and azimuthal angle-dependent because the array has different projected distances in different directions. However, in general, if we estimate $d \approx 5$ km then

$$\Delta\theta \approx \frac{\lambda}{10\text{ km}}. \tag{6.50}$$

We also calculate resolution for our array by producing $\mathcal{M}\mathbf{M}_{\text{true}}$ where $\mathbf{M}_{\text{true}}$ corresponds to an East-propagating wave for wave type m. The SVD cutoff in this case is 10^{-3} for all cases. The resolution for the array is estimated by drawing a contour around the region containing 95 % of the total map power and finding the maximum

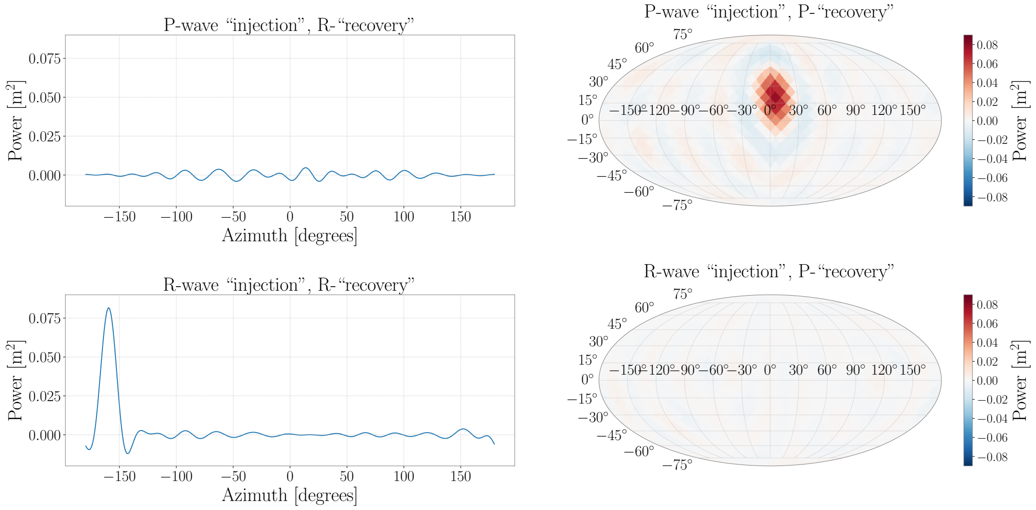

Figure 6.21: $\mathcal{M}\mathbf{J}_{\mathrm{true}}$ for a combined P- and R-wave overlap reduction function for two different choices of $\mathbf{J}_{\mathrm{true}}$. The top row corresponds to a simple P-wave injection and the bottom row corresponds to a single R-wave injection. Regularization is done with $s_{\mathrm{min}} = 10^{-3}$. These are not full-scale injections where we calculate cross-spectrum, $\mathbf{Y}$ between all of our channels and solve equation (6.37), but instead correspond to the zero-noise situation of equation (6.44).

extent in azimuthal and polar angles that the contour encompasses. The resolution as a function of wavelength, along with the diffraction limit estimate, is shown in figure 6.22. We observe better resolution in the azimuthal angle than in the polar angle, which is likely due to the fact that the array is just ∼1.5 km deep but is ∼5 km wide. We have also put the diffraction limit estimate, given by equation (6.49), on each plot. We see that in general after a certain wavelength we stop being limited due to the diffraction limit. This is because we are using polarization information for the direction recovery, as opposed to time-delays between stations. We must be careful when working in this regime, because in this regime it can be difficult to distinguish between two waves propagating with roughly equal amplitude, like the case shown below in figure 6.23.

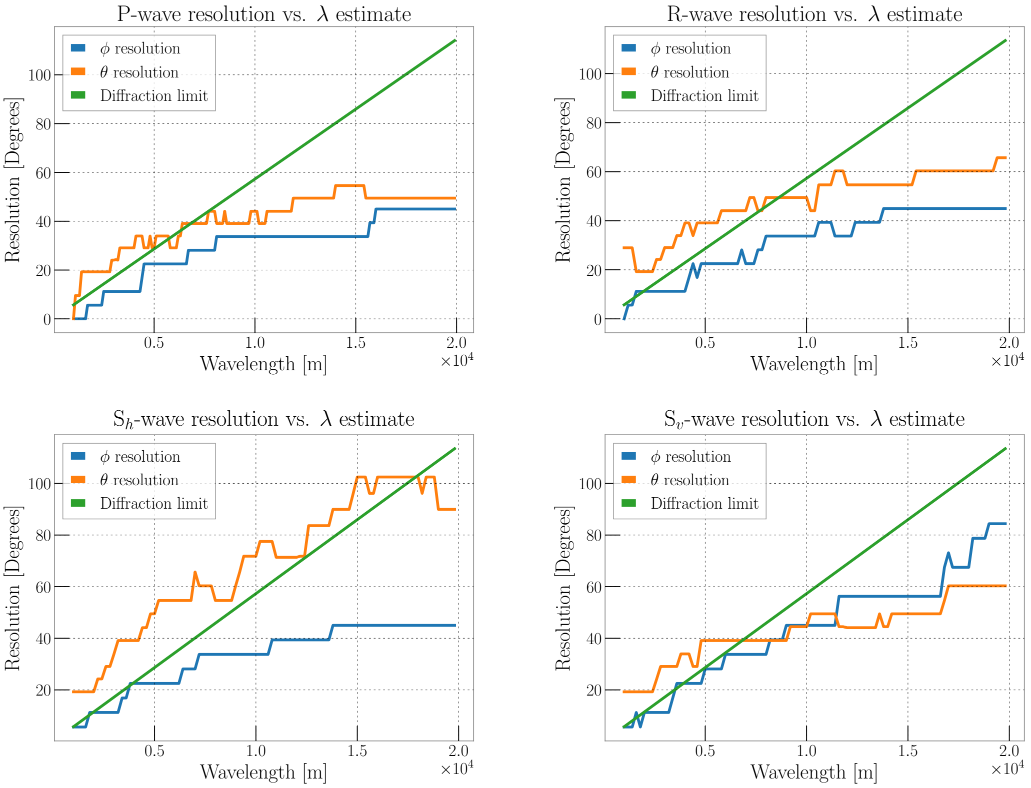

Figure 6.22: An estimate of the angular resolution for the different components of the seismic field. We calculate this resolution using $\mathcal{M}\mathbf{M}_{\text{true}}$ where $\mathbf{M}_{\text{true}}$ corresponds to an East-propagating wave for each wave type. The resolution is estimated by drawing a contour around the region containing 95 % of the total map power and finding the extent in azimuth and polar angle that contour encompasses. We see that in general we have better azimuth resolution than polar angle, which is likely due to the fact that the array is just ~1.5 km deep but is ~5 km wide. We have also put the diffraction limit estimate on each plot. We see that in general after a certain wavelength we stop being limited due to the diffraction limit. This is likely because we are primarily using polarization information for the recovery, as opposed to time-delays between the instruments. We must be careful when working in this limit because it can be difficult to distinguish between two waves propagating of roughly equal amplitude, like the case shown below in figure 6.23.

6.4.5 Software injections

We perform software injections for various situations to validate our method and to test end-to-end examples of what might arise in practice. All software injections presented below are performed at 1 Hz. We generate a 1 Hz sinusoidal timeseries with amplitude 10^{-4} m for different components of the seismic field. We then apply phase delays for the data for each individual station such that the phase difference in the data between each station is consistent with the travel time between those stations. As a first check, we verified by eye, using simple examples, that the injected signals propagate across the array in the correct direction and with the correct polarization. This includes checking the vertical-to-radial phase for R-waves and the polarization direction for East-traveling P-, S-, and R-waves.

These injections do not include any sort of simulated instrument noise, as the instrument noise is generally expected to be at least an order of magnitude lower than the seismic field. For all recoveries we use 200 s of data and calculate the cross-spectrum between each channel pair by multiplying the Fourier transforms of the two channels at the frequency of interest (1 Hz for all injections in this section). We use 50 s Fourier transforms, meaning the final cross-spectrum for each channel pair is averaged over four time segments. We then multiply the cross-spectra by the frequency bin width (0.02 Hz) so that the units of the cross-spectra are in m^2 as opposed to m^2/Hz. These final cross-spectra constitute the $\mathbf{Y}$ we use in equation (6.37).

Below, we will discuss estimates for the recovered amplitude of the injected waves. In general, this is done by summing the power across all pixels in the map. The implicit assumption here is that pixels not associated with our peak will sum to zero over the rest of the map. An alternative method would be to identify peaks in the map and report total power associated with each peak.

In figure 6.23 we show the recovery when we have injected two point sources of P-waves. In this case, the recovered total amplitude in the map is larger than expected by a factor of $\sim 25\%$. When we inject just a single P-wave, we recover the correct direction and amplitude reliably. The “expected” recovery assumes that the two waves will add incoherently, i.e. that if one wave has Fourier amplitude $\tilde{a}_1(f)$ and the other has Fourier amplitude $\tilde{a}_2(f)$, then total recovered power in the radiometer map would be $|\tilde{a}_1(f)|^2 + |\tilde{a}_2(f)|^2$. Given that we have injected two sinusoidal waves with stationary phases, these waves will be coherent and so there will be cross terms and the amplitude we measure will be larger than if we were to add the amplitude of the two waves incoherently. In fact, the recovery amplitude when there are two P-waves depends strongly on the direction of the two waves: If one is traveling East and the other is traveling vertically, then there is no coherence and the amplitudes add incoherently. If they are both traveling East, then the waves add completely coherently.

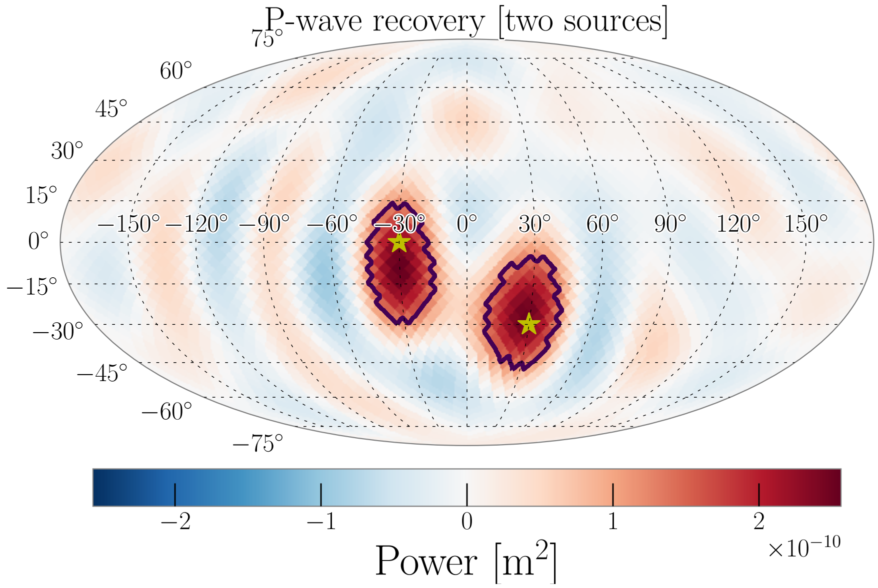

Figure 6.23: We show the injection and recovery of pressure waves. There are two injected sources indicated by stars. In this case the recovered amplitude in the map is larger than expected, at 2.6×10^{-8} m^2 instead of 2×10^{-8} m^2. The contours enclose 95 % of the total map power. The larger than "expected" amplitude has to do with coherence between the two signals breaking one of the assumptions of the seismic radiometer. This is discussed further in the text.

In figure 6.24 we show the recovery for an injection of S$_h$-waves and the separate recovery maps for the two different S-wave polarizations. In this case, the amplitude recovered is correct. In figure 6.25 we show the recovery maps when we inject P and R-waves and recover both simultaneously. We recover amplitudes that are within 10 % of the injected values. Finally, in figure 6.26 we show recovery in the case where we have injected P, S_h, and R-waves in different directions, and try to recover all three

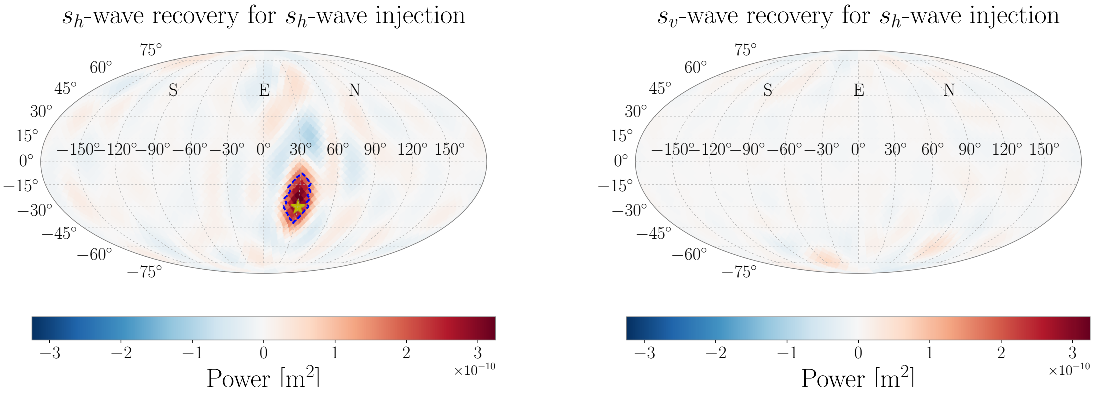

Figure 6.24: Injection and recovery of a horizontally polarized shear wave with $\lambda = 3.3\,\mathrm{km}$ using the full Homestake seismometer array. We clearly see the recovered wave in the map for horizontal polarization and we see nothing in the vertically polarized map. The recovered power in the map is 0.92×10^{-9} m^2 compared with the injected value of 10^{-8} m^2. The contours enclose 90 % of the total map power.

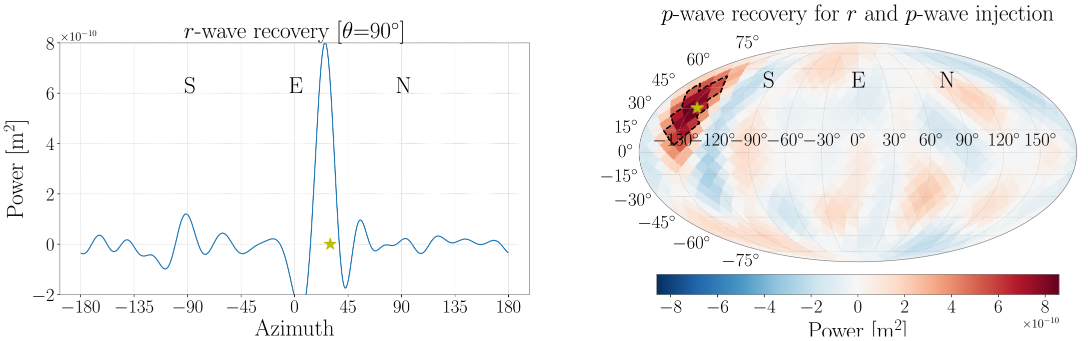

Figure 6.25: Rayleigh and P-wave injection and recoveries. Both injections have power at $10^{-8}\,\mathrm{m}^2$. The R-wave total map power is 1.05×10^{-8} m^2 and the P-wave total map power is 1.16×10^{-8} m^2. The contours enclose 95 % of the total map power.

at once. We see peaks in roughly the correct directions for all cases; however, there appears to be power from P-waves leaking into the S_v wave map, and potentially some R-waves being seen in the P-wave map. The amplitudes of these recoveries (listed in the captions) also show significant bias. In addition, recovery of these different types of waves becomes especially unreliable near the poles (i.e. a vertically propagating wave). Injections within 30° of the poles begin to become degenerate across maps and much more difficult to resolve. This can also be seen by looking at the the model resolution matrix that encompasses all 4 wave types. For situations where we are dominated by a

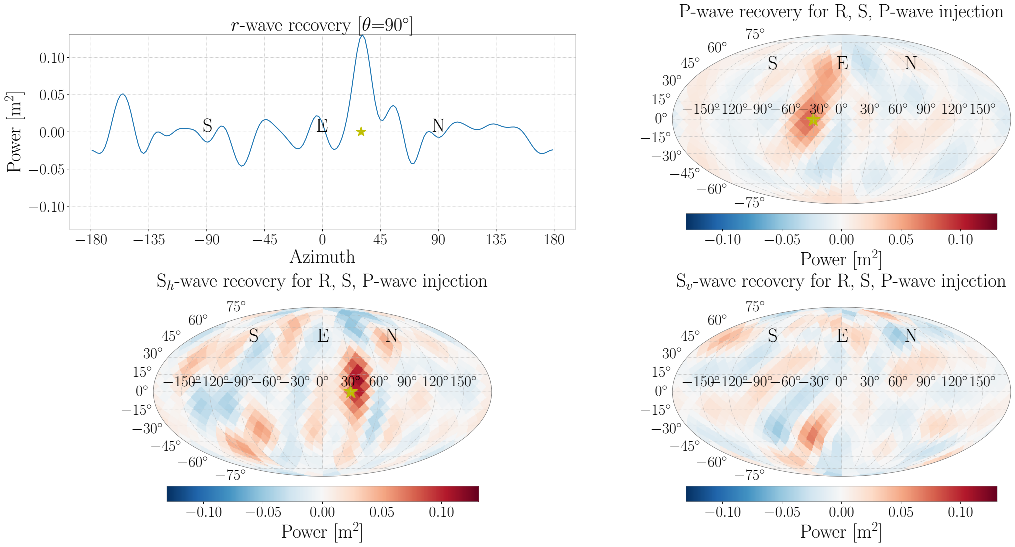
r-wave recovery [θ=90°]

P-wave recovery for R, S, P-wave injection

S$_h$-wave recovery for R, S, P-wave injection

S$_v$-wave recovery for R, S, P-wave injection

Figure 6.26: R-, P-, and S$_h$-wave injection and recovery. The total power in each map is biased. The injection strength was unity for all three injections, while the total power in the R-wave map was 0.55 m^2, for the P-wave map it is 1.50 m^2, and for the S$_h$-wave map it is 2.24 m^2. Adding the power across all four maps yields a total amplitude of 4 m^2, which is too large by a factor of 33 %. For these injections $\lambda_R = 2500$ m, $\lambda_P = 5700$ m, and $\lambda_S = 4000$ m. The contours enclose 95 % of the total map power.

single source of waves, we will likely recover the correct amplitude and direction of the waves. In cases where there are several different wave types with similar amplitudes, our direction recoveries will likely be informative, but the amplitude estimates are unreliable. This likely has to do with the fact that the different modes can also add coherently (like the case of two P-waves above). Understanding this effect will be important for properly interpreting maps we make in the future. While we will run full-scale inversions for R, S, and P-waves together, it is important to keep these issues in mind.

6.4.6 Real data applications

Source at 1.5 Hz

There is an obvious and strong source of seismic waves from $1.5 - 2.0$ Hz that shows up in several stations in the Homestake seismometer array. It is most prominent in the surface stations. The phase between the vertical and horizontal channels for these stations indicates that we see mostly Rayleigh waves. The source also seems to turn on and off at various times during the day. In figure 6.27 we show the phase difference between vertical and horizontal channels for the `YATES` station, and a timeseries plot with a narrow band-pass filter around 1.5 Hz for a period of twelve hours. It shows the source going from off to on about half an hour into the time-period. We would like to use this source as a test bed for the radiometer algorithm. To do this, we first attempt to use only the time-delays between the seismometers to localize the direction of the source assuming the field consists of plane-waves. Then we run the radiometer algorithm. We show that there is obvious consistency between these two approaches, and that the radiometer algorithm shows indication for much higher amplitudes for R-waves than for body waves.

Timing analysis—The phase delay, ϑ, for a surface plane-wave between two different seismometer channels will depend on the velocity, v, the azimuth of the source, ϕ, and a vector pointing between the two stations, $\vec{x}_1 - \vec{x}_2$

$$\vartheta = \frac{2\pi f(\vec{x}_1 - \vec{x}_2) \cdot \hat{\Omega}}{v} \tag{6.51}$$

where $\hat{\Omega} = (\cos\phi, \sin\phi)$. We measure the phase delay between stations 1 and 2, ϑ_{12}, by multiplying the Fourier transforms of detectors 1 and 2 together and finding the complex phase of that cross-spectrum:

$$\rho = \tilde{Z}_1^*(f) \times \tilde{Z}_2(f) \tag{6.52}$$

$$\vartheta_{12}(f) = \arctan\left(\frac{\mathrm{Imag}\,\rho}{\mathrm{Real}\,\rho}\right). \tag{6.53}$$

In this case $\tilde{Z}_I(f)$ is the Fourier transform of the vertical channel of seismometer I and star indicates complex conjugation. We use only stations YATES, ROSS, ORO, DEAD,

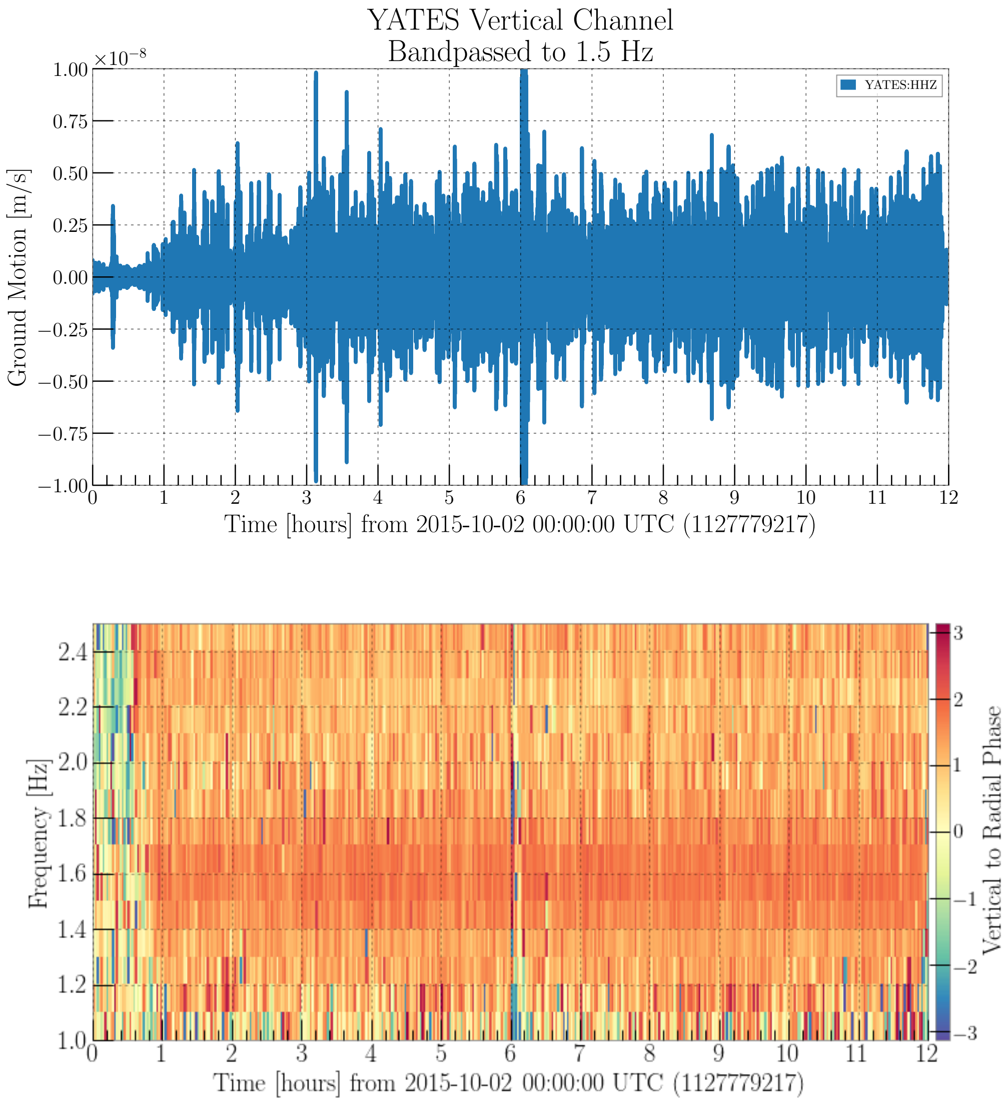

Figure 6.27: Top: Timeseries for YATES station, bandpass filtered between 1.49 and 1.51 Hz for the first twelve hours of October 2nd, 2015. Bottom is the vertical-to-horizontal phase between the East and the Vertical channels of the `YATES` station. It is clear that the phase hovers near $\pi/2$ radians, which is consistent with the retrograde motion we expect from Rayleigh waves. We also see that there are periods where this source of surface waves appears to turn off and then turn back on.

TPK, and 300, as these stations see the source most strongly. We use 1 hour of data

Parameter	**Recovered Value**
ϕ	$2.4^{+0.7}_{-0.7}$ degrees
c	$2.94^{+.07}_{-.07}$ km/s
$\log \mathcal{B}^{\text{surface plane}}_{\text{noise}}$	794

Table 6.6: We show results for parameter estimation using only a subset of stations for the timing-only analysis where we model the phases between pairs of seismometers as if the data consists of a single surface plane-wave. The log Bayes factor is calculated by comparing the marginal likelihood using our model to the marginal likelihood in the case where we replace our model with zeros. It shows strong evidence for the surface-plane-wave model compared to a model with no preference for direction.

starting from October 2nd, 2015 03:00 UTC. We use 100 s fast Fourier transforms at 1.5 Hz, which corresponds to 36 phase measurements for each channel pair.

We then use data in a student's-t likelihood (because we do not have a reliable method of finding the variance on ϑ) to try to estimate ϕ and v. The likelihood function is

$$p(\{\vartheta\}\,|\hat{\Omega}, v) = \Pi_{i=1}^{N_{pairs}} \frac{\Gamma(m_i/2-1)}{2\pi^{m_i/2-1}} \left(\sum_{k=1}^{m_i} \left|\vartheta_{i,k} - \frac{2\pi f \hat{\Omega}\cdot\Delta\vec{x}_i}{v}\right|^2\right)^{-m_i/2}, \tag{6.54}$$

where m_i is the number of phase measurements for detector pair i (in this case 36), and Γ is the gamma function. We ran a Bayesian analysis where we evaluated the above likelihood function on a grid of points for the propagation direction ϕ and velocity v. We also constructed Bayes factors to determine whether the surface-plane-wave model is preferred to a noise-only model. The parameters for the analysis and the results are summarized in table 6.6. The 2-D posterior and 1-D marginalized posteriors for the velocity and direction using this model can be found in figure 6.28.

We see that the posterior distributions are very strongly peaked for both azimuth of the source, ϕ, and velocity, v. The velocity is consistent with the expected velocity of R-waves at a frequency of 1.5 Hz, and the azimuth roughly corresponds to a wave traveling in the East direction. This analysis offers a solid basis for cross-checking the

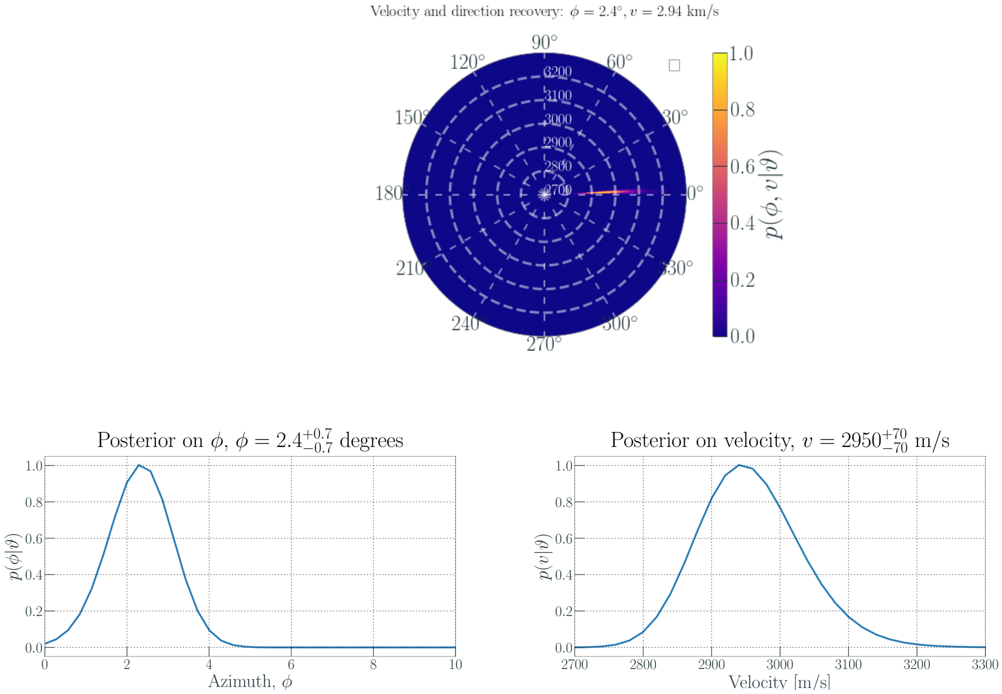

Velocity and direction recovery: $\phi = 2.4°, v = 2.94$ km/s

Posterior on ϕ, $\phi = 2.4^{+0.7}_{-0.7}$ degrees

Posterior on velocity, $v = 2950^{+70}_{-70}$ m/s

Figure 6.28: Above we show the posterior distribution for the phase-delay analysis for a persistent 1.5 Hz source. The source direction is roughly consistent with a second gold mine located outside of Lead, SD.

results of the radiometer analysis.

Radiometer matrix inversion analysis—We run the radiometer recovery using cross-correlations averaged over 12 hours of data, although using shorter periods of time yields self-consistent results. The results are summarized in the plots in figure 6.29, where we see clear evidence for R-waves in roughly the same direction as the timing-only analysis above. The plots also show a histogram of pixels normalized by the median of the absolute value of all pixels in the map. This should help add intuition to the idea that we see a strong peak for R-waves, while for P-waves (despite the bold colors) there are no obvious directions that dominate. The total sum power in each map are 1.2×10^{-19} m^2 for body waves and 7.2×10^{-19} m^2 for R-waves, again indicating that we see strong evidence for R-waves.

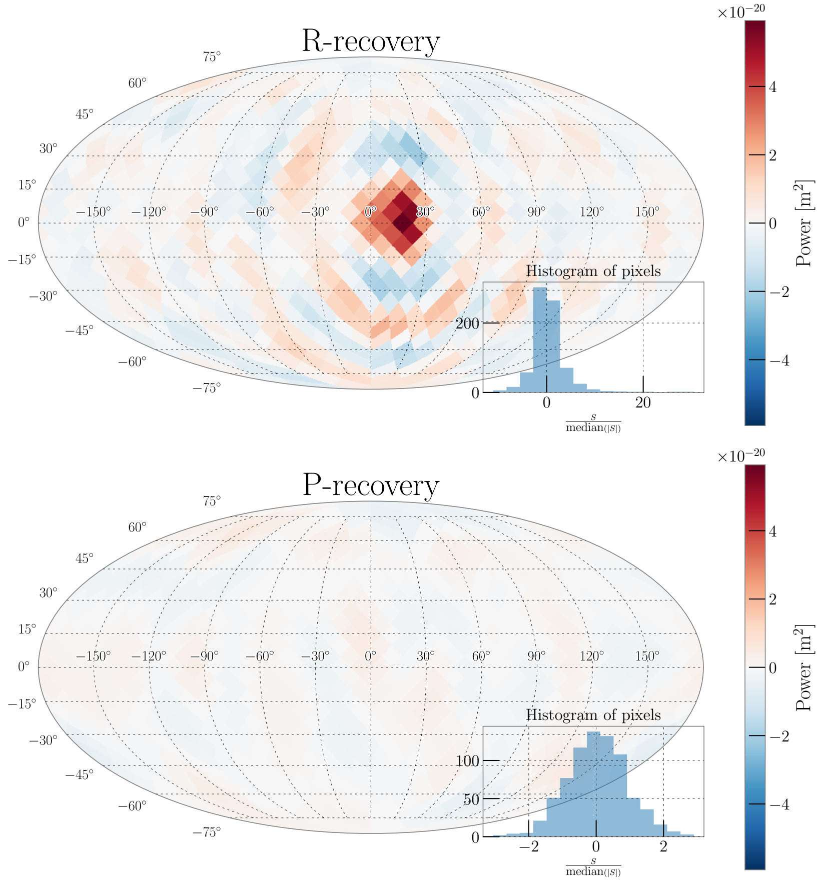

Figure 6.29: Recovery of 1.5 Hz source from October 2nd 03:00-04:00 UTC. We see that there is a strong peak between 0 and 30° for R-waves, while for P-waves there is no obviously preferred direction. The total power in the R-wave map is 7.2×10^{-19} m^2 while for P-waves it is more than a factor of 5 times lower at 1.2×10^{-19} m^2.

Microseism measurements

The oceanic microseism is the cause of the peaks that dominate the spectra seen in section 6.2.3 at low frequencies. These peaks are caused by ocean waves interacting with the continent, and tend to be elevated when wave heights are higher. There is evidence in our data that indicates that during times when the microseism has low amplitude in our data, the dominant source of seismic waves at low frequencies are body waves, while when the microseism has high amplitude, the dominant source of seismic waves in our array is R-waves. This evidence is discussed further in [213].

As a second test of the seismic radiometer, I attempted to recover P-, S-, and R-waves at 0.2 Hz on a day when the microseism is relatively quiet and a day when the microseism is at a higher level.

The first recovery comes on a day when the microseism is elevated, and the results show evidence for a preference for R-waves propagating in the westward direction. By comparison, there is no obviously preferred direction in the body-wave maps. The total power in each map is summarized in table 6.7, which shows that there is slight preference for R-waves over body waves in our data. The power in the individual body wave maps fluctuates with the choice of SVD cutoff, but the total power across all three of those maps remains relatively consistent. This likely has to do with the fact that there is very little information gained from the phase differences between individual stations due to the very large wavelengths of the body-waves, and so most of this information comes solely from the amplitude seen in the individual NS/EW/vertical channels. The properties of the R-wave eigenfunctions, however, can help us to distinguish between R-waves and body waves, even in the absence of the information from phase-delays between stations.

Wave type	Total map power [m^2]
R	1.7×10^{-14}
P	2.4×10^{-15}
S_h	2.9×10^{-15}
S_v	8.7×10^{-15}
Total Body	1.4×10^{-14}

Table 6.7: Results for seismic radiometer at 0.2 Hz July 10th, 2015, when the microseism is elevated. The results above are made using an SVD regularization cutoff of 0.005. While total power in each individual body-wave map recovery varies with the choice of the SVD regularization, the ratio of R-wave to body-wave total power does not. We see that the total power in R-waves is larger than that of body waves, although we do not have estimates of the uncertainty on these values yet.

The second test of the radiometer method on the microseism comes on a day when

---

[11] The reason for this is that a recovery for R-waves with an incorrect polar angle is often what happens when one performs a recovery with an incorrect velocity

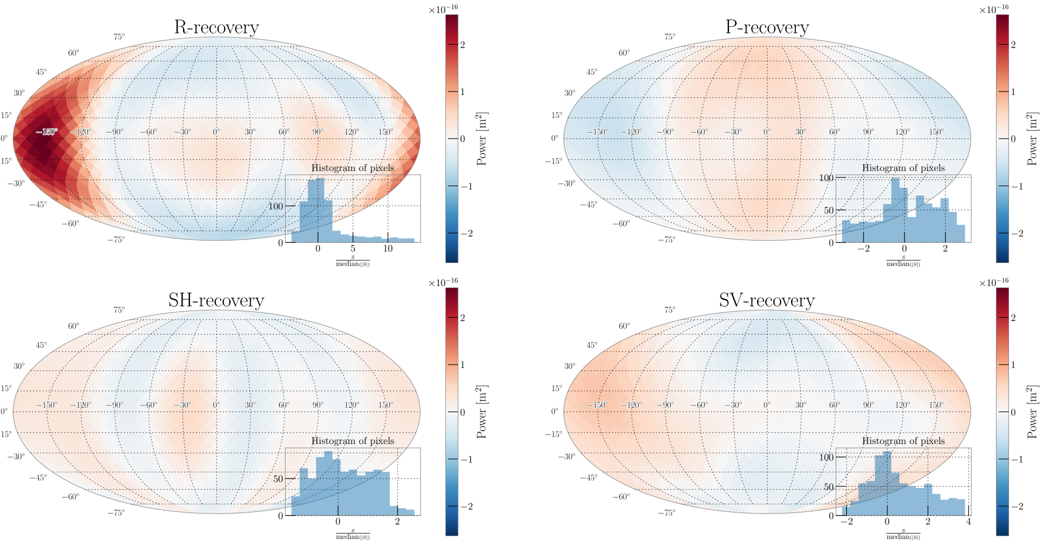

Figure 6.30: Surface and body wave recoveries for microseism on July 10th, 2015, for three hours. In this case, we allow the polar angle of the surface waves to vary[11]. The color scale on all four plots is the same, to emphasize the strong preference for R-waves. We use velocities of 3500 m/s for R-waves, 7000 m/s for P-waves, and 5000 m/s for S-waves. The R-wave velocity comes from an estimate using very-long-duration correlations [213], as do the body wave velocity estimates. The total sum power power across the body-wave maps is 1.4×10^{-14} m^2 while for R-waves it is 1.7×10^{-14} m^2. The ratio of the total power in body waves to surface waves is independent of the choice of cutoff for the SVD regularization, as is the dominant direction. The choice of SVD regularization cutoff for the maps above is 0.005. The pixel histograms are normalized by the median of the absolute value of all pixels across all maps.

the microseism is relatively quiet. On these days, there is evidence that there is significant body-wave content in our data [213]. This is borne out in the recoveries with the seismic radiometer. The total map power across all of the body-wave recoveries is significantly larger than the R-wave recovery. As in the previous case, the individual body-wave map recoveries show varying total power with a change in the choice of the cutoff for SVD regularization, but the overall ratio of R-wave to body-wave power is relatively stable. There is no preferred direction across any of the maps, which are shown in figure 6.31. The total map power in the recoveries for an SVD-cutoff of 0.005 are shown in table 6.8.

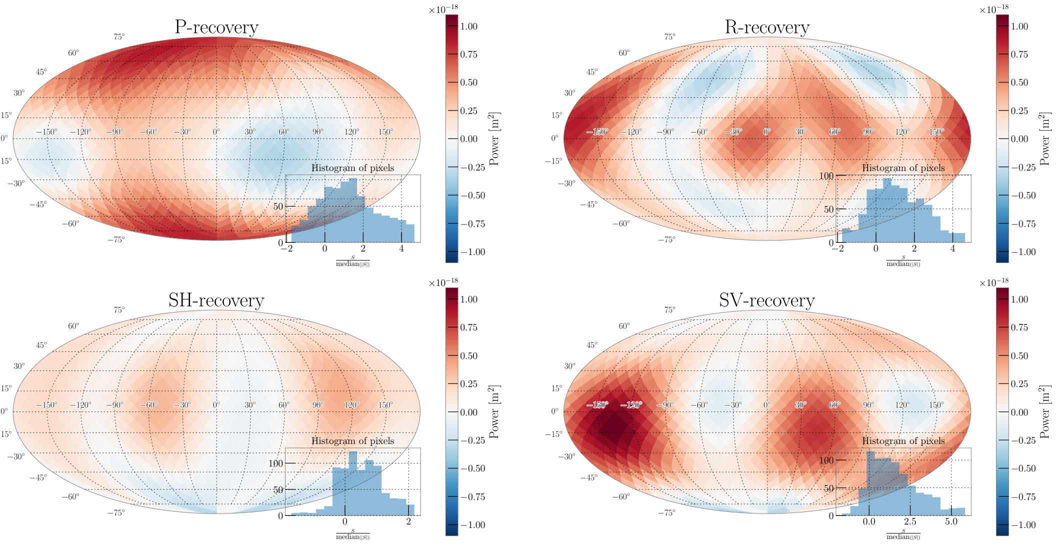
P-recovery

R-recovery

SH-recovery

SV-recovery

Figure 6.31: Surface and body wave recoveries for microseism on June 3rd, 2015 for twelve hours. In this case, we allow the polar angle of the surface waves to vary. The color scale on all four plots is the same, to emphasize that in this case there is little preference between wave types. We use velocities of 3500 m/s for R-waves, 7000 m/s for P-waves, and 5000 m/s for S-waves. The R-wave velocity comes from an estimate using very-long-duration correlations [213], as do the body wave velocity estimates. The total sum power across the body-wave maps is 5.8×10^{-15} m^2 while for R-waves it is 2.0×10^{-15} m^2. The result for the total power in body waves vs. surface waves is independent of the choice of cutoff for the SVD, as, generally, is the direction result across all three maps. The maps above are calculated with an SVD regularization cutoff at 0.005. The pixel histograms are normalized by the median of the absolute value of all pixels across all maps, and it shows no obviously preferred directions in any of the maps.

6.4.7 Newtonian noise estimates

Now we use the seismic radiometer to estimate the Newtonian noise from 0.5 − 5 Hz at several depths. As we discussed in section 6.1.2, the fluctuations in the acceleration field at a specific location, $\vec{r}_0$, due to a changing displacement field, $\vec{u}(\vec{r},t)$, is given by

$$\delta\vec{a}(\vec{r}_0,t) = -G\int dV\,\rho(\vec{r})(\vec{u}(\vec{r},t)\cdot\nabla_0)\frac{\vec{r}-\vec{r}_0}{|\vec{r}-\vec{r}_0|^3}, \tag{6.55}$$

Wave type	Total map power [m^2]
R	2.0×10^{-15}
P	2.2×10^{-15}
S_h	9×10^{-16}
S_v	2.7×10^{-15}
Body waves	5.8×10^{-15}

Table 6.8: Results for seismic radiometer at 0.2 Hz on June 3, 2015, when the microseism is generally quiet. The results above are made using an SVD regularization cutoff of 0.005. While total power in each individual body-wave map recovery varies with the choice of the SVD regularization, the ratio of R-wave to body-wave total power does not.

where G is Newton's gravitation constant, ρ is the density field of the solid we are considering, $\vec{u}$ is the displacement field, and ∇_0 is the gradient with respect to the reference point $\vec{r}_0$.

The noise in the GW channel of an interferometer is the differential length change between the two arms induced by something other than GWs, and so we convert this acceleration noise into displacement noise

$$h = \frac{\delta x - \delta y}{L} = \frac{\delta a_x - \delta a_y}{(2\pi f)^2 L} \tag{6.56}$$

where L is the length of the arms of the interferometer. If we assume that the motion of the four test masses adds incoherently, then the noise in the GW channel due to the acceleration induced by Newtonian noise can be found by multiplying x and y accelerations by $\sqrt{2}$ and considering the incoherent sum of the RMS accelerations

$$h_{\mathrm{NN}} = \frac{\sqrt{2\left(\delta a_{x,\mathrm{rms}}^2 + \delta a_{y,\mathrm{rms}}^2\right)}}{(2\pi f)^2 L}. \tag{6.57}$$

The fluctuations themselves, $\delta a(\vec{r}_0, t)$, are strongly dependent upon $\rho(\vec{r}, t)$ and $\vec{u}(\vec{r}, t)$. The former changes if we are considering a ground-air interface, or a geometry like a spherical cavity, or a depth-dependent density profile. The latter depends upon the seismic wave we are considering. In section 6.1.1 we discuss the displacement field due to a few different types of seismic waves. A treatment of $\delta a(\vec{r}_0, t)$ at different depths and due to many different types of seismic waves and density geometries can be found in [48]. Here we briefly summarize the different geometries and waves types considered in that manuscript

1. Incident P-waves interacting with the surface, displacing the air above the interface, and generating a reflected P-wave and a reflected S_v-wave.
2. Incident P-wave inducing density fluctuations in the rock.
3. Incident P-wave interacting with the wall of a spherical cavity, inside of which is the point of reference.
4. Incident S_v-wave interacting with the surface, displacing the air above the interface
5. Incident S_v-wave reflecting off of the surface and generating a P-wave and S_v-wave. The P-wave can then cause density fluctuations in the rock.
6. Incident S-wave interacting with the wall of a spherical cavity, inside of which is the point of reference.
7. Incident R-waves interacting with the surface. The vertical component of the wave displaces the air above the surface of the earth and the radial component generates density perturbations.
8. Incident R-waves interacting with the wall of a spherical cavity, inside of which is the point of reference.

We use maps generated by the seismic radiometer and code written by Andrew Matas, Vuk Mandic, and myself to estimate the Newtonian noise under a few different assumptions. The code is based on the calculations in [48]. The estimates are made on the same two days used for the microseism measurements. In all Newtonian noise estimates below, we assume a constant density profile of $\rho = 2.5 \times 10^3$ kg/m^3. We estimate the Newtonian noise for a set of test masses on the surface and at 4850 ft below ground. In the latter case we assume that the test masses are in a small cavity, and consider the interaction of seismic waves with the walls of that cavity as well.

On both days we generate seismic radiometer maps with data from the first two hours of the day at frequencies of $0.5 - 5$ Hz in intervals of 0.5 Hz. For each frequency, we average together many Fourier transforms that are 10 s long to calculate cross-spectra, and run the seismic radiometer inversion with an SVD cutoff of 10^{-3}.

We then calculate the total sum power across all pixels in all four maps, P_{maps}. We make sure to multiply the R-wave maps by a factor of $(1 + N_{vh}^2)$ to account for the vertical amplitude of the R-waves. This arises due to the interpretation of the R-wave maps as being the *radial* amplitude on the surface associated with the R-waves. We also calculate the total power, $P_{seis,i}$ in each seismometer, i, on the surface, summed across the three directional channels. We renormalize our radiometer maps by

$$\text{norm} = \max(P_{seis,i})/P_{maps}.$$

In this way, we interpret our maps as having correct relative amplitudes, but not necessarily correct absolute amplitudes.

Using the radiometer maps to estimate Newtonian noise requires certain assumptions and it is currently unclear how to handle certain aspects of the data. Specifically, dealing with negative power in some pixels – an artifact of the maximum likelihood method we are currently using – has proved difficult. Therefore, for the results below we assume that the total map power is distributed isotropically across all directions for each polarization. This means that the relative difference in total map power across each polarization is the main byproduct of the radiometer method used in our estimates.

The results for the Newtonian noise estimate for the two days, June 3rd 2015 and July 10th, 2015 are shown in figures 6.32 and 6.33. For these estimates we assume a Cosmic Explorer-like instrument with 40 km long arms and an "L" shaped interferometer. The figures show a design Cosmic Explorer sensitivity curve and a design Einstein Telescope sensitivity curve. The latter is not directly comparable to the Newtonian noise estimates because the interferometer has a triangular shape and 10 km long arms.

July 10th showed elevated levels of microseism compared to June 3rd, however, the levels of Newtonian noise estimated at 0.5 Hz and above are comparable, indicating that the elevated microseism has little effect on higher frequencies in the seismic field. It does appear that the 1.5 Hz source is larger on June 3rd than it is on July 10th. It is important to note that as we move from the surface to 4850 ft, we move from the Newtonian noise being domianted by surface waves to the Newtonian noise being dominated by body waves.

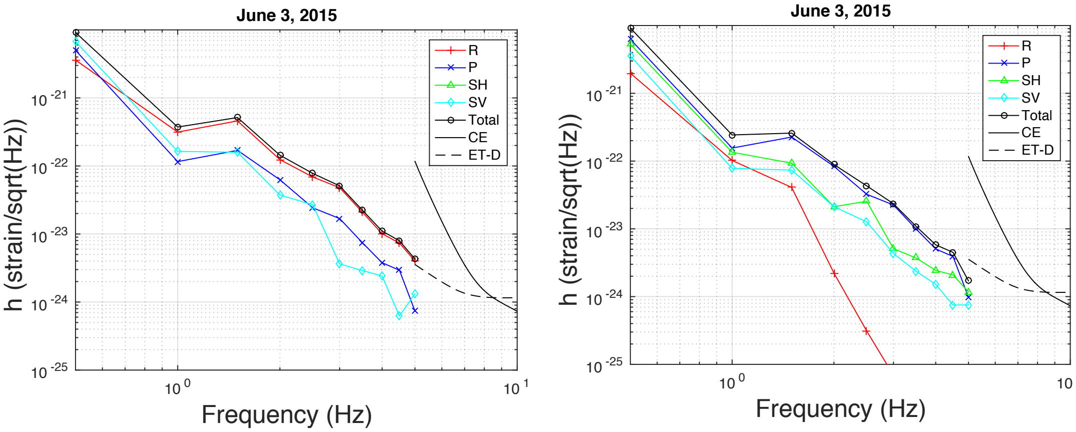

Figure 6.32: Newtonian noise estimate assuming a Cosmic Explorer-like instrument for June 3rd, 2015. The colored lines are Newtonian noise estimates using the different mechanisms above and the seismic radiometer recoveries for a cavity on the surface (left) and at 4850 ft (right). The black line (with circles) is the total Newtonian noise estimate. The solid black curve on the right of each plot indicates the estimated sensitivity for the proposed Cosmic Explorer experiment [11], while the dashed black curve indicates the estimated sensitivity for the proposed Einstein Telescope experiment. It appears that on the surface the Newtonian noise is dominated by surface waves, while at depth the body waves are dominant.

6.5 Conclusions

In this chapter, we have discussed the deployment and maintenance of a 3-dimensional seismometer array in the Homestake gold mine. We discussed the general seismic environment at the mine, before introducing analysis techniques used to extract interesting and important information from the data that was acquired. We made a measurement of the fundamental Rayleigh-wave eigenfunction, and then used that information in the seismic radiometer, which attempts to decouple different seismic field components and map the directional dependence of the seismic field. While the seismic radiometer method has drawbacks and limits, illustrated with some of our software injections, the initial results when one component of the seismic field is dominant are promising. We have also attempted to use the seismic radiometer to estimate the Newtonian noise at

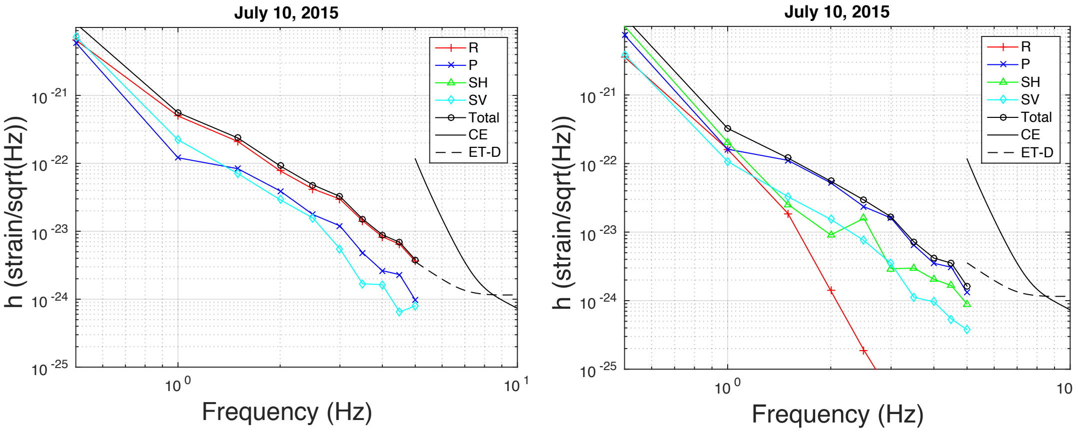

Figure 6.33: Newtonian noise estimate assuming a Cosmic Explorer-like instrument for July 10th, 2015. The colored lines are Newtonian noise estimates using the different mechanisms above and the seismic radiometer recoveries for a cavity on the surface (left), and at 4850 ft (right). The black line (with circles) indicates the total Newtonian noise estimate. The solid black curve on the right indicates the estimated sensitivity for the proposed Cosmic Explorer experiment, while the dashed black curve indicates the estimated sensitivity for the proposed Einstein Telescope experiment [11]. It appears that on the surface the Newtonian noise is dominated by surface waves, while at depth the body waves are dominant.

low frequencies. While a more complete understanding of the seismic radiometer is still necessary to consider the Newtonian noise estimates reliable, the results thus far give answers that are on the same order of magnitude of prior Newtonian noise estimates and illustrate that such an approach is feasible.

Chapter 7

Conclusion and Discussion

Throughout this thesis I have covered a wide array of subjects related to gravitational waves (GWs) and gravitational-wave detectors. The overarching theme has been the overall improvement of the noise level and data quality of the ground-based interferometeric detectors like Advanced LIGO, and the impact that improvement has on current and future searches for a stochastic gravitational-wave background (SGWB).

In chapters 2 and 3 I discussed searches for persistent gravitational waves using LIGO detectors, including searches for an isotropic and anisotropic SGWB, and a directed search for continuous GWs that spans the frequency band from $20 - 1700$ Hz. I implemented a new method for the narrowband radiometer search that set limits on the strain amplitude, h_0, of a potential source of GWs from Scorpius X-1, the galactic center, and Supernova 1987a. Those limits were, at the time they were published, the best limits on h_0 from a potential GW source in those directions.

In chapter 4 I laid out in detail how we come to understand and characterize different aspects of the instrumental noise in the LIGO detectors. This included a discussion of the tools and methods we use in identifying and mitigating “noise lines,” including details about a new tool that I designed called STAMP-PEM. I also describe a pervasive class of glitches in the detectors caused by radio-frequency pickup throughout the instrument. I designed a method for tracking the source of the glitches and estimating their rate of occurrence, while also helping to characterize the local radio frequency environment at the LIGO Livingston detector.

One of the takeaways from the search for an isotropic SGWB is that increasing the sensitivity of GW detectors at lower frequencies drastically improves the sensitivity to $\Omega_{GW}(f)$, and so improved low-frequency sensitivity will be vital for a detection of the SGWB from unresolved compact binary coalescences. The goal of improving sensitivity at lower frequencies is motivation for the work on understanding seismic and Newtonian noise in the Homestake seismometer array (chapter 6), as well as correlated noise (chapter 5). In chapter 6 I outlined the installation and commissioning of the 3D Homestake seismometer array, and then I used data from the array to make novel measurements of the seismic environment. This included a measurement of the surface-wave eigenfunctions, which determine how surface-wave amplitude decays as a function of depth. I then used that eigenfunction measurement in an attempt to separate and measure the individual contribution of each component of the seismic field, which in turn can be used to make an estimate of the Newtonian noise. While the seismic radiometer method is still under development, the results on real data that we presented are a promising step forward in this field.

In chapter 5 I outlined a framework for parameter estimation and model selection using the data products from chapter 2. I then introduced a new code package that can be used to set limits on and distinguish between different models of the SGWB. I then used this method to simultaneously measure an injected SGWB and account for correlated magnetic noise between the GW detectors. While this method is still under development, the current results are encouraging. I have shown that I can successfully perform parameter estimation and model selection on models consisting of both correlated magnetic noise and a combination of correlated magnetic noise and an SGWB. We hope to apply this method to upcoming SGWB searches it Advanced LIGO and Advanced Virgo data.

With the recent observations of the signals from merging black holes and neutron stars, the SGWB now stands as one of the next unexplored frontiers of GW astrophysics. We first hope to measure the SGWB due to unresolved compact binary systems, but down the road a measurement of relic GWs from the early Universe should be a target for future detectors. Those detectors will require phenomenal sensitivity at lower frequencies than LIGO or Virgo have yet reached. Understanding Newtonian noise and correlated noise due to long-wavelength magnetic fields will be vital to the operation and utility of those future detectors.

References

[1] Michael W. Coughlin *et al.*, (2018), arXiv: 1802.00885.

[2] A. Einstein, Sitzungsberichte der Königlich Preußischen Akademie der Wissenschaften (Berlin), Seite 844-847. (1915).

[3] R. A. Hulse and J. H. Taylor, ApJL **195**, L51 (1975).

[4] J. H. Taylor and J. M. Weisberg, ApJ **253**, 908 (1982).

[5] B. P. Abbott *et al.*, Phys. Rev. Lett. **116**, 061102 (2016).

[6] J. Weber, Physical Review Letters **18**, 498 (1967).

[7] The LIGO Scientific Collaboration, Classical and Quantum Gravity **32**, 074001 (2015).

[8] F. Acernese *et al.* (VIRGO), Class. Quant. Grav. **32**, 024001 (2015), arXiv: 1408.3978.

[9] Yoichi Aso, Yuta Michimura, Kentaro Somiya, Masaki Ando, Osamu Miyakawa, Takanori Sekiguchi, Daisuke Tatsumi, and Hiroaki Yamamoto (The KAGRA Collaboration), Phys. Rev. D **88**, 043007 (2013).

[10] H. Grote (LIGO Scientific), Class. Quant. Grav. **27**, 084003 (2010).

[11] Benjamin P. Abbott *et al.* (LIGO Scientific), Class. Quant. Grav. **34**, 044001 (2017), arXiv: 1607.08697.

[12] S Hild *et al.*, Classical and Quantum Gravity **28**, 094013 (2011).

[13] P. Amaro-Seoane *et al.*, ArXiv e-prints (2017), arXiv: 1702.00786.

[14] B. P. Abbott *et al.*, Phys. Rev. Lett. **116**, 241103 (2016).

[15] B. P. Abbott *et al.*, Phys. Rev. Lett. **118**, 221101 (2017).

[16] B. P. Abbott *et al.*, The Astrophysical Journal Letters **851**, L35 (2017).

[17] B. P. Abbott *et al.* (LIGO Scientific Collaboration and Virgo Collaboration), Phys. Rev. Lett. **119**, 141101 (2017).

[18] B. P. Abbott *et al.* (LIGO Scientific Collaboration and Virgo Collaboration), Phys. Rev. Lett. **119** (2017).

[19] B. P. Abbott *et al.*, The Astrophysical Journal Letters **848**, L12 (2017).

[20] M. Maggiore and Oxford University Press, *Gravitational Waves: Volume 1: Theory and Experiments*Gravitational Waves (OUP Oxford, 2008).

[21] Peter R. Saulson, *Fundamentals Of Interferometric Gravitational Wave Detectors (Second Edition)* (World Scientific Publishing Company, 2017).

[22] Benjamin P. Abbott *et al.* (Virgo, LIGO Scientific), Annalen Phys. **529**, 1600209 (2017), arXiv: 1608.01940.

[23] Abbott, B. P., and others, The Astrophysical Journal **839**, 12 (2017).

[24] Abbott, B. P., and others, Phys Rev Lett **118**, 121102 (2017).

[25] L. Sun, A. Melatos, P. D. Lasky, C. T. Y. Chung, and N. S. Darman, Phys. Rev. D **94**, 082004 (2016).

[26] Eric Thrane, Shivaraj Kandhasamy, Christian D. Ott, Warren G. Anderson, Nelson L. Christensen, Michael W. Coughlin, Steven Dorsher, Stefanos Giampanis, Vuk Mandic, Antonis Mytidis, Tanner Prestegard, Peter Raffai, and Bernard Whiting, Phys. Rev. D **83**, 083004 (2011).

[27] Ryan Lynch, Salvatore Vitale, Reed Essick, Erik Katsavounidis, and Florent Robinet, Phys. Rev. D **95**, 104046 (2017).

[28] Benjamin P. Abbott *et al.* (Virgo, LIGO Scientific), (2017), arXiv: 1710.05837.

[29] Dipongkar Talukder, Eric Thrane, Sukanta Bose, and Tania Regimbau, Phys. Rev. D **89**, 123008 (2014).

[30] V. Mandic and A Buonanno, Phys. Rev. D **73**, 063008 (2006).

[31] Michael S Turner, Phys. Rev. D **55**, R435 (1997).

[32] John T Giblin Jr and Eric Thrane, Phys. Rev. D **90**, 107502 (2014).

[33] D. V. Martynov, E. D. Hall, B. P. Abbott, *et al.*, Phys. Rev. D **93**, 112004 (2016).

[34] Tobin T Fricke, Nicols D Smith-Lefebvre, Richard Abbott, Rana Adhikari, Katherine L Dooley, Matthew Evans, Peter Fritschel, Valery V Frolov, Keita Kawabe, Jeffrey S Kissel, Bram J J Slagmolen, and Sam J Waldman, Classical and Quantum Gravity **29**, 065005 (2012).

[35] R De Rosa, F Garufi, L Milano, S Mosca, and G Persichetti, Journal of Physics: Conference Series **228**, 012018 (2010).

[36] L Carbone, S M Aston, R M Cutler, A Freise, J Greenhalgh, J Heefner, D Hoyland, N A Lockerbie, D Lodhia, N A Robertson, C C Speake, K A Strain, and A Vecchio, Classical and Quantum Gravity **29**, 115005 (2012).

[37] Ryan DeRosa, Jennifer C Driggers, Dani Atkinson, Haixing Miao, Valery Frolov, Michael Landry, Joseph A Giaime, and Rana X Adhikari, Classical and Quantum Gravity **29**, 215008 (2012).

[38] B. P. Abbott *et al.* (LIGO Scientific Collaboration), Phys. Rev. D **95**, 062003 (2017).

[39] E. Goetz, P. Kalmus, S. Erickson, R. L. Savage, Jr., G. Gonzalez, K. Kawabe, M. Landry, S. Marka, B. O'Reilly, K. Riles, D. Sigg, and P. Willems, Classical and Quantum Gravity **26**, 245011 (2009).

[40] Carlton M. Caves, Phys. Rev. Lett. **45**, 75 (1980).

[41] Carlton M. Caves, Phys. Rev. D **23**, 1693 (1981).

[42] Peter R Saulson, Phys. Rev. D **30**, 732 (1984).

[43] Brian J Meers and Kenneth A Strain, Physical Review A **44**, 4693 (1991).

[44] Alessandra Buonanno and Yanbei Chen, Phys. Rev. D **64**, 042006 (2001).

[45] A V Cumming, A S Bell, L Barsotti, M A Barton, G Cagnoli, D Cook, L Cunningham, M Evans, G D Hammond, G M Harry, A Heptonstall, J Hough, R Jones, R Kumar, R Mittleman, N A Robertson, S Rowan, B Shapiro, K A Strain, K Tokmakov, C Torrie, and A A van Veggel, Classical and Quantum Gravity **29**, 035003 (2012).

[46] Gregory M Harry, Andri M Gretarsson, Peter R Saulson, Scott E Kittelberger, Steven D Penn, William J Startin, Sheila Rowan, Martin M Fejer, D R M Crooks, Gianpietro Cagnoli, Jim Hough, and Norio Nakagawa, Classical and Quantum Gravity **19**, 897 (2002).

[47] Gregory M Harry, Matthew R Abernathy, Andres E Becerra-Toledo, Helena Armandula, Eric Black, Kate Dooley, Matt Eichenfield, Chinyere Nwabugwu, Akira Villar, D R M Crooks, Gianpietro Cagnoli, Jim Hough, Colin R How, Ian MacLaren, Peter Murray, Stuart Reid, Sheila Rowan, Peter H Sneddon, Martin M Fejer, Roger Route, Steven D Penn, Patrick Ganau, Jean-Marie Mackowski, Christophe Michel, Laurent Pinard, and Alban Remillieux, Classical and Quantum Gravity **24**, 405 (2007).

[48] Jan Harms, Living Reviews in Relativity **18**, 074001 (2015).

[49] Scott A Hughes and Kip S Thorne, Phys. Rev. D **58**, 325 (1998).

[50] Abbott, B. P. and others, Classical and Quantum Gravity **33**, 134001 (2016).

[51] Covas, P.B., and others, arxiv.org (2018), 1801.07204.

[52] E Thrane, N Christensen, and RMS Schofield, Physical Review D **87**, 123009 (2013).

[53] E. Thrane, N. Christensen, R. M. S. Schofield, and A. Effler, Phys. Rev. D **90**, 023013 (2014).

[54] N. Christensen, LIGO Scientific Collaboration, and Virgo Collaboration, Classical and Quantum Gravity **27**, 194010 (2010).

[55] Bruce Allen, Warren G. Anderson, Patrick R. Brady, Duncan A. Brown, and Jolien D. E. Creighton, Phys. Rev. D **85**, 122006 (2012).

[56] Benjamin J. Owen, Phys. Rev. D **53**, 6749 (1996).

[57] Benjamin J. Owen and B. S. Sathyaprakash, Phys. Rev. D **60**, 022002 (1999).

[58] Piotr Jaranowski, Andrzej Królak, and Bernard F. Schutz, Phys. Rev. D **58**, 063001 (1998).

[59] M. Pitkin, M. Isi, J. Veitch, and G. Woan, (2017), arXiv: 1705.08978.

[60] S Klimenko, I Yakushin, A Mercer, and G Mitselmakher, Classical and Quantum Gravity **25**, 114029 (2008).

[61] Patrick J Sutton, Gareth Jones, Shourov Chatterji, Peter Kalmus, Isabel Leonor, Stephen Poprocki, Jameson Rollins, Antony Searle, Leo Stein, Massimo Tinto, and Michal Was, New Journal of Physics **12**, 053034 (2010).

[62] Eric Thrane and Michael Coughlin, Phys. Rev. Lett. **115**, 181102 (2015).

[63] B. Allen and J. D. Romano, Phys. Rev. D **59**, 102001 (1999).

[64] John T Whelan, Santosh Sundaresan, Yuanhao Zhang, and Prabath Peiris, Phys. Rev. D **91**, 102005 (2015).

[65] T. Regimbau, Res. Astron. Astrophys. **11**, 369 (2011).

[66] X.-J. Zhu, E. Howell, T. Regimbau, D. Blair, and Z.-H. Zhu, Astrophys. J. **739**, 86 (2011).

[67] P. A. Rosado, Phys. Rev. D **84**, 084004 (2011).

[68] S. Marassi *et al.*, Phys. Rev. D **84**, 124037 (2011).

[69] C. Wu, V. Mandic, and T. Regimbau, Phys. Rev. D **85**, 104024 (2012).

[70] X.-J. Zhu, E. J. Howell, D. G. Blair, and Z.-H. Zhu, Mon. Not. R. Ast. Soc. **431**, 882 (2013).

[71] I. Kowalska-Leszczynska *et al.*, Astron. Astrophys. **574**, A58 (2015).

[72] Alejandro Lopez and Katherine Freese, Journal of Cosmology and Astroparticle Physics **2015**, 037 (2015).

[73] Jessica L Cook and Lorenzo Sorbo, Phys. Rev. D **85**, 023534 (2012).

[74] Neil Barnaby, Enrico Pajer, and Marco Peloso, Phys. Rev. D **85**, 023525 (2012).

[75] Richard Easther, John T Giblin Jr, and Eugene A Lim, Phys Rev Lett **99**, 221301 (2007).

[76] Richard Easther and Eugene A Lim, Journal of Cosmology and Astroparticle Physics **2006**, 010 (2006).

[77] Rennan Bar-Kana, Phys. Rev. D **50**, 1157 (1994).

[78] Marc Kamionkowski, Arthur Kosowsky, and Michael S Turner, Phys. Rev. D **49**, 2837 (1994).

[79] Arthur Kosowsky, Michael S Turner, and Richard Watkins, Phys Rev Lett **69**, 2026 (1992).

[80] T. Damour and A. Vilenkin, Phys. Rev. D **71**, 063510 (2005).

[81] T. W. B. Kibble, Journal of Physics A Mathematical General **9**, 1387 (1976).

[82] S. Sarangi and S.-H. H. Tye, Physics Letters B **536**, 185 (2002).

[83] X. Siemens, V. Mandic, and J. Creighton, Physical Review Letters **98**, 111101 (2007).

[84] B. P. Abbott *et al.*, Phys. Rev. Lett. **118**, 121101 (2017).

[85] B. P. Abbott *et al.* (LIGO Scientific Collaboration and Virgo Collaboration), Phys. Rev. Lett. **116**, 131102 (2016).

[86] B. P. Abbott *et al.*, Phys. Rev. Lett. **116**, 131102 (2016).

[87] Pablo A. Rosado, Phys. Rev. **D84**, 084004 (2011), arXiv: 1106.5795.

[88] P Ajith, Phys. Rev. D **84**, 6 (2011).

[89] E. Vangioni *et al.*, Mon. Not. R. Ast. Soc. **447**, 2575 (2015).

[90] B. Abbott *et al.*, Astrophys. J. Lett. **818** (2016).

[91] B.P. Abbott, et al (LIGO Scientific Collaboration and Virgo Collaboration), Phys. Rev. X **6**, 041015 (2016).

[92] Eric Thrane and Joseph D Romano, Phys. Rev. D **88**, 124032 (2013).

[93] Abbott, B. P., and others, Phys. Rev. D **76**, 042001 (2007).

[94] C. Palomba, Astron. Astrophys. **354**, 163 (2000), astro-ph/9912356.

[95] Anna L Watts, dx.doi.org **50**, 609 (2012).

[96] Deepto Chakrabarty, Edward H Morgan, Michael P Muno, Duncan K Galloway, Rudy Wijnands, Michiel van der Klis, and Craig B Markwardt, Nature **424**, 42 (2003).

[97] Lars Bildsten, The Astrophysical Journal Letters **501**, L89 (1998).

[98] Riccardo Giacconi, Herbert Gursky, Frank R Paolini, and Bruno B Rossi, Phys Rev Lett **9**, 439 (1962).

[99] Abbott, B. P., and others , Phys. Rev. D **76**, 082001 (2007).

[100] D. R. Lorimer, L. Nicastro, A. G. Lyne, M. Bailes, R. N. Manchester, S. Johnston, J. F. Bell, N. D'Amico, and P. A. Harrison, Astrophys. J. **439**, 933 (1995).

[101] Xilong Fan, Yanbei Chen, and Christopher Messenger, Phys. Rev. D **94**, 084029 (2016).

[102] M Gasperini and G Veneziano, Modern Physics Letters A **08**, 3701 (2011).

[103] Vuk Mandic and Alessandra Buonanno, Phys. Rev. D **73**, 063008 (2006).

[104] M Gasperini and G Veneziano, Astroparticle Physics **1**, 317 (1993).

[105] M. Maggiore, Physics Reports **331**, 283 (2000).

[106] R M Shannon, V Ravi, L T Lentati, P D Lasky, G Hobbs, M Kerr, R N Manchester, W A Coles, Y Levin, M Bailes, N D R Bhat, S Burke-Spolaor, S Dai, M J Keith, S Osłowski, D J Reardon, W van Straten, L Toomey, J B Wang, L Wen, J S B Wyithe, and X J Zhu, Science **349**, 1522 (2015).

[107] Z Arzoumanian, A Brazier, S Burke-Spolaor, S J Chamberlin, S Chatterjee, B Christy, J M Cordes, N J Cornish, K Crowter, P B Demorest, X Deng, T Dolch, J A Ellis, R D Ferdman, E Fonseca, N Garver-Daniels, M E Gonzalez, F Jenet, G Jones, M L Jones, V M Kaspi, M Koop, M T Lam, T J W Lazio, L Levin, A N Lommen, D R Lorimer, J Luo, R S Lynch, D R Madison, M A McLaughlin, S T McWilliams, C M F Mingarelli, D J Nice, N Palliyaguru, T T Pennucci, S M Ransom, L Sampson, S A Sanidas, A Sesana, X Siemens, J Simon, I H Stairs, D R Stinebring, K Stovall, J Swiggum, S R Taylor, M Vallisneri, R van Haasteren, Y Wang, W W Zhu, and The NANOGrav Collaboration, The Astrophysical Journal **821**, 13 (2016).

[108] L Lentati, S R Taylor, C M F Mingarelli, A Sesana, S A Sanidas, A Vecchio, R N Caballero, K J Lee, R van Haasteren, S Babak, C G Bassa, P Brem, M Burgay, D J Champion, I Cognard, G Desvignes, J R Gair, L Guillemot, J W T Hessels, G H Janssen, R Karuppusamy, M Kramer, A Lassus, P Lazarus, K Liu, S Osłowski, D Perrodin, A Petiteau, A Possenti, M B Purver, P A Rosado, R Smits, B Stappers, G Theureau, C Tiburzi, and J P W Verbiest, Monthly Notices of the Royal Astronomical Society **453**, 2576 (2015).

[109] Pau Amaro-Seoane *et al.*, (2017), 1702.00786.

[110] Curt Cutler and Jan Harms, Phys. Rev. D **73**, 042001 (2006).

[111] Naoki Seto, Seiji Kawamura, and Takashi Nakamura, Phys Rev Lett **87**, 221103 (2001).

[112] Paul D Lasky, Chiara M F Mingarelli, Tristan L Smith, John T Giblin Jr, Eric Thrane, Daniel J Reardon, Robert Caldwell, Matthew Bailes, N D Ramesh Bhat,

Sarah Burke-Spolaor, Shi Dai, James Dempsey, George Hobbs, Matthew Kerr, Yuri Levin, Richard N Manchester, Vikram Ravi, Pablo A Rosado, Ryan M Shannon, Renée Spiewak, Willem van Straten, Lawrence Toomey, Jingbo Wang, Linqing Wen, Xiaopeng You, and Xingjiang Zhu, arXiv.org (2015), 1511.05994v2.

[113] Abbott, B. P., and others, Phys Rev Lett **118**, 121101 (2017).

[114] M. J. Mortonson and U. Seljak, ArXiv e-prints (2014), arXiv: 1405.5857.

[115] P. A. R. Ade *et al.* (Planck), Astron. Astrophys. **594**, A13 (2016), arXiv: 1502.01589.

[116] R. Keisler *et al.*, The Astrophysical Journal **807**, 151 (2015).

[117] Luca Pagano, Laura Salvati, and Alessandro Melchiorri, Phys. Lett. **B760**, 823 (2016), arXiv: 1508.02393.

[118] Joseph D. Romano and Neil J. Cornish, Living Rev. Rel. **20**, 2 (2017), arXiv: 1608.06889.

[119] B. Allen and J. D. Romano, Phys. Rev. D **59**, 102001 (1999).

[120] T. Regimbau, Research in Astronomy and Astrophysics **11**, 369 (2011).

[121] J. Aasi *et al.* (LIGO Scientific Collaboration and Virgo Collaboration), Phys. Rev. D **91**, 022003 (2015).

[122] B et. al. Abbott, Phys. Rev. D **76**, 082003 (2007).

[123] J. T. Whelan, E. L. Robinson, J. D. Romano, and E. H. Thrane, Journal of Physics Conference Series **484**, 012027 (2014).

[124] Bruce Allen and Adrian C Ottewill, Phys. Rev. D **56**, 545 (1997).

[125] Stefan W Ballmer, Class. Quantum Gravity **23**, S179 (2006).

[126] Eric Thrane *et al.*, Phys. Rev. D **80**, 122002 (2009).

[127] Sanjit Mitra *et al.*, Phys. Rev. D **77**, 042002 (2008).

[128] J. Aasi *et al.*, Phys. Rev. D. **91**, 062008 (2015).

[129] C. Messenger *et al.*, Phys. Rev. D. **92**, 023006 (2015).

[130] J. Aasi *et al.*, Phys. Rev. D. **88**, 102002 (2013).

[131] C. T. Y. Chung, A. Melatos, B. Krishnan, and J. T. Whelan, Mon. Not. R. Astron Soc. **414**, 2650 (2011).

[132] Chris Messenger, `https://dcc.ligo.org/LIGO-T1000195`.

[133] B P Abbott *et al.*, The Astrophysical Journal Letters **847**, 47 (2017).

[134] Albert Lazzarini, `https://dcc.ligo.org/LIGO-T040128`.

[135] B. P. Abbott *et al.*, **460**, 990 (2009).

[136] J. Aasi *et al.*, Physical Review Letters **113**, 231101 (2014).

[137] Jordan Palamos, `https://alog.ligo-wa.caltech.edu/aLOG/index.php?callRep=23579`, 650 Hz wandering line.

[138] Jordan Palamos, `https://alog.ligo-wa.caltech.edu/aLOG/index.php?callRep=24062`, Evidence that mystery 650Hz noise caused by COMM VCO.

[139] C. Biwer *et al.*, `https://dcc.ligo.org/LIGO-P1600285/public`.

[140] `https://awiki.ligo-wa.caltech.edu/wiki/Resonances`, aLIGO LHO Resonances - T1200415.

[141] M. Coughlin, Ligo Scientific Collaboration, and Virgo Collaboration, Journal of Physics Conference Series **243**, 012010 (2010).

[142] Patrick Meyers, `https://stochastic-alog.ligo.org/aLOG/index.php?callRep=339328`.

[143] Patrick Meyers, `https://stochastic-alog.ligo.org/aLOG/index.php?callRep=339338`.

[144] Letizia Sammut, `https://stochastic-alog.ligo.org/aLOG/index.php?callRep=339346`.

[145] Patrick Meyers *et al.*, `https://dcc.ligo.org/G1601069/`.

[146] B P Abbott *et al.*, Living Reviews in Relativity **19**, 1 (2016).

[147] B. P. Abbott *et al.* (LIGO Scientific Collaboration and Virgo Collaboration), Phys. Rev. D **95**, 122003 (2017).

[148] Patrick Meyers and Rich Ormist, `https://git.ligo.org/patrick-meyers/stamp-pem`.

[149] Duncan Macleod, Alex L. Urban, Scott Coughlin, Thomas Massinger, Joseph Areeda, Eric Quintero, and The Gitter Badger, gwpy/gwpy: 0.10.0, 2018.

[150] `https://d3js.org/`.

[151] Michael Coughlin, the Ligo Scientific Collaboration, and the Virgo Collaboration, Journal of Physics: Conference Series **243**, 012010 (2010).

[152] Schumann, W., Zeitschrift für Naturforschung A **7**, 149 (1952).

[153] J.D. Jackson, *Classical Electrodynamics* (Wiley, 2012).

[154] `http://www.lemisensors.com/?p=245`.

[155] `https://www.geo-metronix.de/mtxgeo/index.php/mfs-06e-overview`.

[156] A. Kulak, J. Kubisz, S. Klucjasz, A. Michalec, J. Mlynarczyk, Z. Nieckarz, M. Ostrowski, and S. Zieba, Radio Science **49**, 361 (2014), 2014RS005400.

[157] Robert Schofield, Anamaria Effler, Julia Kruk, and Philip Nguyen, `https://alog.ligo-wa.caltech.edu/aLOG/index.php?callRep=39199`.

[158] A. Zangwill, *Modern Electrodynamics*Modern Electrodynamics (Cambridge University Press, 2013).

[159] The Astropy Collaboration *et al.*, ArXiv e-prints (2018), arXiv: 1801.02634.

[160] E Thrane, N Christensen, R M S Schofield, and A Effler, Phys. Rev. D **90**, 023013 (2014).

[161] Cody Messick, Kent Blackburn, Patrick Brady, Patrick Brockill, Kipp Cannon, Romain Cariou, Sarah Caudill, Sydney J. Chamberlin, Jolien D. E. Creighton, Ryan Everett, Chad Hanna, Drew Keppel, Ryan N. Lang, Tjonnie G. F. Li, Duncan Meacher, Alex Nielsen, Chris Pankow, Stephen Privitera, Hong Qi, Surabhi Sachdev, Laleh Sadeghian, Leo Singer, E. Gareth Thomas, Leslie Wade, Madeline Wade, Alan Weinstein, and Karsten Wiesner, Phys. Rev. D **95**, 042001 (2017).

[162] Samantha A Usman, Alexander H Nitz, Ian W Harry, Christopher M Biwer, Duncan A Brown, Miriam Cabero, Collin D Capano, Tito Dal Canton, Thomas Dent, Stephen Fairhurst, Marcel S Kehl, Drew Keppel, Badri Krishnan, Amber Lenon, Andrew Lundgren, Alex B Nielsen, Larne P Pekowsky, Harald P Pfeiffer, Peter R Saulson, Matthew West, and Joshua L Willis, Classical and Quantum Gravity **33**, 215004 (2016).

[163] Eric Thrane and Michael Coughlin, Phys. Rev. D **88**, 083010 (2013).

[164] Florent Robinet, `https://tds.ego-gw.it/?content=3&r=12119`.

[165] D. Foreman-Mackey, D. W. Hogg, D. Lang, and J. Goodman, Publications of the Astronomical Society of the Pacific **125**, 306 (2013), arXiv: 1202.3665, Provided by the SAO/NASA Astrophysics Data System.

[166] M Zevin, S Coughlin, S Bahaadini, E Besler, N Rohani, S Allen, M Cabero, K Crowston, A K Katsaggelos, S L Larson, T K Lee, C Lintott, T B Littenberg, A Lundgren, C sterlund, J R Smith, L Trouille, and V Kalogera, Classical and Quantum Gravity **34**, 064003 (2017).

[167] Michael Zevin *et al.*, `https://www.zooniverse.org/projects/zooniverse/gravity-spy`.

[168] Duncan Macleod *et al.*, `https://ldas-jobs.ligo.caltech.edu/~detchar/summary/`.

[169] Michael Zucker, `https://dcc.ligo.org/T020113/public`.

[170] D. Shoemaker, R. Schilling, L. Schnupp, W. Winkler, K. Maischberger, and A. Rüdiger, Phys. Rev. D **38**, 423 (1988).

[171] Rainer Weiss, Patrick Meyers, and Steffen Kaufer, `https://alog.ligo-la.caltech.edu/aLOG/index.php?callRep=19752`.

[172] Richard Abbott, `https://dcc.ligo.org/LIGO-D1001460`, Rack Layout for ISC Input Mode Cleaner electronics and Arm Length Stabilization electronics. Rack is located in LVEA near HAM1. Rack #1.

[173] Richard Abbott and Daniel Sigg, `https://dcc.ligo.org/LIGO-D1001427`.

[174] Michael Laxen, `https://alog.ligo-la.caltech.edu/aLOG/index.php?callRep=26227`.

[175] Richard Abbott, `https://alog.ligo-wa.caltech.edu/aLOG/index.php?callRep=21010`.

[176] Michael Laxen, `https://alog.ligo-la.caltech.edu/aLOG/index.php?callRep=32252`.

[177] Peter Fritschel, `https://dcc.ligo.org/LIGO-E1400180`.

[178] Thomas Callister *et al.*, (2017), arXiv: 1704.08373.

[179] V. Mandic, E. Thrane, S. Giampanis, and T. Regimbau, Phys. Rev. Lett. **109**, 171102 (2012).

[180] Rutger van Haasteren, Yuri Levin, Patrick McDonald, and Tingting Lu, Monthly Notices of the Royal Astronomical Society **395**, 1005 (2009).

[181] Rory Smith and Eric Thrane, Phys. Rev. **X8**, 021019 (2018), arXiv: 1712.00688.

[182] Joseph Romano, (2017), `https://stochastic-alog.ligo.org/aLOG/index.php?callRep=339483`.

[183] T. Callister, L. Sammut, S. Qiu, I. Mandel, and E. Thrane, Physical Review X **6**, 031018 (2016).

[184] Robert E. Kass and Adrian E. Raftery, Journal of the American Statistical Association **90**, 773 (1995), `https://www.tandfonline.com/doi/pdf/10.1080/01621459.1995.10476572`.

[185] John Skilling, Nested Sampling, in *BAYESIAN INFERENCE AND MAXIMUM ENTROPY METHODS IN SCIENCE AND ENGINEERING: 24th International Workshop on Bayesian Inference and Maximum Entropy Methods in Science and Engineering*, pp. 395–405, AIP, 2004.

[186] John Skilling, Bayesian Analysis **1**, 833 (2006).

[187] John Veitch, Walter Del Pozzo, Cody, Matt Pitkin, and ed1d1a8d, johnveitch/cpnest: Minor optimisation, 2017.

[188] W. K. Hastings, Biometrika **57**, 97 (1970).

[189] F Feroz and M P Hobson, Monthly Notices of the Royal Astronomical Society **384**, 449 (2008).

[190] F Feroz, M P Hobson, and M Bridges, Monthly Notices of the Royal Astronomical Society **398**, 1601 (2009).

[191] F Feroz, M P Hobson, E Cameron, and A N Pettitt, (2013), 1306.2144.

[192] D. Sivia and J. Skilling, *Data Analysis: A Bayesian Tutorial*Data Analysis: A Bayesian Tutorial (OUP Oxford, 2006).

[193] J Buchner, A Georgakakis, K Nandra, L Hsu, C Rangel, M Brightman, A Merloni, M Salvato, J Donley, and D Kocevski, Astronomy & Astrophysics **564**, A125 (2014).

[194] Dan Foreman-Mackey, Will Vousden, Adrian Price-Whelan, Matt Pitkin, Victor Zabalza, Geoffrey Ryan, Emily, Michael Smith, Gregory Ashton, Kelle Cruz, and et al., (2016).

[195] Bohua Li, Paul R. Shapiro, and Tanja Rindler-Daller, Phys. Rev. D **96**, 063505 (2017).

[196] P M Shearer, *Introduction to Seismology* (Cambridge University Press, 2009).

[197] K Aki and P G Richards, *Quantitative Seismology*Geology (University Science Books).: Seismology (University Science Books, 2002).

[198] Matthew M Haney and Victor C Tsai, GEOPHYSICS **80**, EN167 (2015).

[199] USGS, Love waves, `https://earthquake.usgs.gov/learn/glossary/?term=Love%20wave`, Accessed: 2018-04-18.

[200] USGS, Rayleigh waves, `https://earthquake.usgs.gov/learn/glossary/?term=Rayleigh%20wave`, Accessed: 2018-04-18.

[201] F E Richart, J R Hall, and R D Woods, *Vibrations of soils and foundations*Civil Engineering (Prentice-Hall, 1970).

[202] Bruce T Cleveland, Timothy Daily, Jr Raymond Davis, James R Distel, Kenneth Lande, C K Lee, Paul S Wildenhain, and Jack Ullman, The Astrophysical Journal **496**, 505 (1998).

[203] J Harms, F Acernese, F Barone, I Bartos, M Beker, J F J van den Brand, N Christensen, M Coughlin, R DeSalvo, S Dorsher, J Heise, S Kandhasamy, V Mandic, S Márka, G Mueller, L Naticchioni, T O'Keefe, D S Rabeling, A Sajeva, T Trancynger, and V Wand, Classical and Quantum Gravity **27**, 225011 (2010).

[204] M Coughlin, J Harms, and N Christensen, Classical and Quantum Gravity **31**, 215003 (2014).

[205] Tanner Prestegard, *Unmodeled searches for long-lasting gravitational-wave signals with LIGO and studies of underground seismic noise for future gravitational-wave detectors*, PhD thesis, University of Minnesota, 116 Church St. SE, Minneapolis, MN, 55455, 2016.

[206] Streckeisen sts-2 seismometer, `https://www.passcal.nmt.edu/content/instrumentation/sensors/broadband-sensors/sts-2-bb-sensor`, Accessed: 2017-01-15.

[207] Guralp cmg-3t, `https://www.passcal.nmt.edu/content/instrumentation/sensors/broadband-sensors/cmg-3t-bb-sensor`, Accessed:2017-01-15.

[208] Q330, `http://www.q330.com`, Accessed:2017-01-15.

[209] Vip 110-24 series advanced wireless ethernet bridge user guide, `http://l2a.ucsd.edu/local/Manuals/wilan_operators_manual.pdf`, Accessed: 2018-04-18.

[210] J Peterson, (1993 (unpublished)), U.S. Department of Interior Geological Survey Report No. OFR 93-322.

[211] E. Wielandt, NMSOP **1** (2002).

[212] T. Lay and T.C. Wallace, *Modern Global Seismology*International Geophysics (Elsevier Science, 1995).

[213] M. Coughlin *et al.*, In preparation.

[214] N. Christensen, Phys. Rev. **D46**, 5250 (1992).

[215] G.H. Golub and C.F. Van Loan, *Matrix Computations*Johns Hopkins Studies in the Mathematical Sciences (Johns Hopkins University Press, 1996).

[216] Christopher C. Paige and Michael A. Saunders, ACM Trans. Math. Softw. **8**, 43 (1982).

[217] Jonathan R Shewchuk, (1994), An Introduction to the Conjugate Gradient Method Without the Agonizing Pain.

[218] K M Gorski, E Hivon, A J Banday, B D Wandelt, F K Hansen, M Reinecke, and M Bartelmann, The Astrophysical Journal **622**, 759 (2005).

Appendix A

Notches made for O1 analysis

Line or Comb	Frequency (Hz)	Description/justification
Comb	Offset 0.5 Hz, Spacing 1 Hz	1 Hz comb
Comb	Offset 0 Hz, Spacing 16 Hz	16 Hz comb
Comb	Offset 60 Hz, Spacing 1 Hz	Power mains
Line	20.22	Unknown, H1 aux
Line	20.40	Unknown, turns on mid-run at H1 only
Line	23.36	Unknown, overlaps comb at LLO
Line	24.25	Unknown, part of comb at both sites
Line	25.00	Unknown, part of comb at both sites
Line	26.17	Unknown, very strong single-detector line at H1 only
Line	30.00	Unknown, 1 Hz comb
Line	47.69	Unknown, aux channel coherence
Line	100.00	Unknown, 1Hz comb
Line	453.32	Unknown, aux channel coherence
Line	1352.90	Unknown, likely digital line at LHO
Line	34.7	Calibration (L1)
Line	35.3	Calibration (L1)
Line	36.7	Calibration (H1)
Line	37.3	Calibration (H1)
Line	331.3	Calibration (L1)
Line	331.9	Calibration (H1)
Line	1083.1	Calibration (L1)
Line	1083.7	Calibration (H1)
Line	3001.1	Calibration (L1)
Line	3001.3	Calibration (H1)
Line	480-520	Violin mode first harmonic region
Line	960-1040	Violin mode second harmonic region
Line	1455-1540	Violin mode third harmonic region

Line	1200-1300	Wandering line at Hanford
Line	12.43	Pulsar injection
Line	26.34	Pulsar injection
Line	31.42-31.43	Pulsar injection
Line	38.43-38.51	Pulsar injection
Line	52.80-52.81	Pulsar injection
Line	108.85-108.87	Pulsar injection
Line	146.11-146.21	Pulsar injection
Line	190.95-191.09	Pulsar injection
Line	575.11-575.22	Pulsar injection
Line	265.55-265.60	Pulsar injection
Line	763.77-763.92	Pulsar injection
Line	848.88-849.06	Pulsar injection
Line	1220.43-1220.68	Pulsar injection
Line	1393.23-1393.79	Pulsar injection

Table A.1: Notch list used in SGWB searches for O1. This table lists the frequencies which were not analyzed in SGWB searches in O1 due to strong instrumental contamination. A 0.1 Hz region around each of the harmonics of the 60 Hz lines was removed. Calibration lines at each site, and frequencies with hardware injections simulating pulsars were also removed. For the pulsar injections, we account for the Doppler shift and the spin-down of the pulsar over the course of the run. We remove a broad band around the harmonics of the violin modes because of excess noise in these regions. We also remove a wandering line seen at H1. Finally, we remove lines seen as coherent between H1 and L1 which have been determined to contaminated with instrumental artifacts.